Transport in laser-produced plasmas

Adam Devlin Dearling

Doctor of Philosophy

University of York

School of Physics, Engineering and Technology

May 2024

Abstract

Heat-flow is of fundamental interest in plasmas with extreme temperature gradients. Transport effects such as heat-flow are driven by anisotropy within the distribution function in plasma systems. When these plasmas are magnetised, there is a fundamental coupling between the anisotropic transport and magnetic field dynamics. As anisotropy increases, the system is driven from local thermodynamic equilibrium (LTE). Fluid models, which often assume the anisotropy leads to only a small perturbation away from a Maxwellian distribution, can then fail to accurately describe transport effects far from LTE. This thesis examines how magnetisation suppresses anisotropic transport perpendicular to the magnetic field axis and restores local thermodynamic equilibrium.

Kinetic modelling of electron transport is performed using a Vlasov-Fokker-Planck (VFP) code. Magnetisation of a plasma most significantly affects the relatively collisionless heat-carrying electron population, reducing the heat-carrying velocity. Suppression of anisotropic transport is demonstrated by increasing the magnetisation, which can be done by both increasing the magnetic field strength and decreasing the collision frequency. On decreasing the collision frequency in the weakly magnetised regime anisotropy initially increases. However, once the heat-carrying electrons are strongly magnetised transport becomes increasingly local as the collision frequency decreases further. This result is attributed to a reduction in the heat-carrying electron mobility relative to the thermal electron population.

An experiment is then described that provides the first direct measurement of the Nernst effect, the transport of magnetic fields driven by heat flow. Proton radiography and interferometry measurements were used to demonstrate a decoupling of the magnetic field advection from the bulk flow. Despite the demagnetisation of the hot plasma, the transport was found to be kept in a relatively local regime due to the formation of a magnetic transport barrier at the edge of the heat-front. On decreasing the gas density used in the experiment suppression of the Nernst effect was observed.

Acknowledgements

My PhD has certainly been a journey - one in which I have seemingly attempted to 'complete all the side-quests', in the words of a wise physicist. While a more direct route may have perhaps been easier it would also not have allowed me to meet so many great physicists, and more importantly good people. There is no better way to learn during a PhD than from others.

The journey would not have been possible without my supervisors. First, my thanks go to Nigel Woolsey who has been pivotal in my development as a scientist. I always looked forward to our conversations and will miss not being able to knock on his door every day! I am also sincerely grateful to Christopher Ridgers for his wisdom and humour.

From my time in Osaka I have to thank Youichi Sakawa and the laboratory astrophysics group for making me feel so welcome. I sincerely hope our paths continue to cross in the future, if for no other reason than to share a glass of shochu and enjoy good humour at the end of a long week's experiment. Meeting Bruno Albertazzi and Michel Koenig during this time also had a significant impact on my PhD - thank you both for inviting me to LULI, I thoroughly enjoyed my time working and learning from you both.

During time closer to home I have to thank those in the YPI. First to Nigel's group past and present - Phillip Bradford, Luca Antonelli, Matthew Khan, Arun Nutter, Calum Freeman, Yuyao Wang, and Ben Fisher. I'd also like to thank the others in the YPI who made the community there so special - Christina Ingelby, Louis Ingle, Emma Hume, Bob Davies, Nathan Smith, and others. In particular, a shout-out goes to office GN/110, thank you for not letting me go down all those rabbit holes alone.

There is one other individual in the YPI who has gone above and beyond in all aspects though. The beating heart of the YPI - Christopher Arran. I would never have accomplished anywhere near as much without you, and I am sure many others can say the same. Despite my incessant pestering, you were always there for a chat.

To my closest friends Barney, Ali, Mikey, and Chris, thank you for always looking out for me and helping me escape over the years.

A special thanks go to my Mum, Karolyn, for looking after me once again during the twilight hours of my PhD. I also have to thank my Dad, Bruce, without whom I may never have started looking up at the stars in the first place. Finally to my brother, Luke, thank you for always making me laugh and getting me out of there once it was all over.

To Lauren - thank you for making it all worthwhile.

Author's Declaration

The kinetic code IMPACT used in this report was written by Robert Kingham (Imperial College), who also kindly updated the code for use on Viking 2, with extensions by Christopher Ridgers. Simulations with this code were conducted on the Viking cluster, a high performance compute facility provided by the University of York. The fluid code CTC was written by John Bissel (University of York). All simulations presented here were conducted by the author.

The experimental results described in this thesis were obtained during experiments at the Vulcan laser facility, conducted as part of large collaborations. In chapter 5 proton radiography data was obtained from an experiment led by David Carroll; the author contributed to set-up and measurement during the experiment and performed the analysis shown here. In chapter 7 proton radiography and interferometry were obtained from an experiment led by Nigel Woolsey for which the author was not present. The proton tracking and reconstruction codes used in chapters 5 and 7 were written by the author. Reconstructions of the experimental proton-radiography and interferometry data were provided by Christopher Arran.

The following publication contains work that is discussed in this thesis:

- C. Arran et al. "Measurement of Magnetic Cavitation Driven by Heat Flow in a Plasma". In: *Physical Review Letters* 131.1 (July 2023), p. 015101. ISSN: 10797114. DOI: 10.1103/PHYSREVLETT.131.015101/FIGURES/5/MEDIUM. URL: https://journals.aps.org/prl/abstract/10.1103/PhysRevLett.131.015101

I declare that this thesis is a presentation of original work and I am the sole author. This work has not previously been presented for a degree or other qualification at this University or elsewhere. All sources are acknowledged as references.

Contents

List of Figures

Chapter 1

Introduction

1.1 Motivation

Most of the known universe is permeated by matter in the plasma state, and where there is plasma, there are almost always magnetic fields. Their interaction is significant in the most extreme astrophysical events, such as supernovas and pulsars. Closer to home they have also played a part in human evolution, with the Earth's magnetic field protecting us from the solar wind. This thesis will consider the interplay between magnetic field dynamics and heat transport in high energy-density (HED) matter, which is more closely aligned to supernovas than the solar wind.

High-energy-density systems are typically defined as having a pressure above 1 Mbar, which can be true of a system at high temperature and low density ($\sim$ 1 keV at $10^{-3}\times$ solid density) or relatively low temperature and high pressure ($> 10\times$ solid density) [2]. As one enters this regime, compression or thermal ionisation leads to the delocalisation of large numbers of electrons and as such high-energy-density matter is plasma. It shares with both ideal plasmas and condensed matter the fact that collective behaviour is an essential part of its description. Unlike ideal plasmas, the behaviour of high-energy-density matter is more strongly correlated. Additionally, it differs from condensed matter physics in that ionisation and Coulomb interactions play a fundamental role in its description.

The key regimes and boundaries in high-energy-density plasmas are outlined in fig. 1.1 at pressures above 1 Mbar. The ideal plasma state is found at higher temperatures and lower densities. Here the plasma can be approximated as a classical gas, with thermal pressure resulting from Coulomb collisions resisting compression of the plasma. It is in this regime where the kinetic and fluid models discussed in this thesis operate. As the plasma transitions into the cold, dense regime, non-ideal behaviour

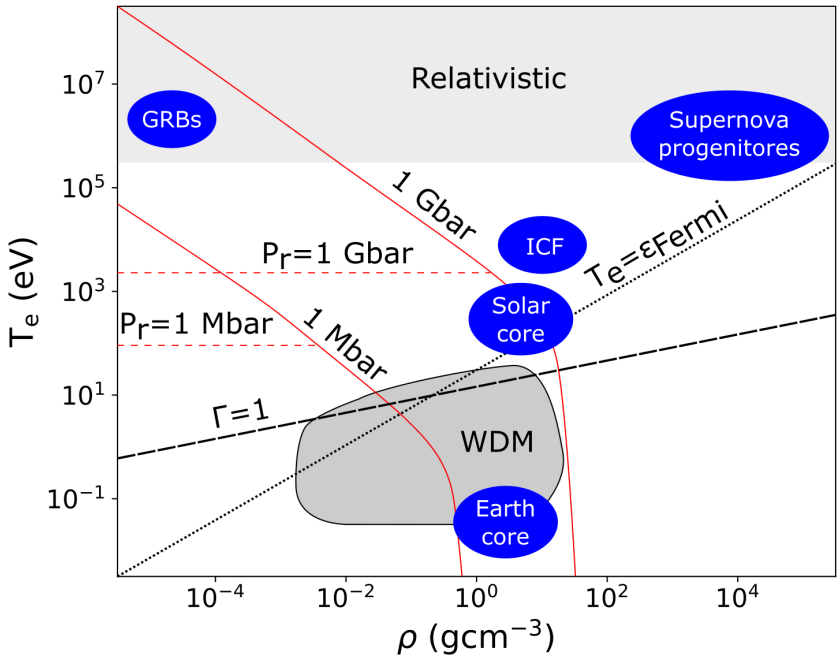

Figure 1.1: The high energy density parameter space. The locations where the matter pressure is equal to 1 Mbar and 1 Gbar are shown (solid red), as well as the radiation pressure $P_r \propto T^4$ (dashed red). A diagonal line (dotted) shows the boundary where $T_e = \epsilon_{\text{Fermi}}$ at which point the electron temperature is equal to the Fermi temperature. Below this line electrons are Fermi-degenerate, and the pressure far above that of an ideal plasma. The boundary where the strong coupling parameter $\Gamma = |e\phi|/T_e = 1$ is shown (dashed). Above this line the plasma gradually transitions to being weakly coupled, resulting in regions where the plasma is not Fermi-degenerate but cannot be treated as an ideal plasma. In the centre of the plot the region of parameter space corresponding to warm dense matter (WDM) is shown (dark grey), where the matter is too ionised for a condensed matter model but too strongly correlated to be treated as an ideal plasma. Finally, at temperatures of hundreds of keV, the electrons become relativistic (light grey). The approximate location of a burning ICF plasma is indicated, along with examples of several astrophysical environments including gamma-ray bursts (GRBs).

begins to emerge. In particular, electrons and ions become strongly coupled, with the thermal energy no longer significantly greater than the potential energy from particle interactions, leading to increased particle correlations. This behaviour is further explored in section 2.1, where electron screening and the Debye length are introduced. At sufficiently high densities, quantum mechanical effects, resulting from the Pauli exclusion principle, generate pressure that resists compression. This phenomenon occurs at the Fermi temperature.

The high-energy-density plasmas considered in this thesis will be those generated by high-intensity ($> 10^{14}$ Wcm^{-2}) long-pulse ($\sim$ ns) lasers, which in the context of magnetic field dynamics and heat transport have the important property of having

large gradients in temperature and density. Magnetic fields can be present in these plasmas for several reasons. They can be self-generated via effects such as the Biermann battery, a source of magnetic field in plasmas with misaligned density and temperature gradients. Alternatively, they can be applied externally to the plasma, for example with an electromagnet. Classically, the dynamics of magnetic fields and heat-flow can be investigated using Braginskii's magnetohydrodynamic (MHD) equations [3], which tell us how heat flow is both modified by a magnetic field, resulting in a reduction in conductivity, while also advecting the magnetic field via the Nernst effect.

However, in plasmas generated by high-intensity lasers, the assumptions of the classical model begin to break down as the electron mean free path becomes comparable with the system length scale due to large gradients in the temperature. In the field of fluid dynamics this ratio is quantified by the Knudsen number. At this point non-local' transport effects are observed, and a resulting deviation in the predictions of computational fluid models when compared to experimental results. Key issues relate to the interaction of magnetic field dynamics and non-local heat-flow in these systems, and the validity of magnetohydrodynamic simulations needs to be addressed.

1.2 Inertial confinement fusion

Much of the progress in high-energy-density science has been driven by the pursuit of inertial confinement fusion (ICF) [4]. Alongside magnetic confinement fusion (MCF) [5], ICF forms one of the two primary branches of fusion physics. The objective of both approaches is to assemble fusion fuel at sufficiently high temperature and density, such that the energy released by thermonuclear fusion during confinement surpasses the energy input to the fuel, resulting in a net energy gain. Achieving net energy gain from fusion has long been regarded as the 'holy grail' of clean energy research.

In ICF confinement is achieved by rapidly compressing and heating a capsule containing the fusion fuel, relying upon material inertia to hold the fuel together long enough that a significant fraction fuses. The favoured fuel is a 50:50 mix of deuterium (D) and tritium (T), which react according to the equation

$$\mathrm{D} + \mathrm{T} \rightarrow \alpha(3.5\ \mathrm{MeV}) + \mathrm{n}(14.1\ \mathrm{MeV}) \tag{1.1}$$

where the energy released during the reaction is partitioned between the kinetic

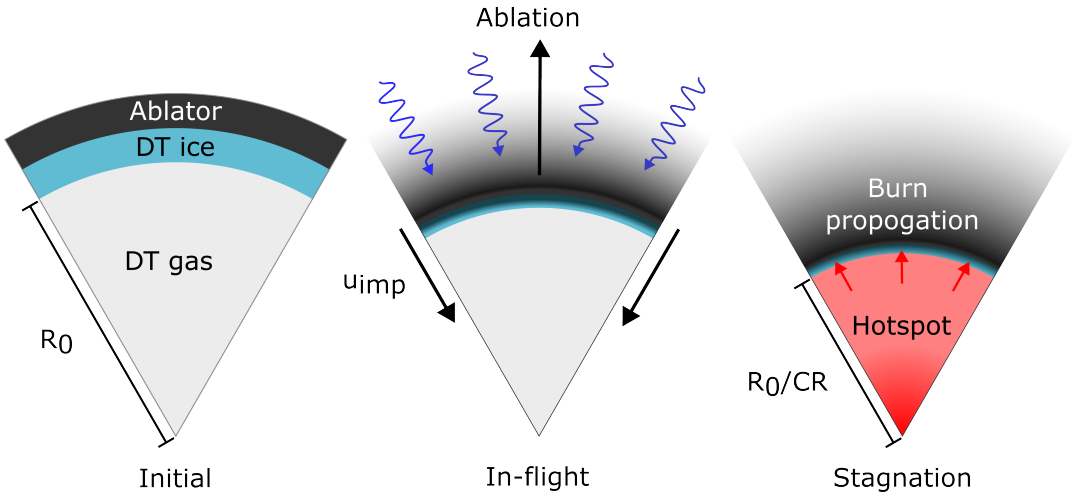

Figure 1.2: Schematic diagram of a spherical ICF capsule undergoing hotspot ignition. The target consists of concentric shells, with the outermost the ablator. This surrounds a layer of DT ice that has inner radius R_0, with the remainder of the capsule filled with DT gas. Radiation incident on the capsule heats the ablator, causing it to explode outwards. The ablation of material launches a shock that compresses the DT fuel, imploding the target by conservation of momentum at velocity u_{imp}. As the capsule converges it begins to decelerate as kinetic energy is converted into internal energy, until reaching stagnation. If the convergence ratio CR is sufficient to heat and compress the fuel to ignition conditions, a burn wave propagates from the hotspot into the ice layer.

energy of the products. The alpha particles deposit some of their energy in the fuel causing self-heating, raising the temperature of the fuel. As the DT reaction rate increases with temperature, self-heating results in an increase in the rate of alpha particle production rate, further increasing the temperature. The aim is for heating from alpha particles created during the fusion process overcome the loss mechanisms in the system; these losses are attributed to radiation, hydrodynamic disassembly, and thermal conduction. At this point *ignition* occurs, corresponding to a dramatic increase in fuel temperature and energy yield. Fusion neutrons that escape the plasma can be used for a variety of applications, including use as an energy source.

There are several approaches to achieving ignition in the fuel capsule, with the most common being *hotspot* ignition. Here, a small portion of the total fuel is heated, which can then ignite and drive a propagating burn wave into the surrounding cold, dense fuel. This approach significantly increases the potential for energy gain, while reducing the drive energy required. In fig. 1.2 a typical design for a hotspot ignition target is shown; it consists of a solid, low atomic (low-Z) *ablator*, followed by a layer of DT ice and a gaseous DT core. An alternative approach, in which the entire fuel is uniformly brought to ignition conditions, is known to as *volume* ignition [6].

The two main drivers used for compression and heating in current ICF research

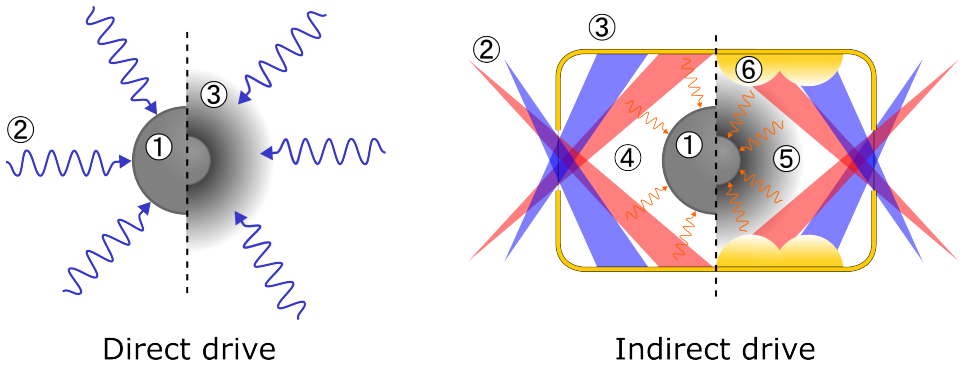

Figure 1.3: The direct drive and indirect drive ICF schemes. In each scheme the target is shown when lasers are initially incident (left half) and mid-implosion (right half). In direct drive, the fuel capsule (1) is directly heated by laser beams (2). This result in ablation (3) that implodes the fuel capsule. Meanwhile in indirect drive, the fuel capsule (1) is indirectly driven by the lasers (2). Here, lasers enter through the entrance of the gold hohlraum (3), which is filled with gas, irradiating the inner surface and generating a thermal x-ray bath (4). It is the x-rays that then drive ablation (5) of the target surface and implosion of the fuel capsule. As the lasers continue to irradiate the hohlraum inner surface it is ablated, forming gold bubbles (6).

are laser drivers and pulsed power drivers. Of these, laser drivers are the most advanced ICF technologies, with the primary schemes used to supply energy to the ablator *direct drive* and *indirect drive* as outlined in fig. 1.3. In direct drive, laser beams directly irradiate the fuel capsule, whereas in indirect drive, the lasers heat a hohlraum surrounding the capsule, generating a thermal x-ray bath that irradiates the capsule. Direct drive offers the greatest advantages to future inertial fusion energy schemes over indirect drive, as it is not limited by energy conversion in the hohlraum. However, it is more susceptible to drive non-uniformity, seeding both low and high mode perturbations that can grow unstable, as well as the effect of laser plasma instabilities within the corona [7]. In contrast, indirect drive is less sensitive to these challenges.

Early experiments were primarily limited by implosion symmetry and the growth of hydrodynamic instabilities during compression, as achieving uniformity was crucial to maximising fuel heating and compression. Low mode asymmetries typically result in reduced compression of the fuel compared to the desired spherical implosion. For example, if the capsule was driven harder at the poles than the equator, the implosion will form a pancake. High mode asymmetries result in instabilities, such as the Rayleigh-Taylor and Richtmeyer-Meshkov instabilities, which grow during compression, shredding the capsule and mixing ablator material into the DT fuel. This radiatively cools the hotspot, reducing the temperature and the alpha reaction rate. Key improvement were made in controlling implosion symmetry and

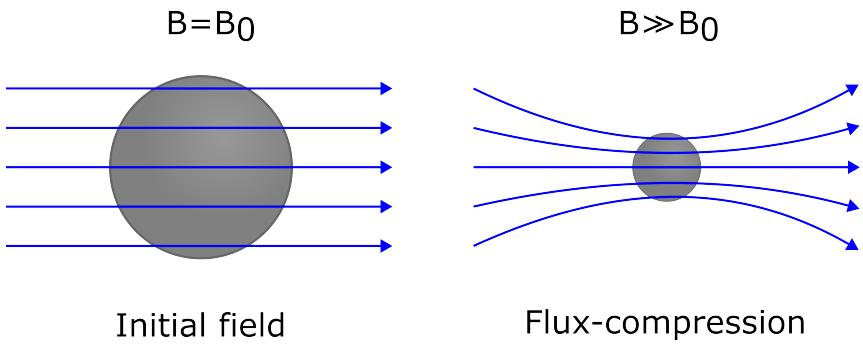

Figure 1.4: Schematic diagram showing the flux-compression of an initially spatially uniform magnetic field B_0. During implosion of the fuel capsule, Alfvén's frozen-in-flux theorem states that magnetic fields will move together with the fluid if it is an ideal plasma. The result is an increase in the magnetic field flux for a spherical target undergoing compression of $B = B_0 CR^2$ where CR is the convergence ratio of the target.

instability growth by careful tuning of the laser drive. These include varying the pulse shape of the laser, allowing control of the timing and strength of the shocks that are launched through the ablator and fuel, to set the adiabat [8]. Increasing the adiabat makes fuel less compressible, but more stable to hydrodynamic instabilities. Another development was the use of crossed-beam energy transfer to improve implosion symmetry [9].

The last few years have marked a turning point in the pursuit of fusion, driven by the first demonstration of ignition in an ICF experiment at the National Ignition Facility (NIF) in 2021 [10]. Since then, the first target gain exceeding unity ($G \sim 1.5$) has been measured in 2022 [11]. This corresponds to a yield of 3.1 MJ with an input energy of 2.05 MJ. The indirect drive facility has since produced yields of $\sim$ 5.2 MJ, with gain exceeding $G > 2$, driven by facility upgrades that have increased the laser energy to 2.2 MJ [12]. Many of these improvements have been incremental, allowing current experiments to access the 'ignition cliff' where small changes in target dynamics can lead to large changes in yield when entering the burning plasma regime [13].

In order to accelerate the progress towards the realisation of inertial fusion energy, novel ICF designs are now being explored that offer pathways to higher gain. These include the use of an applied magnetic field to pre-magnetise the target, which can modify energy balance in the fuel by reducing thermal conduction losses while increasing alpha particle heating [14]. This allows higher hotspot temperatures to be achieved, relaxing the ignition criteria and boosting yield. It is with this application in mind that this thesis will explore the coupling between magnetic field dynamics and heat-flow, seeking to observe how magnetic fields both suppress thermal conduction while also being advected by it through the Nernst effect.

For magnetic fields to modify heat-transport in the plasma, the fields must be of sufficient strength to magnetise charged particles, such that their gyro-radius decreases below the mean-free-path ($r_g < \lambda$). As the mean-free-path scales with velocity as $\lambda \propto v^4$, while the gyro-radius scales as $r_g \propto v$, the transport of hotter particles is more strongly suppressed by a magnetic field, a property that will be central to the discussion of electron transport trends in chapters 3 and 4. Due to their lower mass electrons are magnetised before ions; fields on the order of $B \sim 1$ kT are need to magnetise electrons within the hotspot, while a stronger field of $B \sim$ 7 kT is required to confine 3.5 MeV alpha particles in a hotspot of radius ~ 40 µm [15]. While such fields are difficult to generate directly, magnetic flux compression (fig. 1.4) can amplify a seed field by factors of over 100 [16].

There is an inherent anisotropy between transport perpendicular and parallel to the magnetic field lines, with electron transport only confined to gyro-orbits in the plane perpendicular to the field. As transport becomes more strongly magnetised, the thermal conductivity is only modified in the direction perpendicular to the field. Important symmetry considerations arise, as this affects the distribution of laser heat and reduces uniformity during the implosion [17]. While the thermal pressure is typically much larger than the magnetic pressure, so hydrodynamic evolution is not directly affected, the indirect effects resulting from the modification of thermal conductivity have the greatest impact on symmetry. There are open questions regarding experiment designs that seek to maximise the benefits of magnetic field while minimising potential drawbacks.

The study of magnetic fields is crucial not only for ICF designs that incorporate an applied magnetic field but also initially unmagnetised plasmas due to field generation mechanisms, with the Biermann battery being the most notable example. These self-generated fields emerge during laser ablation [18] and at unstable interfaces [19]. Since instability growth is a common challenge in most ICF schemes, enhancing our understanding of magnetic field dynamics is essential for advancing the development of high-gain ICF targets.

A final consideration regards the correct treatment of heat-transport and magnetic field dynamics in ICF experiments. Accurate models are required to predict the performance of fusion targets, as the complexity of the integrated physics problem is such that relying solely upon experiments would be both prohibitively expensive and time-consuming. In both direct- and indirect-drive experiments, temperature and density gradients are such that our current best fluid models, which are necessary due to the spatial and timescales involved, cannot fully capture transport effects throughout the entire target. This limitation arises from kinetic effects linked to non-local transport of electrons and ions, whose mean-free-path is of the order of the

plasma length scale [20]. Chapters 3 and 4 are motivated by a desire to understand the regimes in which the extended magnetohydrodynamic model remains valid, and to investigate how non-local electron transport influences both heat-transport and magnetic field dynamics. The plasma conditions explored in the simulations and experiments discussed in chapters 4, 6, and 7 are representative of those encountered in ICF targets, particularly those found at the ablation front in direct-drive experiments or within the hohlraum, where the laser heats the gas fill and ablates the gold walls during indirect-drive experiments.

1.3 Laboratory astrophysics

The advancement of facilities capable of conducting high-energy-density matter experiments has made it possible to study astrophysical systems in a laboratory setting, with the breadth of application clear from fig. 1.1. Observations of astrophysical systems from Earth are inherently constrained by the great distances and timescales associated with these events. Even for space plasmas, which are those located within our solar system, the spatial scales of shocks and waves are much larger than the *in situ* probes used to measure them. However, experimental studies can complement these observations, provided that they can be recreated in a laboratory setting, allowing new insights to be obtained from perspectives that would be otherwise inaccessible.

Laboratory measurements of astrophysical systems can be broadly categorised into two types [21, 22]. The first category focuses on material properties and microphysics, including the equation of state, opacity, and nuclear cross-sections. The second category of experiment is concerned with the dynamics of astrophysical systems. Dynamic processes that can be studied at HED facilities include astrophysical jets [23], the formation of magnetic fields [24], turbulence [25], collisionless shocks [26], magnetic reconnection [27], and star formation[28].

To enable laboratory astrophysics experiments to be related to their astrophysical counterparts, a formalism is required that allows us to understand the degree to which a given comparison is physically reliable and valid. For this purpose, scaling laws have been derived [29, 30, 31], which take the key characteristics of one system and map them to another. This approach does not rely on the individual variables of a system (such as the mass, temperature or size). Instead, it combines various variables to create a set of scaled quantities. If these scaled quantities are invariant between systems, then the laboratory experiment can model the astrophysical system.

When deriving these scaled quantities, the equations used to describe the evolution of both systems must be the same. For example, both systems may be governed by the equations of hydrodynamics. Additionally, the key terms in these equations that are critical for describing the overall dynamics must be the same for both systems. In the case of systems described by hydrodynamics, this might mean that both systems have a large Reynolds number, implying that inertial forces dominate and viscosity can be neglected. If a magnetic field is present in the astrophysical system for which scaling relations are sought, the magnetohydrodynamic equations should be used instead, introducing additional scaled quantities. It may appear to become increasingly unrealistic to obtain a perfectly scaled experiment as the complexity of the modelled system increases, but for dimensionless scaling parameters sufficiently far from unity the numbers need to be identical.

1.4 Thesis outline and author's contribution

The main focus of this thesis will be on the suppression of anisotropic electron transport in magnetised laser-plasmas. When anisotropy in the electron distribution function is significant non-local transport occurs, which is a major challenge for fluid models that are used to simulate HED plasmas, such as those encountered during ICF and laboratory astrophysics experiments. In chapter 3 kinetic theory is used to develop a model that identifies trends in the growth of the relative anisotropy in magnetised plasmas, which is then tested in chapter 4. Chapters 6 and 7 apply this model to simulations and experimental data obtained using a platform designed to measure the Nernst effect, with chapter 5 reviewing the proton radiography diagnostic which was required to make this measurement possible.

- **Chapter 2 - Theory of magnetised plasmas:** An overview of the kinetic equations governing plasma evolution is provided, with the Vlasov-Fokker-Planck equation expanded in Cartesian tensors to reduce the complexity of the equation. This is first step in the derivation of classical transport theory, which will be key in understanding heat and magnetic field transport effects relevant to the laser plasmas discussed in this thesis. Mechanisms via which the fluid approximation is invalidated are highlighted, namely inverse bremsstrahlung heating and non-local transport.
- **Chapter 3 - Local transport phenomena in magnetised plasmas:** The kinetic equation governing anisotropy in the electron distribution function is examined, providing insight into the regimes where fluid models are valid, including when the plasma is magnetised. Fluid models assume the relative

anisotropy is small, ensuring that transport remains local and the distribution function stays close to Maxwellian. The kinetic equation naturally leads to the definition of an effective mean-free-path, which relates the growth of relative anisotropy to plasma parameters in the local limit. To identify the electron populations most influential in transport trends, the velocities of the current- and heat-carrying electrons are obtained as a function of magnetisation. The trends associated with effective mean-free-path are then discussed in the context of increasing relative anisotropy and non-local transport.

- **Chapter 4 - Kinetic transport phenomena in magnetised plasmas:** Simulations are performed exploring the key trends predicted when using the effective mean-free-path to predict the growth of the relative anisotropy in magnetised plasmas. This approach identifies regimes in which the fluid approximation fails due to non-local transport when applied to the heat-carrying electron population, provided electron inertia is not significant. The connection between the relative anisotropy and transport effects is highlighted, emphasising the relationship between heat-flow and magnetic field dynamics.

- **Chapter 5 - Proton radiography in laser-plasma experiments:** The use of proton radiography as a diagnostic for electric and magnetic field structures is reviewed. This technique plays a central role in the experimental results presented in this thesis, which includes the first direct measurements of the Nernst effect in a laser-plasma experiment, providing the motivation for this comprehensive discussion. First, the process of extracting dose information from radiochromic film is explained, enabling the determination of proton beam characteristics such as the temperature. Secondly, the method of deflection mapping is reviewed, which allows the electric and magnetic field structures to be obtained. Finally, the effect of smearing caused by imaging in a large applied magnetic field is explored.

- **Chapter 6 - Simulations investigating transport in laser-plasmas:** A laser-plasma experiment is simulated in which an under-dense gas jet is heated by a long-pulse laser. The symmetry of the experiment allows extended MHD effects to be investigated. Specifically, the thermo-electric effect, which is related to the Biermann battery, and Nernst effect are dominant when the plasma is either initially unmagnetised or magnetised along the laser axis respectively. These effects are important in magnetised laser-plasma experiments, and can be modified by non-local transport. Comparisons are made between kinetic and fluid simulations, allowing the validity of the fluid model to be tested. These comparisons are supported by the analysis of the relative anisotropy performed earlier in this thesis.

- **Chapter 7 - Experiments investigating transport in laser-plasmas:** An experiment providing the first direct measurement of the Nernst effect is analysed, utilising the platform discussed in chapter 6. The Nernst effect was found to be suppressed by increasing magnetisation at lower density, a result that leads to increasingly local transport following the model developed in chapters 3 and 4. Measurements of the thermo-electric field are also discussed. Using a combination of synthetic radiography and experimental results, the separation of the electric and magnetic field structures in this cylindrical geometry is demonstrated.

The work in chapter 3 describing the use of the effective mean-free-path to characterise non-local transport trends, which is validated in the first half of chapter 4, is original work I have performed which is in preparation for submission. I plan on then developing the second half of chapter 4 into another paper once this is completed. Specifically, the relationship between the relative anisotropy of the distribution function and transport effects, such as the heat-flow and Nernst effect.

The research contained within chapter 7 has been published [1]. In this paper I lead the simulation efforts utilising kinetic and fluid simulations, and provided the theoretical explanation as to why both models agreed so closely. Building upon this, I am developing a longer paper which will utilise the results in chapter 6 to address the remaining discrepancies between simulated and experimental results.

Chapter 2

Theory of magnetised plasmas

In this chapter, the fundamental physics required for an understanding of transport processes in high-energy-density plasmas relevant to this thesis will be examined. A variety of models exist for the treatment of these dynamics systems, which in the broader picture fall into one of two regimes. The most general are kinetic or particle descriptions. These provide a microscopic understanding of the plasma behaviour, with the most quantitatively accurate predictions. Meanwhile, fluid descriptions, which often find their origin in kinetic theory, offer a macroscopic treatment typically better suited to developing our phenomenological understanding. Elucidating the regime in which the fluid approximation is valid, and where kinetic models are required to provide an accurate description of magnetised laser-plasma systems is one of the primary goals of this thesis.

The most comprehensive model explored here is collisional kinetic theory, which itself is an extension of the kinetic theory of gases. To introduce this topic the first task will be to outline the plasma state, and its distinguishing macroscopic and microscopic properties (section 2.1). A discussion of the kinetic theory of plasmas follows as this description provides the foundation for the theoretical, computational, and experimental investigations throughout this thesis. In particular, the Vlasov-Fokker-Planck equation will be examined and simplified using a Cartesian tensor expansion (section 2.2). From this, the fluid model known as *classical transport theory* [3] is derived, providing an intuitive framework to translate microscopic transport behaviour into macroscopic phenomena (section 2.3). The interaction between magnetic field dynamics and transport, in particular effects surrounding the transport of heat and its interplay with the magnetic field, will then be studied.

Under intense laser-heating the fluid description of transport phenomena diverges from the kinetic description. This is driven both by the laser heating mechanism, and the formation of sharp gradients in the plasma parameters, which distort the

distribution away from a Maxwellian as discussed in sections 2.4 and 2.5. To support this work kinetic and fluid codes are used, which will be outlined in the final section of this chapter.

2.1 Characterisation of plasmas

A plasma is a state of matter consisting of charged particles, in which the behaviour is collective and dominated by electromagnetic forces [32]. Plasmas have the key property of being *quasi-neutral* which means that despite consisting of both electrons and ions, the charge density of both is equal such that locally there is no net charge at thermal equilibrium. The number density, n, of electrons can then be written

$$n_e \simeq \sum_\alpha n_\alpha Z_\alpha \tag{2.1}$$

where the subscript e denotes the electron species and the sum is performed over all ion species α with charge Z. In this thesis, the plasmas that will be considered will be assumed to have a constant ionisation state, such that $n_e = Zn_i$ where the subscript i refers to ions.

When at thermal equilibrium the electron and ion populations within the plasma have equal temperature ($T_e = T_i$). The average kinetic energy of each species is equal

$$\frac{1}{2}m_e\langle v_e\rangle^2 = \frac{1}{2}m_i\langle v_i\rangle^2 = k_B T_e, \tag{2.2}$$

allowing us to show that the ratio of the electron velocity to the ion velocity $\langle v_e\rangle/\langle v_i\rangle = (m_i/m_e)^{1/2}$ is dependent on the mass ratio. For hydrogen ions where m_i is given by the proton mass m_p the mass ratio is $m_p/m_e \approx 1836$ resulting in $\langle v_e\rangle/\langle v_i\rangle \approx 43$. Typically this increases proportionally to $\sqrt{A}$ for increasing atomic number, so larger ions are slower still relative to the electrons. Additionally, the lower mass of the electrons means that they are accelerated much more rapidly than ions for a given applied force.

For these reasons, electrons are highly mobile compared to ions which are typically treated as stationary on the electron timescale. As a result, electrons are of particular importance in dictating transport behaviour, as they can respond rapidly whenever the system is driven from equilibrium. This is particularly true for laser-plasmas due to the coupling of laser energy into the electron population, which will be discussed in section 2.4.

The electric **E** and magnetic **B** fields that drive plasma behaviour are governed by Maxwell's equations

$$\nabla \cdot \mathbf{E} = \frac{\rho_q}{\epsilon_0} \qquad \text{Gauss's law} \tag{2.3}$$

$$\nabla \cdot \mathbf{B} = 0 \qquad \text{Gauss's law of magnetism} \tag{2.4}$$

$$\nabla \times \mathbf{E} = -\frac{\partial \mathbf{B}}{\partial t} \qquad \text{Faraday's law} \tag{2.5}$$

$$\nabla \times \mathbf{B} = \frac{1}{c^2}\frac{\partial \mathbf{E}}{\partial t} + \mu_0 \mathbf{J} \qquad \text{Ampère's law} \tag{2.6}$$

These fields are typically macroscopic, surpassing the effects of microscopic fluctuations. Local imbalances in charge density, given by $\rho_q = Zen_i - en_e$, arise from the spatial distribution of particles. According to Gauss's law, these imbalances generate an electrostatic field. The resulting deviations from quasi-neutrality are just large enough to counterbalance other forces within the plasma, a relationship that will be explored in greater detail when examining Ohm's law. Meanwhile, the velocity **v** of these particles leads to a flow of charge, or current density, given by $\mathbf{J} = e(Zn_i\langle \mathbf{v}_i \rangle - n_e \langle \mathbf{v}_e \rangle)$. According to Ampères law a magnetic field is then induced.

Behaviour on the microscopic scale can be understood by considering the magnitude of the Coulomb force between two particles of charge q_1 and q_2 separated by a distance r

$$|\mathbf{F}| = \frac{|q_1 q_2|}{4\pi\epsilon_0 r^2}, \tag{2.7}$$

where it would appear natural to assume that the electric field arising from any given particle may extend over the entire volume of the plasma. However, a local charge imbalance will lead to a rapid response from the mobile electrons, redistributing themselves to form a neutralising cloud around the disturbance.

At thermal equilibrium the electrons with charge $q = -e$ surrounding an ion will obey a Boltzmann distribution $n_e = n_0 \exp(e\phi/T_e)$, where ϕ is the electrostatic potential and T_e the temperature in energy units. Poisson's equation can be used to solve for the electrostatic potential, which on assuming spherical symmetry reads

$$\frac{1}{r^2}\frac{d}{dr}\left(r^2 \frac{d\phi}{dr}\right) = -\frac{n_e e}{\epsilon_0}\left[1 - \exp\left(\frac{e\phi}{T_e}\right)\right] \tag{2.8}$$

where the relationship $Zn_i = n_e$ has been utilised. As $\phi(r) \to 0$ as $r \to \infty$ we assume

$e\phi \ll T_e$ in which case the exponential may be expanded as $\exp(e\phi/T_e) \approx 1 + e\phi/T_e$. The resulting equation

$$\frac{1}{r^2}\frac{d}{dr}\left(r^2\frac{d\phi}{dr}\right) = \frac{n_e e^2}{\epsilon_0 T_e}\phi \tag{2.9}$$

has a standard solution, which on matching the boundary condition $\phi(r) = Ze/4\pi\epsilon_0 r$ at $r \to 0$ give

$$\phi(r) = \frac{Ze}{4\pi\epsilon_0 r}\exp\left(-\frac{r}{\lambda_D}\right) \quad \text{where} \quad \lambda_D = \left(\frac{\epsilon_0 T_e}{n_e e^2}\right)^{1/2}. \tag{2.10}$$

Here it is seen that the Coulomb potential is effectively screened over a distance given by the Debye length λ_D.

Together the nature of the Coulomb force, and the response of electrons to charge imbalances, fundamentally lead to the concept of quasi-neutrality. The effectiveness of Debye shielding means that on length scales greater than the Debye length the plasma can be considered almost neutral. Within the Debye sphere, the interaction of electrons with each other and their response to microscopic charge perturbations caused by particle motion result in collisions.

The Debye length leads to a natural separation of the Coulomb force into a macroscopic component (self-consistent field) and a microscopic component (collisions). Particles only interact with each other if they are less than a distance $\sim \lambda_D$ from each other. On a scale greater than λ_D macroscopic fields result from collective behaviour amongst many charged particles, with any individual particle then interacting with a continuous distribution of charge and current.

However, the treatment of Debye shielding relies on two aspects which turn out to be related. First, there are enough particles inside a sphere with radius given by the Debye length for a statistical approach to be valid. An *ideal plasma* is one where the number of particles in the Debye sphere can be considered to approach infinity. Many high-energy-density plasmas may have fewer than tens of particles in the Debye sphere, so are rarely ideal plasmas [2]. Second, and more importantly, it is assumed that $e\phi \ll T_e$ so that the distribution can be expanded in terms of the small parameter $e\phi/T_e$. This is the case when the thermal energy of the electrons is much larger than the average electrostatic potential between electrons a distance Λ_D apart such that

$$\frac{e^2}{\epsilon_0 \Lambda_D T_e} = \frac{1}{n_e \lambda_D^3} = g \ll 1. \tag{2.11}$$

The condition is equivalent to saying there are many particles in the Debye sphere. Plasmas for which $g \ll 1$ are referred to as *weakly coupled*, with interactions for which the potential energy is large relative to a particle's kinetic energy rare. When the opposite is true, which tends to be the case for cold and dense plasmas, a plasma is known to be *strongly coupled*. Strongly coupled plasmas, such as those in the warm-dense-matter regime, are beyond the scope of this thesis.

Despite the rapid response of electrons to charge imbalances, their finite mass means that there exists a characteristic response frequency. This is demonstrated by considering the propagation of a transverse electromagnetic wave with electric and magnetic field

$$\mathbf{E} = \mathbf{E}_0 \exp[I(\mathbf{k}\cdot\mathbf{r} - \omega t)] \quad \text{and} \quad \mathbf{B} = \mathbf{B}_0 \exp[I(\mathbf{k}\cdot\mathbf{r} - \omega t)] \tag{2.12}$$

where $\mathbf{k}$ is the wavevector and ω the angular frequency. These fields evolve according to Faraday's and Ampère's law. By taking the curl of Ampere's law a wave equation may be developed

$$\nabla \times (\nabla \times \mathbf{E}) = -\frac{\partial}{\partial t}\nabla \times \mathbf{B} \tag{2.13}$$

where on using the identity $\nabla \times (\nabla \times \mathbf{E}) = \nabla(\nabla \cdot \mathbf{E}) - \nabla^2\mathbf{E}$ on the left-hand side and substituting Faraday's law on the right

$$\nabla(\nabla \cdot \mathbf{E}) - \nabla^2\mathbf{E} = -\frac{1}{c^2}\left(\frac{\partial^2\mathbf{E}}{\partial t^2} + \frac{1}{\epsilon_0}\frac{\partial \mathbf{J}}{\partial t}\right). \tag{2.14}$$

If the ions are considered static relative to the electrons, which can be motivated by their mass ratio, then the current is given by the mean electron velocity $\mathbf{J} = -en_e\langle\mathbf{v}\rangle$. The evolution of this current can be obtained from the Lorentz force, which for non-relativistic currents the magnetic field can be neglected as for an electromagnetic wave $|\mathbf{B}| = |\mathbf{E}|/c$. Then

$$\frac{\partial \mathbf{J}}{\partial t} = -en_e\frac{\partial\langle\mathbf{v}\rangle}{\partial t} = \frac{n_e e^2}{m_e}\mathbf{E} \tag{2.15}$$

where it is has been assumed that $n_e\partial_t\langle\mathbf{v}\rangle \gg \langle\mathbf{v}\rangle\partial_t n_e$.

Substituting this expression into the wave equation developed earlier

$$\nabla(\nabla \cdot \mathbf{E}) - \nabla^2\mathbf{E} = -\frac{1}{c^2}\left(\frac{\partial^2\mathbf{E}}{\partial t^2} + \frac{n_e e^2}{\epsilon_0 m_e}\mathbf{E}\right) \tag{2.16}$$

which for the electric field of a propagating electromagnetic wave (eq. 2.12)

$$\nabla(i\mathbf{k}\cdot\mathbf{E}) + k^2\mathbf{E} = -\frac{1}{c^2}\left(-\omega^2 + \frac{n_e e^2}{\epsilon_0 m_e}\mathbf{E}\right). \tag{2.17}$$

where k is the wavenumber. Note that as the electromagnetic wave is transverse $\mathbf{k}\cdot\mathbf{E} = 0$ and the dispersion relationship is obtained

$$\omega^2 = c^2k^2 + \omega_{pe}^2 \quad \text{where} \quad \omega_{pe} = \sqrt{\frac{n_e e^2}{m_e\epsilon_0}}. \tag{2.18}$$

The plasma frequency ω_{pe} is key in determining a plasma's ability to screen electric fields. For an electric field of frequency ω to propagate through a plasma it is required that $\omega > \omega_{pe}$. If the frequency is equal to the plasma frequency then the plasma will be driven resonantly, with the wave unable to propagate as $k = 0$. However, when the plasma frequency exceeds this frequency the electrons will respond and screen the perturbation, with the wavenumber becoming imaginary. If the electric field is that of a laser a critical density n_c is then defined after which the laser cannot propagate, becoming evanescent beyond this point.

2.1.1 Charged particle motion in a magnetic field

The general description of the motion of individual charged particles in and electric $\mathbf{E}$ and magnetic $\mathbf{B}$ fields is given by

$$\mathbf{a} = \frac{\mathrm{d}\mathbf{v}}{\mathrm{d}t} = \frac{\mathbf{F}}{m} \quad \text{where} \quad \mathbf{F} = q(\mathbf{E} + \mathbf{v}\times\mathbf{B}) \tag{2.19}$$

is the Lorentz force on a particle of charge q by an electric $\mathbf{E}$ and magnetic $\mathbf{B}$ field. If there is no electric field ($\mathbf{E} = 0$) then perpendicular to the magnetic field the equation of motion is that of a simple harmonic oscillator with frequency given by the gyro-frequency

$$\omega_g = \frac{q|\mathbf{B}|}{m} \quad \text{and} \quad r_g = \frac{v_\perp}{\omega} \tag{2.20}$$

the gyro-radius of the orbit.

The significance of the magnetic field on a particles trajectory is known as the magnetisation or 'Hall parameter, given by the ratio of the gyro-frequency to the characteristic collision frequency ν

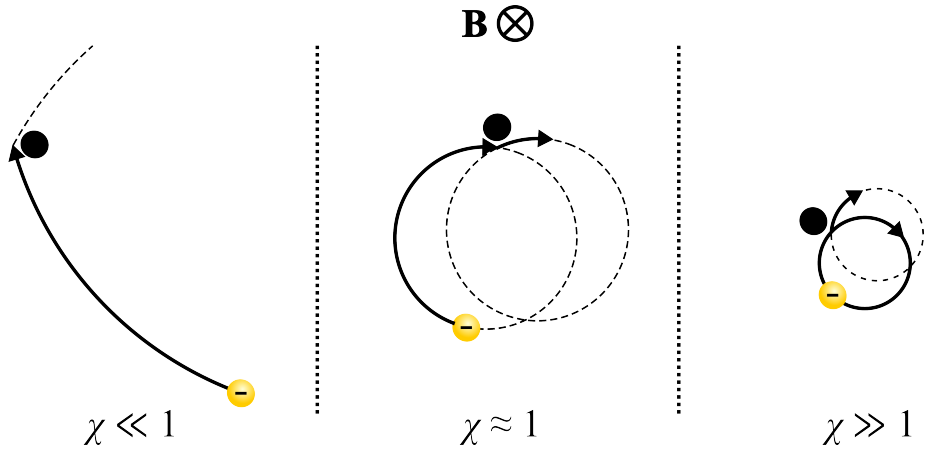

Figure 2.1: Electron orbits in different magnetisation regimes for a magnetic field orientated into the page. When $\chi \ll 1$ the trajectory approaches a straight line. As the magnetisation increases the gyro-radius decreases relative to the mean-free-path and the trajectory begins to approach an orbit when $\chi \approx 1$. When $\chi \gg 1$ the electron will complete full orbits before a shift in its guiding centre. Note that right-angle deflections in a plasma are often the result of many small-angle scattering events, with large-angle scattering events such as those depicted here for illustrative purposes very infrequent.

$$\chi = \frac{\omega_g}{\nu} = \frac{\lambda}{r_g}. \tag{2.21}$$

This is equivalent to the ratio of the characteristic mean-free-path $\lambda = v\tau$, where τ is the time between collisions, to the gyro-radius. A schematic of the electron orbits when the magnetisation is increased from the weakly magnetised regime ($\chi \ll 1$) to the strongly magnetised regime ($\chi \gg 1$) is shown in fig. 2.1.

2.2 Particle kinetics

A complete description of a classical, non-relativistic plasma at any moment in time t requires knowledge of the position $\mathbf{r} = (x, y, z)$ and velocity $\mathbf{v} = (v_x, v_y, v_z)$ of all particles at a time t. The Klimontovich distribution function [32]

$$f_K(\mathbf{r}, \mathbf{v}, t) = \sum_1^N \delta[\mathbf{r} - \mathbf{r}_i(t)][\mathbf{v} - \mathbf{v}_i(t)] \tag{2.22}$$

provides such a description in six-dimensional phase space for all N particles of a given species. The function is zero except at the points where $\mathbf{r} = \mathbf{r}_i$ and $\mathbf{v} = \mathbf{v}_i$.

The evolution of the distribution function is given by the Liouville equation,

found by taking the time derivative of eq. 2.22

$$\frac{\mathrm{d}f_K}{\mathrm{d}t} = \frac{\partial f_K}{\partial t} + \sum_1^N \left(\mathbf{v}_i \cdot \frac{\partial f_K}{\partial \mathbf{r}_i} + \frac{\partial \mathbf{v}_i}{\partial t} \cdot \frac{\partial f_K}{\partial \mathbf{v}_i} \right) = 0. \tag{2.23}$$

The acceleration these particles experience $\partial_t \mathbf{v} = \mathbf{F}/m$ is attributed to the force $\mathbf{F}$, which is in general a function of the position and velocity of all other plasma particles. However, the solution of such a problem is both analytically and numerically intractable as the number of particles in a laser-plasma experiment can easily exceed 10^{12}.

Progress is usually made using one of several routes. The most common numerical approach is the particle-in-cell (PIC) method, where many particles are grouped to form 'macroparticles'. The charge and current distributions

$$\mathbf{j}(\mathbf{r}, t) = \sum_1^N e_i \mathbf{v}_i(t) \delta[\mathbf{r} - \mathbf{r}_i(t)] \tag{2.24}$$

$$q(\mathbf{r}, t) = \sum_1^N e_i \delta[\mathbf{r} - \mathbf{r}_i(t)] \tag{2.25}$$

arising from these particles are then used in combination with Maxwell's equations to compute the macroscopic electric and magnetic field, which in turn accelerate the macroparticles via the Lorentz force (eq. 2.19). While often used to model collisionless phenomena, binary collision operators can be included to capture collisions to be treated [33, 34]. As PIC codes do not assume the form of the distribution function they are well-suited to problems with substantial anisotropy. However, numerical noise can be significant, seeding instabilities, with a large number of particles per cell required to provide accurate statistics.

An analytical solution can be approached by adopting a continuum description whereby integration of eq. 2.22 is performed over a volume element, through a procedure referred to as the 'BBGKY hierarchy' [32]. Central to this approach is the assumption that particle correlations are limited to within the Debye sphere, following the weak coupling approximation. This then introduces the distribution function $f(\mathbf{r}, \mathbf{v}, t)$, which is the statistically averaged number density of particles in phase space. Provided no particles are created or destroyed the distribution function obeys a continuity equation, with the rate of change with time given by

$$\frac{\mathrm{d}f}{\mathrm{d}t} = \frac{\partial f}{\partial t} + \nabla_{\mathbf{r}} \cdot (f\mathbf{v}) + \nabla_{\mathbf{v}} \cdot \left(f \frac{\partial \mathbf{v}}{\partial t} \right) = 0. \tag{2.26}$$

where $\nabla_{\mathbf{r}} = (\partial_x, \partial_y, \partial_z)$, $\nabla_{\mathbf{r}} = (\partial_{v_x}, \partial_{v_y}, \partial_{v_z})$, and setting $\nabla_{\mathbf{v}} \cdot \partial_t \mathbf{v} = 0$

$$\frac{\partial f}{\partial t} + \mathbf{v} \cdot \nabla_{\mathbf{r}} f + \frac{\mathbf{F}}{m} \cdot \nabla_{\mathbf{v}} f = 0 \tag{2.27}$$

with $\partial_t \mathbf{v} = \mathbf{F}/m$. This is the Vlasov equation, describing collisionless phenomena in a plasma. Along any trajectory in phase space the distribution function then remains unchanged. For a plasma where the only forces are electromagnetic then $\mathbf{F}$ is given by the Lorentz force $\mathbf{F} = q(\mathbf{E} + \mathbf{v} \times \mathbf{B})$, where $\mathbf{E}$ and $\mathbf{B}$ are the self-consistent electric and magnetic field. The full set of equations required for solution are then the Vlasov equation in combination with Maxwell's equations which form the Vlasov-Maxwell system of equations.

Generally, it cannot be assumed that $\nabla_{\mathbf{v}} \cdot \partial_t \mathbf{v} = 0$ as the force experienced by particles, specifically due to collisions, can be velocity dependent. However, by assuming that this force is the sum of both non-collisional forces $\mathbf{F}$ and those due to collisions one arrives at the Boltzmann equation

$$\frac{\partial f}{\partial t} + \mathbf{v} \cdot \nabla_{\mathbf{r}} f + \frac{\mathbf{F}}{m} \cdot \nabla_{\mathbf{v}} f = C(f) \tag{2.28}$$

where $C(f)$ accounts for the change in time due to collisions. This separation of effects arises naturally due to Debye shielding, splitting the macroscopic and microscopic field components. A treatment of collisions is typically complex but crucial for an accurate description of the phenomena explored in this thesis, and a brief overview will be provided in the following section.

The distribution function can be used to obtain macroscopic transport properties by taking velocity moments, with the mth order moment defined by

$$\langle \mathbf{v}^m \rangle = \frac{1}{n} \int \mathbf{v}^m f(\mathbf{r}, \mathbf{v}, t) d^3 v \tag{2.29}$$

where the integral $d^3 v = dv_x dv_y dv_z$ is performed over velocity space. The velocity moments give the expected, or average, value of the quantity $\mathbf{v}^m$ at a given position $\mathbf{r}$ and time. For electron transport the quantities of interest are the number density given by the zeroth moment $n_e = \int f d^3 v$, current $\mathbf{J} = -e n_e \langle \mathbf{v} \rangle$, anisotropic pressure $\underline{\underline{\mathbf{P}}}_e = n_e m_e \langle \mathbf{v}^2 \rangle$, and heat-flow $\mathbf{q} = 1/2 n_e m_e \langle v^2 \mathbf{v} \rangle$ for a single fluid treatment of the plasma where ions are considered stationary. If instead moments of the Boltzmann equation are taken, then fluid equations governing the time evolution of these quantities are obtained; these will be reviewed in section 2.3.

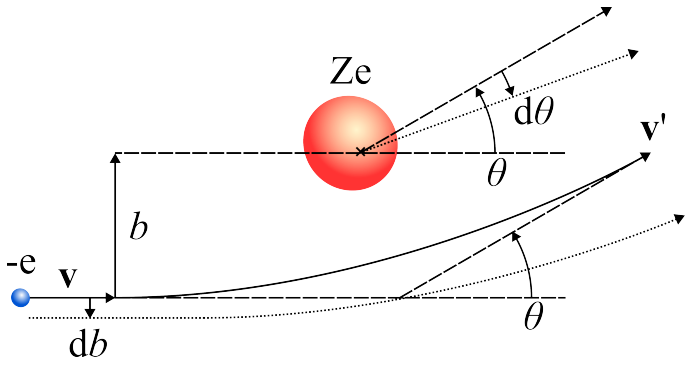

Figure 2.2: Scattering of an electron by an ion in the centre of mass frame.

2.2.1 Collisions and the Fokker-Planck equation

Due to the long-range nature of the Coulomb force collisions in a plasma occur through many-body interactions between particles in the Debye sphere. The effect of many small-angle scattering events, where the thermal energy is much larger than the potential energy, outweighs that of infrequent large-angle scattering events. The probabilistic, rather than determinant, nature of multiple collisions means that a Fokker-Planck approach is appropriate when defining the collision operator [32].

The Fokker-Planck collision operator is defined

$$C(f) = -\nabla_{\mathbf{v}} \cdot \left(\frac{f\langle \Delta \mathbf{v} \rangle}{\Delta t} \right) + \frac{1}{2} \nabla_{\mathbf{v}} \nabla_{\mathbf{v}} : \left(\frac{f\langle \Delta \mathbf{v} \Delta \mathbf{v} \rangle}{\Delta t} \right) \tag{2.30}$$

where $\Delta \mathbf{v}$ is a small increment acquired by a particle with velocity $\mathbf{v}$ in a time Δt. The term $\langle \Delta \mathbf{v} \rangle$ represents the coefficient of dynamical friction, which quantifies the average deflection of electrons resulting from Coulomb collisions within an ensemble. On the other hand, $\langle \Delta \mathbf{v} \Delta \mathbf{v} \rangle$ refers to the coefficient of dynamical diffusion, describing how collisions cause the velocities within the ensemble to spread out. Substituting eq. 2.30 into eq. 2.28 yields the Vlasov-Fokker-Planck equation. The remaining challenge in implementing the collision operator is an assessment of the average change in $\Delta \mathbf{v}$ and $\Delta \mathbf{v} \Delta \mathbf{v}$ in time Δt.

Following the derivation of Rosenbluth *et al.* [35] the collision mechanism can be treated via the binary interaction of a particle of species α with a scattering species β in the centre of mass frame. The key results relate to the fundamental relationship between the impact parameter b and the scattering angle θ

$$b = b_0 \cot(\theta/2) \quad \text{where} \quad b_0 = \frac{Z_\alpha Z_\beta e^2 (m_\alpha + m_\beta)}{4\pi \epsilon_0 m_\alpha m_\beta |\mathbf{u}|^2} \tag{2.31}$$

is the impact parameter for right-angle scattering and $\mathbf{u} = \mathbf{v}_\alpha - \mathbf{v}_\beta$ is the relative

velocity. A small impact parameter, indicating a close encounter, results in a large scattering angle. In contrast, a large impact parameter, corresponding to a collision with a distant particle, leads to a small scattering angle.

In fig. 2.2 a schematic is shown for the scattering of an electron by an ion, where it is seen that for an increase in the initial impact parameter b the scattering angle θ is reduced. Defining the differential scattering cross-section $\mathrm{d}\sigma/\mathrm{d}\Omega$ this is related to the impact parameter by

$$\frac{\mathrm{d}\sigma(\theta, |\mathbf{u}|)}{\mathrm{d}\Omega} = \frac{b}{\sin\theta}\left|\frac{\mathrm{d}b}{\mathrm{d}\theta}\right| \tag{2.32}$$

which on substituting eq. 2.31 gives

$$\frac{\mathrm{d}\sigma(\theta, |\mathbf{u}|)}{\mathrm{d}\Omega} = \left(\frac{Z_\alpha Z_\beta e^2(m_\alpha + m_\beta)}{4\pi\epsilon_0 m_\alpha m_\beta |\mathbf{u}|^2}\right)^2 \frac{1}{4\sin^4(\theta/2)}. \tag{2.33}$$

The dependence $\sigma(\theta) \propto 1/\sin^4(\theta/2)$ means that small-angle collisions are significantly more likely than large-angle collisions.

The expectation value of $\Delta\mathbf{v}$ is then found, which after integrating the probability distribution over solid angle and speed of the scattering species leads to the results

$$\frac{\langle\Delta\mathbf{v}\rangle}{\Delta t} = \Gamma_\alpha \nabla_\mathbf{v} H \quad \text{and} \quad \frac{\langle\Delta\mathbf{v}\Delta\mathbf{v}\rangle}{\Delta t} = \Gamma_\alpha \nabla_\mathbf{v}\nabla_\mathbf{v} G \quad \text{where} \quad \Gamma_\alpha = \frac{Z_\alpha^2 e^4}{4\pi\epsilon_0^2 m_\alpha^2}\ln\Lambda_{\alpha\beta}. \tag{2.34}$$

The functions $G(\mathbf{v})$ and $H(\mathbf{v})$ are known as the Rosenbluth potentials and are given by

$$H(\mathbf{v}) = \sum_\beta Z_\beta^2 \left(\frac{m_\alpha + m_\beta}{m_\beta}\right) \int \frac{f_s(\mathbf{v}_\beta)}{|\mathbf{v}_\alpha - \mathbf{v}_\beta|}\mathrm{d}\mathbf{v}_\beta \tag{2.35}$$

$$G(\mathbf{v}) = \sum_\beta Z_\beta^2 \int |\mathbf{v}_\alpha - \mathbf{v}_\beta| f_\beta(\mathbf{v}_\beta)\mathrm{d}\mathbf{v}_\beta \tag{2.36}$$

with the sum performed over all scattering species.

Substituting eq. 2.34, eq. 2.35 and eq. 2.36 into the Fokker-Planck equation

$$C(f) = -\Gamma_\alpha \nabla_\mathbf{v} \cdot (f_\alpha \nabla_\mathbf{v} H) + \frac{\Gamma}{2}\nabla_\mathbf{v}\nabla_\mathbf{v} : (f_\alpha \nabla_\mathbf{v}\nabla_\mathbf{v} G) \tag{2.37}$$

which is the usual form of the collision term.

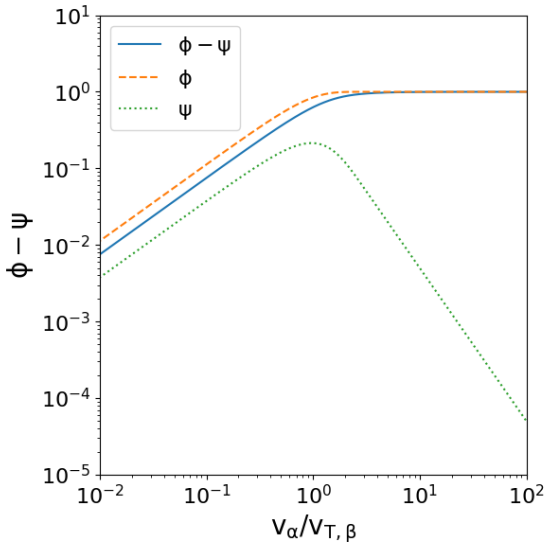

Figure 2.3: The difference between ϕ and ψ as a function of the ratio between the test-particle velocity and the thermal velocity of the scattering species. The individual functions ϕ and ψ are also shown.

2.2.2 Properties of the Fokker-Planck equation

Coulomb collisions in velocity space result in the transfer of momentum and energy between particles, driving the system toward a local Maxwellian distribution. The only distribution functions for which the collision operator $C(f) = 0$ are Maxwellian distributions, meaning that the system's distribution function will asymptotically approach this state, consistent with Boltzmann's H-theorem. The H-theorem describes the tendency of particles to evolve toward thermodynamic equilibrium. The Fokker-Planck equation serves as an approximation to the more general Boltzmann equation in the limit of small-angle scattering. Additionally, the Fokker-Planck operator ensures that the distribution function remains non-negative, effectively filling in any gaps in velocity space, while also conserving particle number, momentum, and energy.

Useful collision parameters can be derived from the Fokker-Planck equation using the 'test particle' model [32]; a single particle is considered in a field-free plasma at thermal equilibrium. Moments of the Fokker-Planck equation are then taken. A parameter of particular interest is the collision frequency, $\nu_{\alpha\beta}$, defined as the inverse of the mean time taken for a particle of species α to undergo right-angle scattering by species β. This provides a timescale over which an initially anisotropic distribution will become isotropic, a process central in collisional transport considered later in this thesis.

The collision frequency for scattering of species α with velocity v_α by a scattering

species β at thermal equilibrium is

$$\nu_{\alpha\beta} = \frac{2\Gamma}{v_\alpha^3} Z_\beta^2 n_\beta \left[\phi(v_\alpha/v_{T,\beta}) - \psi(v_\alpha/v_{T,\beta})\right] \tag{2.38}$$

where $\phi(x)$ is the error function, $\psi(x) = (\phi - x\mathrm{d}\phi/\mathrm{d}x)/2x^2$, and v_T is the thermal velocity. The scaling with velocity means that the collision frequency is much lower for higher velocity electrons. Scattering from higher Z species is also much more likely, as expected from eq. 2.33, and is also linearly dependent on their density. For $v_\alpha \gg v_{T,\beta}$, as is typically the case for the electron-ion collisions, the term in square brackets is constant with the collision frequency scaling as $\nu_{\alpha\beta} \propto v_\alpha^{-3}$. Meanwhile when $v_\alpha \ll v_{T,\beta}$, which often occurs in ion-electron collisions or the collisions of cold and hot electrons, the scaling is instead $\nu_{\alpha\beta} \propto v_\alpha^{-2}$.

A similar approach can be used to define the frequency of energy exchange between species α and β due to scattering interactions

$$\nu_{\alpha\beta}^E = \frac{8\Gamma n_\beta z_\beta^2 \psi(v_\alpha/v_{T,\beta})}{v_\alpha^3}. \tag{2.39}$$

For like-species this occurs on the order of the collision frequency near the thermal speed. However, when the test particle velocity is far above that of the scatterer relaxation can occur over substantially longer timescales. The high velocity tail of the distribution function can then remain far from Maxwellian. Energy exchange also becomes increasingly inefficient as the mass difference between the two species increases, resulting in much longer equilibration times between the electron and ion species temperatures.

For a plasma containing multiple ion species, the ion charge can be replaced by the average ion charge $\langle Z \rangle$, with n_i now the total ion density. This is made exact by multiplying by the (usually small) correction factor $\sum n_\alpha Z_\alpha^2/(n_i \langle Z \rangle^2)$. Additionally, by setting $v_\alpha = v_{\alpha,T}$ estimates can be obtained in terms of the plasma temperature, with hotter plasmas relatively collisionless compared to colder plasmas. However, it is important to remember that due to the velocity scaling the thermal estimate is only useful for the bulk of the distribution, and not appropriate when considering hotter electrons which are found to be responsible for transport.

The appearance of the Coulomb logarithm $\ln \Lambda_{\alpha\beta} \approx \ln(\lambda_D/b_0)$ in these equations arises after setting a cut-off at small scattering angle, with a maximum impact parameter of $b_{\max} = \lambda_D$. While the argument is velocity dependent this is often neglected as it lies inside the logarithm. The Coulomb logarithm measures the importance of small-angle collisions relative to large-angle collisions. Provided the

Coulomb logarithm is not close to unity, so small angle collisions are dominant, the Fokker-Planck collision operator remains valid with the plasma weakly coupled. Plasmas for which the Coulomb logarithm is small have few particles in the Debye sphere, and often high density or low temperature, causing them to be strongly coupled.

2.2.3 Vlasov-Fokker-Planck equation

Electron transport is of primary concern in this thesis, so the scattered species α are now assumed to be electrons, with the scattering species either other electrons or a single ion species with charge Z. For the scattered species then $\mathbf{v}_\alpha = \mathbf{v}$ is the electron velocity, $f_\alpha = f$ is the electron distribution function, $m_\alpha = m_e$ is the electron mass, and $Z_\alpha = -1$.

Considering electron-ion collisions where $\mathbf{v}_\beta = \mathbf{v}_i$, $f_\beta = f_i$, $m_\beta = m_i$, and $Z_\beta = Z$ the complexity of the Fokker-Planck operator is simplified by treating the ion velocity as the average ion velocity $\mathbf{u}$. This assumption works well provided the electron velocity is much greater than the ion velocity, which is often the case as $m_e \ll m_i$. The difference in relative speed is then $|\mathbf{v} - \mathbf{u}|$, which for the case $\mathbf{u} = 0$ (which again is a reasonable assumption for the reasons noted previously) gives the Rosenbluth potentials as

$$H(\mathbf{v}) = \frac{n_i Z^2}{v} + h_{ee}(\mathbf{v}) \quad \text{and} \quad G(\mathbf{v}) = n_i Z^2 v + g_{ee}(\mathbf{v}) \tag{2.40}$$

where n_i is the ion number density, which arises after taking the zeroth moment of f_i, and the result $(m_e + m_i)/m_i \approx 1$ has been used. Here $h_{ee}(\mathbf{v})$ and $g_{ee}(\mathbf{v})$ contain the terms relevant to scattering via electron-electron collisions, which remain unevaluated. Using these forms of the Rosenbluth potentials, eq. 2.37 can be combined with eq. 2.28 to give the Vlasov-Fokker-Planck equation in an explicit form [36]

$$\frac{\partial f}{\partial t} + \mathbf{v}\cdot\nabla_{\mathbf{r}} f - \frac{e}{m}(\mathbf{E} + \mathbf{v}\times\mathbf{B})\cdot\nabla_{\mathbf{v}} f = C_{ee} + n_i Y_{ei} \nabla_{\mathbf{v}} \cdot \left[\frac{f\mathbf{v}}{v^3} + \frac{1}{2}\nabla_{\mathbf{v}} \cdot \left(\underline{\underline{I}} - \frac{\mathbf{v}\mathbf{v}}{v^2} \right) \right] \tag{2.41}$$

where $Y_{ei} = Z^2 \Gamma_e$ with $\Gamma_e = 4\pi(e^2/4\pi\epsilon_0 m_e)^2 \ln \Lambda_{ei}$, and the effects of electron-electron collisions are represented by C_{ee}.

2.2.4 Expanding the distribution function

The solution of the Vlasov-Fokker-Planck equation remains complex as the problem is six-dimensional in phase space, rendering a computational solution intractable for many systems of interest. However, a reduction in the dimensionality is possible by exploiting symmetry. For sufficiently collisional systems, the anisotropic component of the distribution function can be considered a perturbation to the isotropic component f_0 which contains no directional information. The distribution can then be expanded in terms of increasing anisotropy. This is done by selecting an appropriate basis function, which contains the directional information, while the velocity magnitude is retained.

The choice of basis function used in the expansion is not unique, with a common choice being an expansion in spherical harmonics $Y_{lms}(\theta, \phi)$

$$f(\mathbf{v}, \mathbf{r}, t) = \sum_{l,m,s} f_{lms}(v, \mathbf{r}, t) Y_{lms}(\theta, \phi) \tag{2.42}$$

due to the tendency of collisions to make the distribution function spherical in velocity space. Alternatively, an expansion in Cartesian tensors can be performed

$$f(\mathbf{v}, \mathbf{r}, t) = \sum_{l=0}^{\infty} \{\mathbf{f}(v, \mathbf{r}, t)_l\} \vdots_l \{\hat{\mathbf{v}}^l\} \tag{2.43}$$

where $\mathbf{f}_l$ is a tensor of rank l, $\hat{\mathbf{v}} = \mathbf{v}/v$ is the velocity unit vector, and the contraction is performed over l indices. Both methods have been shown to be equivalent [37] with the expansions the same to first order, but differences arise between the higher order terms. The number of velocity dimensions is then reduced to one.

Here the distribution will be expanded in Cartesian tensors

$$f(\mathbf{v}, \mathbf{r}, t) = f_0(v, \mathbf{r}, t) + \mathbf{f}_1(v, \mathbf{r}, t) \cdot \frac{\mathbf{v}}{v} + \mathbf{f}_2(v, \mathbf{r}, t) : \frac{\mathbf{vv}}{v^2} + ... \tag{2.44}$$

where it can be seen that f_0 is isotropic in velocity space. Anisotropy within the distribution function which describes flows, and thus, transport effects, is associated with $\mathbf{f}_1$ and higher order terms. Taking velocity moments of eq. 2.44 with the appropriate tensor function then allows the physical properties of the plasma to be obtained.

Expressing the system in spherical coordinates (v, θ, ϕ) the velocity is then written in terms of a set of direction cosines $\mathbf{v} = (v\cos\theta_x, v\cos\theta_y, v\cos\theta_z)$ where

$\cos\theta_x = \sin\theta\cos\phi, \cos\theta_y = \sin\theta\sin\phi, \cos\theta_z = \cos\theta$. To obtain moments the integration over velocity then becomes one over speed, polar, and azimuthal angle such that $d^3v \rightarrow v^2 sin\theta d\theta d\phi$ (equivalent to speed and solid angle). For tensor functions $\phi = \phi(v), \mathbf{Q} = Q(v)\mathbf{v}/v$, and $\mathbf{QQ} = Q(v)^2\mathbf{vv}/v^2$ the moments are then

$$\langle\phi\rangle = \frac{1}{n_e}\int \phi f(\mathbf{v},\mathbf{r},t)d^3v = \frac{4\pi}{n_e}\int \phi f_0 v^2 dv \tag{2.45a}$$

$$\langle\mathbf{Q}\rangle = \frac{1}{n_e}\int \mathbf{Q} f(\mathbf{v},\mathbf{r},t)d^3v = \frac{4\pi}{3n_e}\int Q\mathbf{f}_1 v^2 dv \tag{2.45b}$$

$$\langle\mathbf{QQ}\rangle = \frac{1}{n_e}\int \mathbf{QQ} f(\mathbf{v},\mathbf{r},t)d^3v = \frac{4\pi}{3n_e}\int Q^2 f_0 \underline{\underline{\mathbf{I}}} v^2 dv + \frac{8\pi}{15n_e}\int Q^2 \underline{\underline{\mathbf{f}}}_2 v^2 dv \tag{2.45c}$$

where due to the orthogonal nature of the basis tensors only the parallel component is non-zero [36].

The terms in the expanded distribution function can then be linked to the macroscopic quantities. Moments of the isotropic component are related to macroscopic scalar fields such as the electron density and temperature

$$n_e = 4\pi\int_0^\infty f_0 v^2 dv \tag{2.46}$$

$$T_e = \frac{1}{3}m_e\langle v^2\rangle = \frac{4\pi m_e}{3n_e}\int_0^\infty f_0 v^4 dv \tag{2.47}$$

where the latter equation defines a temperature even in systems out of thermal equilibrium. The first-order anisotropic component $\mathbf{f}_1$ describes vector fields such as the current and heat-flow

$$\mathbf{J} = -en_e\langle\mathbf{v}\rangle = -\frac{4\pi e}{3}\int_0^\infty \mathbf{f}_1 v^3 dv \tag{2.48}$$

$$\mathbf{q} = \frac{1}{2}n_e m_e\langle v^2\mathbf{v}\rangle = \frac{2\pi m_e}{3}\int_0^\infty \mathbf{f}_1 v^5 dv. \tag{2.49}$$

The second-order anisotropic component $\mathbf{f}_2$ is related to the pressure tensor

$$\underline{\underline{\mathbf{P}}}_e = \frac{1}{3}n_e m_e\langle\mathbf{v}^2\rangle = \frac{4\pi}{3}m_e\int_0^\infty v^2 f_0 \underline{\underline{\mathbf{I}}} v^4 dv + \frac{8\pi}{15}m_e\int_0^\infty \underline{\underline{\mathbf{f}}}_2 v^4 dv = P_e\underline{\underline{\mathbf{I}}} + \underline{\underline{\Pi}}_e \tag{2.50}$$

where $P_e = n_e T_e$ is the isotropic pressure, $\underline{\underline{\mathbf{I}}}$ is the identity matrix and $\underline{\underline{\Pi}}_e$ is the anisotropic pressure. The pressure has both isotropic and anisotropic components

owing to $\mathbf{f}_2$ being traceless. If the velocity distribution is isotropic then $\underline{\underline{\Pi}}_e = 0$.

A series of equations governing the evolution of the tensor components of the distribution are found by substituting the expanded distribution function (eq. 2.44) into the Vlasov-Fokker-Planck equation (eq. 2.41) [36]. This yields an infinite series of coupled equations, where the first three are

$$\frac{\partial f_0}{\partial t} + \frac{\mathbf{a}\cdot\mathbf{f}_1}{v} = C_{ee0} \tag{2.51}$$

$$\frac{\partial \mathbf{f}_1}{\partial t} + v\nabla_{\mathbf{r}} f_0 + \mathbf{a}\frac{\partial f_0}{\partial v} + \boldsymbol{\omega}\times\mathbf{f}_1 + 2\mathbf{a}\cdot\mathbf{f}_2 = \mathbf{C}_{ee1} - \frac{n_i Y_{ei}}{v^3}\mathbf{f}_1 \tag{2.52}$$

$$\frac{\partial \mathbf{f}_2}{\partial t} + v\nabla\mathbf{f}_1 + v\mathbf{a}\frac{\partial \mathbf{f}_1/v}{\partial v} + 2\boldsymbol{\omega}\mathbf{f}_2 + 3\mathbf{a}\cdot\mathbf{f}_3 = \mathbf{C}_{ee2} - 3\frac{n_i Y_{ei}}{v^3}\mathbf{f}_2. \tag{2.53}$$

using the notation

$$\mathbf{a} = \frac{q\mathbf{E}}{m} \quad \text{and} \quad \boldsymbol{\omega} = \frac{q\mathbf{B}}{m}. \tag{2.54}$$

As each equation in the series is orthogonal they must then vanish independently. These are known as the f-equations, with the f_0 equation (eq. 2.51) and $\mathbf{f}_1$ equation (eq. 2.52) central to much of the work in this thesis.

The collision terms in this set of equations are also expanded in Cartesian tensors. Due to the use of a simplified electron-ion collision operator only electron-electron collisions contribute to the isotropic component. As this term relates to energy equilibration of the distribution function this is justified by previous arguments, with energy exchange between electrons and ions much slower due to the significant mass difference.

Conversely, while both electron-electron and electron-ion collisions contribute to the higher order anisotropic terms, ions have a much larger scattering cross-section in the limit $Z \gg 1$ and dominate angular scattering. Neglecting electron-electron collisions in this limit is known as the Lorentz approximation. In the electron-ion collision terms

$$\nu_{ei} = \frac{1}{\tau_{ei}} = \frac{n_i Y_{ei}}{v^3} = \frac{n_i Z^2 (e^2/\epsilon_0 m_e)^2 \ln\Lambda_{ei}}{4\pi v^3} \tag{2.55}$$

is the electron-ion collision frequency, with the reciprocal giving the electron-ion collision time τ_{ei}. Using a collision fix to approximate the effect of electron-electron collisions via $\nu^*_{ei} = \nu_{ei}\zeta$ is common. A popular choice given by Epperlein and Short [38] to recover the correct ionisation dependence of the parallel thermal conductivity

in the local limit is $\zeta = (Z + 4.2)/(Z + 0.24)$. However, the applicability of this approach is limited, as other transport coefficients remain incorrect and it does not account for magnetisation [39].

Having defined the electron-ion collision frequency two key parameters dependent on this quantity are also defined. The first of these is the mean-free-path

$$\lambda_{ei} = \frac{v}{\nu_{ei}} \propto v^4 \tag{2.56}$$

which is the average distance travelled by a particle before right-angle scattering. Next is the magnetisation

$$\chi_{ei} = \frac{\omega_g}{\nu_{ei}} = \frac{\lambda_{ei}}{r_g} \propto v^3 \tag{2.57}$$

providing the number of gyro-orbits performed by an electron per collision, or equivalently the ratio of the mean-free-path to the gyro-radius. Note that both of these quantities are strongly dependent upon the velocity. Higher velocity electrons will have substantially longer mean-free-paths, but are more prone to being magnetised and confined to gyro-orbits perpendicular to the field.

Truncation of the expansion beyond the desired degree of anisotropy provides a means of closure of the equation set and is known as 'polynomial' closure. If this closure is performed at terms of order $\mathbf{f}_2$ and higher then this is known as the *diffusive approximation* and

$$\frac{\partial f_0}{\partial t} + \frac{v}{3}\nabla \cdot \mathbf{f}_1 + \frac{1}{3v^2}\frac{\partial}{\partial v}\left(v^2 \mathbf{a} \cdot \mathbf{f}_1\right) = C_{ee0} \tag{2.58}$$

$$\frac{\partial \mathbf{f}_1}{\partial t} + v\nabla f_0 + \mathbf{a}\frac{\partial f_0}{\partial v} + \boldsymbol{\omega} \times \mathbf{f}_1 = -\nu_{ei}\mathbf{f}_1 + \mathbf{C}_{ee1} \tag{2.59}$$

$$v\nabla \mathbf{f}_1 + v\frac{\partial}{\partial v}\left(\frac{\mathbf{a}\mathbf{f}_1}{v}\right) - \frac{v}{3}\mathrm{Tr}\left\{\nabla \mathbf{f}_1 \frac{\partial}{\partial v}\left(\frac{\mathbf{a}\mathbf{f}_1}{v}\right)\right\}\underline{\underline{\mathbf{I}}} = 0 \tag{2.60}$$

using the result for vectors $\mathbf{A}$ and $\mathbf{B}$ that $\mathrm{Tr}(\mathbf{AB}) = \mathbf{A} \cdot \mathbf{B}$. This can be a good approximation in more collisional plasmas due to the tendency of collisions to reduce anisotropy, although the ordering $f_0 \gg |\mathbf{f}_1| \gg \mathbf{f}_2 \gg ...$ is not strict [40]. The computational efficiency can then be greatly increased without significant loss of accuracy [41].

In the kinetic modelling of plasmas the f-equations in combination with Maxwell's equations often provide the starting point for calculations. In the case of kinetic codes such as IMPACT [42], which solves the f_0 and $\mathbf{f}_1$ equation under the Lorentz

approximation, the electron distribution is only described by these two equations over velocity magnitude, compared to the full Vlasov-Fokker-Planck equation with is three-dimensional (3D) in velocity space. These codes do not assume the form of f_0 or $\mathbf{f}_1$, greatly enhancing their generality compared to fluid models which require an assumption on the form of f_0. However, they are limited instead by their choice of basis set and the number of terms retained in the expansion, preventing the distribution from taking an arbitrary form which may occur in collisionless plasmas.

2.3 Fluid modelling

The fluid approximation greatly simplifies the modelling of plasmas by integrating the velocity information related to the distribution function, retaining only the position. A set of fluid equations is obtained by taking moments of the Boltzmann equation (eq. 2.28) for electrons, where the zeroth, first, and second moments (eq. 2.29) are

$$\frac{\partial n_e}{\partial t} + \nabla \cdot n_e \langle \mathbf{v} \rangle = 0 \tag{2.61}$$

$$m_e \frac{\partial n_e \langle \mathbf{v} \rangle}{\partial t} + \nabla \cdot \underline{\underline{\mathbf{P}}}_e + e n_e (\mathbf{E} + \langle \mathbf{v} \rangle \times \mathbf{B}) = \Delta \mathbf{p}_{ei} \tag{2.62}$$

$$\frac{3}{2}\frac{P_e}{\partial t} + \frac{\partial}{\partial t}\left(\frac{1}{2} m_e \langle \mathbf{v} \rangle \cdot \langle \mathbf{v} \rangle\right) + \nabla \cdot \mathbf{q} + e n_e \langle \mathbf{v} \rangle \cdot \mathbf{E} = 0 \tag{2.63}$$

where $\Delta \mathbf{p}_{ei}$ accounts for momentum exchange during electron-ion collisions. Energy exchange between electrons and ions is neglected in eq. 2.63. These equations provide the continuity, momentum, and energy equations respectively and have the structure of conservation laws.

Each moment of the Vlasov-Fokker-Plank equation depends on a higher order moment of $\mathbf{v}$, representing an infinite series of coupled equations. Here the third moment generates an equation for $\mathbf{q}$, though this involves the fourth moment of $\mathbf{v}$ and so forth. If the equation set is to be used to find the parameters n_e, $\langle \mathbf{v} \rangle$ and T_e a relationship between $\underline{\underline{\mathbf{P}}}_e$, $\mathbf{Q}$ and $\Delta \mathbf{p}_{ei}$ and the lower order moments must be established.

To close the fluid equations the Chapman-Enskog scheme is employed [43], where the distribution function is expanded in increasing degrees of anisotropy. The small parameter in this expansion is the non-locality parameter, given by the Knudsen number λ/l where λ is the mean-free-path of the system and l is the length scale. In the Lorentz limit $\lambda = \lambda_{ei}$ with the length scale taken as the temperature length scale

l_T. A local solution where the plasma is at thermodynamic equilibrium is assumed, with the following orderings

$$\frac{\partial}{\partial t} \ll \nu_{ei} \tag{2.64}$$

$$\lambda_{ei} \ll L \tag{2.65}$$

where $L = \nabla_{\mathbf{r}}^{-1}$ is the length scale over which the macroscopic plasma parameters vary. Note that when the gyro-frequency is larger than the collision frequency the condition is relaxed perpendicular to the magnetic field, so in a magnetised plasmas

$$\lambda_{ei} \ll L_\perp \quad \text{and} \quad r_g \ll L_\perp. \tag{2.66}$$

To zeroth order the electrons are then described by a Maxwellian

$$f_0 = f_m = \frac{n_e}{\pi^{3/2} v_T^3} \exp\left(-\frac{v^2}{v_T^2}\right). \tag{2.67}$$

and to first order the Vlasov-Fokker-Planck equation gives

$$C(f_1) + (\boldsymbol{\omega} \times \mathbf{v}) \cdot \nabla_{\mathbf{v}} f_1 = \mathbf{v} \cdot \nabla_{\mathbf{r}} f_0 + \mathbf{a} \cdot \nabla_{\mathbf{v}} f_0 \tag{2.68}$$

where anisotropic terms on the left are proportional to the large terms $\nu_{ee} \sim \nu_{ei}$ or ω_g. This can then be solved by linearising the collision operator [44].

Essentially, these requirements state that gradients in space and time are small, allowing thermodynamic equilibrium to be maintained via collisions. If gradients are vanishingly small then these assumptions are exact, but even for small perturbations the distribution remains close to Maxwellian. The transport quantities of interest are then proportional to the terms that drive the system from equilibrium, with the constants of proportionality known as *transport coefficients*. The transport coefficients were derived by Braginskii following this scheme in his seminal paper outlining classical transport theory [3].

2.3.1 Classical transport theory

The fundamental assumptions of classical transport theory are that the anisotropic perturbation to the distribution function is small and that the isotropic component is Maxwellian. The first step in the derivation is an expansion of the distribution function, allowing closure of the equation set; this was shown using Cartesian tensors

in section 2.2.4, with the diffusive approximation made and higher order terms neglected. Secondly, moments of the expanded distribution function are taken to derive the fluid equations. Central to this step is the calculation of the transport coefficients, which will be done by assuming the distribution function is Maxwellian.

The continuity and energy equations are found by taking the v^0 and v^2 moments of the Vlasov-Fokker-Planck equation, which is equivalent to taking the same moments of the f_0 equation (eq. 2.58). These are given by

$$\frac{\partial n_e}{\partial t} + \nabla \cdot (n_e \langle \mathbf{v} \rangle) = 0 \tag{2.69}$$

$$\frac{\partial U}{\partial t} + \nabla \cdot \mathbf{q} + e n_e \langle \mathbf{v} \rangle \cdot \mathbf{E} = 0 \tag{2.70}$$

where $U = (3/2) n_e T_e$ is the internal energy density. As the electron-electron collision operator conserves particle number and energy the v^0 and v^2 moments of C_{ee0} are zero.

To determine $\mathbf{E}$ and $\mathbf{q}$ expressions for Ohm's law and the heat-flow equation are required, forming a complete equation set. These are obtained from the $\mathbf{f}_1$ equation (eq. 2.59), which will introduce transport effects related to anisotropic collisions in the plasma. Epperlein [45] provided an analytical derivation of these transport coefficients in the Lorentz limit, which is followed here. The $\mathbf{C}_{ee1}$ term is then neglected under the assumption that electron-ion collisions dominate over electron-electron collisions.

A second assumption required for the formation of an analytic solution is that the electron inertia term $\partial \mathbf{f}_1 / \partial t$ may be neglected. As seen in eq. 2.62 this results in the temporal evolution of the electron current. A consequence of this is that the electron response to perturbations is now instantaneous, with the distribution function anisotropy assuming a *steady-state* where $\partial \mathbf{f}_1 / \partial t = 0$, with Ohm's law now an equality. This approach is often taken in fluid codes and is justified on the basis that the electron-inertia term is small compared to the electron-ion collision term

$$\left| \frac{1}{\mathbf{f}_1} \frac{\partial \mathbf{f}_1}{\partial t} \right| \ll \nu_{ei}. \tag{2.71}$$

This relation says that the characteristic frequency with which $\mathbf{f}_1$ evolves must be much shorter than the collision frequency, which implies that the time-scale of interest must exceed the collision time. As will be explored later, this is related to the assumption that anisotropy in the distribution function is small.

The $\mathbf{f}_1$ equation then reads

$$v\nabla f_0 + \mathbf{a}\frac{\partial f_0}{\partial v} + \boldsymbol{\omega} \times \mathbf{f}_1 = -\nu_{ei}\mathbf{f}_1 \tag{2.72}$$

which can be rearranged to expressions for $\mathbf{f}_1$ defined relative to the magnetic field unit vector $\mathbf{B}/|\mathbf{B}|$. The magnetic field leads to a separation of effects parallel and perpendicular to the field axis, which will be reflected in the form of the transport coefficients; particles travel according to their mean-free-path parallel to the magnetic field, while perpendicular their trajectory is confined by the gyro-orbit.

On assuming a form of f_0, which is taken to be a Maxwellian, moments of 2.72 can be taken to give expressions for Ohm's law and the heat-flow equation in terms of n_e, $\langle \mathbf{v} \rangle$, and T_e. These are found by taking the $\mathbf{v}$ and $v^2\mathbf{v}$ moments of the Vlasov-Fokker-Planck equation, which give the v and v^3 moments of the $\mathbf{f}_1$ equation. Ohm's law and the heat-flow equation then read

$$en_e\mathbf{E} = \mathbf{J} \times \mathbf{B} - \nabla P_e + \frac{m_e}{e\tau_B}\underline{\underline{\alpha}}^c \cdot \mathbf{J} - n_e\underline{\underline{\beta}}^c \cdot \nabla T_e \tag{2.73}$$

$$\mathbf{q} = -\frac{n_e\tau_B T_e}{m_e}\underline{\underline{\kappa}}^c \cdot \nabla T_e - \underline{\underline{\beta}}^c \cdot \mathbf{J}T_e \tag{2.74}$$

where defining the thermal velocity v_T

$$\begin{aligned} &v_T = \left(\frac{2T_e}{m_e}\right)^{1/2}, \quad \tau_T = \tau_{ei}(v_T) = \frac{4\pi v_T^3}{n_i Z^2 (e^2/\epsilon_0 m_e)^2 \ln\Lambda_{ei}} \propto T_e^{3/2}, \\ &\tau_B = c_B\tau_T \quad \text{with} \quad c_B = \frac{3\sqrt{\pi}}{4}, \quad \lambda_T = v_T\tau_T, \quad \text{and} \quad \chi_T = \omega_g\tau_T \end{aligned} \tag{2.75}$$

The subscript 'T' refers to the properties of thermal electrons. The distribution averaged collision time for a Maxwellian τ_B was adopted by Braginskii, and these values will be referred to using the subscript 'B'.

The coefficients $\underline{\underline{\alpha}}^c$, $\underline{\underline{\beta}}^c$ and $\underline{\underline{\kappa}}^c$ are the classical transport coefficients known as the resistivity, thermo-electric and thermal conductivity tensors. They are dimensionless functions dependent only on the macroscopic plasma parameters χ_B and Z as shown in fig. 2.4; the latter dependence on ionisation arises when electron-electron collisions are included [46]. The relationships with the dimensional versions are

$$\underline{\underline{\alpha}} = \underline{\underline{\alpha}}^c\frac{m_e n_e}{\tau_B}, \quad \underline{\underline{\beta}} = \underline{\underline{\beta}}^c, \quad \text{and} \quad \underline{\underline{\kappa}} = \underline{\underline{\kappa}}^c\frac{n_e T_e \tau_B}{m_e}. \tag{2.76}$$

The transport coefficients are defined relative to the magnetic field axis and that

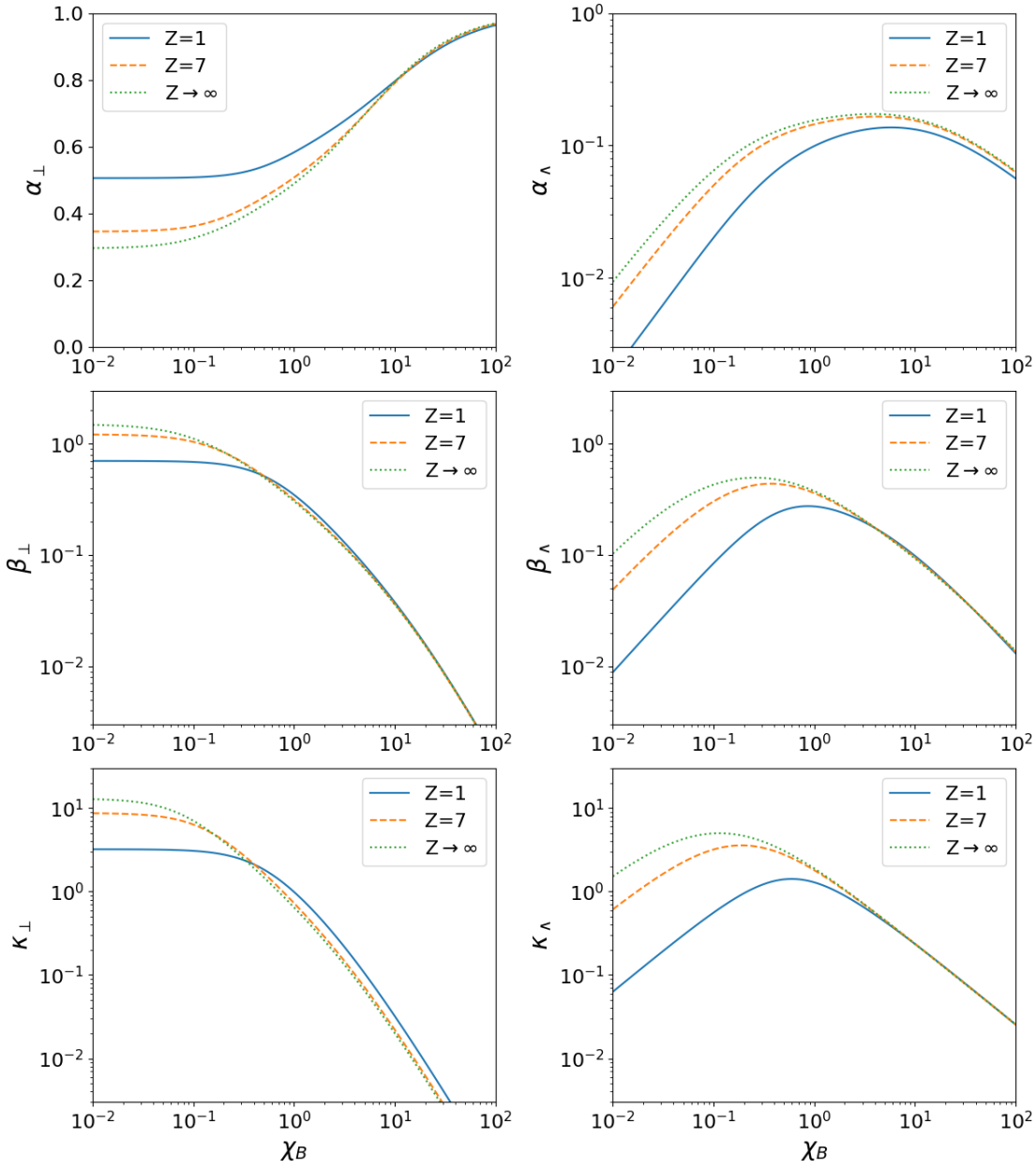

Figure 2.4: The dimensionless transport coefficients $\underline{\underline{\alpha}}^c$, $\underline{\underline{\beta}}^c$ and $\underline{\underline{\kappa}}^c$ as a function of the magnetisation χ_B reproduced from Epperlein and Haines [46]. These are shown for ionisations of $Z = 1$ and 7, as well as for the Lorentz limit $Z \to \infty$.

of the driving force behind the transport. Each coefficient consists of components which describe transport behaviour parallel '$\parallel$' and perpendicular '$\perp$' to the magnetic fields, as well as perpendicular to both the magnetic field and driving term '$\wedge$'. For a general transport coefficient $\underline{\underline{\eta}}^c$ with driving force given by the vector $\mathbf{s}$ the components are then defined

$$\underline{\underline{\eta}}^c \cdot \mathbf{s} = \eta_\parallel \mathbf{b}(\mathbf{b}\cdot\mathbf{s}) + \eta_\perp \mathbf{b}\times(\mathbf{s}\times\mathbf{b}) + \eta_\wedge \mathbf{b}\times\mathbf{s} \tag{2.77}$$

which on defining the z-axis as the magnetic field axis such that $\mathbf{B} = B_z\hat{\mathbf{k}}$ gives

$$\underline{\underline{\eta}}^c = \eta_\parallel \begin{pmatrix} 0 \\ 0 \\ s_z \end{pmatrix} + \eta_\perp \begin{pmatrix} s_x \\ s_y \\ 0 \end{pmatrix} + \eta_\wedge \begin{pmatrix} -b_z s_y \\ b_z s_x \\ 0 \end{pmatrix}. \tag{2.78}$$

The driving force for the resistivity and thermal conductivity tensors are the current and temperature gradient respectively, while the thermo-electric term is driven by both effects. The same formalism can be applied to unmagnetised plasmas by freely defining the magnetic field axis, with $\eta_\perp(\chi_B = 0) = \eta_\parallel$ and the wedge coefficient tending to zero in the unmagnetised limit.

Integral expressions for the transport coefficients were provided by Epperlein in the Lorentz limit [45]. For example, in the weakly magnetised limit the thermal conductivity tensors were given as

$$\kappa_\perp = \frac{8\sqrt{\pi}}{9}\left(\langle V^9\rangle - \frac{\langle V^7\rangle^2}{\langle V^5\rangle}\right) \tag{2.79}$$

$$\kappa_\wedge = \frac{8\sqrt{\pi}}{9}\chi_B\left(\langle V^{12}\rangle - 2\frac{\langle V^{10}\rangle\langle V^7\rangle}{\langle V^5\rangle} - \frac{\langle V^7\rangle^2\langle V^8\rangle}{\langle V^5\rangle^2}\right). \tag{2.80}$$

The same approach can then be used to calculate transport coefficients for arbitrary distribution function, as was done by Ridgers *et al.* for the case of the super-Gaussian transport coefficients [47]. Obtaining the ionisation dependence as is shown in fig. 2.4 requires including the electron-electron collision operator, which is done using numerical methods due to the complexities of the collision operator. The fits provided by Epperlein and Haines [46] for this purpose will be used throughout this thesis unless stated otherwise.

As will be found in the coming chapter, transport behaviour as a function of magnetisation is intimately tied to the distribution function. Consider the origin of the collision force, which arises when electrons are scattered by ions and consequently

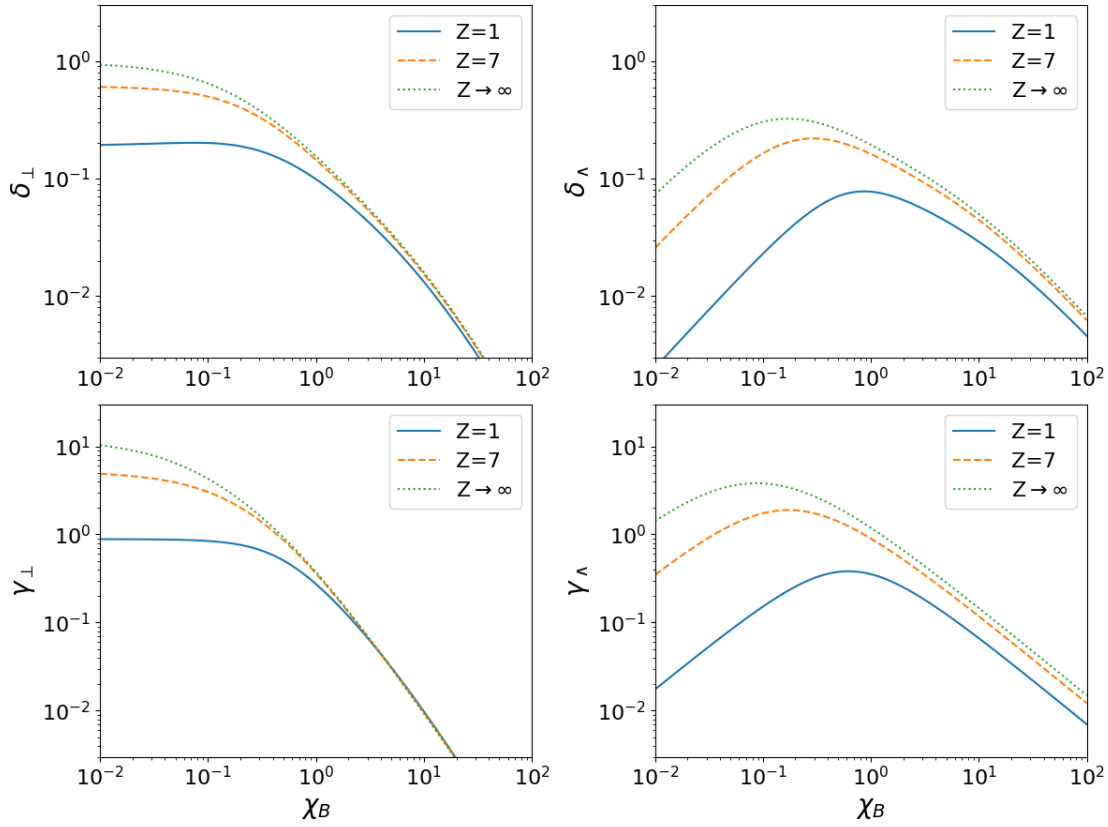

Figure 2.5: The dimensionless transport coefficients $\underline{\underline{\delta}}^c$ and $\underline{\underline{\gamma}}^c$ as a function of the magnetisation χ_B reproduced from Sadler *et al.*[48]. These are shown for ionisations of $Z = 1$ and 7, as well as for the Lorentz limit $Z \to \infty$.

lose momentum. For a net force to arise there must be anisotropy in the velocity distribution. The thermal force arises due to an imbalance of hot and cold electrons; while the net flux is zero, more hot electrons pass in one direction than another. Due to the velocity dependence of the collision frequency v^{-3}, the ions exert a greater force on lower velocity electrons [3]. The current force is similar but now occurs because the outgoing and return currents required for quasi-neutrality are in opposite directions.

A natural symmetry arises in the transport coefficients, identified by Sadler *et al.* [48] who noted that a subtle inaccuracy of the fits provided by Epperlein and Haines significantly modified magnetic transport. This affects the cross-gradient Nernst term and cross-gradient Hall effect, where it is the difference between transport parallel and perpendicular to the axis that determine transport. These new resistivity terms are defined

$$\delta_\perp = \frac{\alpha_\wedge}{\chi_B} \quad \text{and} \quad \delta_\wedge = \frac{\alpha_\perp - \alpha_\parallel}{\chi_B} \tag{2.81}$$

with the new thermo-electric terms

$$\gamma_\perp = \frac{\beta_\wedge}{\chi_B} \quad \text{and} \quad \gamma_\wedge = \frac{\beta_\parallel - \beta_\perp}{\chi_B}. \tag{2.82}$$

The symmetric coefficients are then formed by the set $\underline{\underline{\beta}}^c$, $\underline{\underline{\kappa}}^c$, $\underline{\underline{\delta}}^c$ and $\underline{\underline{\gamma}}^c$, where the latter two coefficients have been introduced and are shown in fig. 2.5.

2.3.2 Ion hydrodynamics

The treatment of ions has so far been that of a neutralising background; the ion velocity is assumed small relative to that of the electrons, with the average ion velocity $\mathbf{u} = 0$. Neglecting the displacement current $\partial\mathbf{E}/\partial t$ in Ampere's law, a common fluid assumption, enforces quasi-neutrality in the plasma such that $\partial n_e/\partial t = 0$ unless there is a corresponding change in the ion density; this can be shown by taking the divergence of Ampere's law in combination with Gauss's law. Bulk ion motion is then required for hydrodynamic motion of the plasma.

The role of the displacement current can be considered by substituting Ohm's law into Ampere's law, and assuming a harmonic electric field. Provided $\omega_{pe} \gg \nu_{ei}$ and $\omega_{pe} \gg \omega_g$ then for phenomena slowly varying with respect to the plasma frequency the displacement current may be neglected.

A method of assessing the importance of hydrodynamics is to compare the sound

speed with the time and length scales of interest, referred to as t_I and l_I respectively. It can be expected that ion motion is significant when

$$l_I \sim v_s t_I \quad \text{where} \quad v_s = \left(\frac{\gamma P_e}{\rho_i}\right)^{1/2} \tag{2.83}$$

is the sound speed, $\rho_i = m_i n_i \approx m_i n_e/Z$ is the ion mass density, and the ratio of specific heats for a mono-atomic ideal gas is $\gamma = 5/3$. For time and length scales of the order of $l_I = 100$ µm and $t_I = 1$ ns, this gives sounds speeds of the order of 10^5 ms^{-1}.

Ion hydrodynamics can be included by considering electron transport in the frame of motion of the ions [49]. The Vlasov-Fokker-Planck equation is then transformed, modifying the electron transport equation set as follows

$$\frac{\partial n_e}{\partial t} + \nabla \cdot (n_e \mathbf{u}) = 0 \tag{2.84}$$

$$\frac{3}{2} n_e \left(\frac{\partial T_e}{\partial t} + \mathbf{u} \cdot \nabla T_e\right) + n_e T_e \nabla \cdot \mathbf{u} + \nabla \cdot \mathbf{q} - (\mathbf{E} + \mathbf{u} \times \mathbf{B}) \cdot \mathbf{J} = 0 \tag{2.85}$$

$$e n_e (\mathbf{E} + \mathbf{u} \times \mathbf{B}) = \mathbf{J} \times \mathbf{B} - \nabla P_e + \frac{m_e}{e \tau_B} \underline{\underline{\alpha}}^c \cdot \mathbf{J} - n_e \underline{\underline{\beta}}^c \cdot \nabla T_e \tag{2.86}$$

$$\mathbf{q} = -\frac{n_e \tau_B T_e}{m_e} \underline{\underline{\kappa}}^c \cdot \nabla T_e - \underline{\underline{\beta}}^c \cdot \mathbf{J} T_e. \tag{2.87}$$

First, in the continuity equation the inclusion of ion motion now permits the electron density profile proportionally with the ions as $n_e = Z n_i$ is assumed. Secondly, in the energy equation the partial derivative has been replaced with the convective derivative, describing the temperature change in the fluid frame. Additionally, a new term in the energy equation allows changes in the internal energy density via compressional heating. The last correction to the energy equation is in the Joule heating where the force acting on the current is now due to both the electric and magnetic field. Finally, Ohm's law is modified by a similar transformation. The heat-flow equation remains unchanged. The original equation set is returned in the limit $\mathbf{u} = 0$.

An expression for $\mathbf{u}$ can be obtained using the two-fluid equations for ions and electrons derived from the Boltzmann equation. The equations are rearranged in terms of the convective derivative; to do so the pressure tensor is expressed using the intrinsic velocity $\mathbf{w} = \mathbf{v} - \langle \mathbf{v} \rangle$ and the continuity equation subtracted. The ion and electron momentum equations are then

$$\rho_i \left[\frac{\partial \mathbf{u}_i}{\partial t} + (\mathbf{C_i} \cdot \nabla)\mathbf{u}_i \right] + \nabla P_i - Zen_i(\mathbf{E} + \mathbf{u}_i \times \mathbf{B}) = \Delta \mathbf{p}_{ie} \tag{2.88}$$

$$\rho_e \left[\frac{\partial \mathbf{u}_e}{\partial t} + (\mathbf{C_e} \cdot \nabla)\mathbf{u}_e \right] + \nabla P_e + en_e(\mathbf{E} + \mathbf{u}_e \times \mathbf{B}) = \Delta \mathbf{p}_{ei}. \tag{2.89}$$

where conservation of momentum gives $\Delta \mathbf{p}_{ei} = -\Delta \mathbf{p}_{ei}$.

A single fluid equation governing the momentum of their combined centre of mass is obtained by combining these equations. Before doing so the terms in each expression are compared. Electron inertia may be neglected as it is much smaller than ion inertia ($m_i \gg m_e$), while as the laser preferentially heats the electrons $\nabla P_e \gg \nabla P_i$. Noting that $Zn_i = n_e$ due to quasi-neutrality yields and adding the equations yields

$$\rho_i \left[\frac{\partial \mathbf{u}_i}{\partial t} + (\mathbf{u_i} \cdot \nabla)\mathbf{u}_i \right] = -\nabla(P_e) + \mathbf{J} \times \mathbf{B}. \tag{2.90}$$

Using Ampere's Law and neglecting the displacement current allows the current to be substituted to give

$$\rho_i \left[\frac{\partial \mathbf{u}_i}{\partial t} + (\mathbf{u_i} \cdot \nabla)\mathbf{u}_i \right] = -\nabla \left(P_e + \frac{B^2}{2\mu_0} \right). \tag{2.91}$$

Using 2.91 a complete set of equations is again formed, now including hydrodynamic ion motion. Ions are accelerated by gradients in both the thermal pressure and magnetic pressure, where the latter is defined

$$P_B = \frac{B^2}{2\mu_0}. \tag{2.92}$$

The ratio of the thermal pressure to the magnetic pressure is known as the plasma beta

$$\beta = \frac{P_e}{P_B} = \frac{n_e T_e}{B^2/2\mu_0} \tag{2.93}$$

and is a key quantity when identifying the plasma regime [50]. For plasmas considered in this thesis that are hot and dense with moderate magnetic field strengths up to $B \sim 1$ T, the thermal pressure can be assumed to be dominant over the magnetic pressure such that $\beta \gg 1$.

The significance of hydrodynamic effects can be evaluated for the plasmas consid-

ered here using the dimensionless Peclet number Pe and magnetic Reynolds number Re_M [2]. These dimensionless numbers consider the importance of transport phenomena relative to convective effects with characteristic speed u and length scale L. The Peclet number quantifies the importance of the heat-transport term in the energy equation and is defined

$$\mathrm{Pe} = \frac{ul}{\chi} \quad \text{where} \quad \kappa = \chi n k_B \frac{\gamma}{\gamma - 1} \tag{2.94}$$

is the relationship between the thermal conductivity and the thermal diffusivity χ. Heat-transport can be neglected if $\mathrm{Pe} \gg 1$. The magnetic Reynolds number quantifies the importance of advection relative to diffusion in the magnetic induction equation and is defined

$$\mathrm{Re}_M = \frac{uL}{\eta} \quad \text{where} \quad \eta = \frac{\alpha}{\mu_0 e^2 n_e^2} \tag{2.95}$$

is the relationship between the resistivity and the magnetic diffusivity. Magnetic diffusion can be neglected if $\mathrm{Re}_M \gg 1$, which is the case for the plasmas considered here. If both $\mathrm{Pe} \ll 1$ and $\mathrm{Re}_M \gg 1$ then thermal transport will be dominant in both the induction and energy equation.

2.3.3 Heat-flow phenomena

In the heat-flow equation (eq. 2.87) the total heat-flow has been provided as the sum of both intrinsic heat-flow and that due to the electron's average velocity. The intrinsic velocity represents the thermal motion associated with the internal energy density, separate from the kinetic energy density associated with any bulk-flow. If instead moments of the $\mathbf{f}_1$ equation are taken for the intrinsic velocity, then the thermal heat-flow equation reads

$$\mathbf{q} = -\frac{n_e \tau_B T_e}{m_e} \underline{\underline{\kappa}}^c \cdot \nabla T_e - \left(\underline{\underline{\beta}}^c + \frac{5}{2} \underline{\underline{\mathbf{I}}} \right) \cdot \mathbf{J} T_e. \tag{2.96}$$

The heat-flow can be seen to consist of the conductive heat-flow related to $\underline{\underline{\kappa}}^c$ and driven by the temperature gradient, and thermo-electric effects related to $\underline{\underline{\beta}}^c$ driven by the current. The transport geometry considered will be that of heat-flow perpendicular to the magnetic field, so parallel components will be neglected for simplicity. In the unmagnetised limit only the conductive term remains, at which point $\kappa_\perp = \kappa_\parallel$.

Conductive heat-flow

The most relevant of these effects in this thesis is that of the conductive heat-flow. Observing the energy equation the conductive heat-flow leads to the advection of the internal energy density

$$\frac{\partial U}{\partial t}_{\kappa} = -\nabla \cdot \mathbf{q}_{\kappa} = -\nabla \cdot \left(U \frac{\mathbf{q}_{\kappa}}{(3/2)P_e} \right) \tag{2.97}$$

with velocity $\mathbf{q}_{\kappa}/(3/2)P_e$. The conductive heat-flow is separated into

$$\mathbf{q}_{\kappa} = \mathbf{q}_{\perp} + \mathbf{q}_{\wedge} \tag{2.98}$$

which are the diffusive and Righi-Leduc heat-flows respectively.

The diffusive heat-flow is known as such because it results in the diffusion of temperature, which is seen on substitution into the energy equation

$$\frac{\partial U}{\partial t}_{\perp} = -\nabla \cdot \mathbf{q}_{\perp} = -\nabla \cdot \left(\frac{n_e T_e \tau_B}{m_e} \kappa_{\perp} \nabla T_e \right). \tag{2.99}$$

where if $\nabla n_e = 0$ the diffusion coefficient is given by

$$d_{\perp} = \frac{c_B}{3} v_T \lambda_T \kappa_{\perp}. \tag{2.100}$$

Noting that $\tau_B \propto n_e^{-1}$ further highlights the diffusive character, with the heat-flow largely independent of density in the unmagnetised local limit. The increase in particle flux with density is balanced by the decrease in the collision time, with only a weak dependence on the Coulomb logarithm remaining.

Magnetisation initially has limited effect on the diffusive heat-flow, as the mean-free-path of the electrons remains effectively unchanged relative to that of an umagnetised plasma. However, this is ionisation dependent with a reduction in the heat-flow of $\sim 50\%$ occurring at a magnetisation of $\chi_B \approx 10^{-2}$ in the Lorentz limit, but at ~ 0.6 for a hydrogen plasma. Note that while the magnetisation initially has less effect at lower Z, the perpendicular conductivity is also lower. When strongly magnetised the diffusive heat-flow is strongly suppressed as $\kappa_{\perp} \propto \chi_B^{-2}$. Ionisation has less effect in this regime, although now lower Z plasmas tend to have increased conductivity of the order of $\sim 50\%$ relative to the Lorentz limit. The form of the diffusion coefficients is found to vary between these two regimes with

$$d_\perp(\chi_B \ll 1) \propto v_T \lambda_T \quad \text{and} \quad d_\perp(\chi_B \gg 1) \propto v_T \frac{r_g}{\chi_B} \tag{2.101}$$

the dependence in the weakly and strongly magnetised regime respectively. As diffusion coefficients take the form of the product of the velocity v and the step-size l, this suggests a reduction in the step-size from λ_T to r_g/χ_B.

The Righi-Leduc arises as a result of the rotation of the electrons by the magnetic field, driving heat-flow perpendicular to both the temperature gradient and magnetic field, so as such only occurs in magnetised plasmas. In the weakly magnetised regime this scales as $\kappa_\wedge \propto \chi_B$, increasing with magnetisation, while in a strongly magnetised plasma the dependence is $\kappa_\wedge \propto \chi_B^{-1}$, decreasing with magnetisation. However, as the scaling is weaker than that of the diffusive heat-flow, the Righi-Leduc effect can be found to exceed diffusive heat-flow. Comparing eq. 2.79 and eq. 2.80 it is seen that the Right-Leduc heat-flow is dependent upon higher velocity moments of the electron distribution function.

Simulations by Walsh *et al.* [19, 51] demonstrated that the Righi-Leduc effect can lead to significant reductions in the hot spot temperature of indirect drive implosions, when self-generated magnetic fields cause moderate magnetisation of the plasma ($\chi_B \approx 1$). Additionally, there is a coupling of the Righi-Leduc and Nernst effect, the latter of which will be discussed shortly, which can result in the field compressing magneto-thermal instability when temperature gradients are perpendicular to the magnetic field [52]. These effects are both amplified by asymmetry.

While it seems natural to assume the cross-over from mean-free-path dominated (weakly magnetised) to gyro-radius dominated (strongly magnetised) transport occurs at $\chi_B = 1$, this is not the case. Observation of the transport coefficients shows that the diffusive heat-flow can be suppressed well before this, while the peak in the Righi-Leduc heat-flow is also shifted towards lower magnetisation. Due to the velocity scaling of the magnetisation $\chi_B \propto v^3$ hotter electrons with $v > v_T$ are magnetised at lower χ_B than the thermal population; these electrons are responsible for heat-flow, so it is their behaviour which is most important when considering transport trends.

Thermo-electric heat-flow

The thermo-electric terms are driven by the current, which only occurs when there are gradients in the magnetic field if the displacement current is neglected. The heat-flow due to thermo-electric effects is separated as

$$\begin{gathered}\mathbf{q}_\beta = \mathbf{q}_u + \mathbf{q}_E \\ \text{where} \quad \mathbf{q}_u = -\frac{T_e}{e}(5/2 + \beta_\perp)\mathbf{J} \quad \text{and} \quad \mathbf{q}_E = -\frac{T_e}{e}\beta_\wedge \mathbf{b} \times \mathbf{J}\end{gathered} \tag{2.102}$$

are the heat-flow associated with the mean electron velocity ($\mathbf{J} = -en_e\langle\mathbf{v}\rangle$)and Ettingshausen effect respectively.

The importance of the Ettingshausen term can be considered by finding its ratio to the diffusive heat-flow

$$\frac{\mathbf{q}_\perp}{\mathbf{q}_E} = \frac{n_e T_e \tau_B \kappa_\perp \nabla T_e}{m_e} \frac{e\mu_0}{T_e \beta_\wedge \nabla |\mathbf{B}|} = \frac{\beta}{2}\frac{\kappa_\perp}{\gamma_\perp}\frac{l_B}{l_T} \tag{2.103}$$

where the current has been substituted using Ampere's law. The ratio $\kappa_\perp/\gamma_\perp$ is approximately constant for varying χ_B, so it is the plasma beta and ratio of the magnetic field to temperature length scales that are important. Generally, for the plasmas considered here, $\beta \gg 1$ and $l_B \sim l_T$ due to a coupling between the magnetic field and heat-flow dynamics. The Ettingshausen effect will only be found to modify heat-flow at the edge of pre-magnetised plasmas, where the plasma is cooler and less dense.

The heat-flow associated with the current is known as the Peltier effect. It can be considered a deflection of the Ettingshausen heat-flow in an analogous manner to the relationship between the Righi-Leduc and diffusive heat-flow.

2.3.4 Magnetic field phenomena

To derive the induction equation, which governs the evolution of the magnetic field, Ohms law eq. 2.86 is substituted into Faraday's equation

$$\frac{\partial \mathbf{B}}{\partial t} = -\nabla \times \left(-\mathbf{u} \times \mathbf{B} - \frac{\nabla P_e}{n_e e} + \frac{\mathbf{J} \times \mathbf{B}}{n_e e} + \frac{m_e \underline{\underline{\alpha}}^c \cdot \mathbf{J}}{n_e e^2 \tau_B} - \frac{\underline{\underline{\beta}}^c \cdot \nabla T_e}{e} \right) \tag{2.104}$$

allowing the relationship between the electric field terms and transport to be explored. Note that there are no inertial terms as these have been neglected in Ohm's law.

As demonstrated by Walsh *et al.*, all terms in the induction equation can either be written as a source, diffusion, or advection term. In this form eq. 2.104 reads

$$\frac{\partial \mathbf{B}}{\partial t} = \nabla \times (\mathbf{v_B} \times \mathbf{B}) - \nabla \times \left(\frac{m_e \alpha_\parallel}{n_e e^2 \tau_B \mu_0} \nabla \times \mathbf{B} \right) + \frac{\nabla T_e \times \nabla n_e}{n_e e} \tag{2.105}$$

where magnetic field is advected with velocity

$$\mathbf{v_B} = \mathbf{u} - \frac{\tau_B \nabla T_e}{m_e} \gamma_\perp + \frac{\tau_B \nabla T_e \times \mathbf{b}}{m_e} \gamma_\wedge - \frac{\mathbf{J}}{n_e e} (1 + \delta_\perp) + \frac{\mathbf{J} \times \mathbf{b}}{n_e e} \delta_\wedge. \tag{2.106}$$

Following this convention Ohm's law becomes

$$\mathbf{E} = -\mathbf{v_B} \times \mathbf{B} + \frac{m_e \alpha_\parallel}{n_e e^2 \tau_B \mu_0} \nabla \times \mathbf{B} - \frac{\nabla P_e}{n_e e} - \frac{\beta_\parallel}{e} \nabla T_e \tag{2.107}$$

allowing a clearer distinction between terms that are relevant to unmagnetised ($\mathbf{B} = 0$) and magnetised plasmas. In an initially unmagnetised plasma, an electric field arises in response to gradients in the pressure and temperature and will be referred to as the thermo-electric effect.

Any equation of the form

$$\frac{\partial \mathbf{B}}{\partial t} = \nabla \times (\mathbf{v} \times \mathbf{B}) \tag{2.108}$$

can be expanded using the identity $\nabla \times (\mathbf{A} \times \mathbf{B}) = \mathbf{A}(\nabla \cdot \mathbf{B}) - \mathbf{B}(\nabla \cdot \mathbf{A}) + (\mathbf{B} \cdot \nabla)\mathbf{A} - (\mathbf{A} \cdot \nabla)\mathbf{B}$ with Gauss's law for magnetism $\nabla \cdot \mathbf{B} = 0$ to give

$$\frac{D\mathbf{B}}{Dt} = \frac{\partial \mathbf{B}}{\partial t} + (\mathbf{v} \cdot \nabla)\mathbf{B} = -\mathbf{B}(\nabla \cdot \mathbf{v}) + (\mathbf{B} \cdot \nabla)\mathbf{v}. \tag{2.109}$$

This is an advection equation where the term of the left is the convective derivative which describes the change in the magnetic field strength in the frame of a fluid element. The second term describes compression or rarefaction of magnetic fields due to gradients in the advection velocity. The third term can twist the magnetic field, but for the geometries considered here it is assumed that $\mathbf{B} = |\mathbf{B}|\hat{\mathbf{k}}$ with the plasma invariant along the z-axis such that $\mathbf{B} \cdot \nabla = 0$.

Following this reasoning, the first term in the induction equation (eq. 2.104) is understood. This describes the advection of the magnetic field at the hydrodynamic ion velocity $\mathbf{u}$, and is known in the framework of *ideal* hydrodynamics as 'frozen-in-flow'. In an ideal plasma the magnetic field moves exactly with the plasma flow. Note that for a plasma modelled using the single-fluid equation derived previously

electron motion is tied to ion motion. This behaviour is described by eq. 2.109. Hydrodynamic advection causes the transport of field with the bulk ion velocity, with gradients in the velocity resulting in compression , rarefaction, and twisting of the field.

Biermann battery

Field generation in the induction equation occurs via the Biermann battery, which occurs when there is a curl in the pressure gradient

$$\left[\frac{\partial \mathbf{B}}{\partial t}\right]_{\nabla P_e} = \nabla \times \left(\frac{n_e \nabla T_e + T_e \nabla n_e}{n_e e}\right) = \frac{\nabla T_e \times \nabla n_e}{n_e e} \tag{2.110}$$

using the identities $\nabla \times \nabla f = 0$ and $\nabla f \times \nabla f = 0$ for a scalar function f. If there are misaligned gradients in temperature and density a magnetic field is then created. The effect is most significant in plasmas which are initially unmagnetised, as magnetisation can dramatically alter the transport properties as has been shown using classical transport theory.

There is significant interest in this term both astrophysically, where the Biermann battery provides a means through which the early universe is magnetised [53], and in inertial confinement fusion experiments [19, 54, 55]. These fields are common in laser-plasma experiments, particularly in laser-solid interactions where the temperature gradient is predominantly normal to the laser beam but the ablation of material from the target results in density gradients parallel to the beam. The flux density during the interaction can be of the order of 100 T [56, 57, 58]. Furthermore, as the magnetic field geometry is azimuthal to the laser, magnetic reconnection can be studied by focussing two laser spots adjacent to each other [59].

Under non-local conditions, where the distribution function is no longer described by a Maxwellian, Kingham and Bell demonstrated the general extension to this effect [60]. Here, magnetic field generation occurs via misaligned gradients in the electron distribution function, which can occur even when $\nabla n_e = 0$ during non-uniform heating. Strong anisotropy can also cause the generation of magnetic field via the Weibel instability [61, 62, 40]. This is associated with the anisotropic pressure, and as such does not appear in the equation due to truncation of the expansion at $\mathbf{f}_1$ following the diffusive approximation.

Hall advection

The next term in the induction equation is the $\mathbf{J} \times \mathbf{B}$ term which describes the Hall effect. From the definition of the current $\mathbf{J} = -en_e\langle\mathbf{v}\rangle$ this can be seen to drive advection with the electron population at velocity $\langle\mathbf{v}\rangle$

$$\left[\frac{\partial \mathbf{B}}{\partial t}\right]_{\mathbf{J}} = \nabla \times \left(-\frac{\mathbf{J} \times \mathbf{B}}{en_e}\right) = \nabla \times (\langle\mathbf{v}\rangle \times \mathbf{B}). \tag{2.111}$$

Using Ampere's law $\nabla \times \mathbf{B} = \mu_0 \mathbf{J}$ this can be expressed as $\mathbf{J} \times \mathbf{B} = -\nabla|\mathbf{B}|^2/\mu_0 + (\mathbf{B}\cdot\nabla)\mathbf{B}/\mu_0$, with the latter term contributing to advection as the curl of the gradient is zero. This term can become significant when the gradient in the magnetic field is large, relaxing magnetic tension.

Resistive diffusion

Resistivity is included in the induction equation via the transport coefficient $\underline{\underline{\alpha}}^c$, and as such can be seen to arise from collisional transport. The resistivity tensor is expanded as

$$\begin{aligned}\left[\frac{\partial \mathbf{B}}{\partial t}\right]_{\underline{\underline{\alpha}}^c} &= -\nabla \times \left(\frac{m_e}{n_e e^2 \tau_B} \underline{\underline{\alpha}}^c \cdot \mathbf{J}\right) \\ &= -\nabla \times \left(\frac{m_e}{n_e e^2 \tau_B}(\alpha_\parallel \mathbf{b}(\mathbf{b}\cdot\mathbf{J}) + \alpha_\perp \mathbf{b} \times (\mathbf{J} \times \mathbf{b}) + \alpha_\wedge \mathbf{b} \times \mathbf{J})\right)\end{aligned} \tag{2.112}$$

where using the vector triple product $\mathbf{b}(\mathbf{b}\cdot\mathbf{J}) = \mathbf{J} - \mathbf{b} \times (\mathbf{J} \times \mathbf{b})$ in combination with Ampere's law

$$\begin{aligned}\left[\frac{\partial \mathbf{B}}{\partial t}\right]_{\underline{\underline{\alpha}}^c} &= -\nabla \times \left(\frac{m_e \alpha_\parallel}{\mu_0 n_e e^2 \tau_B} \nabla \times \mathbf{B}\right) \\ &\quad + \nabla \times \left(\frac{(\alpha_\perp - \alpha_\parallel)}{n_e e \chi_B}(\mathbf{J} \times \mathbf{b}) \times \mathbf{B} + \frac{\alpha_\wedge}{n_e e \chi_B} \mathbf{J} \times \mathbf{B}\right).\end{aligned} \tag{2.113}$$

The first term in this equation results in resistive diffusion, which smooths gradients in the magnetic field. The importance of this quantity relative to advection is given by the magnetic Reynolds number (eq. 2.95).

The next two terms are advective and alter the Hall velocity in the parallel ($\alpha_\wedge$) and perpendicular ($\alpha_\perp - \alpha_\parallel$) directions. The advection velocities are expressed in

terms of the transport coefficient $\underline{\underline{\delta}}^c$ derived by Walsh *et al.* [63] as follow

$$\mathbf{v}_{R\perp} = \frac{\alpha_\wedge}{n_e e \chi_B}\mathbf{J} = \frac{\delta_\perp}{e n_e}\mathbf{J} \tag{2.114}$$

$$\mathbf{v}_{R\wedge} = \frac{\alpha_\perp - \alpha_\parallel}{n_e e \chi_B}(\mathbf{J}\times\mathbf{b}) = \frac{\delta_\wedge}{e n_e}(\mathbf{J}\times\mathbf{b}) \tag{2.115}$$

with the relationship to the dimensional form of the transport coefficient

$$\underline{\underline{\delta}} = \frac{\underline{\underline{\delta}}^c}{n_e}. \tag{2.116}$$

By expressing the transport coefficients this way it appears that it is the difference between the $\alpha_\perp$ and $\alpha_\parallel$ coefficients that gives the cross-Hall velocity, instead of $\alpha_\perp$. As this was not recognised by Epperlein and Haines [46], their fits allowed a degree of freedom such that $\partial\alpha_\perp/\partial\chi_B \neq 0$ when $\chi_B = 0$. This was corrected by Sadler *et al.* [48] who then demonstrated the symmetry of the transport coefficients. While the new fit for $\underline{\underline{\delta}}^c$ appears similar to the original fit, the absence of this degree of freedom significantly reduces the calculated cross-gradient Hall velocity when $\chi_B < 1$ and prevents discontinuities.

Nernst advection

The final term in the induction equation describes the Nernst effect, where advection of the magnetic field is driven by gradients in the temperature. As it depends on the transport coefficient $\underline{\underline{\beta}}^c$ collisions are a requirement for this effect to be observed. To show this the thermo-electric term in the induction equation as written in eq. 2.104 is expanded

$$\begin{aligned}\left[\frac{\partial\mathbf{B}}{\partial t}\right]_{\underline{\underline{\beta}}^c} =& \frac{1}{e}\nabla\times(\underline{\underline{\beta}}^c\cdot\nabla T_e)\\ =& \frac{1}{e}\nabla\times(\beta_\parallel\mathbf{b}(\mathbf{b}\cdot\nabla T_e) + \beta_\perp\mathbf{b}\times(\nabla T_e\times\mathbf{b}) + \beta_\wedge\mathbf{b}\times\nabla T_e).\end{aligned} \tag{2.117}$$

To obtain them in the form found in the magnetic advection velocity $\mathbf{v}_B$, where the Nerst effect is associated with the $\underline{\underline{\gamma}}^c$ coefficient, the formalism of Walsh et al. [63] is followed using the vector triple product $\mathbf{b}(\mathbf{b}\cdot\nabla T_e) = \nabla T_e - \mathbf{b}\times(\nabla T_e\times\mathbf{b})$ such that

$$\left[\frac{\partial \mathbf{B}}{\partial t}\right]_{\underline{\underline{\beta}}^c} = \nabla \times \left(\frac{\beta_\parallel}{e} \nabla T_e - \frac{\beta_\perp - \beta_\parallel}{e|\mathbf{B}|} (\nabla T_e \times \mathbf{b}) \times \mathbf{B} - \frac{\beta_\wedge}{e|\mathbf{B}|} \nabla T_e \times \mathbf{B} \right). \quad (2.118)$$

Here $\nabla \times \beta_\parallel \nabla T_e$ is zero as $\beta_\parallel$ is constant for fixed ionisation. Eq. 2.118 then allows the Nernst velocity

$$\mathbf{v}_{N\perp} = -\frac{\beta_\wedge}{e|\mathbf{B}|} \nabla T_e = -\frac{\gamma_\perp \tau_B}{m_e} \nabla T_e \quad (2.119)$$

to be defined, as well as the cross-gradient Nernst velocity

$$\mathbf{v}_{N\wedge} = -\frac{\beta_\perp - \beta_\parallel}{e|\mathbf{B}|} (\nabla T_e \times \mathbf{b}) = \frac{\gamma_\wedge \tau_B}{m_e} (\nabla T_e \times \mathbf{b}). \quad (2.120)$$

The dimensional form of the $\underline{\underline{\gamma}}^c$ coefficient is related by

$$\underline{\underline{\gamma}} = \underline{\underline{\gamma}}^c \frac{\tau_B}{m_e}. \quad (2.121)$$

Again, the advantage of this formalism is that it highlights that it is the difference between the $\beta_\perp$ and $\beta_\parallel$ coefficients that give the cross-gradient Nernst velocity, rather than the $\beta_\perp$ itself. As with the resistivity tensor the fits of Epperlein and Haines [46] resulted in an additional degree of freedom such that $\partial\beta_\perp/\partial\chi_B \neq 0$ when $\chi_B = 0$ result. This resulted in overestimation and discontinuities in the cross-gradient Nernst coefficient at low magnetisation ($\chi_B < 1$) [48].

The Nernst velocity $\mathbf{v}_{N\perp}$ leads to the advection of field down temperature gradients, demagnetising the hot plasma [49], with the process of convective amplification occurring at the base of the heat-front [64]. To consider the effect of magnetisation on $\mathbf{v}_{N\perp}$ either the dimensional $\gamma_\perp$ or dimensionless $\beta_\wedge$ should be considered. This is because in terms of the dimensionless $\gamma_\perp$ the Nernst velocity is proportional to τ_B, which affects the magnetisation and, therefore, the transport coefficient. The Nernst velocity initially increases with magnetisation but is suppressed once $\chi_B \approx 1$.

The Nernst effect has been shown to be coupled with the thermal heat-flow, even in the non-local case [65]. The relationship is highlighted by expressing the Nernst velocity as

$$\mathbf{v}_{N\perp} = \frac{\gamma_\perp}{\kappa_\perp} \frac{\mathbf{q}_\perp}{n_e T_e} \quad (2.122)$$

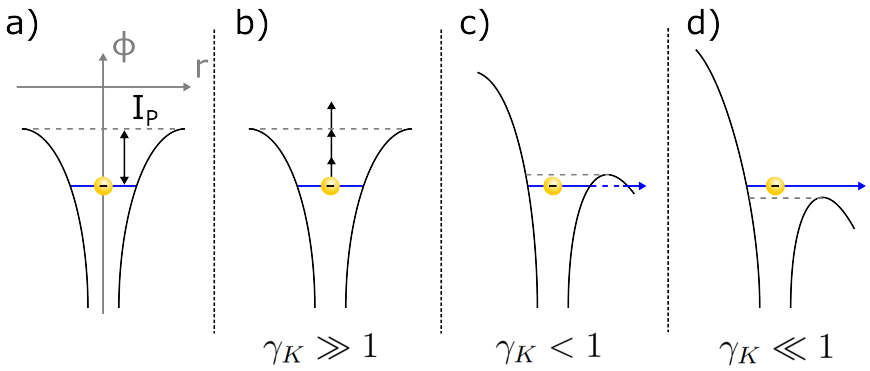

Figure 2.6: Schematic diagram of the ionisation processes that occur in intense laser fields for varying regimes of the Keldysh parameter. In a) the potential felt by a bound electron in the field-free case is shown. The mechanisms via which electrons can overcome the ionisation potential are b) multiphoton ionisation ($\gamma_K \gg 1$), c) tunnelling ionisation ($\gamma_K < 1$), and d) over-the-barrier ionisation ($\gamma_K \ll 1$).

where $\gamma_\perp/\kappa_\perp \approx 2/3$. Fundamentally this is due to a discrepancy between the collision time of hot and cold electrons, resulting in the exertion of a force on the ion population [66, 67].

2.4 Laser heating

Up to now, the focus has been on how heat and magnetic fields are transported within the plasma. However, the mechanism via which the plasma is generated and driven out of equilibrium — the laser — has not yet been addressed. In this context, the laser-matter interaction will be considered. The mechanism by which energy is coupled to the system is dependent upon several parameters. These include the laser intensity I_l, wavelength $\lambda_l = 2\pi c/\omega_l$, pulse length t_l, and the properties of the material being heated. As will be shown the laser characteristics are central to both the evolution of the plasma and the validity of the fluid approach.

Typically, laser intensity is increased by compressing the laser pulse, so broadly speaking lasers are split into two categories: short-pulse lasers with pulse lengths of the order 1 ps or less and intensities exceeding $I_l \approx 10^{18}$ Wcm^{-2}, and long-pulse lasers that are order of 1 ns with $I_l \approx 10^{12} - 10^{16}$ Wcm^{-2}. Here long-pulse interactions will be considered, which are of greater relevance to inertial confinement fusion experiments.

When a laser interacts with an un-ionised target, whether solid or gas, its energy is initially absorbed by the electrons in the material. For photoionisation to occur the photon energy must exceed the ionisation potential, which for hydrogen

at $I_P = 13.6$ eV corresponds to a wavelength of $\lambda_l = 91.2$ nm. High-power laser systems often operate using a wavelength of 1.054 µm, which can be frequency doubled or tripled to 0.527 or 0.351 µm respectively, so photoionisation is often not relevant to laser-driven ionisation. Instead, non-linear processes, such as multiphoton and tunnelling ionisation [68], occur due to the intense electric field of the laser as shown in fig. 2.6. The relative importance of each mechanism is quantified using the Keldysh parameter

$$\gamma_K = \sqrt{\frac{I_P}{2U_P}} \quad \text{where} \quad U_P = \frac{e^2|E_0|}{4m_e\omega_l^2} \tag{2.123}$$

is the ponderemotive energy, E_0 is the amplitude of the laser electric field, and I_P is the ionisation potential. At higher frequency and lower laser intensity ($\lambda_l = 0.351$ µm, $I_P \sim 10^{14}$ Wcm^{-2}) multiphoton ionisation is more significant, but at lower laser frequency and higher intensity ($\lambda_l = 1.054$ µm, $I_P > 10^{15}$ Wcm^{-2}) it is exceeded by tunnelling ionisation.

Once a free electron has been produced it can gain additional energy from the laser via inverse bremsstrahlung, which will be discussed shortly. The free electron can then cause further ionisation via avalanche or cascade ionisation. During avalanche ionisation a free electron ionises an atom after a collision, releasing additional electrons which can then be accelerated by the electric field and cause further ionisation. This results in an exponential increase in the number of free electrons. As inverse bremsstrahlung becomes more prevalent in the presence of ions, ionisation further enhances the coupling of the laser to the electrons. The result is that the target can be considered in the plasma state on the picosecond timescale during the laser interaction. For the case of cascade ionisation, the vacancy in the atoms electronic structure can be filled by electrons in higher energy levels, releasing photons or secondary electrons which can again result in a chain reaction of increasing ionisation.

From the discussion of plasma frequency (eq. 2.18) it was seen that if $\omega_l < \omega_{pe}$ the laser will be screened by the electrons, defining a critical density above which the laser cannot propagate. For this reason *under-dense* plasmas are considered, where the electron density is $n_e \ll n_c$. Near the critical density the absorption of laser light via resonance absorption is important [69]. If the resonance condition is met then the laser can efficiently transfer energy into the plasma by exciting plasma waves, such as Langmuir waves. For a sufficiently intense laser these waves can grow in amplitude until they saturate by accelerating electrons, a process known as wave breaking, generating a hot non-Maxwellian tail in the electron distribution. Further collective absorption effects, such as parametric instabilities, are also tied to the

location of the critical surface.

As the laser propagates through the plasma below the critical density the electrons oscillate in the laser field at the quiver speed

$$v_{osc} = \frac{eE_0}{\omega_l m_e} \quad \text{where} \quad E_0 = \sqrt{\frac{2I_l}{c\sqrt{\epsilon_r}\epsilon_0}} \tag{2.124}$$

where $\epsilon_r = 1 - (\omega_p/\omega_l)^2$ is the dielectric constant which for under-dense plasmas where $\omega_p \ll \omega_l$ is $\epsilon_r \approx 1$. Collisions with ions result in a fraction of the laser energy then being converted into the internal energy of the plasma. This mechanism is known as *inverse bremsstrahlung*, which is assumed to be dominant for the plasmas studied here. Collisional effects tend to damp collective mechanisms. Note that over shorter timescales and at larger quiver velocity, which occurs at higher intensity and longer wavelength, collisions become less important. In these conditions collective mechanisms are become more efficient at coupling energy to the plasma.

Inverse bremsstrahlung preferentially heats the colder electron population. The inverse bremsstrahlung heating operator was developed by Langdon [70], and provides a modification to the kinetic f_0 equation. Langdon demonstrated that electron-electron collisions are insufficient to return the distribution function to a Maxwellian on the heating time scale if $Zv_{osc}/v_T \gtrsim 1$, resulting in a super-Gaussian distribution

$$f_{SG} = C(m)\frac{n_e}{v_T^3}\exp\left[-\left(\frac{v}{\alpha_e v_T}\right)^m\right] \tag{2.125}$$

$$\text{where} \quad C(m) = \frac{m}{4\pi\alpha_e^3\Gamma(3/m)} \quad \text{and} \quad \alpha_e^3 = \frac{3\Gamma(3/m)}{2\Gamma(5/m)} \tag{2.126}$$

with $\Gamma(x)$ the gamma function. When the laser intensity increases the distortion towards a super-Gaussian distribution increases. When the super-Gaussian power $m = 5$ this is referred to as a 'Langdon' distribution.

Taking velocity moments the energy equation can be derived, but now accounting for the effect of inverse bremsstrahlung heating. For a super-Gaussian distribution the heating operator is [47]

$$\frac{\partial U}{\partial t}_{IB} = \frac{4\pi c_B}{3}C(m)\frac{n_e T_{osc}}{\tau_B} \quad \text{where} \quad T_{osc} = \frac{1}{2}m_e v_{osc}^2. \tag{2.127}$$

This introduces the new unknown m, for which the formula derived by Matte *et al.* [71] is used

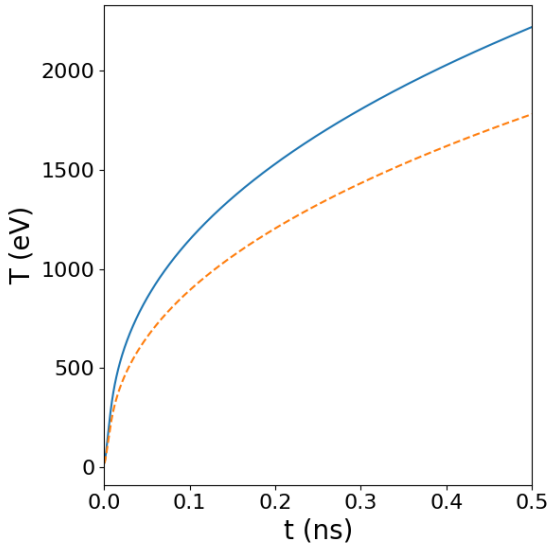

Figure 2.7: Laser heating comparisons between the Maxwellian ($m = 2$) and Langdon operator for a square pulse with intensity of $I_l = 10^{16}$ Wcm^{-2}. The initial conditions of the plasma are $T_e = 20$ eV, $n_e = 10^{25}$ m^{-3}, $Z = 7$ and $\ln \Lambda_{ei} = 6$.

$$m = 2 + \frac{3}{1 + 1.66/\alpha_M^{0.724}} \quad \text{where} \quad \alpha_M = Z(v_{osc}/v_T)^2. \tag{2.128}$$

Note that while the change in internal energy density is independent of density, the change in the plasma temperature scales as $\partial T_e \partial t \propto T_{osc}/\tau_B$. The inverse bremsstrahlung heating rate is greater in more collision plasmas and at higher laser intensity. In fig. 2.7 a comparison between the Maxwellian ($m = 2$) and Langdon heating operators is shown. The latter results in reduced absorption of laser light by the plasma, as the population of colder electrons which are preferentially heated is reduced.

The consequences of inverse bremsstrahlung heating of the plasma are significant. Kinetic simulations show that close to the laser spot the distribution can be far from Maxwellian, with recent experiments confirming this result [72], although it becomes increasingly local further from the laser spot. The fluid model derived previously relied upon the assumption that the distribution function is near Maxwellian in order to obtain accurate transport coefficients. At higher laser intensity this is no longer the case, invalidating the transport theory. To this end, Ridgers *et al.* [47] derived a new set of super-Gaussian transport coefficients for a Lorentz plasma, for which transport is typically reduced compared to the Maxwellian coefficients. The effective implementation of these coefficients remains challenging as typically a value of m must be assumed for the plasma. Knowledge of m requires some knowledge of the instantaneous shape of the distribution function, which is inherently a kinetic problem. However, this theory does provide a bound to the transport coefficients

under strong laser heating.

2.5 Non-local transport

The validity of classical transport theory presents one of the great challenges in modern plasma physics. The theory was built on two assumptions. First, the distribution function may be approximated using a Cartesian tensor expansion truncated after $\mathbf{f}_1$ to close the kinetic equations. Secondly, the isotropic distribution function can be approximated by a Maxwellian. It has already been demonstrated that the second assumption can be invalidated under intense laser heating [70]. Here *non-local transport* is described, which leads to higher order terms being significant in the expansion, and non-Maxwellian distributions.

To demonstrate the inherent weakness of the classical transport theory consider the diffusive heat-flow. This can be expressed as follows

$$|\mathbf{q}_\perp| = \frac{n_e T_e \tau_B}{m_e} \kappa_\perp \nabla T_e = \frac{c_B \kappa_\perp}{2} q_{FS} \frac{\lambda_T}{l_T} \quad \text{where} \quad l_T = \frac{T_e}{|\nabla T_e|} \tag{2.129}$$

and

$$q_{\mathrm{FS}} = n_e T_e v_T \tag{2.130}$$

is the free-streaming limit, an upper limit on the heat-flow which describes the transport of the energy density of the plasma at the thermal velocity. If the ratio of the mean-free-path to the length scale is sufficiently large with $\lambda_T > l_T$ the heat-flow can be found to exceed this free-streaming limit. Note that the free-streaming limit predicts a heat-flow that is density dependent.

Previously, it was stated the Chapman-Enskog expansion was in terms of the small parameter $Kn = \lambda_T / l_T$, so the condition $\lambda_T > l_T$ points to the breakdown of the tensor expansion. This can be demonstrated using the $\mathbf{f}_1$ equation as written in eq. 2.59 by obtaining an expression for the quantity $|\mathbf{f}_1|/f_0$. This quantifies the relative anisotropy for a given velocity in the distribution function. For the relative anisotropy to be small requires $\lambda_{ei} \ll l_f$. For a Maxwellian distribution, it can be shown that $l_f \sim l_T$ while $\lambda_{ei} = V^4 \lambda_T$ with V the ratio of the velocity to the thermal velocity. In this case on retaining higher-order terms in the expansion it can be shown for transport in one-dimension (1D) that near local thermodynamic equilibrium

$$f_0 : |\mathbf{f}_1| : |\mathbf{f}_2| \sim 1 : \left(\frac{\lambda_T}{l_T}\right) : \left(\frac{\lambda_T}{l_T}\right)^2. \tag{2.131}$$

The truncation of the expansion at $\mathbf{f}_1$ is then only valid for $\lambda_T \ll l_T$. If $\lambda_T \gg l_T$ significant anisotropy arises and the distribution function can become highly distorted. This is an inherent problem in laser-plasma experiments, where the length scale is typically short on the order of the laser spot-size (10-100s of µm).

The physical interpretation of non-local electron transport is that when temperature gradients are steep the electrons can stream to regions of the plasma in which they are far from thermal equilibrium. Electron-electron collisions are required to thermalise the electrons, but the scattering cross-section is reduced for these faster particles. For unmagnetised plasmas this effect is most significant for the heat-carrying population, which are those with $V = 2.3$ to $3v_T$ [73]. As $\lambda_{ei} \propto V^4$ the heat-carrying electrons then have mean-free-paths such that $\lambda_{ei} \gg l_T$ when $\lambda_T \approx l_T$. In fact, values of $\lambda_T/|l_T| \ll 0.01$ are typically required for local transport, due to the prevalent effect these suprathermal electrons have on heat-flow.

These particles originate at the top of the heat-front in the hot plasma, where the mean-free-path is long, and stream to the cold plasma down the temperature gradient. Due to a shortage of heat-carrying electrons in the hot plasma, the distribution function becomes super-Gaussian, with heat flow limited relative to a Maxwellian. In the cold plasma at the base of the heat-front there is then an excess of suprathermal electrons with the distribution function bi-Maxwellian. This results in increased heat-flow and pre-heating of the plasma.

In comparison, when transport is local $\lambda_T \ll l_T$ and electrons are scattered in regions approximately at thermal equilibrium with their initial position. Each point in the plasma is then at local thermodynamic equilibrium, and the distribution function remains Maxwellian.

As the classical heat-flow predicts unphysically large heat-flow ($|\mathbf{q}_\parallel| > q_{FS}$) in the hot plasma, the initial solution to the problem was to arbitrarily 'flux-limit' the heat-flow to some fraction f of the free-streaming limit (eq. 2.130) [74]. Typical values range from 0.03 to 0.15 in inertial confinement fusion modelling [75, 76]. There are several methods through which a flux-limiter can be implemented [77], for example using a harmonic average

$$\mathbf{q}_{FL} = \frac{\mathbf{q}_\perp}{1 + |\mathbf{q}_\perp|/f q_{FS}}. \tag{2.132}$$

However, the flux-limited approach cannot capture pre-heating of the cold plasma.

Due to the coupling between magnetic field dynamics and heat-flow it is also necessary to flux-limit the Nernst and Righi-Leduc coefficients [39]. A comprehensive overview of their implementation was provided by Bissell [78].

A more analytic approach that can account for moderate degrees of non-locality ($\lambda_T/l_T \sim 0.1$) is provided by convolution models [79], such as the SNB model [80]. The convolution function takes the form

$$\mathbf{q}_{conv} = \int W(x, x')\mathbf{q}_{\perp}(x')dx' \tag{2.133}$$

where $W(x, x')$ is a kernel designed to account for the heat-flux contribution from surrounding regions. These offer a significant improvement on the flux-limited transport model as they are able to account for the effects of electron pre-heat. While most non-local models have been developed for unmagnetised plasmas, the SNB model has been extended to magnetised regimes [81]. The accuracy of such models remains an open question, with further comparison with VFP codes required.

Due to their complete description of non-local transport effects kinetic codes remain the ultimate tool for the study of plasmas with significant anisotropy. Non-local heat-flux effects were first demonstrated using VFP codes, with Bell *et al.* [20] demonstrating that the heat-flow is no longer uniquely defined for a given value of λ_T/l_T. This result is not predicted by the local Spitzer (unmagnetised) heat-flow. Early kinetic studies of non-local transport in magnetised plasmas demonstrated [82, 83, 65, 84] demonstrated the suppression of non-local effects as the plasma becomes strongly magnetised. In the strongly magnetised regime locality may be restored even in plasmas for which $Kn > 1$, as the mean-free-path is limited by the gyro-radius. The relevant non-locality parameter is then r_g/l_T.

Consider eq. 2.129 in the limit $\chi_B \gg 1$. Here the diffusive transport coefficient becomes $\kappa_{\perp} \propto 1/\chi_B^2$. The equation for the heat-flow in a strongly magnetised plasma is then

$$\mathbf{q}_{\perp} \propto \frac{c_B}{2} q_{FS} \frac{r_{g,T}/\chi_B}{l_T} \tag{2.134}$$

in which it can be seen the heat-flow will exceed the free-streaming limit when $r_g/\chi_B > l_T$, which is the same dependence that was found for the diffusion coefficient in eq. 2.101. This appears to be a stricter non-local condition than originally expected. Thus, the subject of the next chapters will be an investigation of the non-local transport trend in the magnetised regime.

2.6 Computational techniques

Computational simulations play a crucial role in both theoretical and experimental studies of laser-plasma interactions. A variety of well-established codes are available for different plasma models, such as the kinetic and fluid models discussed earlier in this chapter. The choice of model depends on the specifics of the problem, with the best code being one that balances accuracy, efficiency, and the relevant physical processes, rather than simply focusing on complexity. In this thesis two computational codes will be used to investigate magnetised electron transport. These are the kinetic Vlasov-Fokker-Planck code IMPACT, initially developed by Kingham and Bell [42], and the extended magnetohydrodynamics 'Classical Transport Code' (CTC) developed by Bissell [85]. These codes do not include any radiation dynamics, and assume a fully ionised plasma with the equation of state that of an ideal gas ($P_e = n_e T_e$). The following sections will detail the key properties of these codes, along with any features involved in their operation.

2.6.1 IMPACT

IMPACT utilises an implicit finite-difference scheme to solve the Vlasov-Fokker-Planck equation and Maxwell's equations in two-dimensions (2D), including self-consistent magnetic fields. This allows the coupling between heat-flow and magnetic field dynamics to be explored in collisional plasmas, as typically encountered during laser-plasma interactions, in the non-relativistic limit. The advantage of the kinetic approach is that it enables an accurate description of transport properties in the non-local regime, where the electron mean free path is comparable to the temperature and density length scales, by evolving the electron distribution function.

The code utilises a Cartesian geometry solving for the E_x, E_y, and B_z electromagnetic field components. To maximise computational efficiency the electron distribution function is expanded in Cartesian tensors, with the distribution function truncated after terms of higher order than $\mathbf{f}_1$. As discussed earlier, this constitutes the diffusive approximation, and is appropriate for more collisional plasmas. The equations of interest are the f_0-equation (eq. 2.58) and the $\mathbf{f}_1$-equation (eq. 2.59). The Lorentz approximation is made, with a complete description of anisotropic electron-electron collisions not included. Instead, they are approximated by multiplying the collision frequency by the collision fix of Epperlein and Short [38], which will be discussed further in section 2.6.3. This inclusion of this feature is optional; it will typically be disabled when considering temperature relaxation problems, but included in experimentally relevant laser heating simulations. An additional feature

of the code is the ability to disable the electron inertia term $\partial_t \mathbf{f}_1$; this will be included in all simulations unless explicitly stated otherwise.

Extensions to the code were made by Ridgers [49], who added the ability to simulate hydrodynamic ion motion. Previously, ions were treated only as a stationary neutralising background. This was done by transforming the VFP equation into the average rest frame of the ions, with electron transport taking place relative to the motion of the ions. As a result, the effects of ion motion can be included allowing for an improved description of transport during nanosecond laser-plasma interactions. Laser heating in the code is modelled using the Langdon operator [70] although the plasma can also be heated in such a way that f_0 remains Maxwellian; this allows the effect of IB heating to be separated from non-local transport.

2.6.2 CTC

The CTC code provides a fully-implicit solution to the coupled fluid equations outlined in section 2.3. While kinetic codes such as IMPACT that directly evolve the electron distribution function provide a more accurate description of transport phenomena, particularly when non-local effects are important, CTC offers greater flexibility in exploring the physical processes relevant to a given problem. Coupled with the greater efficiency of CTC allows for simulations with greater spatial and temporal scales, broader parameter scans, and faster iteration when exploring complex problems.

Similar to IMPACT, the code operates in a Cartesian geometry solving for the E_x, E_y, and B_z electromagnetic field components. One of the central features of a fluid code such as CTC is the ability to include specific terms in the equations that are solved for a given simulation. This will be relevant when investigating the Nernst effect in chapters 6 and 7, where the importance of Nernst advection relative to hydrodynamic advection will be assessed. This investigation simulations will be performed with all terms included in the equation matrix, hydrodynamic motion excluded, or the Nernst effect excluded.

When solving the coupled Ohm's law (eq. 2.86) and heat-flow (eq. 2.87) equations several choices can be made regarding the transport coefficients, including the polynomial fits of Epperlein and Haines [46] and Sadler [48]. Alternatively, there are the super-Gaussian transport coefficients of Ridgers [47] derived in the Lorentz limit. Here, the $m = 2$ transport coefficients of Ridgers are used with the collision fix. The collision fix applied to the electron-ion collision frequency in Ohm's law and the heat-flow equation. This is done for consistency with IMPACT, with all CTC

simulations in chapters 6 and 7 used to study laser-plasma heating experiments.

A final comment regards the use of flux-limiters CTC, with the code allowing for separate flux-limitation of both the heat-flow and Nernst velocity. Note that several studies [39, 86] have shown that it is most appropriate to limit both the heat-flow and Nernst velocity by the same fraction when seeking to correct for non-local transport effects when compared to kinetic simulations. In this thesis all simulations will be conducted with unrestricted heat-flow and Nernst velocity, in an effort to highlight non-local transport effects that may be occurring in a given fluid simulation when compared to kinetic IMPACT simulations.

2.6.3 Electron-electron collision fix

The inclusion of electron-electron collisions in both IMPACT and CTC is done using the collision fix to the frequency $\nu_{ei}^{*} = \nu_{ei}(Z+4.2)/(Z+0.24)$. This is suitable when correcting $\kappa_{\perp}$ for weakly magnetised plasmas, but can lead to a large over-estimation of other transport coefficients [39]. In fig. 2.8 the effect of the collision fix on $\kappa_{\perp}$ and $\beta_{\wedge}$ is shown, which determine the local perpendicular heat-flow and Nernst velocity respectively, when $Z = 7$. Here $\kappa_{\perp}$ initially demonstrates better agreement when using the collision fix compared to the Lorentz value with the polynomial fits of Epperlein and Haines, agreeing almost exactly when $\chi_B \ll 1$ but decreasing in accuracy as the magnetisation increases. In the strongly magnetised regime where $\chi_T > 10$ the collision fix provides a poorer approximation than the Lorentz limit. For the $\beta_{\wedge}$ coefficient the collision fix provides a better fit when $\chi_T \lesssim 0.1$, but the relative error is now larger than when used to correct $\kappa_{\perp}$, and significantly overestimates the transport coefficients at larger magnetisations. Thus, the collision fix is better than treating the plasma in the Lorentz limit when the plasma is weakly magnetised, although the Nernst velocity will be overestimated without a superior treatment of anisotropic electron-electron collisions.

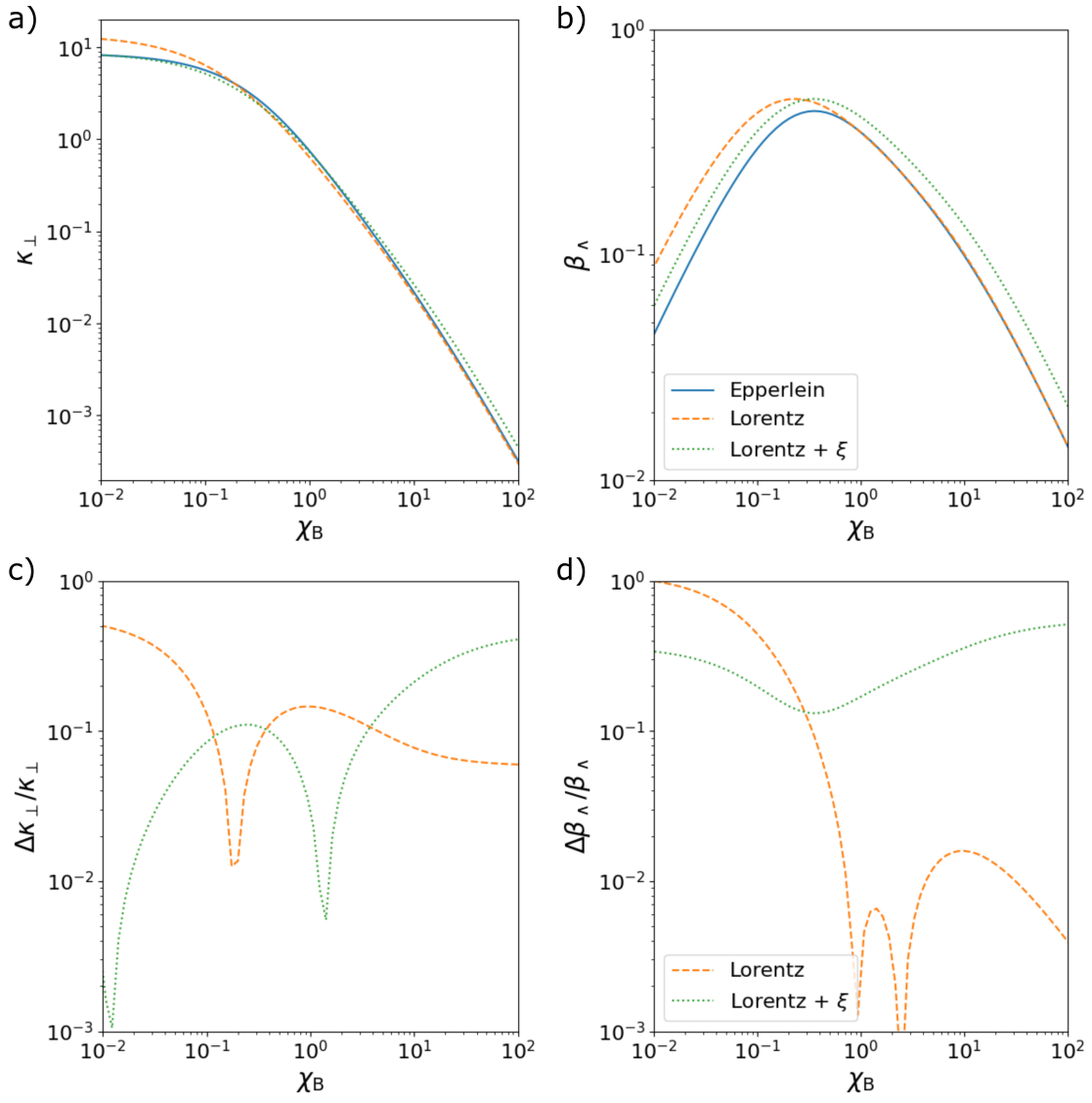

Figure 2.8: The transport coefficients a) $\kappa_\perp$ and b) $\beta_\wedge$ from the polynomial fits of Epperlein and Haines for both $Z = 7$ and in the Lorentz limit, as well when including the collision fix $\xi = (Z + 0.24)/(Z + 4.2)$ with $Z = 7$. The collision fix is applied to the dimensionless transport coefficients by finding $\xi\kappa_\perp(\xi\chi_B)$ and $\beta_\wedge(\xi\chi_B)$; the difference arises because when multiplying the collision time by ξ it appears twice in the dimensional thermal conductivity $\underline{\underline{\kappa}}(\omega_g\tau_B) = (n_e T_e \tau_B/m_e)\underline{\underline{\kappa^c}}(\omega_g\tau_B)$, but only once in $\underline{\underline{\beta}}(\omega_g\tau_B) = \underline{\underline{\beta^c}}(\omega_g\tau_B)$. Additionally, the fractional error is shown for both c) $\kappa_\perp$ and d) $\beta_\wedge$ when using either the Lorentz limit or Lorentz limit in combination with the collision fix.

Chapter 3

Local transport phenomena in magnetised plasmas

This chapter examines the VFP equation to identify novel trends in the growth of relative anisotropy within the electron distribution function. Significant anisotropy leads to non-local transport, shifting the distribution away from a Maxwellian. Anisotropy is quantified by the ratio $\mathbf{f}_1/f_0$, representing the relative anisotropy, and can be expressed in terms of an 'effective mean-free-path', applicable to both weakly and strongly magnetised plasmas. This chapter explores anisotropy in the local limit. The results are used to calculate the electron velocities most influential in determining transport trends as a function of magnetisation, with increasing magnetisation found to preferentially reduce the transport of faster electrons. Non-local transport has the greatest impact on heat-flow and magnetic field dynamics when anisotropy is large for these populations.

The interplay between kinetic electron heat transport and magnetic field dynamics has recently attracted considerable attention, particularly because magnetic fields in many experiments are either self-generated [87, 88, 58] or applied [89, 1]. Magnetic fields are known to substantially alter plasma evolution, notably introducing anisotropy by reducing perpendicular transport, a property which is exploited in MCF and magnetised ICF schemes [90, 14]. The development of diagnostics, such as proton radiography and Thomson scattering, enable unprecedented exploration of magnetic transport effects. These effects, including the Biermann battery and Nernst effect [91, 39, 92, 93], which were previously theorised to be significantly influenced by non-local transport, can now be studied in greater detail.

The local xMHD model developed by Braginskii has provided the foundation for this work [3], relying upon the accurate calculation of transport coefficients [46, 48]. Entering the non-local regime the validity of classical transport theory is limited,

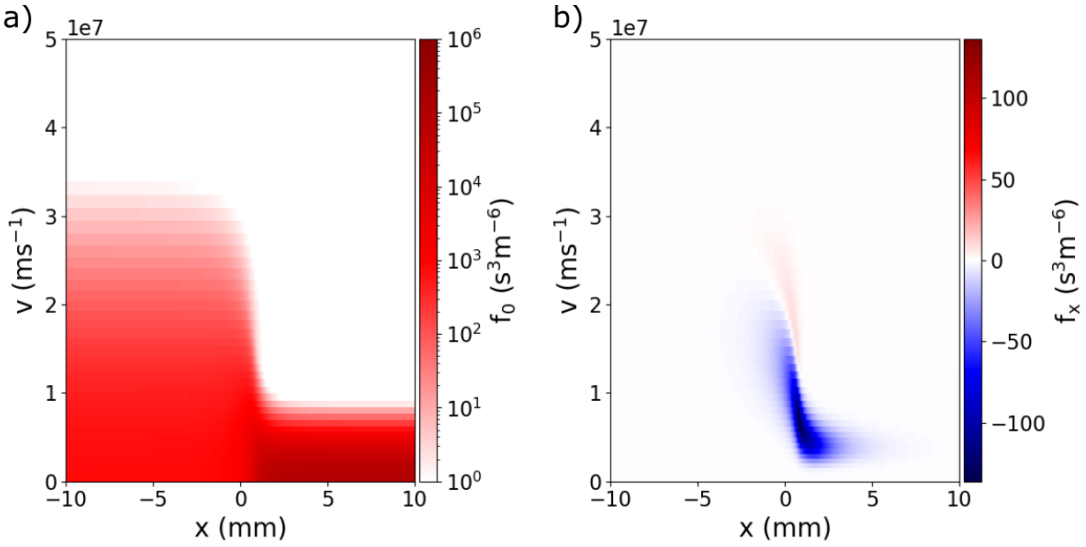

Figure 3.1: A kinetic VFP simulation of a temperature ramp relaxation at $t = 500$ ps with $n_e = 10^{25}$ m^{-3}, $Z = 7$, and $B_0 = 3 \times 10^{-3}$ T. a) The isotropic component, f_0, shows adjacent regions of hot plasma and cold plasma, with a smooth transition between the two regions, where the hotter region at smaller x can be seen to have a greater population of high velocity electrons but smaller population of low velocity electrons. b) The lowest-order anisotropic component, f_{1x}, with regions in red showing the high velocity outgoing current travelling down the temperature gradient and blue corresponding to the lower velocity return current.

although magnetisation has been shown to restore locality even for large values of the Knudsen number, $K_n = \lambda/l$, with l a representative physical length scale [82, 83, 65, 94]. In plasmas non-local transport is often described as being significant when the mean-free-path of the thermal population (λ_T), approaches and exceeds the temperature length scale ($l_T = T_e/|\nabla T_e|$). Incorporating these non-local effects on heat-flow in predictive models is an ongoing challenge, with reduced kinetic [81, 95, 96] or kinetic Vlasov-Fokker-Planck (VFP) models [42, 41, 97] often required.

3.1 Equations governing anisotropy

While the kinetic modelling of plasma solves for f_0 and $\mathbf{f}_1 = (f_{1x}, f_{1y}, f_{1z})$ directly, fluid models which use classical transport theory assume that the isotropic component remains close to Maxwellian. Here, this assumption will be evaluated using the f_0 and $\mathbf{f}_1$-equations (eq. 2.58 and eq. 2.59), which govern the evolution of f_0 and $\mathbf{f}_1$ respectively. In fig. 3.1 an example simulation shows the structure of these two components in velocity phase space. To simplify this analysis the anisotropic e-e collision term ($\mathbf{C}_{e1}$) is neglected as part of the Lorentz approximation, which is valid for high Z.

Defining the axis using the magnetic field unit vector $\mathbf{b} = \mathbf{B}/|\mathbf{B}|$ eq. 2.59 can be separated into components describing transport parallel and perpendicular to the axis. This is done by substitution of the vector triple product $\mathbf{f_1} = \mathbf{b}(\mathbf{f}_1 \cdot \mathbf{b}) + \mathbf{b} \times (\mathbf{f}_1 \times \mathbf{b})$

$$-\nu_{ei}(\mathbf{f}_{1\parallel} + \mathbf{f}_{1\perp}) = \partial_t(\mathbf{f}_{1\parallel} + \mathbf{f}_{1\perp}) + v\nabla f_0 + \mathbf{a}\partial_v f_0 + \boldsymbol{\omega} \times (\mathbf{f}_{1\parallel} + \mathbf{f}_{1\perp}) \tag{3.1}$$

where the parallel and perpendicular components of $\mathbf{f}_1$ are defined $\mathbf{f}_{1\parallel} = \mathbf{b}(\mathbf{f}_1 \cdot \mathbf{b})$ and $\mathbf{f}_{1\perp} = \mathbf{b} \times (\mathbf{f}_1 \times \mathbf{b})$. As the parallel component of $\mathbf{f}_1$ is then perpendicular to $\boldsymbol{\omega}$ the vector $\boldsymbol{\omega} \times \mathbf{f}_{1\parallel} = 0$. This then allows separation of the parallel and perpendicular components

$$-\nu_{ei}\mathbf{f}_{1\parallel} = \partial_t \mathbf{f}_{1\parallel} + v\nabla_\parallel f_0 + \mathbf{a}_\parallel \partial_v f_0 \tag{3.2}$$

$$-\nu_{ei}\mathbf{f}_{1\perp} = \partial_t \mathbf{f}_{1\perp} + v\nabla_\perp f_0 + \mathbf{a}_\perp \partial_v f_0 + \boldsymbol{\omega} \times \mathbf{f}_{1\perp}. \tag{3.3}$$

The perpendicular component can be developed further by inversion

$$-\nu_{ei}\mathbf{f}_{1\perp} = \partial_t \mathbf{f}_{1\perp} + v\nabla_\perp f_0 + \mathbf{a}_\perp \partial_v f_0 - \frac{\boldsymbol{\omega}}{\nu_{ei}} \times (\partial_t \mathbf{f}_1 + v\nabla_\perp f_0 + \mathbf{a}_\perp \partial_v f_0 + \boldsymbol{\omega} \times \mathbf{f}_{1\perp}) \tag{3.4}$$

where the first term in the vector triple product $\boldsymbol{\omega} \times (\boldsymbol{\omega} \times \mathbf{f}_{1\perp}) = \boldsymbol{\omega}(\boldsymbol{\omega} \cdot \mathbf{f}_{1\perp}) - \omega_g^2 \mathbf{f}_{1\perp}$ is zero as $\boldsymbol{\omega}$ and $\mathbf{f}_{1\perp}$ are perpendicular. The two vector components can then be written

$$\left(1 + \frac{\partial_t}{\nu_{ei}}\right)\mathbf{f}_{1\parallel} = -\lambda_{ei}\nabla_\parallel f_0 - \frac{\mathbf{a}_\parallel}{\nu_{ei}}\partial_v f_0 \tag{3.5}$$

$$\begin{aligned}\left(1 + \frac{\partial_t - \chi_{ei}\mathbf{b} \times \partial_t}{\nu_{ei}(1+\chi_{ei}^2)}\right)\mathbf{f}_{1\perp} = -\frac{\lambda_{ei}}{1+\chi_{ei}^2}\Bigg[&(\nabla_\perp - \chi_{ei}\mathbf{b} \times \nabla_\perp) f_0 \\ &+ (\mathbf{a}_\perp - \chi_{ei}\mathbf{b} \times \mathbf{a}_\perp)\frac{\partial_v f_0}{v}\Bigg].\end{aligned} \tag{3.6}$$

The time derivatives on the left-hand side of the equation describes the role of electron inertia; electrons do not respond instantaneously to gradients in the distribution function. Instead, it takes time for flows to build and evolve. In fluid models this term is dropped, as was mentioned earlier, to allow predictions to be made from instantaneous macroscopic plasma parameters - otherwise some knowledge of the time history of the distribution function is required. Furthermore, this assumption is also made in reduced kinetic models, such as the SNB [81] or M1 model

[95], to allow coupling with fluid codes. This will be done here, but is revisited in section 4.4.

The condition with which the time derivative can be dropped varies between the parallel and perpendicular transport regimes. Generally, this requires that the rate of change of $\mathbf{f}_1$ must be small relative to the collision frequency ($|\partial_t \mathbf{f_1}|/|\mathbf{f_1}| \ll \nu_{ei}$). The final expressions that are then obtained are

$$\mathbf{f}_\parallel = -\lambda_{ei}\nabla_\parallel f_0 - \frac{\mathbf{a}_\parallel}{\nu_{ei}}\partial_v f_0 \tag{3.7}$$

$$\mathbf{f}_{1\perp} = -\frac{\lambda_{ei}}{1+\chi_{ei}^2}\left[\left(\nabla_\perp - \chi_{ei}\mathbf{b}\times\nabla_\perp\right) f_0 + \left(\mathbf{a}_\perp - \chi_{ei}\mathbf{b}\times\mathbf{a}_\perp\right)\frac{\partial_v f_0}{v}\right]. \tag{3.8}$$

In the limit that $\chi_{ei} \to 0$ the governing equation for perpendicular transport is equivalent to that of parallel transport. When a magnetic field is present two effects are introduced; the first is a reduction in the anisotropy by an amount $(1+\chi_{ei}^2)^{-1}$ that is significant when the electrons are magnetised, and the second a rotation in the perpendicular plane. The former effect is the primary cause for the reduction in perpendicular transport compared to parallel transport, with electrons exhibiting gyro-motion in this plane once strongly magnetised. As a result, significant anisotropy can arise between the axes. The effects of field line curvature will not be considered in this thesis.

For a magnetic field such that $\mathbf{B} = B_z\hat{\mathbf{k}}$ transport perpendicular to the magnetic field is along $\hat{\mathbf{i}}$ and $\hat{\mathbf{j}}$, with parallel transport along $\hat{\mathbf{k}}$. Expressions giving the components of $\mathbf{f}_1$ are then obtained from eq. 3.7 and eq. 3.8

$$f_{1x} = -\frac{\lambda_{ei}}{1+\chi_{ei}^2}\left(\frac{1}{l_{f,x}} - \frac{b_z\chi_{ei}}{l_{f,y}} + \frac{a_x - b_z\chi_{ei}a_y}{v l_{f,v}}\right) f_0 \tag{3.9a}$$

$$f_{1y} = -\frac{\lambda_{ei}}{1+\chi_{ei}^2}\left(\frac{1}{l_{f,y}} + \frac{b_z\chi_{ei}}{l_{f,x}} + \frac{a_y + b_z\chi_{ei}a_x}{v l_{f,v}}\right) f_0 \tag{3.9b}$$

$$f_{1z} = -\lambda_{ei}\left(\frac{1}{l_{f,z}} + \frac{a_z}{v l_{f,v}}\right) f_0 \tag{3.9c}$$

Here b_z is the sign of the magnetic field and $l_{f,i} = f_0/\partial_i f_0$ provides a length scale of the distribution function where the derivative i is taken with respect to the v, x, y and z-axis. The numerical solution of these expressions is a common feature of many magnetised plasma models based on the VFP equation, with subsequent assumptions about the distribution function dictating whether a fluid, reduced kinetic, or kinetic approach is taken.

Taking a broader view of eqs. 3.9 it can be seen that each equation is in essence formed of two terms. The first describes an effective mean-free-path λ_{f_1}; for terms perpendicular to the magnetic field axis this is given by $\lambda_{f_{1\perp}} = \lambda_{ei}/(1+\chi_{ei}^2)$, reducing to $\lambda_{f_{1\parallel}} = \lambda_{ei}$ along the magnetic field axis or when $B_z = 0$. Here it can be seen that the effective mean-free-path perpendicular to the magnetic field axis is reduced by a factor $(1+\chi_{ei}^2)^{-1}$, which will prove fundamental to the perpendicular transport trends that will be explored in this thesis. The other term in brackets can be interpreted as a length scale and will be referred to as l_{f_1}, and is formed of a harmonic average of the composite length scales. Again, the length scale of the perpendicular terms has the same form as the parallel term when $B_z = 0$. Thus, anisotropy will increase along a given axis if the ratio between λ_{f_1} and l_{f_1} increases.

It is the properties of perpendicular transport and the influence of magnetic fields on non-local transport which are of primary interest here, with parallel transport seen to be a subset of this problem for which $B_z = 0$. Therefore, the $\mathbf{f}_{1\perp}$ component will now be investigated as it includes the magnetic field dependence.

3.2 Anisotropic transport in the local limit

Considering the case in which f_0 is Maxwellian, $f_m = (n_e/\pi^{3/2}v_T^3)\exp(-v^2/v_T^2)$, the derivatives in eq. 2.59 are

$$\nabla f_0 = \left[\frac{\nabla n_e}{n_e} + \left(V^2 - \frac{3}{2}\right)\frac{\nabla T_e}{T_e}\right] f_m \quad \& \quad \frac{\partial f_0}{\partial v} = \frac{-2v}{v_T^2} f_m \tag{3.10}$$

with $V = v/v_T$ which on substitution into eq. 3.8 gives the $\mathbf{f}_{1\perp}$ component as

$$\mathbf{f}_{1\perp} = -\frac{\lambda_{ei}}{1+\chi_{ei}^2}\left[\left(\frac{\nabla_\perp n_e}{n_e} - \frac{\chi_{ei}\mathbf{b}\times\nabla_\perp n_e}{n_e}\right) + \left(\frac{\nabla_\perp T_e}{T_e} - \frac{\chi_{ei}\mathbf{b}\times\nabla_\perp T_e}{T_e}\right)\left(V^2 - \frac{3}{2}\right) - \frac{m_e\left(\mathbf{a}_\perp - \chi_{ei}\mathbf{b}\times\mathbf{a}_\perp\right)}{T_e}\right] f_m \tag{3.11}$$

where terms involving gradients in $\nabla_\perp n_e$ and $\nabla_\perp T_e$ give length scales in the plane perpendicular to the magnetic field axis.

Taking the 1st and 3rd velocity moments of each component allows Ohm's law (eq. 2.86) and the heat-flow equation (eq. 2.87) to then be obtained respectively, as was shown in section 2.3 with the transport coefficients appearing as velocity

moments of f_0 that are dependent upon the magnetisation. The Z dependence arises due to the inclusion of e-e collisions in eq. 2.59, as demonstrated numerically by Epperlein and Haines [46]. As e-e collisions are neglected here the Lorentz limit is taken for these terms. While e-e collisions can lead to significant modifications in the magnitude of transport effects, their impact on the general trends that are identified here are less pronounced.

Neglecting the displacement current in Ampere's law means that a current is only formed perpendicular to $\mathbf{B}$. The acceleration term $\mathbf{a}_\perp = -e\mathbf{E}/m_e$ can then be expressed using Ohm's law (eq. 2.86) as the sum $\mathbf{E}_\perp = \mathbf{E}_{\perp,P} + \mathbf{E}_{\perp,B}$ where

$$\mathbf{E}_{\perp,P} = -\frac{T_e}{e}\left[\frac{\nabla_\perp n_e}{n_e} + \frac{\nabla_\perp T_e}{T_e}(1+\beta_\perp) + \beta_\wedge \frac{\mathbf{b}\times\nabla_\perp T_e}{T_e}\right] \tag{3.12}$$

$$\mathbf{E}_{\perp,B} = -\frac{T_e}{e}\frac{2}{\beta}\left[\frac{\nabla_\perp |\mathbf{B}|}{|\mathbf{B}|}\left(1-\frac{\alpha_\wedge}{\chi_B}\right) + \frac{\alpha_\perp}{\chi_B}\frac{\mathbf{b}\times\nabla_\perp|\mathbf{B}|}{|\mathbf{B}|}\right] \tag{3.13}$$

are contributions arising from gradients in the pressure, $E_{x,P}$, and magnetic field, $E_{x,B}$. Each term here is then dependent on the length scale of either n_e, T_e, or $|\mathbf{B}|$.

For the HED plasmas of interest in this thesis typically $\beta \gg 1$, with thermal pressure dominant over magnetic pressure. Furthermore, the coupling between heat-flow and magnetic field dynamics usually results in $l_{T,x} \geq l_{B,x}$. Combining these results the $\mathbf{E}_{\perp,P}$ terms are found to be dominant in Ohm's law for the scenarios considered here. Accessing a regime where transport terms associated with gradients in $\mathbf{B}$ and $\underline{\underline{\alpha}}^c$ are dominant would require a small β.

Substitution of Ohm's law into eq. 3.11, neglecting the contributions of $\mathbf{E}_{\perp,B}$, then gives

$$\begin{aligned}\mathbf{f}_{1\perp} = -\frac{\lambda_{ei}}{1+\chi_{ei}^2}\Bigg[&\left(\frac{\nabla_\perp T_e}{T_e} - \frac{\chi_{ei}\mathbf{b}\times\nabla_\perp T_e}{T_e}\right)\left(V^2 - \frac{5}{2} - \beta_\perp\right) \\ &+ \left(\frac{\chi_{ei}\nabla_\perp T_e}{T_e} - \frac{\mathbf{b}\times\nabla_\perp T_e}{T_e}\right)\beta_\wedge\Bigg] f_m\end{aligned} \tag{3.14}$$

where it is found that anisotropy that would arise due to gradients in n_e is exactly cancelled by the electric field resulting from the gradient. In this case the x-component is

$$f_{1x} = -\frac{\lambda_{ei}}{1+\chi_{ei}^2}\left[\left(\frac{1}{l_{T,x}} - \frac{b_z\chi_{ei}}{l_{T,y}}\right)\left(V^2 - \frac{5}{2} - \beta_\perp\right) + \left(\frac{\chi_{ei}}{l_{T,x}} - \frac{b_z}{l_{T,y}}\right)\beta_\wedge\right] f_m. \tag{3.15}$$

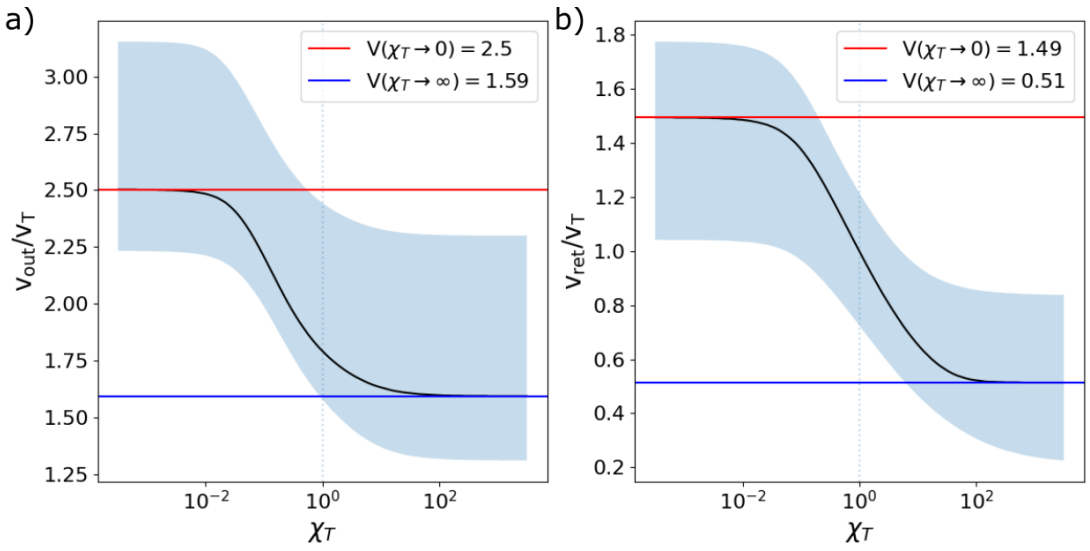

Figure 3.2: The velocities which carry the most a) outgoing and b) return current as a function of χ_T, with horizontal lines showing the asymptotic values in the weakly and strongly magnetised limits. Shaded regions show the velocity band which carries between 10 and 90% of the total current.

3.2.1 Electron current properties

To gain a greater understanding of the kinetics that drive transport a 1D system is now considered, such that the temperature gradient is along the x-axis only ($T_e = T_e(x)$) and $\partial_y T_e = 0$. Note that while the system is 1D this does not prohibit transport from occurring along f_{1y} due to the magnetic field (eq. 3.9b).

In 1D eq. 3.14 then becomes

$$f_{1x} = -\frac{\lambda_{ei}}{1+\chi_{ei}^2}\frac{1}{l_{T,x}}\left(V^2 - \frac{5}{2} - \beta_\perp + \chi_{ei}\beta_\wedge\right) f_m \tag{3.16}$$

allowing the behaviour of the effective length scale l_{f_1} to be more clearly understood. In the local limit this is proportional to l_T, so as expected anisotropy will increase as the relative temperature gradient in the plasma increases. For a given V both the direction and magnitude of the length scale then varies in eq. 3.16; for values where the term in brackets is positive the anisotropy is in the opposite direction to l_T, opposing the temperature gradient, while for negative values it is in the same direction. When the term in brackets is positive, the length scale decreases rapidly as V increases and the magnitude of the anisotropy increases.

Eq. 3.16 is related to the current by taking the first velocity moment $J_x = -(4\pi e/3)\int_0^\infty f_x v^3 dv$. It is then seen that values for which the term in brackets is positive correspond to an outgoing current, which occurs for the hot electron

population, while negative values form a return current of colder electrons. When the term in brackets equals zero the current changes direction. Taking the derivative of the equation with respect to V the velocities which contribute the most to the outgoing and return current can be found in the limits $\chi_T \to 0$ and ∞. These are shown in fig. 3.2. As the plasma being considered is both 1D and quasi-neutral, the current J_x associated with eq. 3.16 is approximately zero. More generally quasi-neutrality requires $\nabla \cdot \mathbf{J} = 0$ so the current carried by the hot electrons $\mathbf{J}_h$ must be such that $\nabla \cdot \mathbf{J}_h = -\nabla \cdot \mathbf{J}_c$.

Returning to the l_{f_1} component of eq. 3.8 there are then two effects at play that control the magnitude and direction of the current, which arise when there are gradients in the distribution function. The first is associated with spatial gradients in f_0 resulting in the diffusion of hot particles to cold regions of the plasma and vice-versa. In the case that two neighbouring points in the plasma are defined by Maxwellian distributions but are not at thermal equilibrium with each other, then in the limit $\Delta T \to 0$ and $\mathbf{E} = 0$ the current changes direction at $V = \sqrt{3/2}$ as can be seen in eq. 3.10. At this point the population of the velocity band for each point is equal.

Meanwhile, the $l_{f,v}$ term modifies the current as a result of the electric field that arises to balance forces within the plasma. This takes the form of the product of the velocity gradient of f_0 with v/a, with $a = -eE/m_e$ the acceleration by the electric field, where the latter term provides a characteristic timescale over which the velocity changes. Together, they describe a distance over which acceleration will lead to a significant change in the velocity of a population of electrons.

For plasmas near LTE where $\beta \gg 1$ the electric field will oppose the temperature gradient. This results in a reduction in the anisotropy of the population travelling in the same direction, the outgoing current, but increasing the anisotropy within the colder return current that travels in the opposite direction. As a result, the velocity at which the current changes direction increases to $V = \sqrt{5/2 + \beta_{\perp 0}}$ in the absence of a magnetic field. Increasing the magnetisation causes the velocity at which the current changes direction to decrease, reaching a minimum of $V = 1.065$ using the $\beta_\wedge$ coefficient of Epperlein and Haines. This arises from the E_y component of the electric field, which suggests that the $\mathbf{E} \times \mathbf{B}$ drift instead causes an increase in the anisotropy of the electrons travelling in the same direction as the electric field. As a 1D problem is being considered this drift is independent of the sign of the magnetic field, as changing the direction of B_z also changes that of E_y.

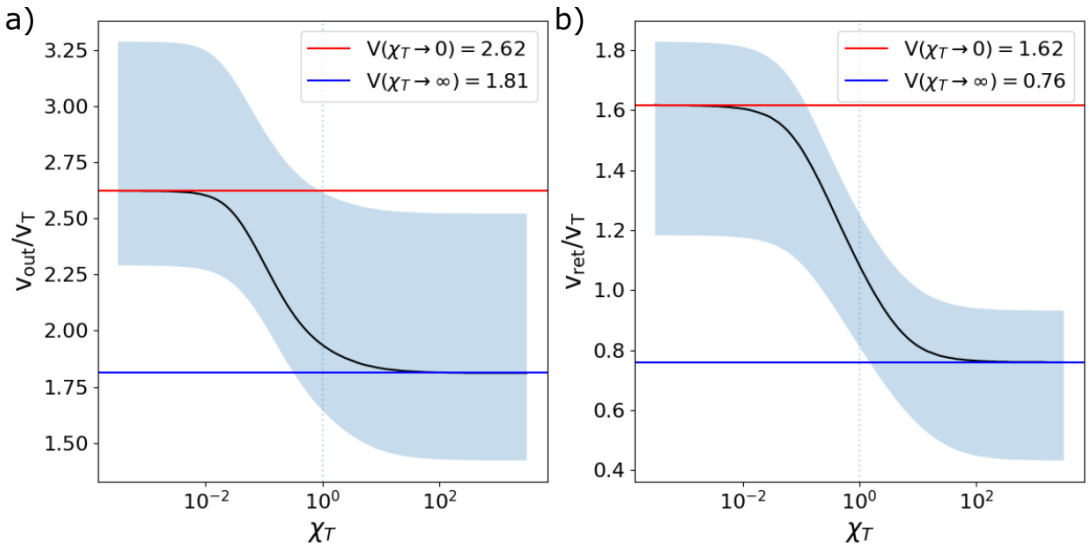

Figure 3.3: The velocities which carry the most heat for the a) outgoing and b) return current as a function of χ_T, with horizontal lines showing the asymptotic values in the weakly and strongly magnetised limits. Shaded regions show the velocity band which carries between 10 and 90% of the total energy.

3.2.2 Heat carrying velocity

Knowing that the heat-flow is given by $q_x \propto \int_0^\infty f_{1x} v^5 d^3v$, the values of V which carry the most heat can be found as a function of χ_T for both the outgoing and return current. Taking the derivative of the integrand using eq. 3.16 there are two asymptotic limits at $\chi_T = 0$ and ∞, with the results shown as a function of χ_T in fig. 3.3. Intermediate values are found through numerical differentiation.

For the outgoing current the heat-carrying velocity is $V = 2.62$ and 1.81 in the limits $\chi_T = 0$ and ∞ respectively. The velocity which carries the most heat in the return current is $V = 1.62$ and 0.76, again for $\chi_T = 0$ and ∞. In the case that $\chi_T = 0$ these maximum values are given by

$$V = \frac{\sqrt{\pm\sqrt{\beta_\perp^2 - 2\beta_\perp + 19} + \beta_\perp + 8}}{\sqrt{2}}. \tag{3.17}$$

This change in the outgoing heat-carrying velocity with magnetisation corresponds to a factor of ~ 3 increase in the collision rate of the heat-carrying electrons as $\nu_{ei} \propto V^{-3}$. As $\chi_{ei} \propto V^3$ hotter electrons are magnetised before colder electrons, demonstrating how their contribution to q_x is most affected by a magnetic field. Defining the heat-carrying electron band as those in the outgoing current which carry between 10 and 90 % of the heat this is 2.25 – 3.25 v_T when $\chi_T = 0$, but reduces to 1.5–2.5 v_T when $\chi_T = \infty$.

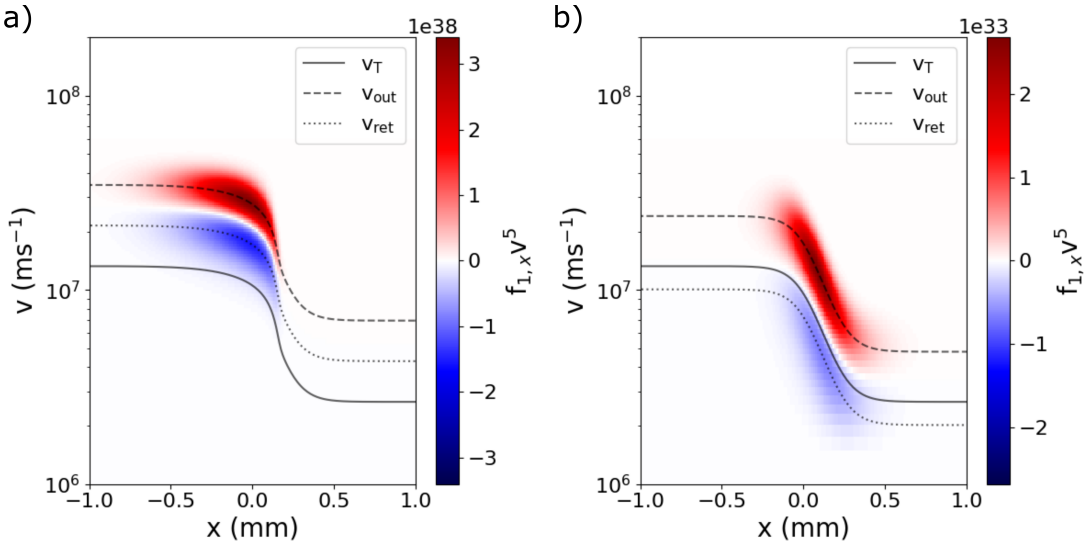

Figure 3.4: Kinetic VFP simulations of a temperature ramp relaxation showing $f_{1x}v^5$, for plasmas (Z=7) that are a) weakly magnetised and b) strongly magnetised at $t = 500$ ps. In the weakly magnetised case $n_e = 10^{27}$ m^{-3} and $B_z = 0.3$ T, while for the strongly magnetised case $n_e = 10^{24}$ m^{-3} and $B_z = 30$ T. Overlaid are the velocities which carry the most heat in the outgoing and return current for $f_0 = f_m$, as well as v_T.

To confirm this behaviour the heat-flow integrand, $q_x v^5$, from IMPACT simulations with electron inertia is plotted in fig. 3.4 for both a weakly and strongly magnetised plasmas, in which the electrons with $V = 2.62$ and 1.81 carry the most heat respectively. It is interesting to note that greater heat-flow is seen in the hot-plasma compared to the cold plasma when weakly magnetised, but the opposite is true when the plasma is strongly magnetised, reflecting the difference in the electron mobility in the two regimes which will now be explored.

3.3 Anisotropy regimes in magnetised plasmas

Examining eq. 3.9 it was previously noted that there are two effects at play that dictate the anisotropy, the effective mean-free-path λ_{f_1} or the length scale l_{f_1}. Here the focus will be on λ_{f_1} in order to explore the electron mobility in different regimes, and the effect this has on anisotropy within the plasma. The length scale l_{f_1} can then be thought of as providing the setting in which diffusion processes that result in anisotropy occur. In other words, it will be shown how λ_{f_1} varies relative to l_{f_1} as system parameters are changed in this section, with l_{f_1} assumed to be either fixed or slowly varying.

Considering the effective mean-free-path perpendicular to the magnetic field axis

$$\lambda_{f_1} = \frac{\lambda_{ei}}{1+\chi_{ei}^2} = \frac{v/\nu_{ei}}{1+(\omega_g/\nu_{ei})^2} \tag{3.18}$$

there is a distinct difference in behaviour between the weakly magnetised regime, $\chi_{ei} \ll 1$, and the strongly magnetised regime, $\chi_{ei} \gg 1$, as highlighted in fig. 3.5.

Expressing the Hall parameter as $\chi_{ei} = \lambda_{ei}/r_g$ it is clear that in the weakly magnetised electrons are able to move freely between collisions, with their diffusion distance limited by λ_{ei} as $r_g \gg \lambda_{ei}$. It is then found that

$$\lambda_{f_1}(\chi_{ei} \ll 1) = \lambda_{ei} = \frac{v}{\nu_{ei}} \propto \frac{T_e^2}{n_e} \tag{3.19}$$

so the effective mean-free-path scales linearly with the inverse of the collision frequency, for which the definition provided in eq. 2.55 is used. As $\lambda_{ei} \propto v^4$, hotter electrons have significantly longer mean-free-paths than colder electrons.

Meanwhile, in the strongly magnetised regime the diffusion distance is limited by the electron gyro-orbit when $r_g \ll \lambda_{ei}$. Here

$$\lambda_{f_1}(\chi_{ei} \gg 1) = \frac{\lambda_{ei}}{\chi_{ei}^2} = \frac{r_g}{\chi_{ei}} = \frac{v\nu_{ei}}{\omega_g^2} \propto \frac{n_e}{T_e B_z^2} \tag{3.20}$$

with the effective mean-free-path now scaling linearly with the collision frequency, and the inverse square of the electron gyro-frequency. It is the scaling $w_g^{-2} \propto B_z^{-2}$ that is exploited in magnetic confinement fusion to increase the confinement time.

It is of note that in the strongly magnetised regime $\lambda_{f_1} = r_g/\chi_{ei} < r_g$, with increasing magnetisation resulting in a decrease of the effective mean-free-path below the gyro-radius. Here, the particle may perform many gyro-orbits per collision. In contrast to the weakly magnetised regime where collisions decrease the rate of diffusion of particles, collisions are in fact now required in the strongly magnetised regime for a drift of the particles guiding centre to occur. As a result, decreasing ν_{ei} for fixed r_g, which requires B_z to be constant, causes particles to be less mobile. This effect is compounded for higher velocity electrons as not only is $\nu_{ei} \propto v^{-3}$, resulting in hotter electrons being magnetised more easily than colder electrons, but $r_g \propto v$ while $\lambda_{ei} \propto v^4$. Together the result is that transport inhibition by a magnetic field for hot electrons is more severe than for colder electrons, with $\lambda_{f_1} \propto v^{-2}$.

At the transition point between these two regimes where $\chi_{ei} = 1$ and $r_g = \lambda_{ei}$

$$\lambda_{f_1}(\chi_{ei} = 1) = \frac{v}{2\nu_{ei}} = \frac{v}{2\omega_g} \propto \frac{T_e^{1/2}}{B_z} \tag{3.21}$$

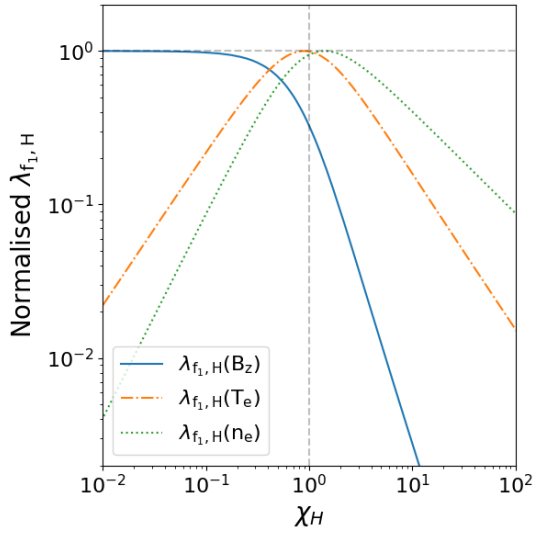

Figure 3.5: The effective mean-free-path $\lambda_{\mathrm{f}_1}(B_z, n_e, T_e)$ of the heat-carrying electrons with $v = v_H(\chi_T)$, where the subscript 'H' refers to the population with this velocity, as a function of $\chi_H(B_z, n_e, T_e)$. Here χ_H is changed indirectly through its dependence on either B_z, n_e, or T_e, with the other variables held constant. Each variable has a unique effect on λ_{f_1}; $\chi_{ei} \propto B_z$ with increasing B_z leading to a reduction in λ_{f_1} that is most significant when $\chi_{ei} > 1$, $\nu_{ei} \propto n_e$ which affects both λ_{ei} and χ_{ei} resulting in a maximum where $\chi_{ei} \approx 1$, and both $v \propto T_e^{1/2}$ and $\nu_{ei} \propto T_e^{-3/2}$ again leading to a maximum but now at $\chi_{ei} \approx \sqrt{2}$.

the effective mean-free-path reaches a maximum as a function of ν_{ei} which has the Bohm diffusion scaling $\propto B_z^{-1}$. At this point cross-field transport can reach a maximum for a given electron velocity as a function of collision frequency.

Treating the diffusion of particles as a random walk of step size Δx and frequency ν [44] the diffusion coefficient is given by

$$D = \Delta x^2 \nu = v \Delta x. \tag{3.22}$$

On substituting $\Delta x = \lambda_{f_1}$ and $\nu = \nu_{ei}$ the correct behaviour is found for perpendicular transport across all magnetisation regimes, with these trends implicit in the dimensionless form of the transport coefficients shown earlier in fig. 2.4.

The rate of diffusion is $D \propto v^5$ for weakly magnetised particles, but $D \propto v^{-1}$ when strongly magnetised. As the magnetisation of particles increases with velocity, the particles which diffuse most rapidly across the magnetic field are found to be those for which $\chi_{ei} = \sqrt{5}$, for which $V \approx 1.31 \chi_T^{-1/3}$. While this suggests colder electrons can diffuse much more effectively than hotter electrons, their small population limits their overall contribution to diffusion processes. Thus, the transport of faster electrons, which dominate heat-flow and are most susceptible to non-local transport

when unmagnetised, are most suppressed by the presence of a magnetic field.

3.4 Effect of anisotropic transport on f_0

At this stage it has been seen how transport properties arise from anisotropy within the distribution function, but the effect of this transport on the isotropic distribution function has not been investigated. The assumptions of classical transport theory rest upon the distribution being nearly Maxwellian, which will be shown to require the anisotropy to be small. It is well known that when anisotropy is significant the distribution will become non-Maxwellian due to non-local transport. To study how anisotropy perturbs the isotropic distribution the f_0-equation (eq. 2.58), which governs the evolution of f_0, will be considered. Here it is expressed as the combination of two competing effects

$$\frac{\partial f_0}{\partial t} = C_{e0} - \frac{\partial f_{0A}}{\partial t} \tag{3.23}$$

where the C_{e0} collision term drives the distribution function towards a Maxwellian, while the second term transfers energy and perturbs the distribution function due to gradients in $\mathbf{f}_1$. The perturbing term is given by

$$\frac{\partial f_{0A}}{\partial t} = -\frac{v}{3}\nabla \cdot \mathbf{f}_1 - \frac{1}{3v^2}\frac{\partial}{\partial v}\left(v^2 \mathbf{a} \cdot \mathbf{f}_1\right) \tag{3.24}$$

which is a function of derivatives of $\mathbf{f}_1$. As the derivative of an arbitrary function g dependent on a variable h can be expressed as the product $\partial_h g = g(h)/l_h$, where l_h is the length scale with respect to h, the perturbing term is written as

$$\frac{f_{0A}}{\partial t} = \sum_i^{x,y,z} f_{1i}/l_{A,i} \tag{3.25}$$

where the summation is taken over the x, y, and z components of $\mathbf{f}_1$ and $l_{A,i}$ is a function describing a length scale over which each component varies. Following the product rule the length scale of a product of multiple variables takes the form of a harmonic mean over the length scales of the composite variables. For this reason $l_{A,i}$ primarily has the form of a harmonic mean over the length scales of the composite variables in $\mathbf{f}_1$. It has units of time, so when the variation in $\mathbf{f}_1$ decreases the frequency with which the distribution function is perturbed also decreases.

For the case of the f_{1x} term

$$\frac{\partial f_{0A,x}}{\partial t} = -\frac{v}{3}\frac{\partial f_{1x}}{\partial x} - \frac{1}{3v^2}\frac{\partial}{\partial v}(v^2 a_x f_{1x}), \tag{3.26}$$

although the same process also follows for the f_{1y} and f_{1z} terms. Without loss of generality this can be written as

$$\frac{\partial f_{0A,x}}{\partial t} = -\frac{f_{1x}}{3}\left(\frac{v}{l_{f_{1x},x}} + \frac{a_x}{l_{f_{1x},v}} + \frac{2a_x}{v}\right) \tag{3.27}$$

using the notation $l_{f,g} = f(g)/\partial_g f(g)$ for a function $f(g)$ dependent on a variable g.

Dividing eq. 3.23 by f_0, and substituting eq. 3.25, yields

$$\frac{\partial_t f_0}{f_0} = \frac{C_{e0}}{f_0} - \sum_i^{x,y,z} \frac{f_{1i}}{f_0}\frac{1}{l_{A,i}} \tag{3.28}$$

an equation providing the characteristic frequency with which f_0 evolves. Here, the perturbing term which drives the distribution away from a Maxwellian is shown to be proportional to f_{1i}/f_0. Provided the amplitude of f_{1i} varies more rapidly than the length scale $l_{A,i}$, or that the length scale over which f_{1i} varies is constant, then this ratio will play the most significant role in perturbing f_0.

Taking the limit $\chi_T = 0$ then in the 1D case described by eq. 3.16

$$l_{A,x} = -\frac{3l_T}{v}\left[g(V) + l_T\frac{\partial_x^2 T_e}{\partial_x T_e}\right]^{-1} \tag{3.29}$$

if $\nabla n_e = 0$ where $g(V)$ is a function of V given by

$$g(V) = V^2 + 3(\beta_{\perp 0} + 1)V - \beta_{\perp 0} - \frac{3/2}{V^2 - 5/2 - \beta_{\perp 0}} - 5/2. \tag{3.30}$$

If the temperature profile remains similar between problems, then $l_{A,i}$ will also remain similar and f_{1i}/f_0 will play the most significant role in dictating the rate at which f_0 is perturbed.

Furthermore, with $f = f_0 + \mathbf{f}_1 \cdot \mathbf{v}/v$ values of $|\mathbf{f}_1| > f_0$ can be seen to result in negative f_0, which is unphysical. As $|\mathbf{f}_1|/f_0$ increases the relative anisotropy at a point in the velocity phase space of a plasma increases, with the maximum of $|\mathbf{f}_1|/f_0 = 1$ corresponding to a unidirectional flow. Once this point is reached then f_0 will only vary more rapidly if $l_{A,i}$ decreases. Thus, the ratio $\mathbf{f}_1/f_0$ is an appropriate quantity that can be used to assess the validity of the fluid approximation in magnetised plasma, with larger values corresponding to a greater departure from

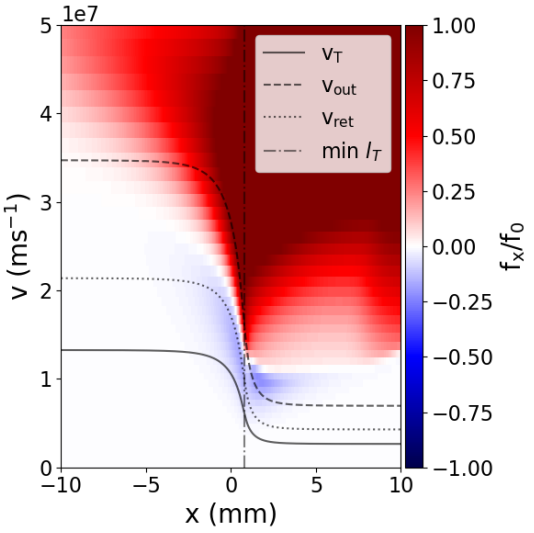

Figure 3.6: The ratio f_{1x}/f_0 at $t = 500$ ps for the temperature ramp relaxation shown in fig. 3.1. Overlaid are the velocities corresponding to v_T, v_{out}, and v_{ret} for a Maxwellian f_0. A vertical line shows the position at which l_T is at a minimum.

LTE and resulting non-local transport.

As can be seen in fig. 3.6 for a 1D temperature ramp relaxation, $|f_{1x}|/f_0$ is largest in the region surrounding the temperature perturbation as expected. Here, the evolution of f_0 with time due to electron transport is most significant, and as such is the primary region of interest when considering non-local effects. At velocities much higher than v_T truncation of the distribution at $\mathbf{f}_1$ in the IMPACT code breaks down, leading to unphysically large values of f_{1x} such that $f_{1x} > f_0$ and negative f_0. However, as there are so few particles in this regime they have little impact on the transport effects considered here.

3.5 Summary

This chapter has shown how the introduction of a magnetic field naturally leads to a separation of transport effects that occur parallel and perpendicular to the magnetic field axis. When applied to the Cartesian tensor expansion of f the first anisotropic term, which governs current and heat-flow, then becomes $\mathbf{f}_1 = \mathbf{f}_{1\parallel} + \mathbf{f}_{1\perp}$. The degree of anisotropy can then be seen to be proportional to λ_{f_1}/l_{f_1}, where $\lambda_{f_1} = \lambda_{ei}/(1+\chi_{ei}^2)$ is an effective mean-free-path and l_{f_1} describes a characteristic distance over which the distribution function varies. The results here are taken in the Lorentz limit, and as such assume electron-electron collisions can be neglected. If they were included, a reduction in the effective mean-free-path for a given Z would be expected due to the increased collision rate.

Assuming that the distribution is close to LTE, where f_0 can be described by a Maxwellian, the properties of the electron current and heat-flow due to the anisotropy can then be found. Due to their significantly increased mobility ($\lambda_{ei} \propto V^4$) and relatively large population, electrons with 2.25–3.25 v_T are found here to be typically responsible for heat-flow in an unmagnetised plasma. However, in a magnetic field, the mobility of hotter electrons is preferentially reduced because they are more readily magnetised ($\chi_{ei} \propto V^3$). This results in a reduction in the heat-carrying electron velocity to 1.5–2.5 v_T. The inclusion of electron-electron collisions are expected to result in a slight reduction in these velocities, with the peak heat-carrying velocity at $Z = 1$ equal to $V = 2.53$, compared to $V = 2.62$ in the Lorentz limit when $\chi_B = 0$. The mobility of the electrons in different magnetisation regimes can be explored in greater detail by considering the effective mean-free-path λ_{f_1}, which the anisotropy is dependent upon.

Finally, it has been seen how the relative anisotropy $\mathbf{f}_1/f_0 = -\lambda_{f_1}/\mathbf{l}_{f_1}$ plays a central role in dictating how the distribution function is perturbed away from a Maxwellian, leading to non-local transport. Thus, in the following chapter the impact of the core trends of the effective mean-free-path, namely the different scaling with ν_{ei} and B_z between the weakly and strongly magnetised regimes, will form the basis of our investigation of non-local transport trends.

Chapter 4

Kinetic transport phenomena in magnetised plasmas

In this chapter, the analysis of electron distribution function anisotropy from the previous chapter is applied to kinetic VFP simulations. The relative anisotropy $\mathbf{f}_1/f_0$ is varied by adjusting the systems magnetisation, which is dependent upon the collision frequency and magnetic field, and its correlation with deviations from a Maxwellian distribution is explored. This approach provides a novel demonstration of how anisotropy, and consequently non-local transport, depends on magnetisation. The chapter discusses a non-locality parameter based on the effective mean-free-path, and compares it with those which use either the mean-free-path or the gyro-radius. The relationship between relative anisotropy and electron transport effects can then be explored, highlighting its impact on heat flow and magnetic field dynamics.

Typically, when seeking to quantify non-local transport trends in laser-plasmas the Knudsen number $\lambda/|l_T|$ is used with $v = v_T$. Motivation arises from the series expansion of the distribution function for a small perturbation, where the perturbation parameter is $\lambda_T/|l_T|$. This result is demonstrated in eq. 3.16 when taking $\chi_{ei} = 0$ in which case it can be seen that $f_{1x} \propto \lambda_T/|l_T|$.

As transport in a plasma occurs across a broad distribution of particle velocities care must be taken when inferring trends based on a single velocity group, as demonstrated by the velocity phase space for f_{1x}/f_0 in fig. 3.6. In the unmagnetised case the scaling $\lambda_{ei} \propto v^4$ means that for suitably large v it will be found that $\lambda_{f_1} \gg l_{f_1}$, causing rapid changes in f_0 and unphysical negative values of f as $f_{1x}/f_0 > 1$. However, it is important to consider the impact a given velocity group has on the transport effect that is being considered. For the heat-flux, the contribution of the higher energy electrons is small as seen in fig. 3.4 due to their small population.

Gray and Kilkenny [73] considered this problem for the case of unmagnetised heat-transport, finding that electrons with 2.3–3 v_T provide a dominant contribution to the heat-flux. Their criteria for non-local transport having an appreciable effect on the heat-flux was then $f_{1x}/f_0 > 1$ for $v_T < 3$ as this resulted in negative values of f for this population. Following this reasoning, values of $\lambda_T/|l_T| \ll 0.01$ are typically associated with local transport, due to the role of electrons with 2.3–3 v_T which in turn have mean-free-paths 16-81 times larger as $\lambda \propto v^4$.

In the previous section, it was shown that magnetisation affects the velocity of the heat-carrying population, so here the criteria for non-local heat-transport is further generalised as being the point at which $f_{1x}/f_0 > 1$ for the electrons which carry the most heat as defined in fig. 3.3. The velocity of these electrons will be referred to as v_H, with the subscript 'H' used to refer to the properties of the heat-carrying population. Notably, this means that strongly magnetised plasmas are more resistant to non-local heat-transport due to the reduction of v_H from 2.62 v_T to 1.81 v_T, for which λ_H is reduced by a factor of ~ 4.

4.1 Temperature ramp relaxations

To investigate the dependence of λ_{f_1} on ν_{ei} and B_z, and how this affects relative anisotropy within the distribution function when varying plasma parameters, a temperature ramp relaxation is considered using the VFP code IMPACT. These problems consist of adjacent hot and cold baths, with a smooth transition between the two regions. Utilising suitably large temperature baths relaxes the requirement for external heating/cooling mechanisms, while also ensuring that boundary effects that arise when using reflective boundary conditions are not of importance. This allows a quasi-static heat-flux to then be reached.

All problems here use an electron density and ionisation state that are homogeneous and do not vary with time. As it is of relevance to the problems considered later in this thesis an under-dense nitrogen plasma ($Z = 7$) is chosen, with the Coulomb logarithm $\log \Lambda_{ei} = 6$. IMPACT does not include the full e-e collision operator, instead using the collision fix provided by Epperlein and Short [38] which is only suitable when correcting $\kappa_\perp$ for unmagnetised plasmas. For this reason, the plasma is treated in the Lorentz limit, following the assumptions of eq. 3.9. However, the variation of Z and the inclusion of e-e collisions should not significantly alter the conclusions here. For example, decreasing Z will result in the point at which $\chi_H = 1$ being shifted to higher density, while including e-e collisions modifies the transport coefficients in eq. 3.16.

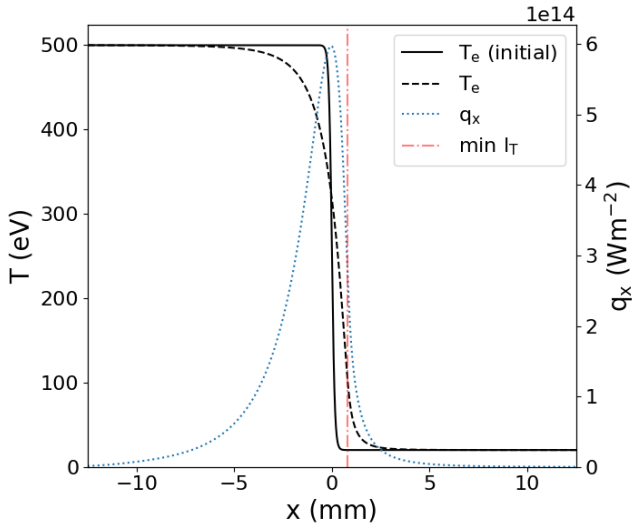

Figure 4.1: A nitrogen temperature ramp relaxation simulated in IMPACT where $n_e = 10^{25}$ m^{-3} and $B_z = 3$ mT. The initial temperature profile is shown, as well as the temperature and heat-flow profile at $t = 500$ ps. The position where l_T is at a minimum is marked.

The temperature ramp is given by

$$T_\mathrm{e} = \frac{T_\mathrm{hot} + T_\mathrm{cold} + (T_\mathrm{hot} - T_\mathrm{cold}) \tanh(-x/L)}{2} \tag{4.1}$$

where the hot and cold bath temperatures are $T_\mathrm{hot} = 500$ eV and $T_\mathrm{cold} = 20$ eV respectively. Setting $L = 150$ µm the minimum length scale is $l_T = 112.5$ µm. An example of this profile can be seen in fig. 4.1. The parameter space is then explored by varying n_e which allows the effect of transitioning from the weakly to strongly magnetised regime to be explored, as $\nu_{ei} \propto n_e$ for $n_e = Zn_i$, while also varying $\lambda_T/l_T \propto 1/n_e$. Additionally, χ_T is controlled by varying the strength of the initially uniform magnetic field B_0 at each density.

Fig. 4.2a) demonstrates the key effects of non-local transport on the heat-flow profile for these test problems, where in this case $\chi_H \ll 1$ and by decreasing the density λ_{ei} is increased relative to l_T. At higher density $q_x \approx q_{SH}$, while at lower density the reduction in the maximum of q_x and extended pre-heat compared to q_{SH} is seen. Despite the difference in density the magnitude of q_x remains similar, a result of the diffusive nature of heat-flow. Plotting q_x/q_{FS} as a function of λ_T/l_T in fig. 4.2b) the non-local nature becomes clear with q_x/q_{SH} no longer uniquely defined for a given set of plasma parameters, a result that is not predicted in the local limit as seen in eq. 2.129.

Having laid out the simulation framework with which the effect of magnetisation on f_{1x}/f_0 is to be investigated, the final considerations in the following analysis will

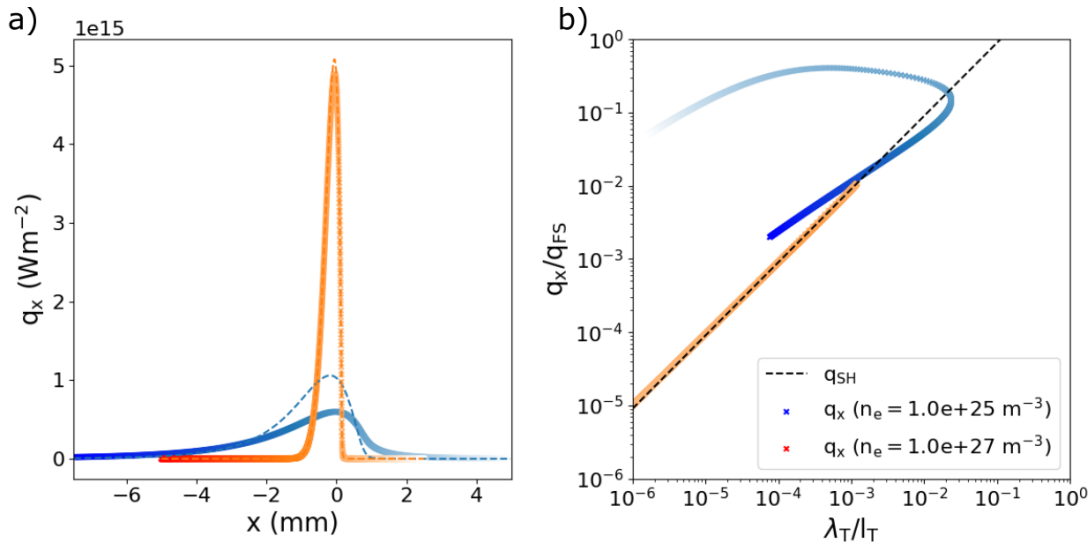

Figure 4.2: Heat-flow profiles obtained from nitrogen temperature relaxation problems where $n_e = 10^{25}$ and 10^{27} m^{-3} with $B_z = 3$ mT are compared to the local q_{SH} prediction at $t = 500$ ps, with a) showing a spatial comparison of the two results. In b) the ratio q_x/q_{FS} is plotted against λ_T/l_T, with the dashed black corresponding to the Spitzer-Härm result where the intercept at $\lambda_T/l_T = 1$ gives the conductivity $\kappa^c_\perp(\chi_B = 0) = 13.6$. Points above and below this line demonstrate increased and decreased heat-flow respectively compared to q_{SH}. The simulated values in both plots are coloured according to their x value; moving from the hot bath down the temperature gradient into the cold plasma the points transition from dark to light.

regard the points in velocity phase space and time at which f_{1x}/f_0 is evaluated when comparing simulations. As explained previously the velocity that is chosen will be v_H, as defined in fig. 3.3 for a Maxwellian f_0. While the value of v_H could be obtained from the kinetic simulations, an estimation of the significance of non-locality based on local parameters is desired.

As can be seen in fig. 4.3a) this assumption works well in the case of local transport. Here 80% of the outgoing heat-flow is typically carried by particles v between 2.29 and 3.29 v_T when $\chi_T \ll 1$. Ahead of the heat-front there is an increase in the upper velocity due to a small population of free-streaming electrons, but the magnitude of q_x here is so low it is not of significance. When transport is non-local in fig. 4.3b) heat-carrying electrons propagate away from the heat-front, leading to a reduction in v_H due to the loss of this population. Ahead of the heat-front these particles now make the most significant contribution to q_x, leading to an increase in v_H to ~ 13 v_T corresponding to the initial velocity of the heat-carrying electrons in the hot bath at $T_{\text{hot}} = 500$ eV.

There are then several points at which the spatial comparison can be made, with the main requirement being that there is consistency between simulations. Ahead of the heat-front the current will change direction as non-local transport causes v_H

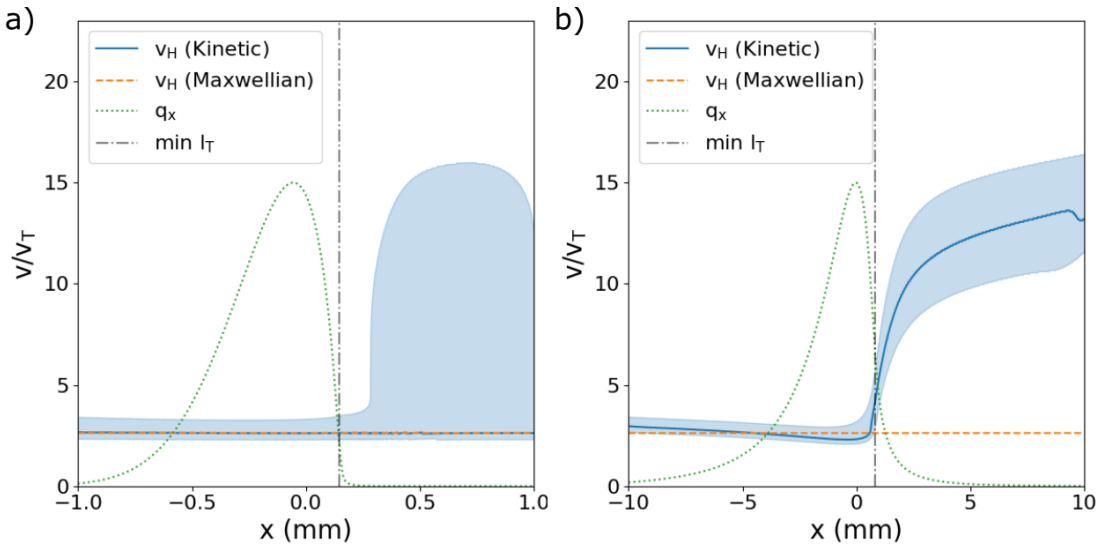

Figure 4.3: Plots showing the velocity of the heat-carrying electrons normalised by v_T for the temperature ramp relaxation simulations shown in fig. 4.2 where n_e is a) 10^{27} m^{-3} and b) 10^{25} m^{-3}. In both plots the value is found from the maximum of the heat-flow integrand $f_{1x}v^5$, with the shaded region highlighting the velocities which contain between 10 and 90% of the cumulative outgoing heat-flow. This is compared to v_H assuming $f_0 = f_m$. The q_x profile and position where l_T is at a minimum are shown.

to increase, so these positions are avoided. Two simple choices are where either q_x is at a maximum or where l_T is at a minimum. Here the position where q_x is at a maximum is chosen, as the behaviour is most clearly understood; velocities above v_H will generally correspond to the outgoing current, with non-local transport causing v_H to decrease. That magnitude of f_{1x}/f_0 at this point is close to its maximum, so will provide a good point to measure whether anisotropy is significantly perturbing the distribution function away from a Maxwellian. Additionally, plasma parameters which are not explicitly being varied are usually found to be similar between simulations. While this position is chosen other choices remain valid, and their choice is not expected to alter conclusions made regarding the influence of anisotropy on f_0.

As these simulations include electron inertia ($\partial_t \mathbf{f}_1$), they are allowed to evolve until $t = 500$ ps at which point the distribution function has reached a quasi-static state ($\partial_t \mathbf{f}_1 \approx 0$) for all but the most non-local simulations ($B_z = 3$ mT, $n_e < 10^{25}$). To check this is the case eq. 3.9 is used to compare f_{1x} with the expected quasi-static value; this allows the impact of electron inertia on the simulations to be quantified, which will be examined further in section 4.4. The convergence of q_x with the quasi-static value is demonstrated in fig. 4.4 where it can be seen that after an initial transient period the two results converge. The length of this transient period depends on both the collision frequency and the gyro-frequency; as these increase

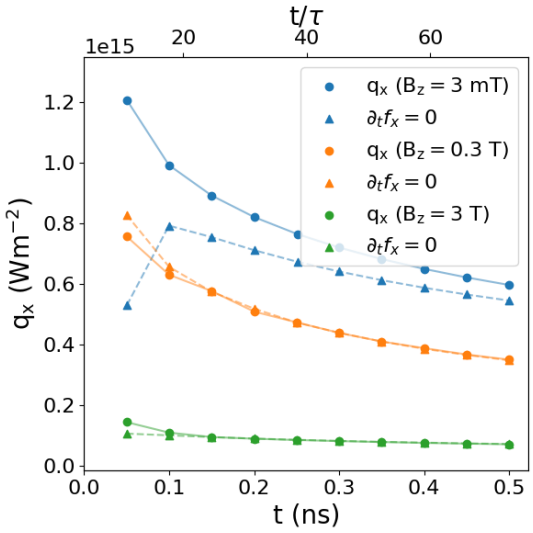

Figure 4.4: Temporal evolution of the maximum heat-flow for a series of nitrogen temperature ramp relaxations where $n_e = 10^{25}$ m^{-3} and B_z is varied. These values are compared to those calculated using eq. 3.9 with the kinetic f_0 which assumes $\partial_t \mathbf{f}_1 = 0$. On the upper axis the time is shown normalised by collision time for thermal particles in the hot-bath with $T_{\text{hot}} = 500$ eV.

the time to reach steady-state decreases.

Once a quasi-static state has been reached a comparison could then be made after some number of collision times, but this is not necessarily an appropriate timescale for when the plasma is magnetised due to the influence of the gyro-frequency. Additionally, for particles with $v = v_H$ at 500 eV the collision times spans the picosecond to nanosecond timescales between $n_e = 10^{27}$ m^{-3} and 10^{24} m^{-3}. Experimentally it is more common to compare measurements at a fixed time, so for these reasons it is deemed more appropriate to examine a single time.

4.2 Transition from local to non-local transport

In the following section trends in the relative anisotropy for both weakly and strongly magnetised plasmas will now be demonstrated by varying ν_{ei} and B_z to investigate the emergence of non-local transport. The quantity of interest is the ratio $\mathbf{f}_1/f_0$, with the most significant term for these 1D temperature ramp relaxations

$$\frac{f_{1x}}{f_0} = \frac{\lambda_{f_{1x}}}{l_{f_{1x}}} = \frac{\lambda_{ei}}{1+\chi_{ei}^2}\frac{1}{l_{f_{1x}}} \tag{4.2}$$

where the result in eq. 3.16 is used in defining $l_{f_{1x}}$.

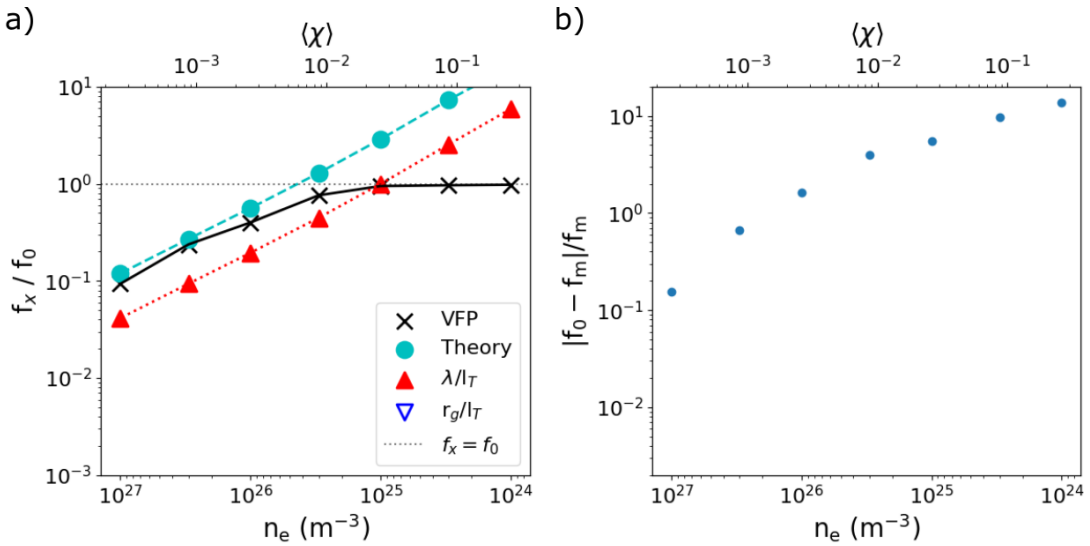

Figure 4.5: Results from a series of temperature ramp relaxations at $t = 500$ ps exploring the weakly magnetised regime, taken at the point where q_x is at a maximum. Here, the initial magnetic field strength was $B_z = 3$ mT and n_e was varied to modify the magnetisation. a) The ratio f_{1x}/f_0 for the heat-carrying electrons is shown, and compared to estimates obtained using eq. 4.2, λ/l_T, and r_g/l_T. Here, $\langle\chi\rangle$ is a representative magnetisation obtained using average plasma parameters. b) The root-mean-square difference between f_0 and a Maxwellian distribution, obtained for electrons in the velocity band $0.5v_R$ to $1.5v_H$.

4.2.1 Dependence on n_e in the weakly magnetised regime

In fig. 4.5a) the weakly magnetised regime is investigated by decreasing n_e for an applied magnetic field of $B_z = 3$ mT, leading to an increase in λ_{ei} relative to the plasma length scale. While the magnetisation also increases for the heat-carrying electrons this remains $\chi_H < 1$. The x-axis is inverted to emphasise the trend of increasing f_{1x}/f_0 with decreasing n_e predicted when using λ_H/l_T, with both λ_H/l_T and eq. 4.2 demonstrating the same trend. VFP simulations show an initial increase in f_{1x}/f_0 in agreement with both models, which tends towards the physical maximum of $f_{1x}/f_0 = 1$ at the lowest density. The agreement is almost exact with eq. 4.2 at the highest density, which is to be expected as the plasma here is near LTE, while λ_H/l_T is offset as this approximation neglects the constant factor dependent on v_H/v_T. The divergence that then occurs between the kinetic result and models is largely a result of f_0 no longer remaining Maxwellian as transport becomes increasingly non-local.

Confirmation that an increase in f_{1x}/f_0 results in a larger deviation away from a Maxwellian f_0 is provided by calculating the root-mean-square (RMS) deviation between f_0 and the best fitting Maxwellian, as shown in fig. 4.5b). This is taken for velocities between $0.5v_R$ and $1.5v_H$ to provide a measurement that is robust to small local variations in f_0. It can be seen that although the kinetic f_{1x}/f_0 reaches

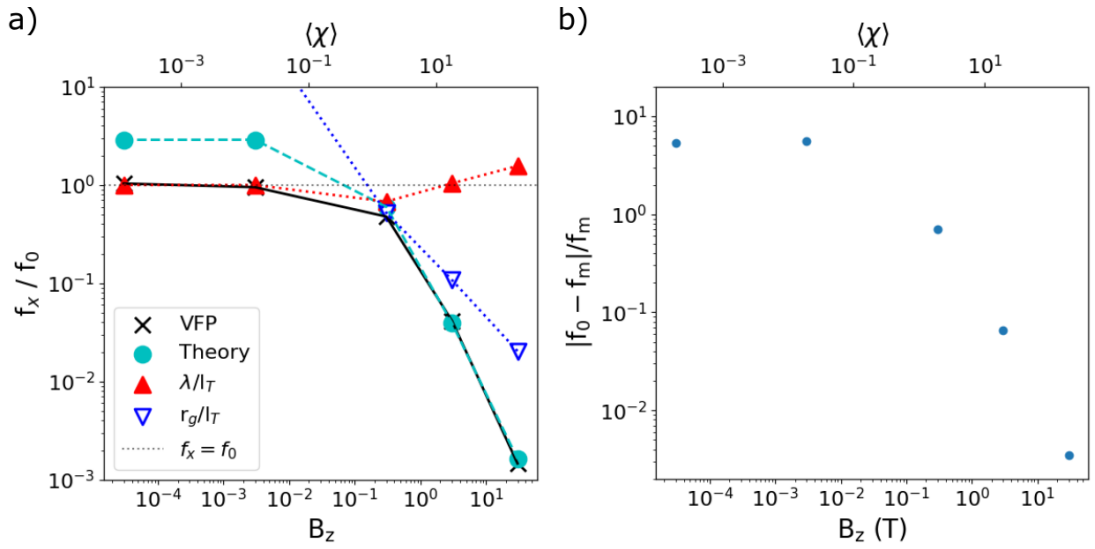

Figure 4.6: Results from a series of temperature ramp relaxations at $t = 500$ ps exploring the transition from the weakly magnetised to strongly magnetised regime, taken at the point where q_x is at a maximum. Here, $n_e = 10^{25}$ m^{-3} and the initial magnetic field strength was varied between $B_z = 3 \times 10^{-5}$ and 3×10^{1} T to modify the magnetisation. The plots are in the same style as fig. 4.5except the magnetic field strength is now varied instead of the electron density.

a maximum in fig. 4.5a), the RMS deviation value continues to increase as the density decreases. This is a result of increasing non-local transport both for the v_H population, as well as an increasing proportion of the lower velocity population for which $\lambda_{f_{1x}}$ begins to exceed l_{f_1} as the density decreases further.

4.2.2 Dependence on B_z in the strongly magnetised regime

To investigate the effect of magnetisation there are two approaches to be taken as discussed earlier; increasing the gyro-frequency, or decreasing the collision frequency. Usually, this regime has been explored using the former approach by varying the magnetic field as $\chi_{ei} \propto r_g^{-1} \propto B_z$ [89]. Electrons for which $\lambda_{ei} > l_T$ can then be localised by a magnetic field, provided r_g is suitably small, allowing local transport to occur in plasmas which would otherwise demonstrate significant non-local transport. As a result, in the strongly magnetised regime r_g is typically used when calculating K_n, given that this now limits the maximum diffusion distance. However, once strongly magnetised the effective mean-free-path instead becomes $\lambda_{f_{1x}} = r_g/\chi_{ei}$. Thus, the effective mean-free-path can be decreased below the gyro-radius, and an increasing magnetic field very rapidly localises transport as $f_{1x}/f_0 \propto B_z^2$.

The effect of increasing B_z is shown in fig. 4.6a) for $n_e = 10^{25}$ m^{-3}. Initially, when $\chi_H \ll 1$, increasing B_z has no impact on the anisotropy as $r_g \gg \lambda_H$. Using λ_H/l_T or

eq. 4.2 the correct trend is identified, with the near exact agreement between λ_H/l_T and the kinetic f_{1x}/f_0 a coincidence arising from the local plasma parameters giving $\lambda_H/l_T = 1$. On increasing B_z further anisotropy begins to reduce once $\chi_H \approx 1$, a result not predicted using λ_H/l_T which is independent of B_z. In this region Bohm diffusion occurs, and r_g/l_T provides a reasonable estimate for the ratio $f_{1x}/f_0 \propto B_z^{-1}$. However, on entering the $\chi_H \gg 1$ regime the anisotropy reduces rapidly and $\lambda_{f_{1x}} = r_{g,H}/\chi_{ei} \propto B_z^{-2}$ must now be used to correctly predict the reduction in anisotropy for increasing B_z. Again, by comparison of f_0 with f_m in fig. 4.6b) the correlation between f_{1x}/f_0 and the variation in f_0 away from a Maxwellian is highlighted, with increasing magnetisation now resulting in an increasingly Maxwellian distribution as transport is localised.

4.2.3 Dependence on n_e in the strongly magnetised regime

If instead the magnetisation is increased by decreasing n_e then in the weakly magnetised regime the relative anisotropy will initially increase as $f_{1x}/f_0(\chi_{ei} \ll 1) \propto \lambda_{ei} \propto n_e^{-1}$. This result was demonstrated in fig. 4.5.

However, $\lambda_{f_{1x}}(\chi_{ei} \ll 1) = \lambda_{ei}$ predicts an unbounded f_{1x}/f_0, increasing towards infinity as the collision rate drops. Instead a maximum is found at $\chi_{ei} = 1$ taking $\partial\lambda_{f_{1x}}/\partial n_e = 0$. At this point $\lambda_{ei} = r_g$ with the maximum set by r_g as $f_{1x}/f_0 = r_g/2l_{f_{1x}}$. Furthermore, not only will the relative anisotropy reach a maximum but in the strongly magnetised regime $f_{1x}/f_0(\chi_{ei} \gg 1) \propto r_g/\chi_{ei} \propto n_e$ and decreasing the density will result in a reduction in f_{1x}/f_0. This relationship has already been suggested in fig. 4.6, where it was found that $f_{1x}/f_0 \propto r_g/\chi_{ei}$ matched the trend in the relative anisotropy when varying B_z.

The transition from a weakly to strongly magnetised plasma when varying n_e is shown in fig. 4.7, where B_z is increased to 0.3 T compared to fig. 4.5. Initially the same trend is found in fig. 4.5a), with decreasing n_e leading to larger f_{1x}/f_0 as predicted by λ_H/l_T. At $\chi_H \approx 1$ a maximum is reached, at which point $r_{g,H}/l_T$ is a more appropriate estimate of f_{1x}/f_0 than λ_H/l_T. However, this maximum does not occur at $\chi_H = 1$ due to variations in v_H and $l_{f_{1x}}$, which are weakly dependent on χ_T. On reaching the strongly magnetised regime f_{1x}/f_0 can then be seen to decrease as the density decreases, a result that is not predicted by $r_{g,H}/l_T$ which remains roughly constant as r_g is independent of n_e. Only $\lambda_{f_{1x}}/l_T$ correctly predicts the trend in f_{1x}/f_0 across both weakly and strongly magnetised regimes, with the use of eq. 4.2 required for closer agreement.

Observing the variation in f_0 compared to f_m in fig. 4.5b), it can be seen that

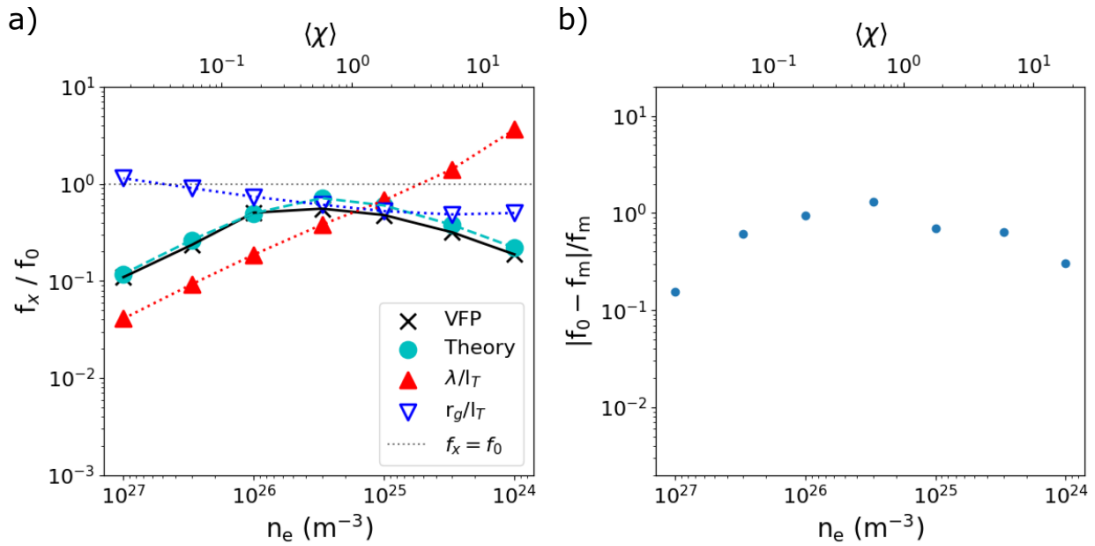

Figure 4.7: Results from a series of temperature ramp relaxations at $t = 500$ ps exploring the transition from the weakly magnetised to strongly magnetised regime, taken at the point where l_T is at a minimum. Here, the initial magnetic field strength was $B_z = 0.3$ T and n_e was varied to modify the magnetisation. The plots are the same as shown in fig. 4.5.

this behaviour is reproduced. Here, as n_e is decreased the deviation initially increases before reaching a maximum at $\chi_H \approx 1$, at which point the distribution function then becomes more Maxwellian. This result, that in a strongly magnetised plasma decreasing collision rate leads to more local transport, has implications for experiments on non-local effects in magnetised plasmas. It implies that for any fixed magnetic field transport is most non-local when $\chi_H \approx 1$.

The two main goals of this investigation have then been met. First, it has been shown that trends in the relative anisotropy f_{1x}/f_0 are proportional to $\lambda_{f_{1x}}$. Secondly, the correlation between f_{1x}/f_0 and the deviation in f_0 away from Maxwellian due to non-local transport has been shown. Previous attempts to understand non-local trends using a Knudsen number with the mean-free-path given by λ_{ei} are only applicable in the weakly magnetised regime, while r_g reproduces trends when $\chi_{ei} \approx 1$. Using the effective mean-free-path $\lambda_{f_{1x}}$ covers both regimes, while also extending the validity to the strongly magnetised plasmas.

While previously the velocity used in these calculations has been taken to be $v = v_T$, which is appropriate when considering transport in unmagnetised plasmas, the heat-carrying electrons should be considered when a magnetic field is present. As heat-carrying electrons are more readily magnetised than thermal electrons due to $\chi_{ei} = \lambda_{ei}/r_g \propto V^3$ the point at which $\chi_H = 1$ is reached and non-local transport is maximised occurs before $\chi_T \approx 1$. For example, in fig. 4.7 using $v = v_T$ would shift the maximum in f_{1x}/f_0 to higher density, which would be offset from where

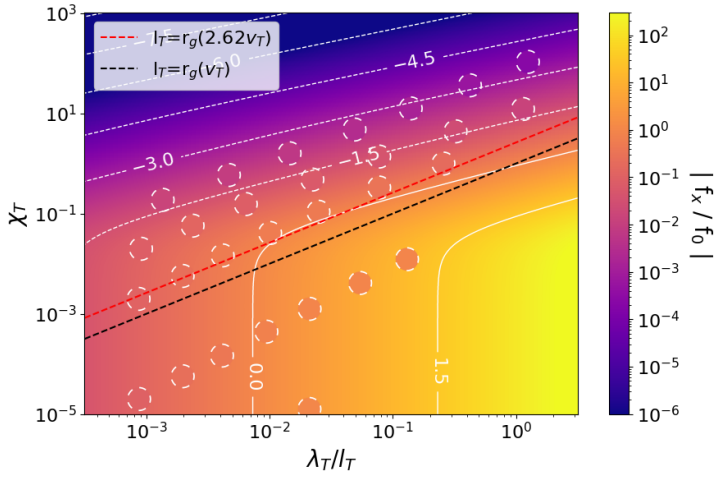

Figure 4.8: A map of f_{1x}/f_0 as a function of λ_T/l_T and χ_T obtained using eq. 4.3 for $v = v_H(\chi_T)$ in the Lorentz limit. Simulation points coloured according to the value of f_{1x}/f_0 are overlaid for $v = v_H$ at $t = 500$ ps. In these simulations the initial n_e is varied, affecting both λ_T/l_T and χ_T, as well as B_0 which changes χ_T. Dashed lines mark where $r_g = l_T$ for electrons with $v_H = 2.62$ and v_T.

the deviation in f_0 is found to be greatest.

4.2.4 Non-local parameter space

Having demonstrated the connection between eq. 4.2 and non-local transport, the equation is now investigated in greater detail to examine its dependence on other plasma parameters. To do so eq. 4.2 is re-written in terms of dimensionless quantities

$$\frac{f_{1x}}{f_0} = \frac{V^4 \lambda_T / l_T}{1 + V^6 \chi_T^2} \left(V^2 - \frac{5}{2} - \beta_\perp(\chi_T) + V^3 \chi_T \beta_\wedge(\chi_T) \right) \tag{4.3}$$

which in turn highlights that while a density regime of $n_e = 10^{24}$ to 10^{27} m^{-3} was investigated earlier, the approach is general for weakly coupled plasmas provided the expansion of the VFP equation (eq. 2.59) holds. For a weakly coupled plasma it is required that $\omega_p \gg \nu_{ei}$. At low temperatures and/or high densities the Fokker-Planck treatment of collisions also breaks down, as the potential energy of the interaction is no longer small relative to the thermal energy.

In fig. 4.8 the parameter space obtained using eq. 4.3 is shown as a function of λ_T/l_T and χ_T for electrons with $v = v_H$. A parameter scan is performed using the temperature ramp relaxation previously described for $n_e = 10^{24}$ to 10^{27} m^{-3} and $B_0 = 3 \times 10^{-5}$ to 30 T and overlaid on the plot, with the simulations shown in the previous section forming a subset of this scan. Here it can be seen that there is excellent agreement between the kinetic and predicted value for $f_{1x}/f_0 < 1$.

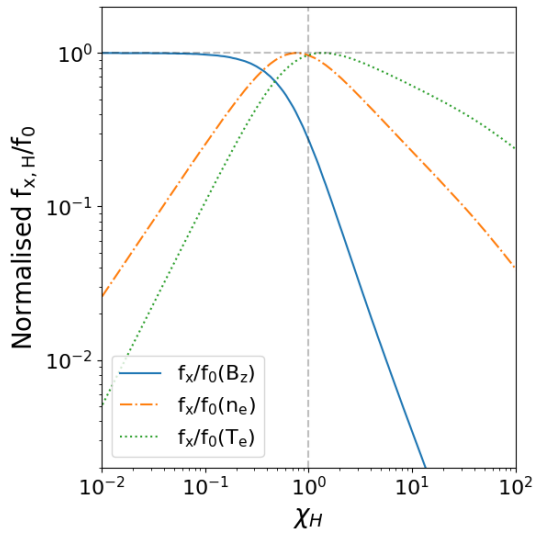

Figure 4.9: Normalised plots of $f_{1x,H}/f_0(B_z, n_e, T_e)$ as a function of $\chi_H(B_z, n_e, T_e)$ where the magnetisation is varied through its dependence on B_z, n_e or T_e.

The key purpose of this plot is to show how f_{1x}/f_0, which was shown previously to be correlated with deviation from a Maxwellian f_0, varies with λ_T/l_T and χ_T. Fundamentally, an increase in the f_{1x}/f_0 perturbation corresponds to not only increasing non-local transport as the distribution is perturbed further, but an increase in the relative magnitude of all transport processes dependent on f_{1x}. By seeking to maximise f_{1x}/f_0 the rate at which the plasma evolves can be increased, or similarly decreased through minimisation. Only once f_{1x}/f_0 reaches a suitably large value for velocity groups that are responsible for transport, will non-local transport begin to significantly impact the underlying value of f_0. Kinetic or non-local models are then required to accurately capture transport processes.

Choosing $v = v_H$ was done on the basis that non-local transport within this population will have the most significant impact on the heat-flow. Above the point where eq. 4.3 predicts $f_{1x}/f_0 = 1$ increasing disagreement with the kinetic value occurs, with non-local transport now significant in this region of parameter space for the heat-carrying electron population. As such it provides a useful marker for observing the region of parameter space where non-local transport is expected to be significant. In the weakly magnetised case this occurs at $\lambda_T/l_T = 7.3 \times 10^{-3}$, although the initial onset of non-local effects can be found to occur before this due to the transport of electrons with $v > v_H$ which still carry a large fraction of the thermal energy (fig. 4.3). When $\chi_T \approx 0.1$ (at which point $\chi_H \approx 1$) the value of λ_T/l_T for which $f_{1x}/f_0 = 1$ increases rapidly as $\lambda_T/l_T \propto \chi_T^2$.

Increasing λ_T/l_T always increases f_{1x}/f_0 for fixed χ_T, while in the reverse case increasing χ_T decreases f_{1x}/f_0 when $\chi_{ei} \gtrsim 1$. Due to the coupling between λ_T/l_T

and χ_T, as they both depend on ν_{ei}, these can only be changed independently by varying either l_T or B_z respectively. Varying l_T or B_z the parameter space in fig. 4.8 is transversed horizontally or vertically respectively. Lines for which $\chi_T = V(l_T/r_g)(\lambda_T/l_T)$ are equivalent to contours of constant B_z for a given l_T and V; here the contours for which $r_{g,T} = l_T$ and $r_{g,H} = l_T$ are shown. The region above these contours satisfies $r_{g,V} < l_T$. Modifying the collision frequency (eq. 2.55) by varying n_e these contours are then traversed as demonstrated in fig. 4.5 & 4.7. If instead T_e is varied $\lambda_T/l_T \propto T_e^2$ increases more rapidly than $\chi_T \propto T_e^{3/2}$ as it has a greater dependence on T_e. If only T_e is varied then these lines have gradient $m = 3/4$ compared to $m = 1$ for variable n_e, while in the strongly magnetised regime the contours for fixed f_{1x}/f_0 have gradient $m = 1/2$. As a result increasing B_z, n_e, or T_e independently will eventually lead to the strongly magnetised regime in which f_{1x}/f_0 decreases, with the trends shown in fig. 4.9.

For these reasons accessing a regime where both $r_{g,H} > l_T$ and $\chi_H > 1$, which may be considered the 'true' magnetised non-local regime, is actually quite difficult. On first inspection this requires the ordering $l_T < r_{g,H} < \lambda_H$ for which the range of possible magnetic field values is found to be approximately

$$3.37 V_H \left(\frac{T_e}{\text{eV}}\right)^{1/2} \left(\frac{l_T}{\text{µm}}\right)^{-1} > B > 22.0 \frac{Z \ln \Lambda_{ei}}{V_H^3} \left(\frac{n_e}{10^{24}}\right) \left(\frac{T_e}{\text{eV}}\right)^{-3/2} \tag{4.4}$$

where T_e and l_T are in units of eV and µm respectively. Non-local effects may be transient, allowing electrons to travel into regions of the plasma where they are out of equilibrium but still remain bound to their original field line, unless the stricter condition $l_T < r_{g,H}/\chi_H$ is met.

In both fig. 4.8 and the simulations examined here the Lorentz limit was taken, despite e-e collisions playing a significant role in transport at $Z = 7$ (e.g. $\beta_\perp$ experiences a 19% reduction). This was done in the simulations to allow the densities to better represent those found in experiments conducted in under-dense gases. A higher Z could have been used increasing the validity of the Lorentz approximation, but this would result in a much higher collision frequency for a given n_e, shifting the maximum in f_{1x}/f_0 to lower n_e. Including e-e collisions would result in a shift of the maximum in f_{1x}/f_0 to lower density due to the increase in collisions. Additionally, considering fig. 4.8 e-e collisions modify the behaviour when $\chi_T < 1$ via the transport coefficients, but have almost no effect when $\chi_T > 1$ as in this regime the transport coefficients do not depend strongly on Z. For $\chi_T < 1$, the plot is largely translated to lower λ_T/l_T with the point at which $f_{1x}/f_0 > 1$ occurring at $\lambda_T/l_T = 5.7 \times 10^{-3}$ at $Z = 1$.

Regarding the transport coefficients, it is useful to note that when $\chi_T << 1$ these take the form

$$\eta_\perp = \eta_\parallel \quad \& \quad \eta_\wedge \propto \chi_T \tag{4.5}$$

while when $\chi_T \gg 1$

$$\eta_\perp \propto \chi_T^{-2} \quad \& \quad \eta_\wedge \propto \chi_T^{-1} \tag{4.6}$$

for a general coefficient $\underline{\underline{\eta}}$. Expressing them in these limits it appears that the perpendicular transport coefficients are related to the magnetic field dependence of χ_T, while the wedge coefficients are due to the ν_{ei} dependence. This symmetry in the transport coefficients was only demonstrated recently by Sadler et al. [48].

A final consideration regards the effect of varying the spatial profile of the plasma parameters, rather than uniformly modifying their magnitude. The collision frequency of a test particle given by eq. 2.38 is independent of the temperature, provided the velocity of the test particle is greater than the thermal velocity. Heat-carrying electrons can then propagate through the plasma without experiencing a significant change in their collision frequency, which can then be found based on the plasma parameters at their initial position. However, this collision frequency is dependent on both Z_s and n_s of the scattering species. If a significant increase occurs over the course of the particles trajectory, for example if the particle arrives at an interface, then the collision frequency will vary depending on the particle position. In this case, the approximated ratio of f_{1x}/f_0 can no longer be used, as the rate of diffusion of the particle is no longer dependent solely on the initial conditions.

4.3 Linking anisotropy and transport effects

Having established that $\mathbf{f}_1/f_0$ provides a measure of the relative significance of anisotropy for a given plasma, and that as this relative anisotropy increases the isotropic distribution function becomes increasingly perturbed, a link with the fundamental transport processes is now sought. Considering the $\mathbf{f}_1$ equation the two transport processes associated with it are current and heat-flow, and by taking appropriate velocity moments Ohm's law and the heat-flow equation are obtained. In the first part of the following section the focus will be on heat-flow, allowing $\mathbf{q}/q_{FS}$ to be shown to be a distribution averaged measure of the relative anisotropy. Then in the second part Ohm's law will be examined allowing the link between anisotropic transport and magnetic field advection to be shown.

4.3.1 Anisotropy and heat-flow relationship

The fundamental link between heat-flow and $\mathbf{f}_1/f_0$ will be shown by considering the heat-flow

$$\mathbf{q} = \frac{2\pi m_e}{3}\int_0^\infty \mathbf{f}_1 v^5 dv = \int_0^\infty \mathbf{q}_v dv \tag{4.7}$$

where $\mathbf{q}_v$ is the heat carried by each velocity band as was shown earlier in fig. 3.4 for heat-flow along the x-axis. It was previously stated that an increase in $\mathbf{f}_1/f_0$ corresponds to an increase in the relative magnitude of transport processes. To show this is true in the case of the heat-flow, the maximum flow of heat that can be carried by each velocity band is given by

$$q_{FS,v} = n_{e,v} E_k v \tag{4.8}$$

where $E_k = m_e v^2/2$ and the kinetic energy density of the band is then transported with velocity v. Using the relation

$$n_e = 4\pi\int_0^\infty f_0 v^2 dv = \int_0^\infty n_{e,v} dv \tag{4.9}$$

allows this to then be written as

$$q_{FS,v} = 2\pi m_e f_0 v^5. \tag{4.10}$$

Taking the ratio of the heat-flow carried by each velocity band to the free-streaming limit

$$\frac{\mathbf{q}_v}{q_{FS,v}} = \frac{(2/3)\pi m_e \mathbf{f}_1 v^5}{4\pi f_0 v^2 E_k v} = \frac{1}{3}\frac{\mathbf{f}_1}{f_0}. \tag{4.11}$$

where we see that the heat-flow as a fraction of $q_{FS,v}$ is proportional to the relative anisotropy. By increasing $\mathbf{f}_1/f_0$ the heat-flow is then increased towards its maximum value. This is true for any distribution as no assumption on the form of f_0 is made. The heat-flow as a function of $q_{FS,v}$ is then

$$\mathbf{q} = \frac{1}{3}\int_0^\infty \frac{\mathbf{f}_1}{f_0} q_{FS,v} dv. \tag{4.12}$$

When the relative anisotropy reaches its maximum value $|\mathbf{q}_v| = q_{FS,v}/3$. If this

occurs for all velocity groups then the maximum heat-flow is obtained such that

$$q_{max} = \frac{1}{3}\int_0^\infty q_{FS,v} dv = \frac{2\pi m_e}{3}\int_0^\infty f_0 v^5 dv. \tag{4.13}$$

For a Maxwellian distribution $f_0 = f_m$

$$q_{max} = \frac{2\pi m_e}{3}\int_0^\infty f_m v^5 dv = \frac{4}{3\sqrt{\pi}} n_e T_e v_T = \frac{q_{FS}}{c_B} \tag{4.14}$$

which is equal to the earlier definition of q_{FS} (eq. 2.130) up to a constant factor of $c_B^{-1} \approx 0.75$. However, this results in a non-zero current of

$$\mathbf{J} = -\frac{4\pi}{3} e \int_0^\infty f_m v^3 dv = -\frac{e n_e}{2 c_B} v_T \tag{4.15}$$

which does not maintain quasi-neutrality. Thus, by enforcing a flux-limited heat-flow $q_{FL} = f q_{FS}$, such that the heat-flow cannot exceed some fraction f of the free-streaming limit, two assumptions are then made about the plasma distribution; that the relative anisotropy equals f for all velocities, and f_0 is Maxwellian.

The link between $\mathbf{q}/q_{FS}$, relative anisotropy, and non-local transport in the plasma can now be highlighted by expressing this ratio as

$$\frac{\mathbf{q}}{q_{FS}} = \frac{\int_0^\infty \mathbf{f}_1 v^5 dv}{\int_0^\infty f_m v^5 dv}. \tag{4.16}$$

This term quantifies the magnitude of the anisotropy, weighted towards the electrons which contribute the most to the heat-flow. As it becomes larger relative anisotropy within the heat-carrying population increases, which leads to a departure from a Maxwellian f_0. It is best suited to cases in which transport is local, as it is strictly valid for $f_0 = f_m$, so when analysing kinetic simulation where f_0 is known the ratio

$$\frac{\mathbf{q}}{q_{max}} = \frac{\int_0^\infty \mathbf{f}_1 v^5 dv}{\int_0^\infty f_0 v^5 dv} \tag{4.17}$$

can provide a superior metric as it accounts for the presence of an arbitrary distribution function.

For the case of the diffusive Braginskii heat-flow the implicit dependence on the effective mean-free-path is then highlighted by noting the variation between the weakly and strongly magnetised regime

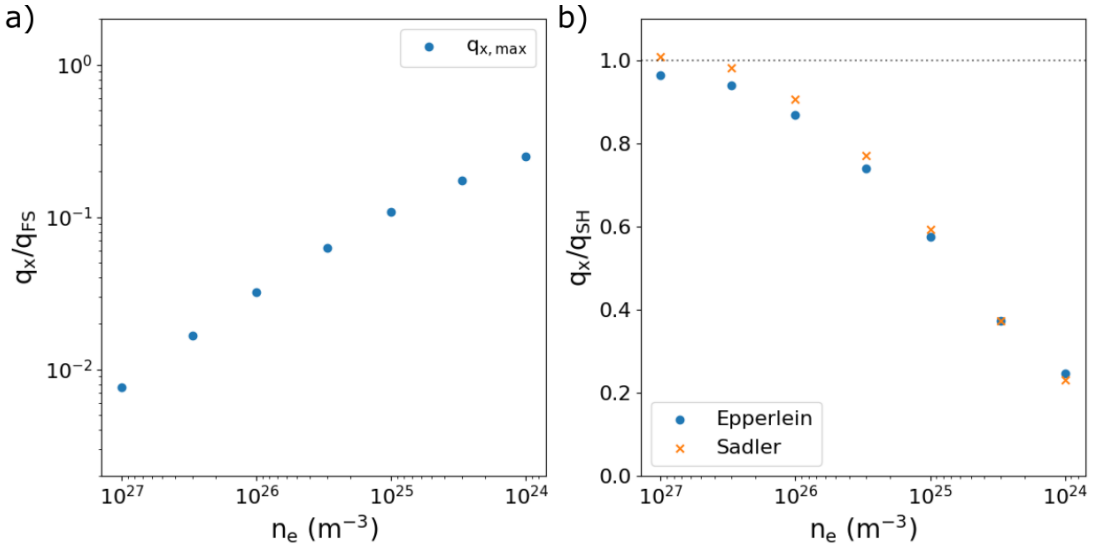

Figure 4.10: Heat-flow results for the simulations shown in fig. 4.5 at $t = 500$ ps where $B_z = 3$ mT and n_e is varied in the weakly magnetised regime. Plots show a) q_x/q_{FS} and b) the fraction q_x/q_{SH} at the position where q_x is at a maximum. Here q_{SH} is calculated using the transport coefficient fittings of both Epperlein and Sadler.

$$\frac{|\mathbf{q}_\perp(\chi_T \ll 1)|}{q_{FS}} \propto \frac{\lambda_T}{l_T} \quad \text{and} \quad \frac{|\mathbf{q}_\perp(\chi_T \gg 1)|}{q_{FS}} \propto \frac{r_g}{\chi_T l_T}. \tag{4.18}$$

The constant of proportionality then describes how the relative anisotropy varies across the electron distribution, weighted towards the higher velocity electrons. In the unmagnetised case this constant is $\kappa_\parallel/2$, while for magnetised plasmas it is slightly different from $\kappa_\perp/2$ as the transport coefficient includes the magnetisation dependence of the effective mean-free-path.

Returning to the simulations shown in section 4.2 trends in the heat-flow are now considered, starting with those shown in fig. 4.5 where the plasma is weakly magnetised. Comparing q_x with the free-streaming heat-flux in fig. 4.10a) it can be seen that as the density decreases the ratio q_x/q_{FS} increases. This is to be expected as $q_{FS} \propto n_e$ while q_x is independent (neglecting the n_e dependence of $\ln \Lambda_{ei}$). As was examined previously q_x/q_{FS} reflects the relative anisotropy of the heat-carrying population (eq. 4.16), which should cause f_0 to deviate from a Maxwellian as it increases. This can be seen to be the case, with the trend in fig. 4.10a) closely reflecting that seen in fig. 4.5b).

If f_0 was Maxwellian then anisotropy would be maximised (i.e. $f_{1x}/f_0 = 1$) within the heat-carrying population $v = v_H$ when $q_x/q_{FS} = 0.066$. Again, this result reflects that found in fig. 4.5 where for the point of maximum heat-flow $f_{1x}/f_0 \approx 1$ for $v = v_H$ when $q_x/q_{FS} = 0.066$ in fig. 4.10a). While it was seen that the distribution

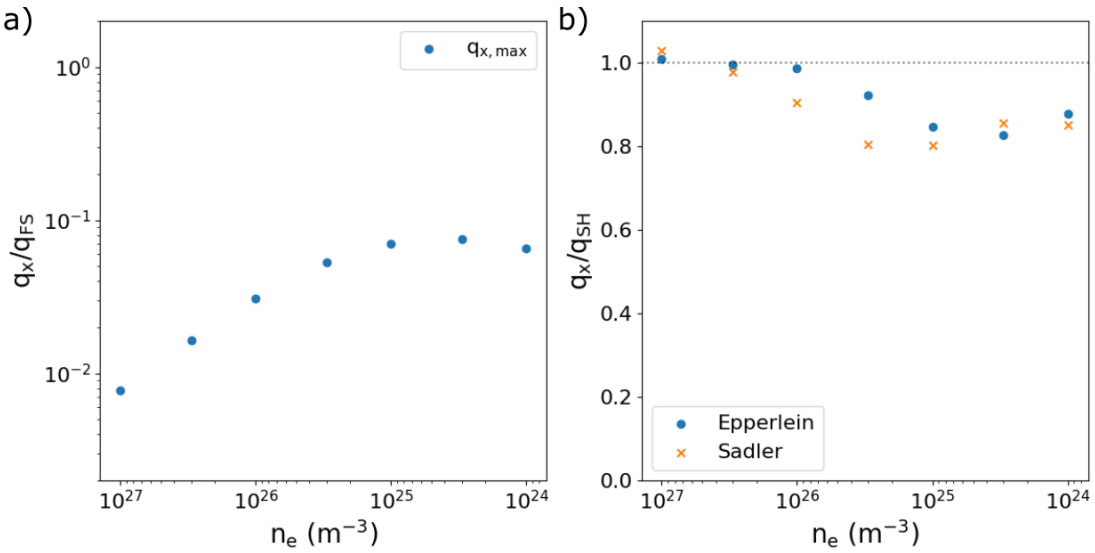

Figure 4.11: Heat-flow results for the simulations shown in fig. 4.7 at $t = 500$ ps where $B_z = 0.3$ T and n_e is varied to transition the plasma from the weakly magnetised to strongly magnetised regime. The plots shown are the same as in fig. 4.10.

function continues to become more non-Maxwellian after the point where $f_{1x}/f_0 = 1$ for electrons with $v = v_H$ in fig. 4.5, this was not reflected in the kinetic value of f_{1x}/f_0 as the whole distribution must be considered rather than just a single velocity group. For this reason, eq. 4.17 may provide a more useful measure when assessing the relative anisotropy in kinetic simulations. While eq. 4.16 can also be used the assumptions which it is based upon are no longer valid, as for the most non-local simulations q_x can be found to exceed q_{FS} as the distribution function is non-Maxwellian.

The non-Maxwellian distribution is reflected in the heat-flow, as demonstrated in fig. 4.10b) when comparing q_x to q_{SH}. Where q_x is at a maximum increasing non-local transport causes a greater reduction in the conductivity compared to the Spitzer prediction, due to the loss of free-streaming suprathermal electrons resulting in a super-Gaussian distribution. As q_x/q_{SH} increases and the relative anisotropy increases, the reduction in q_x increases. These electrons then cause an increase in q_x compared to q_{SH} at the base of the heat-front, where the distribution becomes bi-Maxwellian, which again increases as transport becomes more non-local.

For the simulations in fig. 4.7 where varying n_e transitions the plasma into the strongly magnetised regime it can be seen in fig. 4.11 that the behaviour of q_x/q_{FS} is reflected in q_x/q_{SH}. As q_x/q_{FS} increases the reduction in q_x/q_{SH} increases. Here a maximum is seen in q_x/q_{SH} at $n_e \approx 3 \times 10^{25}$ m^{-3}, following the trend in f_{1x}/f_0 seen earlier that decreasing the collision frequency leads to magnetisation of the plasma and reduced relative anisotropy. At the maximum the reduction in the heat-flow

is most significant with the magnetisation of the heat-carrying electrons $\chi_H \approx 3$ at this point. There are several subtleties associated with both plots that must be considered if they are to be used to assess non-local transport.

Whether this maximum more accurately reflects where transport is most non-local compared to fig. 4.7 is unclear, with the location of maximum differing between these two approaches. Comparing fig. 4.11 with fig. 4.7b), where the variation in the distribution function was calculated, the discrepancy appears to be associated with several effects.

Considering the flaws in the approach taken in fig. 4.7, the most obvious relate to the choice of velocity when performing the comparison. Firstly, as non-local transport increases the heat-carrying velocity decreases. This causes the density at which $\chi_{ei} = 1$ for the heat-carrying electrons to decrease, and the assumption that those with $v = v_H$ contribute most significantly is less accurate. However, this would result in a shift of less than an order of magnitude. Secondly, in fig. 4.7b) a band of electrons was considered with all velocities having a similar weighting (they are not the exact same as the velocity grid follows a geometric sequence, with slightly greater resolution at lower velocity). As heat-flow is due to the 3rd velocity moment of the distribution function, it is likely that deviations in the higher velocity population are more significant.

A fundamental issue that then affects both figures relates to the calculation of the transport coefficients. For the transport coefficients of Epperlein and Haines used here the maximum error is reported as $< 15\%$ [46], while Sadler reported a maximum error of $< 9\%$ [48]. Swapping between the two sets of transport coefficients the latter are found to better match the expected trend. Given that the transport coefficients are taken in the Lorentz limit here a solution may be to calculate the analytic values as demonstrated by Epperlein [45], bypassing the requirement for an accurate fitting.

While fig. 4.11a) does not require transport coefficients to estimate non-local trends, relying solely on the ratio q_x/q_{FS} which can be calculated using the kinetic approach of eq. 4.17, its interpretation is also not simple. As has been shown magnetic fields not only fundamentally reduce anisotropy for the entire distribution, but also preferentially reduce the mobility of heat-carrying electrons. The result is a decrease in the heat-carrying velocity, meaning λ_T/l_T must be larger for similar degrees of non-locality to be achieved. In fig. 4.12 this is demonstrated by considering the ratio of q_{SH}/q_{FS} required for $f_{1x}/f_m = 1$ in the heat-carrying population; the result is that larger values of q_{SH}/q_{FS} can occur before non-local transport is significant. Similarly, the Z dependence that arises in the transport coefficients means

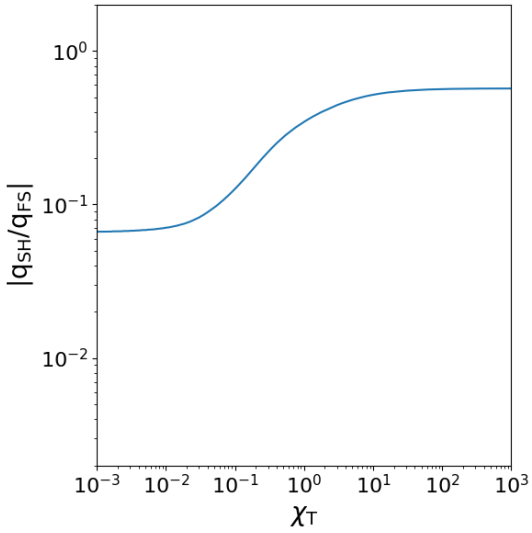

Figure 4.12: The ratio of q_{SH}/q_{FS} after which $f_{1x,H}/f_0 > 1$ as a function of χ_T for a Lorentz plasma. The asymptotic limits are $|q_{SH}/q_{FS}| = 0.066$ and 0.57 at $\chi_T \to 0$ and ∞ respectively.

that lower Z plasmas can sustain high degrees of anisotropy before non-local transport becomes significant. This latter point was highlighted previously by Brodrick et al. [39], who noted the material dependence of the flux-limiter when comparing trends between helium and zirconium plasmas. Less restrictive flux limiters are then required in these plasmas to match kinetic results.

Together, these points along with the data shown in fig. 4.10a) and fig. 4.11a), where q_x/q_{FS} can be seen to vary depending on the relative anisotropy, highlight some of the weaknesses of flux limiters. Consideration must be given to the relative anisotropy, magnetisation, and material when deciding appropriate flux limiters.

4.3.2 Ohm's law and the induction equation

In a similar manner to which heat-flow has been linked to the relative anisotropy, relationships with Ohm's law and the induction equation are now sought. By expressing the $\mathbf{f}_1$ equation (eq. 2.59) without electron inertia in terms of the electric field term

$$\mathbf{a} = -\frac{v\nabla f_0 + \nu_{ei}\mathbf{f}_1 + \boldsymbol{\omega} \times \mathbf{f}_1}{\partial_v f_0} \tag{4.19}$$

the connection between anisotropy and the electric field is highlighted.

Substituting this into Faraday's equation

$$\frac{\partial \mathbf{B}}{\partial t} = -\frac{m_e}{e}\nabla \times \frac{v\nabla f_0 + \nu_{ei}\mathbf{f}_1 + \boldsymbol{\omega} \times \mathbf{f}_1}{\partial_v f_0} \tag{4.20}$$

which can be expanded using the notation $\phi_v = (\partial_v f_0)^{-1}$ to give

$$\begin{aligned}\frac{\partial \mathbf{B}}{\partial t} = -\frac{m_e}{e}[&\nabla\phi_v \times (v\nabla f_0 + \nu_{ei}\mathbf{f}_1 + \boldsymbol{\omega} \times \mathbf{f}_1) \\ &+ \phi_v \nabla \times (v\nabla f_0 + \nu_{ei}\mathbf{f}_1 + \boldsymbol{\omega} \times \mathbf{f}_1)]\end{aligned} \tag{4.21}$$

where $\nabla \times (v\nabla f_0) = 0$. Fully expanded the induction equation then reads

$$\begin{aligned}\frac{\partial \mathbf{B}}{\partial t} = -\frac{m_e}{e}[&v\nabla\phi_v \times \nabla f_0 + \nu_{ei}\nabla\phi_v \times \mathbf{f}_1 + \phi_v\nabla\nu_{ei} \times \mathbf{f}_1 + \phi_v\nu_{ei}\nabla \times \mathbf{f}_1 \\ &+ \nabla\phi_v \times (\boldsymbol{\omega} \times \mathbf{f}_1) + \phi_v\nabla \times (\boldsymbol{\omega} \times \mathbf{f}_1)].\end{aligned} \tag{4.22}$$

The first term in this expansion is the non-local Biermann battery term, capable of the generation of magnetic field even when $\nabla n_e = 0$ due to misaligned gradients within the distribution function such that $\nabla(\partial_v f_0) \times \nabla f_0 \neq 0$ [60]. This can be confirmed after making the substitution $f_0 = f_m$. The following three terms involving ν_{ei} have the appearance of source terms in collisional plasmas, while the fifth term requires a magnetic field to already be present in the plasma.

The final term is an advection equation

$$\left[\frac{\partial \mathbf{B}}{\partial t}\right]_{\text{adv.}} = \frac{1}{\partial_v f_0}\nabla \times (\mathbf{f}_1 \times \mathbf{B}) \tag{4.23}$$

describing the transport of magnetic field due to anisotropy within the electron distribution function. This provides the fundamental link between anisotropic transport processes and the advection of magnetic field. On taking the nth velocity moment of this equation for $n > 0$

$$\left[\frac{\partial \mathbf{B}}{\partial t}\right]_{\text{adv.}} = -\frac{3}{n+2}\frac{\nabla \times (n_e\langle \mathbf{v}^n \rangle \times \mathbf{B})}{n_e\langle v^{n-1}\rangle} \tag{4.24}$$

where $\langle \mathbf{v}^n \rangle = (4\pi/3n_e)\int v^n \mathbf{f}_1 v^2 dv$ and $\langle v^n \rangle = (4\pi/n_e)\int v^n f_0 v^2 dv$. The 3rd velocity moment of $\mathbf{f}_1$ gives the heat-flow $\mathbf{q}$ such that

$$\left[\frac{\partial \mathbf{B}}{\partial t}\right]_{\text{adv.}} = -\frac{2}{5}\frac{\nabla \times (\mathbf{q} \times \mathbf{B})}{P_e} \tag{4.25}$$

is the Nernst effect, leading to the advection of magnetic field with heat-flow where the advection velocity is $\mathbf{q}/(5/2)P_e$. This motivates the flux-limitation of both the heat-flow and Nernst velocity in hydrodynamic simulations [98]. Similarly, taking the 1st velocity moment the magnetic field can be seen to be advected with the current which is the Hall effect.

As no assumption on the form of either f_0 or $\mathbf{f}_1$ is required, this expression is general for both local and non-local transport. While the relationship between heat-flow and the Nernst effect has been demonstrated previously using Ohm's law, use of the induction equation in combination with $\mathbf{f}_1$ makes the broader picture in which the transport is due to anisotropy clear. The general advection velocity for the magnetic field is then $\langle \mathbf{v}^n \rangle / \langle v^{n-1} \rangle$, which is clearly related to the relative anisotropy. In the same way that the transport of heat was shown to be maximised earlier by increasing the relative anisotropy (eq. 4.17), so too is the transport of magnetic field maximised.

4.4 Impact of electron inertia

The inclusion of electron inertia in the preceding analysis was important as otherwise eqs. 3.9 become exact in their description of electron transport within an ideal Lorentz plasma, despite missing a key piece of physics that is important in the non-local regime. Decreasing the collision frequency without electron inertia will then always lead to more local transport in the strongly magnetised regime, even on timescales that are short compared to both the collision rate and gyro-frequency. As will be seen shortly non-local transport can be significant on these timescales whenever λ_H and $r_{g,H} > l_T$. If the condition $r_{g,H}/\chi_H$ is met then this non-local transport can be transient, with the net effect similar to that expected by a fluid code as the hot electrons diffuse slower than the cold electrons.

As eqs. 3.9 describe the anisotropy that is to be expected when $\partial_t \mathbf{f}_1 = 0$, they can be used to assess how electron inertia has impacted the distribution function. By solving them to find $\mathbf{f}_1$ using f_0, $\mathbf{B}$, and $\mathbf{E}$ obtained from kinetic simulations including electron inertia, any discrepancies that then arise when compared to the simulated $\mathbf{f}_1$ are attributed to $\partial_t \mathbf{f}_1$. Similarly, the deviation from a Maxwellian could be assessed in this way by setting $f_0 = f_m$, provided $\partial_t \mathbf{f}_1 = 0$, without the need for transport coefficients.

In fig. 4.13 the heat-flow along the x-axis from a temperature ramp relaxation including $\partial_t \mathbf{f}_1$ is compared to the Braginskii heat-flow, as well as the heat-flow found after calculating $\mathbf{f}_1$ using eq. 3.9. Transport is non-local as can by seen by comparison

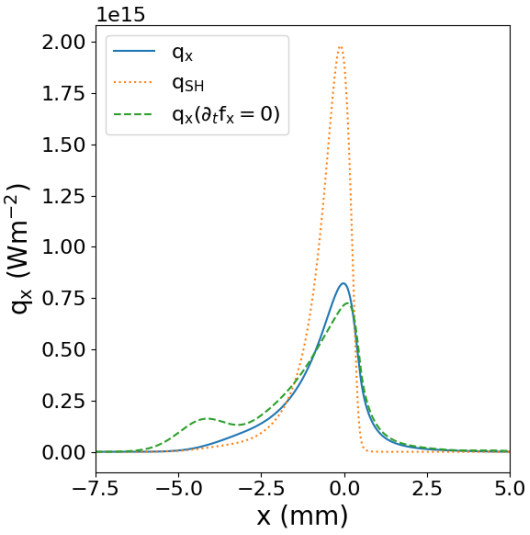

Figure 4.13: Heat-flow profiles from a temperature ramp relaxation at $t = 500$ ps where $n_e = 10^{25}$ m^{-3} and $B_z = 3$ mT. The kinetic result q_x is compared to q_{SH} and $q_x(\partial_x f_x = 0)$, the quasi-static result expected when calculating f_x using eq. 3.9a).

with the Braginskii prediction, with a reduction in the maximum heat-flow and pre-heating of the cold plasma. The expected heat-flow without inertia ($q_x(\partial_t f_x = 0)$) then appears enhanced in the hot plasma, but reduced where the heat-flow is at a maximum. This is a result of anisotropy introduced into the distribution function velocity space by inertia, which does not appear when only the magnitude of each velocity band is considered.

Based on the space and velocity gradients that appear at these positions in space, the heat-flow differs from what is expected; remember that while the kinetic value of **E** and **B** are used, only the properties of f_0 are known about the distribution function. As f_0 is isotropic in velocity space, it assumes that the electron velocity is distributed equally between all axes. However, along the x-axis where gradients in the distribution function are found hot particles, which are collisionless on this timescale, can propagate freely. In the hot plasma there is then a shortage of electrons travelling along x compared to the other axis, resulting in lower heat-flow than expected by f_0. At the heat-front there is then an excess of electrons, causing an increase in the heat-flow. The transport of relatively collisionless particles in this manner is central to non-local transport. Two distinct regimes can be identified depending on the importance of inertia; these will be referred to as the weakly and strongly non-local regime.

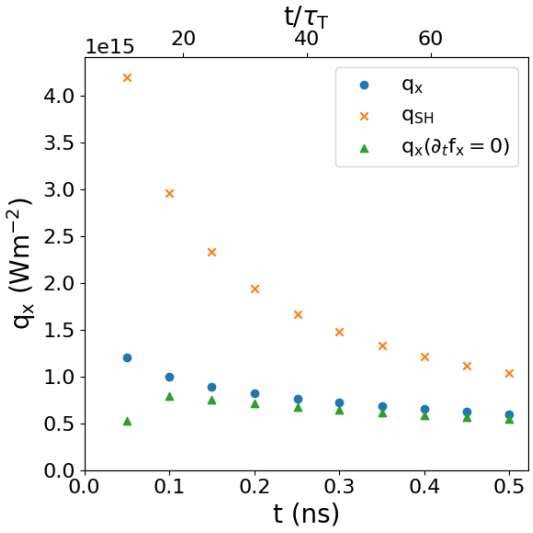

Figure 4.14: Temporal evolution of the maximum heat-flow for a temperature ramp relaxation where $n_e = 10^{25}$ m^{-3} and $B_z = 3$ mT, compared to q_{SH} and $q_x(\partial_t f_x = 0)$ calculated at the same position. On the upper axis the time is shown normalised by τ_T for electrons in the hot bath where $T_{\text{hot}} = 500$ eV.

4.4.1 Emergence of non-local inertial effects

In the weakly non-local regime the collision time is such that while the distribution function is perturbed it remains effectively isotropic in velocity space as the timescale of interest, which can be approximated as $t_c = l_T/v$, is greater than τ_{ei} which restores isotropy. Note that the ratio $\tau_{ei}/t_c = \lambda_{ei}/l_T$, so increasing the collision time relative to t_c is equivalent to increasing the relative anisotropy by making λ_{ei} larger relative to l_T. The distribution function then returns to a Maxwellian due to energy exchange between electrons, which occurs with frequency ν_{ee}^E. The ratio between these two processes can be expressed using eq. 2.38 and eq. 2.39 as

$$\frac{\nu_{ei}}{\nu_{ee}^E} = \frac{Z}{4\psi(V)} \tag{4.26}$$

where if $v \gg v_T$ then $\psi(V) \propto V^{-1}$. The timescale for energy exchange is then much longer than the collision time for suprathermal electrons, with the ordering in the weakly non-local regime $\tau_{ee}^E > t_c > \tau_{ei}$.

However, in the strongly non-local regime isotropy is no longer restored over the timescale of interest, with the ordering $\tau_{ee}^E > \tau_{ei} > t_c$ now applying. This implies that $\lambda_{ei} > l_T$. Electron inertia then plays a significant role in electron transport. These regimes have previously been observed by Brantov et al. [99] following the linear non-local theory, who similarly noted the condition $\lambda_{ei} > l_T$ led to non-stationary effects when considering the relaxation of a temperature perturbation.

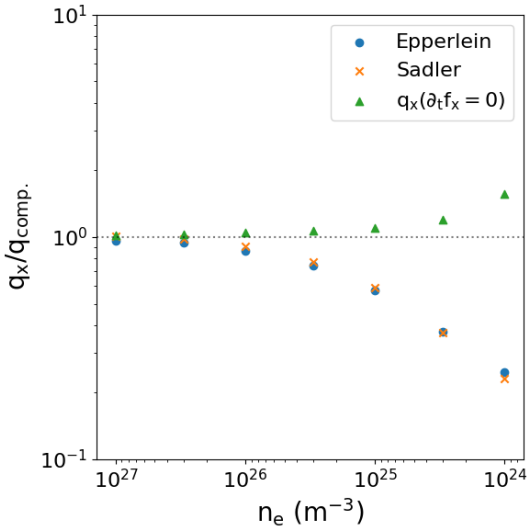

Figure 4.15: Heat-flow results for simulations at $t = 500$ ps where $B_z = 3$ mT and n_e is varied in the weakly magnetised regime. Here the maximum heat-flow is compared to q_{SH} and $q_x(\partial_t f_x = 0)$

.

Following this work Brodrick et at. [100] came to a similar conclusion following a more general approach using the Chapman-Enskog expansion, in the limit that the length scale is of the order of $100\lambda_T$ for unmagnetised plasmas [100].

The differing timescales over which anisotropy and non-Maxwellian distribution function characteristics decay can be observed in fig. 4.14. Initially there is a difference between the heat-flow and $q_x(\partial_t f_x = 0)$, suggesting inertia is important. After a period of $\sim 17.7\tau_T$ the two results begin to converge, which is equivalent to 0.98 τ_H for the electrons in the hot plasma supporting the earlier statement that it takes of the order of τ_{ei} for inertial effects to decay. This initial period of transient inertia can be attributed to the setup of the temperature ramp relaxation, as initially $f_0 = f_m$ and $\partial_t f_x = 0$. In real laser-heating problems one would expect that the initial effects of inertia are not as significant. Over a much longer timescale q_x and the Braginskii result can be seen to converge as energy exchange occurs within the distribution.

In fig. 4.15 the transition between the near local, weakly non-local, and strongly non-local regimes is explored. Initially there is good agreement between q_x, q_{SH} and $q_x(\partial_t f_x = 0)$ with $\lambda_H/l_T \approx 0.03$ for the simulation where $n_e = 10^{27}$ m^{-3}. On decreasing the density the weakly non-local regime is entered, with discrepancies then arising between q_x and q_{SH}. Finally, when $n_e = 10^{25}$ m^{-3} the q_x and $q_x(\partial_t f_x = 0)$ results begin to deviate, with $\lambda_H/l_T \approx 1$.

Investigating electron inertia in this manner highlights the consequences of studying transport problems using a temperature ramp relaxation. Utilising a tempera-

ture ramp relaxation makes no difference for plasmas near LTE, as electron inertia has no significant impact with both τ_{ei} and τ_{ee}^{E} less than t_c, but this is not true further from LTE when $f_{1x}/f_0 \approx 1$ for $v = v_H$ electrons. In problems further from LTE inertial effects are initially maximised.

Laser-heating issues were investigated, as they may reduce electron inertia compared to temperature ramp relaxations, given that the system is not initially perturbed as dramatically. In these simulations, the laser heating rate was kept constant by varying both the intensity and electron density ($\partial_{t,IB} T_e \propto I_l/n_e$), allowing a series of problems with similar temperature profiles to be examined. This also allows the distribution function to be more representative of what is encountered experimentally. However, the nature of inverse bremsstrahlung heating means that for lower densities, and corresponding higher intensities, the plasma is driven towards a Langdon distribution [70]. This then masks whether transport trends are due to non-local transport or the heating mechanism [47], so a Maxwellian heating operator could be beneficial in future to separate effects. As a result, it was not clear if these initial simulations resulted in a reduction in electron inertia.

4.4.2 Electron inertia in magnetised plasmas

Earlier it was seen in eq. 3.6 that the condition required to neglect electron inertia for perpendicular transport is given by

$$|\mathbf{f}_{1\perp}| \gg \frac{|\partial_t \mathbf{f}_\perp - \chi_{ei}\mathbf{b} \times \partial_t \mathbf{f}_{1\perp}|}{\nu_{ei}(1+\chi_{ei}^2)}. \tag{4.27}$$

In the weakly magnetised regime this can be stated as

$$\nu_{ei} \gg \frac{|\partial_t \mathbf{f}_{1\perp}|}{|\mathbf{f}_{1\perp}|} \tag{4.28}$$

so the frequency with which the anisotropy changes must be small relative to ν_{ei}, which is equivalent to the timescale with which the anisotropy evolves being long relative to τ_{ei}.

Rearranging eq. 3.6 the frequency with which the anisotropy evolves is

$$\frac{|\partial_t \mathbf{f}_{1\perp}|}{|\mathbf{f}_{1\perp}|} = \frac{|v\nabla_\perp f_0 + \mathbf{a}_\perp \partial_v f_0 + \omega \times \mathbf{f}_{1\perp} + \nu_{ei}\mathbf{f}_{1\perp}|}{|\mathbf{f}_{1\perp}|}. \tag{4.29}$$

When an initially homogeneous plasma is perturbed the anisotropy is small, so the dominant term in this expression is $v\nabla_\perp f_0$. This justifies the use of t_c as the

timescale of interest as then

$$\frac{|\partial_t \mathbf{f}_{1\perp}|}{|\mathbf{f}_{1\perp}|} \approx \frac{v}{|\mathbf{l}_{f,\perp}|}\frac{f_0}{|\mathbf{f}_{1\perp}|} = \mathbf{t}_c^{-1}\frac{f_0}{|\mathbf{f}_{1\perp}|}. \tag{4.30}$$

Making the crude assumption that the distribution length scale remains constant, and that the contributions of the electric and magnetic fields are not significant, then for a collisionless plasma maximum anisotropy would be reached over a timescale equal to t_c. Considering a similarly ideal case, in the absence of gradients in the distribution then anisotropy would decay exponentially over a timescale given by τ_{ei}.

Combining these effects in a collisional plasma the distribution function will initially reach a quasi-static state once $v\nabla_\perp f_0 \approx -\nu_{ei}\mathbf{f}_{1\perp}$, at which point $\mathbf{f}_{1\perp}/f_0 = \lambda_{ei}/\mathbf{l}_{f,\perp}$ and heat-flow reaches a maximum. In the local limit this occurs at $t \approx \tau_{ei}$, as f_0 is not significantly perturbed. If transport is non-local then f_0 does not remain near Maxwellian and the time to reach a quasi-static state approaches t_c. Inertial effects are seeded when large gradients in f_0 arise and then decay over τ_{ei}.

While it is easier to see the connection with temperature ramp relaxations as the gradients in f_0 vary less with time, similar reasoning can be applied to laser heating problems. As the rate of inverse bremsstrahlung heating is greatest when the plasma is cold for fixed laser intensity and decreases rapidly with temperature, the most significant changes in f_0 typically occur initially over a short time period. During this period, inertia is then most significant.

Fig. 4.16 demonstrates how inertia is impacted as the collision rate decreases with n_e. As ν_{ei} approaches $|\partial_t \mathbf{f}_{1\perp}|/|\mathbf{f}_{1\perp}|$ inertia causes a greater increase in the heat-flow where it is at a maximum. As expected this, effect is greatest initially with the initial transient period decaying on the order of ν_H, although this trend is not seen for the higher density simulations as this occurs before the first output time-step. This point could be judged as being where $q_x(\partial_t f_x = 0)$ reaches its initial maximum in the weakly magnetised case. During the earlier time-steps q_x would also have been seen to reach an initial maximum, which as discussed varies on a timescale from ν_{ei} to t_c as transport becomes more non-local. There is then a prolonged period in all simulations where inertia continues to impact the heat-flow, although this lessens as ν_{ei} increases.

In the strongly magnetised regime the quasi-static condition is modified

$$\omega_g \chi_{ei} \gg \frac{\partial_t \mathbf{f}_\perp - \chi_{ei}\mathbf{b}\times\partial_t \mathbf{f}_{1\perp}}{\mathbf{f}_{1\perp}} \tag{4.31}$$

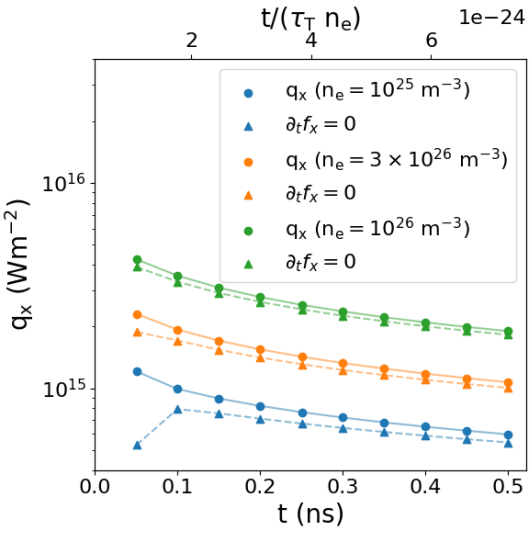

Figure 4.16: Temporal evolution of the maximum heat-flow compared to $q_x(\partial_t f_x = 0)$, obtained from a series of nitrogen temperature ramp relaxations where $B_z = 3$ mT and n_e is varied. The upper axis shows the time normalised by the product of τ_T for the hot bath electrons with n_e.

such that instead of the collision frequency the rate of change of the anisotropy must be less than the gyro-frequency. This trend was demonstrated in fig. 4.4 where increasing the magnetic field strength led to a reduction in the inertia, and a decrease in the time required to reach a quasi-steady state for fixed collision frequency.

Both eq. 4.28 and this expression have a very similar form to eq. 3.5 and eq. 3.6, which had to satisfy the condition $\lambda_{f_1} \ll l_{f_1}$ for transport to be local in the absence of inertia for parallel and perpendicular transport respectively. In those expressions the effective mean free path was given by $\lambda_{ei} = v/\nu_{ei}$ when weakly magnetised but $r_g/\chi_{ei} = v/\omega_g\chi_{ei}$ when strongly magnetised, differing by a factor of χei^2 as these expressions do.

Eq. 4.31 is complicated by the contributions from the other axis in the plane perpendicular to the magnetic field. While previously it was possible to avoid this issue by considering 1D problems, here this assumption provides no assistance as rotation by the magnetic field will result in anisotropy along both perpendicular axes. It is worth noting that in the absence of collisions eq. 3.6 describes particle orbits due to the magnetic field. Coupling this with the arguments made earlier that the particle diffusion rate across a magnetic field increases with collision frequency, making hotter particles less mobile than colder ones, the idea of a transient non-local regime is now briefly discussed.

Occurring when the plasma is strongly magnetised, this regime is described as transient as while instantaneously non-local transport is significant, the overall be-

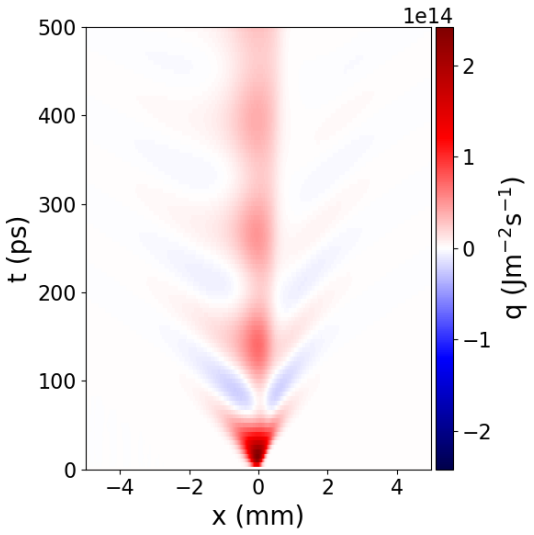

Figure 4.17: Temporal and spatial evolution of the heat-flow obtained from a nitrogen temperature ramp relaxation where $B_z = 0.3$ T and $n_e = 10^{24}$ m^{-3}.

haviour remains similar to and soon converges with the fluid approximation after $t \approx \tau_H$. This is despite both r_g and ω_g exceeding the length and timescale of interest. The condition required to enter this regime, which broadens the parameter space in which the fluid approximation is valid, is that when divided by χ_{ei} these parameters are less than the length and timescale of interest. Thus, it is the result of being confined to multiple orbits that leads to this effect.

Evidence for this regime has already been seen, notably in fig. 4.7 when the relative anisotropy was seen to decrease as n_e decreased with $r_{g,H} \approx l_T$. The distribution function was then found to become increasingly Maxwellian. Observing the structure of the heat-flow profile from this simulation in fig. 4.17 significant oscillations are observed that would not be expected following the fluid approximation. Initially, there is strong heat-flow down the temperature gradient, with significant preheating of the cold plasma. The heat-flow then reduces, before reversing back up the temperature gradient. The frequency of these oscillations is below $\omega_g = 19.0$ ps, while their radius is slightly larger than $\omega_{g,T} = 251$ µm. After $t \approx \tau_H$ these oscillations have decayed, with transport as expected from the fluid approximation.

However, significant variations in the effective mean-free-path of the electron over the course of its orbit, such as due to variations in density or magnetic field, will result in this non-local transport no longer being transient. Questions then remain regarding the accuracy of the diffusion approximation in this regime, as terms of higher order than $\mathbf{f}_1$ may be important initially when the anisotropy is significant.

4.5 Summary

In this chapter the effect of anisotropic transport on the electron distribution function has been explored, with an increase in relative anisotropy shown to distort the isotropic distribution away from a Maxwellian using VFP simulations. To understand trends in the relative anisotropy the effective mean-free-path ($\lambda_{ei}/(1+\chi_{ei}^2)$) can be considered, and is used here to explore the effects of magnetisation. The magnetisation ($\chi_{ei} = \omega_g/\nu_{ei}$) can be controlled by varying either the magnetic field strength ($\omega_g \propto B_z$) or the electron density ($\nu_{ei} \propto n_e$). The former effect is known to suppress non-local transport when the magnetic field strength is increased by restricting particles to their gyro-orbits. Here it is shown that decreasing the electron density can also localise transport.

The effects of varying these parameters are dependent on the magnetisation regime of the electrons. For weakly magnetised plasmas ($r_g \gg \lambda_{ei}$) the magnetic field and the transport is unaffected by the magnetic field. Decreasing the electron density increases relative anisotropy as the mean-free-path increases, provided the electron is not limited by the gyro-radius. When strongly magnetised ($r_g \ll \lambda_{ei}$) the magnetic field restricts transport. Increasing the magnetic field suppresses non-local transport due to a reduction in the gyro-radius. However, the gyro-radius is independent of the electron density, so is not obvious that this should localise transport. Instead, decreasing the electron density further magnetises the electrons, preventing them from escaping their orbits without collisions. As the magnetisation increases as $\chi_{ei} \propto V^3$, hotter electrons are then less mobile. In this regime, it is suggested that the effective mean-free-path is used instead of λ_{ei} or r_g when calculating the non-locality parameter. Furthermore, it is the velocity of the heat-carrying electrons that should be considered as they are more rapidly magnetised.

Connecting the relative anisotropy to the heat-flow it is seen that the ratio $\mathbf{q}/q_{FS}$ is, in essence, a measure of the anisotropy of the distribution, weighted towards the heat-carrying electrons. As the transport coefficients implicitly include the effective mean-free-path, the ratio of the Braginskii heat-flow to the free-streaming limit is an effective non-locality parameter. Some care must be given to its use as the free-streaming limit is also found to be magnetisation dependent. It was then shown that the fundamental link between the magnetic transport dynamics and heat-flow is provided by the relative anisotropy of the distribution function.

The main limitation of this study was that the kinetic code used to investigate the temperature ramp relaxations only included terms up to $\mathbf{f}_1$ in the expansion. When the relative distribution function anisotropy was most pronounced, which occurred in simulations at low density ($\lambda_H > l_T$) and weak magnetic field ($r_{g,H} > l_T$), values

of $f_x/f_0 \approx 1$ were observed. Based on the ratio of successive terms in the expansion given by eq. 2.131, it was expected that $\mathbf{f}_2$ and higher-order terms would also be significant in this regime, making the truncation invalid and altering $\mathbf{f}_1$. However, this may not apply when B_z is small and the plasma is very weakly magnetised, as $\mathbf{f}_2$ is traceless and the system is 1D, so there is no anisotropic transport along other axis and thus $\mathbf{f}_2 \approx 0$. Once the magnetic field is strong enough to magnetise the electrons f_y becomes significant, and $\mathbf{f}_2$ may then modify $\mathbf{f}_1$.

Chapter 5

Proton radiography in laser-plasma experiments

This chapter reviews the use of proton radiography to diagnose the electric and magnetic fields in plasmas. Experimental measurements of plasma parameters, such as the electric and magnetic field, electron and ion density, ion charge, and electron and ion temperature, are crucial for validating theoretical models. In this thesis, this motivates the measurement of the Nernst effect, discussed in chapter 7, to validate the extended MHD model. In laser-plasmas, the fundamental link between the Nernst effect and heat-transport, explored in earlier chapters, makes it particularly valuable for enhancing our understanding of non-local transport effects.

To obtain a conclusive measurement of the Nernst effect proton radiography will be employed, a diagnostic technique often used in laser-plasma experiments to measure transient magnetic and electric field phenomena. This chapter provides a comprehensive review of how data is acquired and analysed using this technique, which was integral to the measurement process, facilitated by an inversion code developed by the author. To support this analysis, a synthetic proton radiography code was also written by the author, which employs the Boris pusher algorithm [101]. Interactions between particles are neglected owing to the quasi-neutral nature of the proton beam. The proton source can be configured with a specified spatial, angular, and energy distribution. To approximate the radiochromic film (RCF) response, the proton distribution is weighted according to the RCF response function.

Section 5.1 covers the characterisation of proton beams using RCF, converting raw proton radiographs into dose measurements. Section 5.2 then explains how the dose information is used to perform a deflection mapping from the object plane to the image plane, recovering the deflection profile caused by the electric and magnetic field structure. In chapter 7, differences in deflection profiles for cylindrically sym-

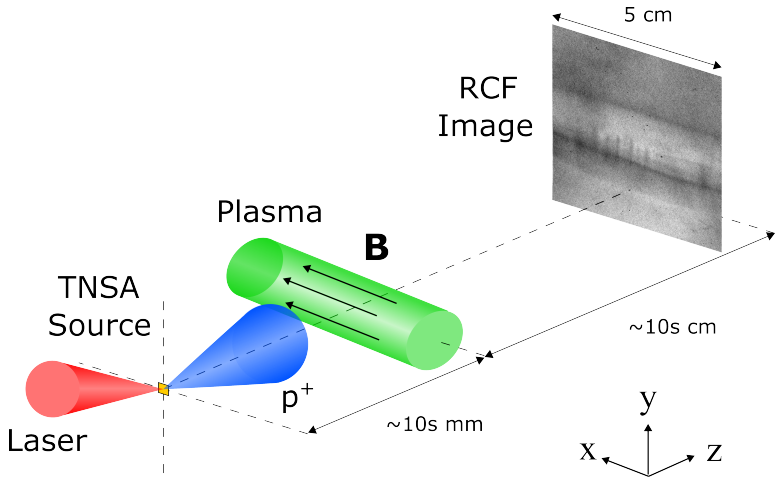

Figure 5.1: A schematic diagram of an experiment using proton radiography to study the magnetic fields in a plasma column. The proton beam, generated via target normal sheath acceleration from a short-pulse laser interacting with a gold foil, propagates through the plasma column. After being deflected by the fields in the plasma, the proton beam's intensity profile is measured on radiochromic film.

metric systems will be used to separate electric and magnetic field structures. The electric field will then be utilised to estimate the temperature profile using Ohm's law, when supported by density measurements. At the end of the chapter analytic calculations are presented to estimate the degree of smearing from a proton source, following the work by Arran *et al.* [102]

In proton radiograph, MeV protons are directed through a target plasma, where they are deflected by the Lorentz force [103]. Changes in the beam intensity profile are measured using a particle detector, typically RCF, as shown in fig. 5.1. This intensity profile is related to the deflection of the protons due to the path-integrated magnetic and electric fields in the plasma, as well as the target density [104]. For the technique to be successful, short pulse durations and a small virtual source size are required, with proton energies exceeding a few MeV. A 3D image of the target can then be constructed with micron-scale spatial resolution and picosecond temporal resolution. The most common proton source uses target normal sheath acceleration (TNSA) to generate a broadband proton beam [105]. The beam is quasi-neutral, co-propagating with an electron cloud. Alternatively, an exploding pusher implosion can be used to generate 14.7 MeV D^3He and 3 MeV DD fusion protons [106].

5.1 Characterisation of proton beams

The development of chirped pulse amplification (CPA) [107] allowed short pulse ($\leq$ ps) lasers to be amplified to terawatt powers, with the current next-generation of

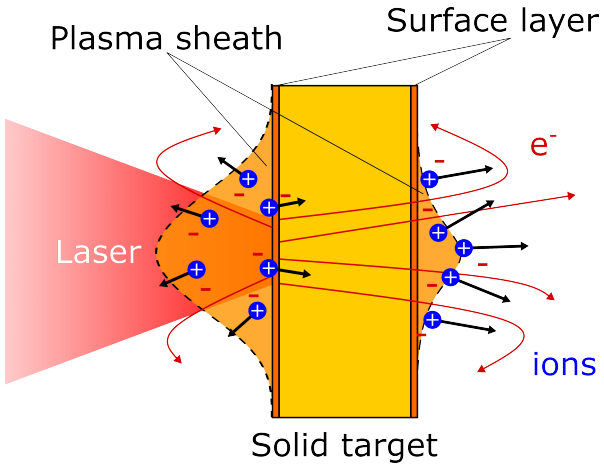

Figure 5.2: The target normal sheath acceleration mechanism during the interaction of an ultra-intense short pulse laser with a solid target. The laser pre-pulse generates a long-length scale plasma, which interacts with the main laser pulse leading to the generation of fast electrons. The highest energy electrons can travel through the target as their mean-free-path is greater than the target thickness, resulting in ionisation of the rear surface. The most energetic electrons can escape the target, which becomes charged, with the remainder refluxing into the expanding plasma sheath. The resulting charge separation of the ion and electron fronts results in a large electric field across a Debye sheath ($\sim$ 1µm).

laser facilities set to reach 10s of petawatts. Focussing these lasers produces ultra-intense ($I_0 \gtrsim 10^{19}$ Wcm^{-2}) pulses of light which can be used to explore novel physics regimes. When interacting with thin ($\sim$10 µm) solid targets numerous high energy particle species are emitted as well as intense electromagnetic radiation; this can include electrons, ions, x-rays and terahertz radiation [105].

Ions accelerated during short-pulse laser interactions are of particular interest as greater energies can be reached than using plasma wave based accelerators, which are limited by the higher mass of ions compared to electrons. One of the most studied mechanisms for ion acceleration is the sheath acceleration mechanism [108], where hot electrons that propagate through the target ionise the rear surface. Charge separation in the expanding plasma occurs across a Debye sheath, which is of the order of a few microns, resulting in a strong electric fields of the order of TV/m. A schematic of this process is shown in fig. 5.2. Hydrogen which contaminates the surface of a target, is preferentially accelerated instead of heavy ions due to their higher charge to mass ratio. The resulting ion energy spectrum spans a broad, multi-MeV range with proton energies up to 100 MeV [109]. Furthermore, while sheath acceleration also occurs on the front surface of the target, the longer length scale due to the extended pre-plasma on the front surface results in a smaller acceleration.

The proton beams generated via TNSA have several characteristics that make them suitable for use as a particle diagnostic; these include the small source size, high

flux, negligible space-charge effects, and short temporal duration. While the source diameter on the rear surface is many times larger than the laser spot (typically 10s to 100s of µm) the beam is divergent, appearing as if it was produced by a virtual source on the front side of the target with a diameter less than 10 µm. The divergence of the beam is approximately 10-30°, decreasing as the particle energy increases [110]. The small virtual source size is a result of the highly laminar nature with which ions are emitted from the target, caused by the neutralisation of space-charge effects by co-propagating electrons and allowing the proton trajectories to be treated realistically [111]. Furthermore, space-charge interactions between the beam and the plasma are also negligible due to the much lower density of the beam, which is of the order of $n_p \approx 10^18$ m^{-3}. If there were space-charge effects associated with the beam, these would be effectively screened by electrons in the target plasma. The lower density also means that the growth rate of the beam-plasma instability, which may excite turbulence in the target plasma, is much longer than the probe time.

As the duration of the ion source is of the order of the laser-pulse duration (a few ps), fast dynamic phenomena can be observed provided the structures can be regarded as quasi-static during the proton transit time. The broadband source can make analysis challenging, as the proton beam will spread out in time as it propagates into and across the target plasmas, with lower energy protons trailing high energy protons. This chirped beam may also experience time varying deflection by electric and magnetic fields. However, the use of spectrally resolved detectors can make these characteristics advantageous. Firstly, the time-of-flight (ToF) from source to target is shorter for higher energy protons, which can allow time evolution of the target to be observed. Secondly, as described by the Lorentz equation the deflection of protons due to a magnetic field varies as a function of $\mathbf{v}$, resulting in magnetic field deflections scaling with kinetic energy as $E_k^{-1/2}$ while for electric fields the scaling is $E_k^{-1/4}$ [112]. This allows the deflections to be characterised as either due to an electric or magnetic field, with the possibility of discriminating between the two.

However, significant shot-to-shot variability is often found in the characteristics of the proton source; variation can be found in properties such as the energy spectrum, position and size of the source, and angular profile. This is problematic for use as an imaging diagnostic, as variations in the source characteristics must then be separated from those caused by the target plasma. As there is no viable method to obtain the beam intensity profile pre- and post-target interaction, the unperturbed source profile must be reconstructed, which can result in large uncertainties during analysis as discussed in section 5.2. These variations may arise from fluctuations in the laser system, such as changes in the quality of the focal spot, or from the TNSA

foil. The sheath that forms on the rear surface of the foil is particularly sensitive to preplasma and x-ray cross talk [113]. As a result, it can be challenging to achieve the desired target magnification and probe timing due to the configuration required to mitigate these effects.

A final consideration relates to the generation of additional high energy species and intense electromagnetic pulses (EMP) during short-pulse laser interactions. In the case of the former, additional species must be accounted for when analysing data obtained from the chosen particle detector, which will be discussed in the following section. Meanwhile, EMP can severely degrade electrical measurements and equipment if not mitigated [114].

5.1.1 Radiochromic film detectors

The primary feature required of the particle detector is the ability to obtain high-resolution spatial measurements of the proton beam intensity profile. Additionally, knowledge of the observed proton energy is needed, and spectral resolution is desirable. Film detectors, such as RCF or image plate (IP), are the most commonly used passive diagnostics. These have the advantage of having high spatial resolution, as well as being resilient to EMP often generated in short-pulse laser interactions. These are single-shot diagnostics and with the advent of high repetition-rate, high-power facilities new techniques, such as scintillator based diagnostics, which can actively monitor shots with a much higher acquisition rate are essential [115]. In the experiments shown in chapters 5 and 7 the particle detector used was a stack of RCF.

When exposed to ionising radiation the active layer in RCF undergoes polymerisation, resulting in transition in colour from nearly transparent to blue [116]. While typically deployed in laser-plasma experiments to detect protons, this colour change can also be induced by heavier ions, electrons, and photons. The RCF types shown here were produced by GafChromic and are either HDV2 or EBT3, composite materials consisting of an active layer bound to a polyester substrate. The active layer in HDV2 is 12 µm thick on a 97 µm substrate, while for EBT3 the active layer is 28 µm and sandwiched between two layers of 125 µm thick substrate.

To take advantage of the broadband TNSA source the RCF films are stacked in order to leverage the physics of ion interactions and stopping with matter; a specific ion energy will primarily deposit its energy at a given depth according to its Bragg peak [110, 117]. As heavier ions have a much higher stopping power, they are typically stopped by the first layer. Meanwhile electrons and photons

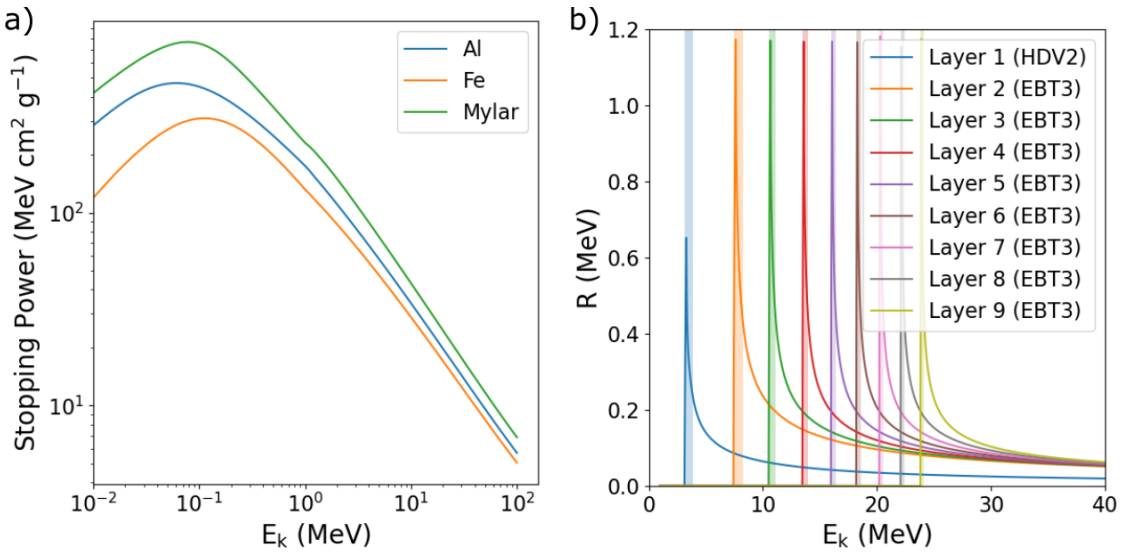

Figure 5.3: a) Proton stopping power as a function of energy for aluminium, iron, and mylar. b) Energy response curves for each active layer in an RCF stack, showing the energy lost in each layer by an incident proton as a function of initial kinetic energy. Energy bands show the regions corresponding to the $1/e$ values. Layer 1 corresponds to the first RCF layer in the stack, with layer 9 the last, and the RCF material has been noted. In this case stack design 'C' from the Vulcan-Nernst experiment investigating the Nernst effect is shown.

have a much lower stopping power, appearing as a much fainter and broader beam which must be background subtracted for quantitative information about the proton beam to be extracted. By placing filter materials between each layer of RCF, the stack can then be tailored such that each layer is only sensitive to a specific proton energy range. Once this proton energy is known, the spatially-resolved ion spectrum can be reconstructed. Furthermore, the time-of-flight from source to detector can be calculated, allowing the time at which the target was sampled to be obtained. Sampling can then be performed at specific energies corresponding to particular time windows at desired intervals.

Acquiring the energy response curves, $R(E)$, for each layer in the RCF stack requires stopping power curves for the different materials, which are obtained using the Stopping and Range of Ions in Matter (SRIM) software [118]. The results for typical aluminium, iron, and mylar filters are shown in fig. 5.3a). Here it can be seen that as the energy of an ion (in this case a proton) decreases the stopping power increases, leading to an exponential increase in the probability that an ion will be stopped at a given depth. While the stopping power of mylar is higher than that of aluminium or iron, the lower density of aluminium means that for a given thickness is has a smaller stopping power per unit length.

Energy response curves are then obtained by numerical integration along the

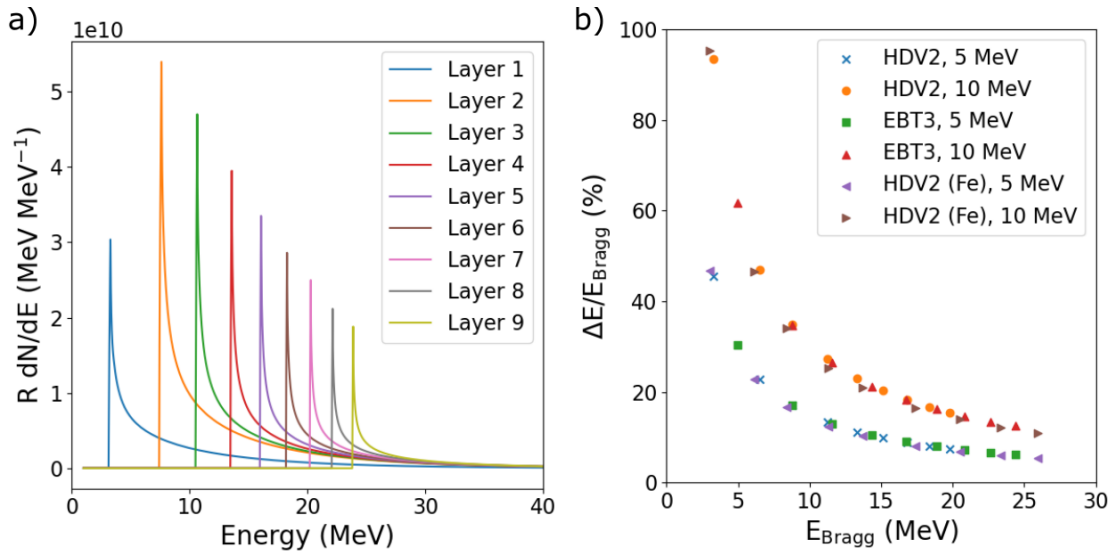

Figure 5.4: a) Energy deposition curves for stack design 'C' for a proton beam containing 10^{12} particles with $T = 10$ MeV. These are given by the product of the response curves, R, and the number of particles per energy band, dN/dE. b) The width of the band containing 50% of the energy relative to the Bragg peak energy, $\Delta E/E_{\text{Bragg}}$, where each point corresponds to an active layer in an RCF stack characterised by its Bragg peak energy. The series utilised mylar filters (as in stack design 'C'), or iron labelled (Fe). Temperatures of 5 and 10 MeV, and HDV2 and EBT3 are compared.

path of the proton over the energy range of interest. In fig. 5.3b) this is done for an RCF stack from the Vulcan-Nernst experiment, consisting of HDV2 and EBT3 separated by aluminium and mylar filters of varying thickness. The response curves show the amount of energy lost by protons in each layer of the stack as a function of their initial kinetic energy. For the first layer of HDV2 protons with an initial energy less than 3.28 MeV are stopped before they can penetrate this far into the stack. Protons whose Bragg peak lies within this layer lose ~ 0.65 MeV, corresponding to approximately 20% of their energy. As the initial energy increases further the amount of energy deposited decreases exponentially. Moving further into the stack the lower cutoff energy increases, and the maximum deposited energy in the active layer increases to ~ 1.15 MeV as the stack material changes from HDV2 to EBT3 due to the increased active layer thickness.

For a typical proton spectrum generated by TNSA, most of the energy deposited in a given layer is from protons whose stopping distance lies within the active layer of that piece of RCF, so the signal is dominated by these particles. However, there is also a contribution from higher energy protons that propagate through the layer without being stopped. This can be inferred from fig. 5.3b) as the maximum response in each layer remains the same despite the initial particle energy increasing, showing that this corresponds to a smaller fraction of the particle's total energy. The effect

is most significant at the front of the stack and can result in an over-estimate in the number of protons if not accounted for.

To further illustrate this behaviour the energy deposited in each active layer of an RCF stack by an energy band is shown in fig. 5.4a) for a Maxwellian spectrum. This is obtained via the product of $R(E)$ with the number of particles per energy band, dN/dE, where for a Maxwellian

$$\frac{dN}{dE} = \frac{4\pi V}{m}\sqrt{\frac{2E}{m}} f_0(E). \tag{5.1}$$

Obtaining the relative width of the energy band containing half of the deposited energy (fig. 5.4b) it can be seen that the energy spread is of the order of E_{Bragg} for the first layers in the stack. As the energy increases further into the stack the relative energy spread decreases as the contribution from higher energy protons lessens, with the effect more pronounced experimentally due to the high energy cutoff.

As the temperature of the spectrum is increased the energy spread increases as there are now more higher energy particles, with an increase from 5 to 10 MeV leading to an energy spread approximately twice as large in each layer. On swapping the RCF material and filters the energy spread curves have much the same form, suggesting that the shape of the distribution function for a layer with a given E_{Bragg} is largely independent of the composition of the preceding stack. This is due to the physics of proton scattering in solids as shown in the stopping power curves (fig. 5.3a), whose gradient is very similar for $E_{\text{k}} > 0.1$ MeV. Thus, for common filter materials the energy spread can be easily approximated when the spectrum is close to Maxwellian and T and E_{Bragg} are known.

5.1.2 Dosimetry of radiochromic film

The response of RCF to radiation dose is measured using a colour flatbed scanner, which returns a 16-bit pixel value (PV) for a given output channel (red, green, or blue) of the film. Several characteristics affect dose-response, so to improve measurement accuracy the aim is to keep as many factors constant between the calibration, measurement, and unexposed film datasets; these include film model and lot number, radiation particle type and energy, and the readout system and time [116]. The RCF used in this report, HDV2 and EBT3, are designed to deal with higher dose ($10 - 10^3$ Gy) and lower dose ($10^{-2} - 40$ Gy) respectively [119]. Thus, when constructing an RCF stack HDV2 is placed at the front of the stack, where the highest dose is expected, with EBT3 at the back to maximise the dynamic

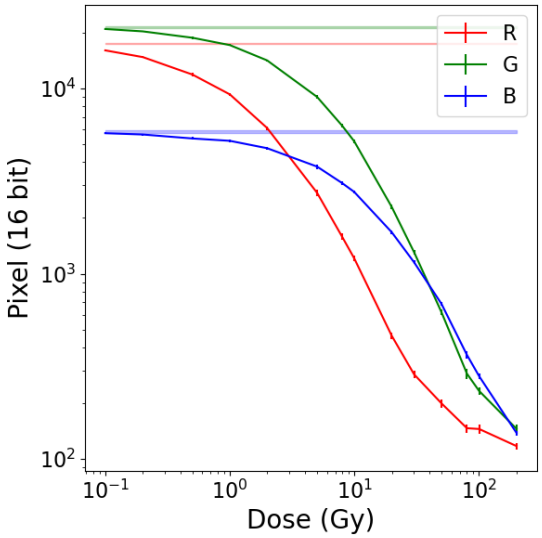

Figure 5.5: Dose-pixel response curves for the red (R), green (G) and blue (B) channels for EBT3 obtained using a Nikon CoolScan 9000 in 2014.

range of the stack.

To obtain dose-response curves RCF samples are irradiated with known proton doses and then scanned. In the calibration data sets this was done using a 36 MeV proton beam obtained from a synchrotron, where the beam current and duration were varied to deliver the required dose. The dose was measured using a Markus ionisation chamber, which works on the principle of Bragg-Gray cavity theory. The RCF was then scanned with either a Nikon CoolScan 9000 or an Epson 12000 XL.

In fig. 5.5 the dose-PV calibration curves obtained for EBT3 in 2014 are shown. Here it can be seen that as the dose increases the PV decreases, corresponding to a darkening of the film. This process is non-linear with three key stages; an initial plateau at low dose where the response of a given channel is indistinguishable from the unexposed result, a region where PV changes rapidly with dose, and plateau at high dose where the film saturates. Measurements are sought in the second of these regions, where the response of the film to a given dose is most noticeable. The red channel is typically most sensitive to lower doses, while the blue channel is more suited to higher dose measurements. These colour channels can be combined to improve the dynamic range for a single layer.

Updated calibration data sets were obtained in 2021 for modern batches of HDV2 and EBT3, as well as new scanners. To calculate the PV associated with a given dose a 2D super-Gaussian fitting was performed to find the centre of the beam on the RCF, which had a FWHM of $\sim$ 12 mm. The average and standard deviation, σ_{PV}, were then found over a $\sim$ 1.2 mm region in the centre of the beam where the PV is fairly uniform. Fig. 5.6a) shows a comparison between the different calibration

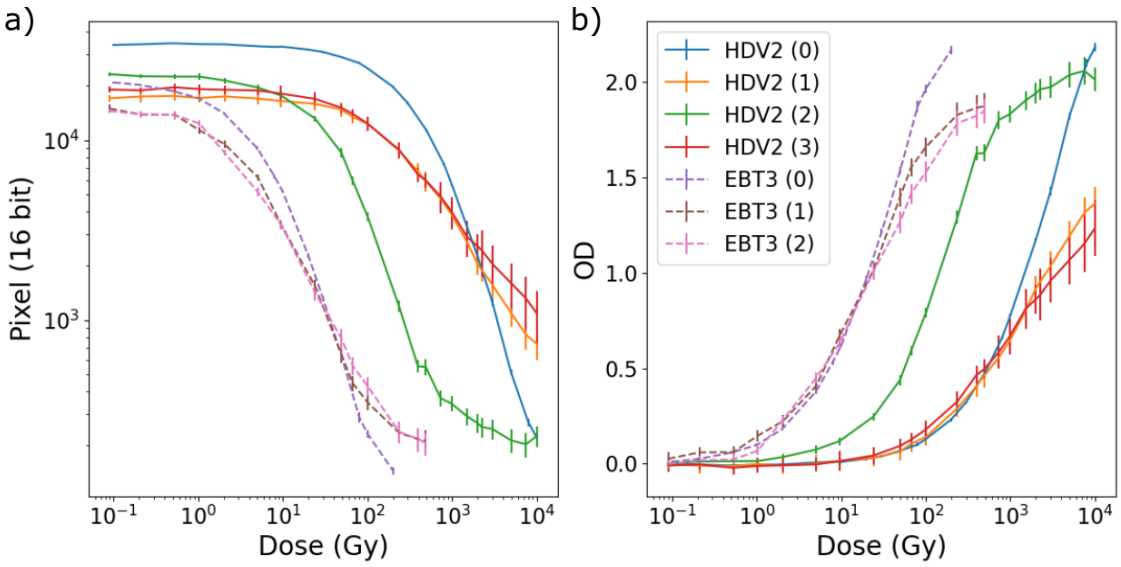

Figure 5.6: Calibration curves showing the a) dose-PV and b) dose-ODnet response for the green channel obtained using a Nikon CoolScan 9000. The curves are shown for multiple types of HDV2 and EBT3, with those denoted 0 obtained in 2014 and 1, 2 and 3 in 2020.

curves, including both the 2014 and 2021 data sets. Significant differences are seen between the dose-PV response of the 2014 and 2021 batches of both HDV2 and EBT3, demonstrating the importance of using the same lot number for calibration, measurement, and null data.

Optical density (OD) is another measure by which dose-response can be measured with $\mathrm{OD} = \log_{10}(I_0/I)$, where I_0 and I are the light intensity recorded by the scanners without and with the film respectively. The conversion $OD = \log_{10}(2^{16}/PV)$ can be used for 16-bit PV data, so an increase in OD corresponds to a decrease in PV. However, it is often more useful to convert to net optical density by scanning unexposed films. In this case the change in OD between the signal and unexposed (fog) value is $\mathrm{OD_{net}} = \mathrm{OD_{sig}} - \mathrm{OD_{fog}} = \log_{10}(I_{\mathrm{fog}}/I_{\mathrm{sig}})$. While it is preferable to use dose-PV curves for dosimetry, as this does not introduce uncertainties associated with the unexposed film, often it is convenient to work with dose-$\mathrm{OD_{net}}$ curves due to slight variations in film composition between different lots and batches. This is demonstrated in fig. 5.6b), where it can be seen that the dose-$\mathrm{OD_{net}}$ response of different lot numbers of HDV2 and EBT3 is generally similar, although differences to arise most noticeably at higher dose.

To convert pixel values corresponding to intermediate doses in the calibration data requires fitting functions or interpolation. The dose-$\mathrm{OD_{net}}$ calibration curves can be fit using several functions [110, 120], including one of the form $y(x) = y_{\min} + (y_{\max} - y_{\min})/(1 + 10^{c(\log x_0 - \log x)})$. In this function $y_{\min}$, $y_{\max}$, c, and x_0 are

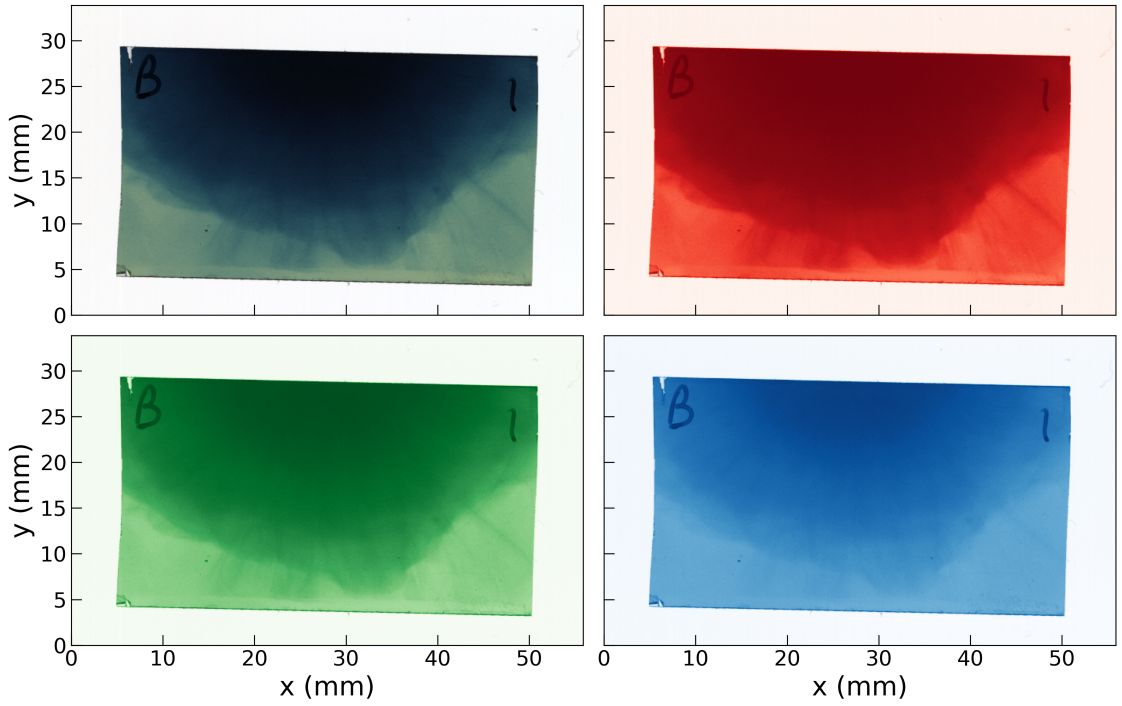

Figure 5.7: A proton beam imaged on RCF (HDV2, layer 2) during the interaction of a 168 J, 0.6 ps, 4.5 µm FWHM laser pulse with a 25 µm gold target from the Vulcan-EMP campaign at Vulcan TAP. The images shown are the full colour, red, blue, and green channels (clockwise from upper-left) scanned using an Epson 12000 XL.

fitting parameters corresponding to the minimum OD, maximum OD, width of the region where OD changes rapidly with dose, and centre of this region respectively. Extrapolation can also be performed to higher doses for films which have not yet saturated. If available it is better to interpolate the raw PV or OD_{net} data, as utilising a given fitting function assumes the underlying response of the film. When linearly interpolating raw data the underlying function is assumed to be smooth, or the separation between sample points sufficiently small. For this reason, it is better to interpolate in log(dose)-OD_{net} space as the behaviour is more linear. The standard deviation of the dose is then found using the upper and lower bounds for a given PV value.

By converting PV to dose raw data obtained from experiments can be processed. Shown in fig. 5.7 is an example layer from an RCF stack covering half the proton beam placed normal to a 25 µm gold foil after the interaction with a 168 J, 0.6 ps, 4.5 µm FWHM laser pulse. This data was obtained during the Vulcan campaign investigating EMP sources at Vulcan Target-Area-Petawatt (TAP). The main feature seen in this image is a beam of protons with a Bragg peak of 5.4 MeV. Comparing the colour channels, as expected the red channel can be seen to be the darkest while blue is the lightest due to their differing sensitivity to dose.

The dose-PV (or equally OD_{net}) response curves due to a proton beam define a unique trajectory in RGB space, as each dose corresponds to a unique RGB value with associated standard deviation. During data post-processing, this information is used to remove artifacts such as marks and dust that can occur pre- and post-shot before scanning [121]. The relationship between the R, G, and B values for the Vulcan-EMP proton beam are shown in fig. 5.8a) where a well-defined curve can be seen due to the proton beam. Points lying on this curve are identified as lying within 5 standard deviations of the calibration data, with these bounds marked. Values that are not bounded by these curves are removed by applying a mask. The cleaned data, shown in fig. 5.8b), is interpolated over in the masked regions after the PV values have been converted to dose. This is done as the spatial variation in dose response is expected to be smooth and more linear than the PV response. Channels for which the dose has saturated are not used, as the PV response becomes multi-valued [115].

After converting each colour channel to the corresponding dose with standard deviation σ_{dose}, the channels are combined in order to make full use of the dynamic range. This is done using an inverse-variance weighted average of the colour channels, such that the weighting for each channel is $w = 1/\sigma^2_{\text{dose}}$. Again, channels which have been saturated are avoided when performing the average dose calculation. Processing the data in fig. 5.7 results in the dose map shown in fig. 5.9. This has a

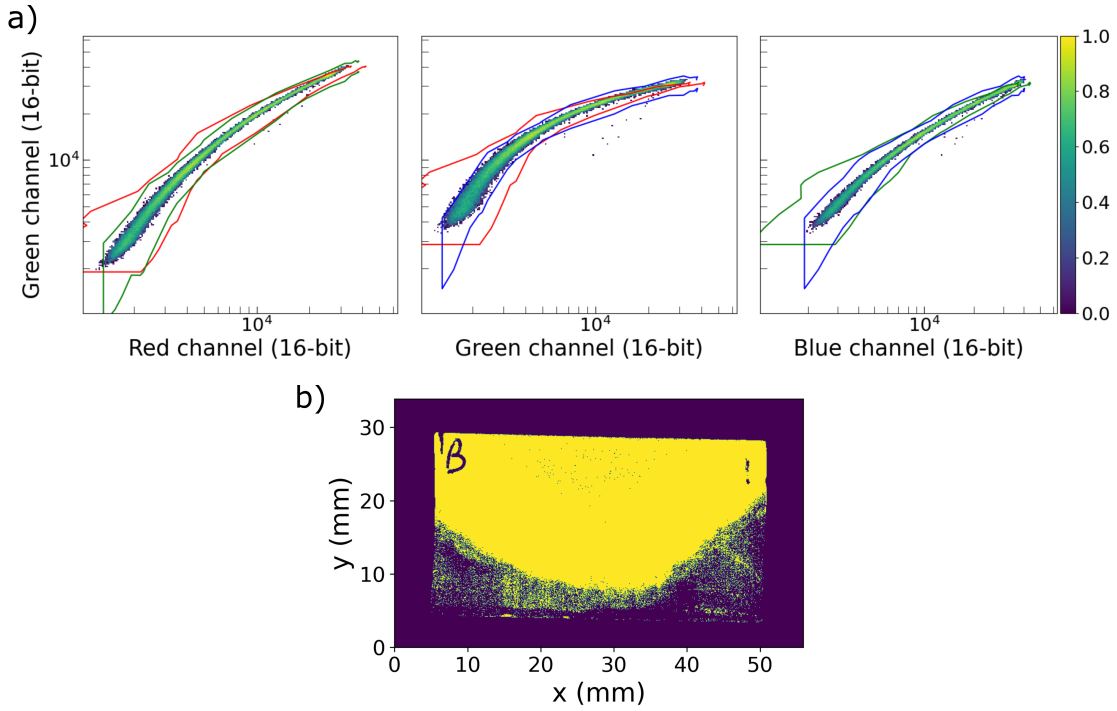

Figure 5.8: a) Normalised histograms of the RGB space obtained from the images of the proton beam shown in fig. 5.7. In each figure the lower and upper values expected from the dose-PV calibration data are taken to 5 standard deviations, coloured according to the channel they are from. Values outside these bounds are removed. b) The resulting mask which is then used to clean the raw data, where yellow points are kept and blue are discarded.

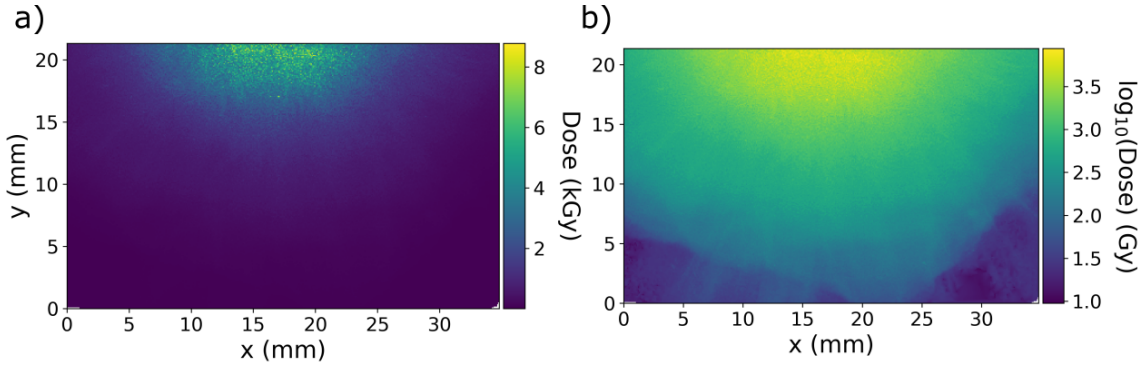

Figure 5.9: Dose maps of the proton beam shown in fig. 5.7 where the artifact cleaning process has been implemented, showing a) the linear data and b) after taking the logarithm of the dose to the base 10 allowing finer structure to be seen.

maximum proton dose of ~ 8 kGy.

The dose provides the energy deposited per unit mass, so to convert from dose to energy the mass of the active layer is required. Using the scan resolution of 300 dpi for the Vulcan-EMP data the volume of the active layer per pixel in the HDV2 film is 86.0×10^3 µm^3, which with a density of 1.08 gcm^{-3} has a mass of 92.9 ng. Thus, the energy deposited per pixel per Gy is 580 MeV. For EBT3 with a density of 1.20 ng the mass is 241 ng, with the energy deposited per pixel per Gy 1500 MeV.

5.1.3 Measurements of the proton spectrum

The energy deposited in a layer of the film, D_i, where the subscript i is used to indicate the stack layer, is

$$D_i = \int \frac{dN}{dE} R_i(E) dE \tag{5.2}$$

where dN/dE can vary spatially depending on the structure of the proton beam incident on the RCF. The deposited energy can then be either considered as the total deposited in the film, summing all values for a given layer, or a particular region can be chosen for a spatially resolved analysis.

Extracting the proton spectrum from eq. 5.2 requires knowledge of both D_i and R_i, with the latter found as demonstrated earlier in fig. 5.3b). A simple method for extracting dN/dE is performed by making two assumptions about the nature of the proton spectrum and the response. The first is that the response curves are localised to some region $E_1 \leq E \leq E_2$, where E_1 and E_2 are taken as the $1/e$ values of the response curves as shown in fig. 5.3b), with $R_i = 0$ otherwise. Secondly, dN/dE is

then assumed to be constant in this region, allowing eq. 5.2 to be rearranged to give

$$\frac{dN_i}{dE} = \frac{D_i}{\int R_i(E)dE}. \tag{5.3}$$

Values for dN_i/dE are attributed to $E_{\mathrm{Bragg},i}$, with intermediate points obtained via interpolation. This is referred to as the Bragg peak dominated (BPD) assumption, as it assumes that only protons whose Bragg peak lies within a given layer contribute to the spectrum.

To obtain an improved result when reconstructing the proton spectrum the contribution of all protons must be included. The standard approach is to work iteratively from the back of the stack to the front, accounting for the effect of the higher energy protons in each successive layer. This process starts with the final layer in the stack which measures a signal, the nth layer, corresponding to the maximum proton energy of the beam. For this reason, it is desirable that the stack is designed to measure energies in excess of the expected cutoff energy. In this layer the BPD assumption provides a reasonable starting estimate of the dose, as the contribution from higher energy protons is small, and can be used to obtain dN_n/dE.

The $(n-1)$th layer is then considered by initially making the BPD assumption. However, by interpolating dN/dE between the $(n-1)$th layer and nth layer the integral in eq. 5.2 can be calculated. Comparing the calculated value of D_i with that found experimentally, dN_{n-1}/dE in this $(n-1)$th layer is then adjusted until the deposited energy is within a specified tolerance. Fixing dN_{n-1}/dE in this layer the next layer (n-2) can then be considered, and the process is repeated until the front of the stack is reached.

This approach is sensitive to noise in the values of D_i extracted from the RCF. If D_i is overestimated in a layer at the back of the stack, the value of dN_i/dE at this point will be overestimated, then in the next layer dN_{i-1}/dE will be underestimated in order to ensure the calculated D_{i-1} agrees with the experimental value. This accumulates in all following layers, with values that are underestimated then causing the next layer to be overestimated. The layer which is most sensitive to noise is usually the final layer of the stack, for which the BPD assumption is applied.

To further develop the approach instead of initialising the final layer of the stack with the BPD assumption, dN/dE is assumed to be Maxwellian between dN_n/dE and the high energy cutoff $dN_{\mathrm{max}}dE$. Initial values for T and the cutoff energy are provided, and N varied until the value of D_n calculated using eq. 5.2 agrees with the measured value. This process proves to be much more robust to noise in the final layer, and is only weakly dependent on the initial value of T which can be provided

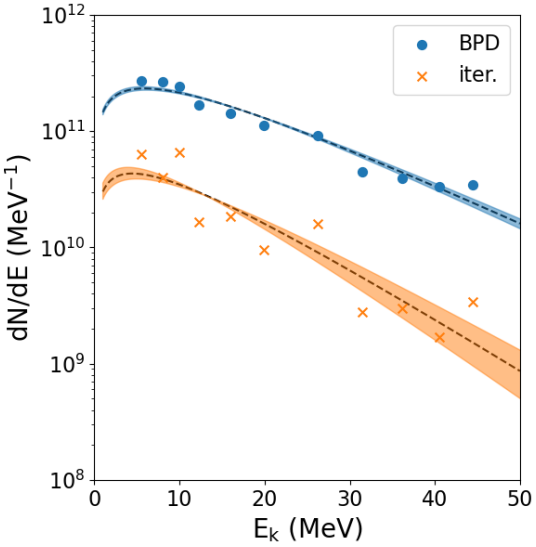

Figure 5.10: The reconstructed proton spectrum for a proton beam generated via TNSA from the shot examined in the previous section from the Vulcan-EMP experiment. Markers show the results obtained when using the Bragg peak dominated (BPD) assumption and when employing the iterative (iter.) approach. Maxwellian distributions (dashed lines) are fitted to each result; for the BPD approach $N = 5.7 \times 10^{12}$ and $T = 11.8$ MeV, while for the iterative approach $N = 7.9 \times 10^{11}$ and $T = 8.9$ MeV. Shaded regions show lower and upper T estimates.

based on the BPD approximation for the stack. The important consideration is the high energy cutoff, which has a greater impacted on the extracted dN/dE. Lower and upper bounds for this value can be found through observation of the RCF stack by finding the last layer with an observable dose. The resulting algorithm was tested using arbitrary input distribution functions to obtain D_i with various stack designs, for which the spectrum was then obtained.

In fig. 5.10 a reconstructed proton spectrum is shown using both methods. The most significant difference arises in the number of protons accelerated during the interaction, which varies by a factor of ~ 7, and can significantly modify the conversion efficiency of laser-energy to proton-energy.

Estimates for the proton temperature are similar, although here the value obtained from the BPD approximation is slightly higher than the iterative result. Examining the behaviour of the BPD assumption with arbitrary distribution functions and stack designs, it generally performs well with protons beams for lower T spectrums. This is to be expected, as the contribution of higher energy protons layers at the front of the stack is small. In these cases the BPD approach will produce higher estimates of T than the iterative approach.

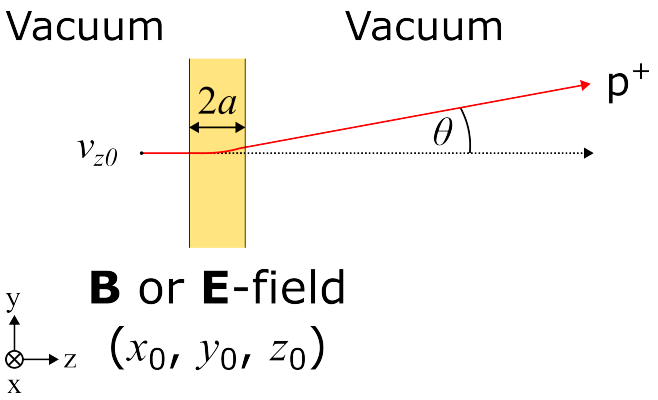

Figure 5.11: Deflection of a proton with initial velocity v_{z0} by an angle θ due to a magnetic or electric field contained within a region of width $2a$.

5.2 Proton radiography of electric and magnetic field structures

5.2.1 Deflection of charged particles

The deflection of charged particles by electric and magnetic fields can be examined by considering the case of a test particle initially travelling along the z-axis with velocity $v = (0, 0, v_{z0})$. As the particle passes through a region containing electric and/or magnetic fields it is accelerated by the Lorentz force (fig. 5.11). Velocity components in x and y can be introduced, resulting in a net deflection by an angle θ. The particle then propagates ballistically to the detector, due to the quasi-neutral nature of the proton beam. To obtain the magnitude of this deflection whilst the particle passes through the target, the acceleration

$$\mathbf{a} = \frac{\mathrm{d}\mathbf{v}}{\mathrm{d}t} = \frac{q}{m}\left(\mathbf{E} + \mathbf{v} \times \mathbf{B}\right) \tag{5.4}$$

must be computed for a charge q. While $\mathbf{E}$, $\mathbf{B}$, and $\mathbf{v}$ can vary in both space and time, analytic solutions can be obtained for many systems of interest [112, 122]. Usual assumptions are a well-defined geometry and quasi-static field structures along the particle path. For the latter assumption the limit is given by $2a/v_{z0}$, which for a plasma with $2a = 1$ mm probed by a 1 MeV proton with $v_{z0} = 13.8 \times 10^6$ ms^{-1} is 72.3 ps.

In the limit of small deflections the z-component of the velocity is treated as being constant in time, allowing the removal of the time dependence of the deflection as $\mathrm{d}z = v_{z0}\mathrm{d}t$. For plasmas generated during long-pulse laser interactions this is approximately true, which is demonstrated by considering the ideal accelerating

structure given by a uniform **E**. The relative change in the velocity can be shown to be $\Delta\mathbf{v}/v_z = L_z\mathbf{E}/2E_k$, where $L_z = 2a$ is the length scale of the field structure and the kinetic energy is in eV. For a 1 MeV proton probing a plasma with $2a = 1$ mm, $\mathbf{E} = 10$ MVm^{-1} would be required to increase v by 1%, which is on the upper-limit of the thermo-electric fields simulated earlier. Furthermore, the path-integrated electric field $\int E_z \mathrm{d}z$ is usually zero due to the symmetry of many systems.

In the case of an electric field aligned along x, the deflection angle is developed from

$$\frac{\mathrm{d}v_x}{\mathrm{d}t} = \frac{q}{m}E_x(x_0, y_0, z_0) \tag{5.5}$$

where the subscript '0' is used to refer to deflections in the target region containing the **E**-field structure. Making use of $\mathrm{d}z = v_{z0}\mathrm{d}t$ and that x_0 and y_0 are constant for an unperturbed trajectory

$$v_x = \frac{q}{mv_{z0}}\int E_x(x_0, y_0, z_0)\mathrm{d}z_0. \tag{5.6}$$

For small angles deflections are given by the ratio $v_{x,y}/v_{z0}$ as

$$\theta_{x,E} = \frac{q}{2E_{k,z0}}\int E_x(x_0, y_0, z_0)\mathrm{d}z_0 \tag{5.7a}$$

$$\theta_{y,E} = \frac{q}{2E_{k,z0}}\int E_y(x_0, y_0, z_0)\mathrm{d}z_0. \tag{5.7b}$$

A further assumption is the proton radiography is operated in the paraxial limit, where dimensions of the imaging system are much larger than the target region (2a). Small angle deflections can occur even if the field strength is large provided the particle energy is high, the length scale is short, or the integrated field small.

Using similar reasoning the deflection due to a magnetic field can be assessed. The structure which will introduce the largest net deflection to the particle trajectory is a uniform **B**-field, aligned perpendicular to the initial particle velocity. Note that when **B** is parallel to the initial **v** the particle experiences no deflection as $\mathbf{v}\times\mathbf{B} = 0$. The path of a particle in a uniform magnetic field is given by the gyro-radius, so the equation for the velocity in the x-y plane perpendicular to the probe axis is $v_\perp/v_{z0} = \sin(\omega_g t)$. Thus, provided $t \ll \omega_g$ the deflection will be small, which is equivalent to the condition $L_z = 2a \ll r_{g,z0}$. For reference the gyro-radius of a 1 MeV proton with $\mathbf{B} = 1$ T is $r_g = 144$ mm.

Again, beginning with the x-component the acceleration is

$$\frac{\mathrm{d}v_x}{\mathrm{d}t} = \frac{q}{m}\left(v_y B_z(x_0, y_0, z_0) - v_z B_y(x_0, y_0, z_0)\right) \tag{5.8}$$

so for an unperturbed trajectory through the target region (where $v_y/v_{z0} \ll 1$)

$$v_x = -\frac{q}{m}\frac{v_z}{v_{z0}}\int B_y(x_0, y_0, z_0)\mathrm{d}_{z0}. \tag{5.9}$$

The ratio v_z/v_{z0} gives the sign of v_z, and will be referred to as s_z. Obtaining the deflection for the x and y-components the results are then

$$\theta_{x,B} = -\frac{s_z q}{\sqrt{2m_p E_{k,z0}}}\int B_y(x_0, y_0, z_0)\mathrm{d}z_0 \tag{5.10a}$$

$$\theta_{y,B} = \frac{s_z q}{\sqrt{2m_p E_{k,z0}}}\int B_x(x_0, y_0, z_0)\mathrm{d}z_0. \tag{5.10b}$$

Comparing equations 5.7 and 5.10, it can be seen that the scaling of the deflection angle with particle energy differs depending on whether an electric or magnetic field is probed. For an electric field $\theta_E \propto E_{k,z0}^{-1/4}$ while for a magnetic field $\theta_B \propto E_{k,z0}^{-1/2}$. This allows the two effects to be separated on a single shot when utilising a broadband particle source in combination with a spectrally resolved detector, by comparing the change in deflection angle as a function of energy. Furthermore, the appearance of s_z in eq. 5.10 opens up another avenue with which to separate the two effects, by probing in either the forward or reverse directions. This has little impact in the case of an electric field, but for a magnetic field the dependence on s_z means that the sign of the deflection flips depending on which direction along z is probed. While this can provide clearer information about the nature of the target field, there are additional costs associated as two laser pulses are required as well as access to both probe geometries.

For most plasmas both electric and magnetic fields are present. Provided the deflection angle remains small (the foundation upon which the preceding equations were derived), equations 5.7 and 5.10 can be summed without compromising accuracy to give a more general solution. This is

$$\theta_x = \frac{q}{2E_{k,z0}}\int\left(E_x - \sqrt{\frac{2E_{k,z0}}{m_p}}s_z B_y\right)\mathrm{d}z_0 \tag{5.11}$$

for the x-component of the deflection. Thus, a given deflection is related to the path-integrated fields experienced by a particle as it traverses the target region.

By re-casting the electric and magnetic fields in term of the electrostatic potential, $\mathbf{E}(x_0, y_0, z_0) = \nabla\phi(x_0, y_0, z_0)$, and vector potential, $\mathbf{B}(x_0, y_0, z_0) = \nabla \times \mathbf{A}(x_0, y_0, z_0)$, respectively it is possible to consider the deflections as being due to some general potential $\Phi(x_0, y_0, z_0)$ such that $\theta_\perp \propto -\nabla\Phi$. Again, considering the x-components

$$\theta_{x,E} \propto \int E_x \mathrm{d}_{z0} = -\frac{\partial}{\partial x_0}\int \phi \mathrm{d}z_0 \tag{5.12a}$$

$$\theta_{x,B} \propto \int B_y \mathrm{d}_{z0} = -\frac{\partial}{\partial x_0}\int A_z \mathrm{d}z_0 + \int \frac{\partial A_x}{\partial z_0}\mathrm{d}z_0. \tag{5.12b}$$

Gauge invariance allows a vector potential to be chosen such that $A_x = A_y = 0$, as for our geometry B_z is arbitrary as it does not contribute to deflections, making the second integral in eq. 5.12 zero. Combining these results $\theta_\perp$ and Φ are given by

$$\theta_\perp = -\frac{q}{2E_{k,z0}}\nabla\Phi \tag{5.13}$$

where

$$\Phi = \int \left(\phi - \sqrt{\frac{2E_{k,z0}}{m_p}} s_z A_z\right) \mathrm{d}z_0. \tag{5.14}$$

For the common scenario in this thesis, where changes in the magnetic field arise due to a curl in the electric field, the rotational component introduced in the electric field can be shown to be small compared to the curl-free component provided $\tau \ll a^2/(T_e/eB)$ [112].

5.2.2 Mapping procedure

The ultimate aim of the proton radiography setup is to identify the structure of the **E** and **B**-fields, and there are several approaches that can be taken to this end. Initial inspection can yield some qualitative data, which can be followed by quantitative estimates using analytic scalings of the Lorentz force derived from eq. 5.11 [122, 123]. Other common techniques include the comparison between real and synthetic proton deflectometry images, and utilising a grid placed before the target to track deflections [124, 59, 125]. An analytic relation can be derived between the particle

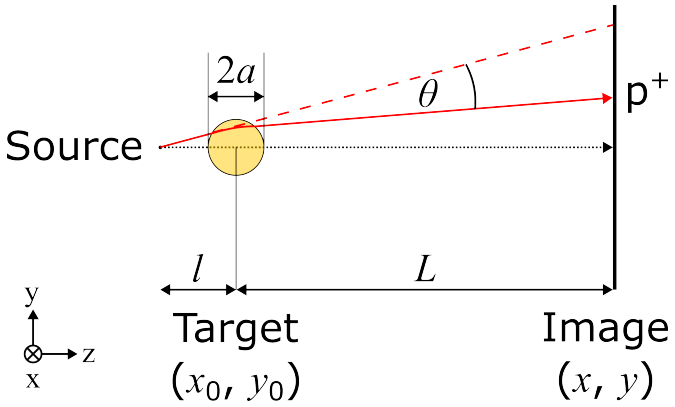

Figure 5.12: Schematic diagram of the proton radiography imaging system. A proton source is located a distance l from the target to be imaged, with dimensions $2a$ where $2a \ll l$ is required to operate in the paraxial limit. Protons experience a deflection θ due to electric and magnetic fields at the object plane at (x_0, y_0), before continuing to propagate ballistically to the image place. For high magnification $l \ll L$ is desired.

deflection due to the path-integrated fields in eq. 5.11 with the mapping of the proton intensity profile from the object to the image plane [112]. Establishing this link allows a 2D deflection map of $\theta_{x,y}$ to be constructed from the intensity profile found in the image plane, from which the path-integrated fields can be identified.

For a given subset of the beam, which will be referred to as a beamlet, the mapping from the object plane to the image plane is

$$x(x_0, y_0) = x_0 \left(1 + \frac{L}{l}\right) + \theta_x(x_0, y_0) L \tag{5.15a}$$

$$y(x_0, y_0) = y_0 \left(1 + \frac{L}{l}\right) + \theta_y(x_0, y_0) L \tag{5.15b}$$

where l is the source-target distance and L is the target-detector distance following the small deflection angle approximation. Here, L/l arises in the first term due to the divergence of the beam from a point source a distance l from the target, and the final term is the deflection term explored in the previous section. Fig. 5.12 illustrates this arrangement.

Two additional conditions are imposed on the geometry of the imaging system for eq. 5.15 to hold. First, the ratio a/l, known as the paraxiality parameter, must be small such that the angle subtended by the object is much smaller than the distribution of the source. Variations in the intensity in the image plane can then be attributed to the target, rather than the proton beam. This also ensures that the passage of a beamlet through the target region is close to parallel with the probe axis,

so the angle with which it passes through the target does not matter. Secondly, the displacement of the beamlet as it passes through the target is neglected, requiring $a \ll L$ so that deflections acquired during transit across the target are small relative to the total deflection. Small deflections can then be treated as if acquired from a point on the z-axis.

The system magnification for a point source is defined as $M = 1 + L/l$, where M increases as the target-detector distance is increased relative to the source-target distance. High magnification is often desired for many systems as the length scale over which features may vary can be smaller than 100 µm, which approaches the typical scanner resolution of 1000 dpi (25.4 µm). In the limit of high magnification ($L/l \gg 1$) eq. 5.15 can be reduced such that

$$x(x_0, y_0) = L\left(\frac{x_0}{l} + \theta_x(x_0, y_0)\right) \tag{5.16a}$$

$$y(x_0, y_0) = L\left(\frac{y_0}{l} + \theta_y(x_0, y_0)\right) \tag{5.16b}$$

in which case varying L only affects the final size of the image rather than the shape. For this reason, it is usually better to increase L instead of l when seeking higher magnification. Care must be taken to ensure there is still adequate flux in the object plane though, as the proton beam flux varies inversely with the square of the source-detector distance. However, in certain circumstances varying l can be desirable as it allows control over the ratio of the magnification term to the deflection term. This in turn can be used to control the formation of caustics, a subject which will be investigated shortly.

Of note when considering the magnification is that while the distance between the source and target-centre is often taken as l, the virtual source position can lie of the order of 100 µm from the front surface of the foil [126]. Provided $l \gg 100$ µm the virtual source position does not need to be considered when calculating the magnification, which is the case for experiments in this thesis where typically $l \approx 10$ mm.

Mapping of a surface in the object plane, $\mathrm{d}S_0$, to the image plane, $\mathrm{d}S$, is done using the Jacobian determinant

$$J(x_0, y_0) = \frac{\partial x}{\partial x_0}\frac{\partial y}{\partial y_0} - \frac{\partial x}{\partial y_0}\frac{\partial y}{\partial x_0} \tag{5.17}$$

such that

$$\mathrm{d}S = |J(x_0, y_0)|\mathrm{d}S_0 = \left|\frac{\partial(x,y)}{\partial(x_0,y_0)}\right|\mathrm{d}S_0 \tag{5.18}$$

where the absolute value is taken as it is only the relative size of the image that is of interest. A beamlet that passes through the surface $\mathrm{d}S_0$ then also passes through $\mathrm{d}S$, allowing the intensity in the image plane, I, to be related to the intensity in the object plane, I_0, as

$$I(x,y) = I_0(x_0,y_0)\frac{\mathrm{d}S_0}{\mathrm{d}S} = I_0|J(x_0,y_0)|^{-1}. \tag{5.19}$$

For an unperturbed beam $I_0(x,y) = I_0(x_0,y_0)/M^2$ in 2D. To successfully retrieve the deflection map $I_0(x,y)$ should be such that intensity increases can be seen without saturating the RCF. This introduces a complication in retrieving deflection maps from RCF, I_0 is required yet cannot be retrieved on-shot. Ideally, a measurement of the unperturbed beam would be made with no target present, but due to shot-to-shot variation (associated with laser and target alignment) this must often be inferred post-shot from the perturbed beam.

The Jacobian determinant in eq. 5.19 is invertible provided it is non-zero at all points. Substituting eq. 5.15 into eq. 5.17

$$J(x_0,y_0) = \left(1 + \frac{L}{l} + \frac{\partial\theta_x}{\partial x_0}L\right)\left(1 + \frac{L}{l} + \frac{\partial\theta_y}{\partial y_0}L\right) - L^2\frac{\partial\theta_x}{\partial y_0}\frac{\partial\theta_y}{\partial x_0} \tag{5.20}$$

which can be further simplified to

$$J(x_0,y_0) = \frac{L^2}{l^2}\left[1 + l\left(\frac{\partial\theta_x}{\partial x_0} + \frac{\partial\theta_y}{\partial y_0}\right) + l^2\left(\frac{\partial\theta_x}{\partial x_0}\frac{\partial\theta_y}{\partial y_0} - \frac{\partial\theta_x}{\partial y_0}\frac{\partial\theta_y}{\partial x_0}\right)\right] \tag{5.21}$$

in the high magnification limit. If the gradient in the deflection angle is large - which typically occurs when $\theta_{x,y}$ is large - the determinant can be close to zero. At these points the intensity in the image plane becomes very large, as can be seen from eq. 5.19, corresponding to the formation of caustic structures. These caustics appear as sharp lines in the RCF image, and occur at the point where beamlets are found to cross.

The relative magnitude of deflections can be characterised using a dimensionless variable $\mu = L\theta/a$ [112], providing an estimate of the terms which describe gradients in the deflection angle in eq. 5.20. It is often referred to as the contrast parameter, as for increasing μ the amplitude of the intensity contrast in the RCF image increases.

As μ is dependent on both θ and L/a, it is possible for large deflection angles to result in smoothly varying images provided $L \ll a$, or for small deflection angles to result in caustic structures if $L \gg a$. The former case will not be considered here, as small angle deflections are assumed in the mapping process with $L \gg a$. There are then four distinct contrast regimes which have been identified; these are the linear ($\mu \ll 1$), non-linear injective ($\mu < \mu_c \sim 1$ where μ_c is some critical value), caustic ($\mu \geq \mu_c$), and diffusive ($\mu \gg 1$) regimes [127].

In the linear regime where $\mu \ll 1$ the second order terms in eq. 5.20 can be neglected and the equation can be linearised, allowing a simplified expression for eq. 5.19 if $M \gg 1$

$$I(x_0, y_0) = I_0(x_0, y_0)\left[1 - l\left(\frac{\partial \theta_x}{\partial x_0} + \frac{\partial \theta_y}{\partial y_0}\right)\right] \tag{5.22}$$

where the fact $\theta_{x,y} \ll 1$ has been used to Taylor expand the inverse of $D(x_0, y_0)$.

For arbitrary μ, eqs. 5.15, 5.17, and 5.18 form a set of equations which must be solved to obtain the deflection mapping. Their application will first be demonstrated by considering the example case of a 1D mapping in the linear regime where deflections only occur in the y-axis, which provides a reasonable approximation for the experiments explored in chapter 7. In this case $\theta_x = 0$ making the $x(x_0, y_0)$ mapping $x = Mx_0$. As a result, $\partial x/\partial x_0 = M$ in eq. 5.17, while the second term in this equation is zero as $\partial x/\partial y_0 = 0$. Substituting this result into eq. 5.18

$$I(x, y) = I_0(x_0, y_0)\frac{1}{M}\frac{\partial y_0}{\partial y} \tag{5.23}$$

from which the point corresponding to a given y in the image plane can be found in the object-plane can be found using

$$y_0 = M\int \frac{I(x, y)}{I_0(x_0, y_0)}\partial y = \frac{1}{M}\int \frac{I(x, y)}{I_0(x, y)}\partial y. \tag{5.24}$$

Eq. 5.24 is solved by numerical integration in the image plane, with the results linearly interpolated to return a regularly spaced grid. To obtain an estimate for I_0 the signal $I(x, y)$ is convolved with a large 2D circular Hann window, whose diameter is varied to ensure a balance between removal of the signal while retaining information regarding the structure of the beam. Alternative approaches may be to assume a flat mean-field, but this would produce spurious effects at the beam edge, or a 2D 2nd order polynomial fit [128]. The calibrated dose signal can then be normalised to obtain I/I_0. Finally, the deflections resulting from the path-integrated

fields are found using $\theta_y = (My_0 - y)/l$.

For a 2D mapping, where the field structures result in deflections in both x and y, a more considered approach is required. Noting that the deflection can be written in the form of the gradient of a deflection potential (eq. 5.13), the analytic linear mapping (eq. 5.22) can be used to construct a Poisson equation of the form

$$\nabla^2 \Phi = \frac{1}{l} \frac{2E_{k,z0}}{q} \left(\frac{I}{I_0} - 1 \right). \tag{5.25}$$

Several solvers exist for Poisson's equation, with this equation highlighting the analogous nature of optical shadowgraphy; instead of probing with protons rays of light are used, and deflections arise due to gradients in the refractive index instead of a potential field. For proton radiography, algorithms have been designed for the extraction of quantitative information, based on the solution of the Monge-Ampère equation. Kasim *et al.* [129] used a Voronoi cell based reconstruction technique, where the cell sizes are optimised such that the proton flux passing through each surface is equal. This is first done in the object plane, before the sites are redeployed in the image plane and the cell weights varied to achieve the same flux as in the object plane. The deflection potential can then be obtained by finding the displacement between cell centres in the object plane and image plane. This method produced errors of 10% for test data sets even when the intensity modulation, and thus μ, was large.

Further developments in reconstruction techniques have followed [130, 127], where eq. 5.18 was shown to pose a Monge-Kantorovich optimal transport problem. Reconstruction can then be performed in the non-linear injective regime, $\mu < \mu_c$, where Poisson's equation is no longer accurate. In a later work, Kasim *et al.* [131] developed a technique allowing the recovery of the deflection potential in the absence of a source profile. Here, source profiles are generated statistically using hyperparameters, obtained by making a reasonable prior assumption regarding the amplitude of the deviations in the source intensity profile and the correlation lengths.

After recovering the deflection potential, integrated electric or magnetic fields can be recovered using eq. 5.14 after making an assumption about the origin of the field. While for many problems the electric and magnetic fields cannot be further extracted from the path-integrated fields, some problems with well-defined symmetry allow for further processing. Notably, those with cylindrical symmetry, which occurs in many of the examples in this thesis. In these cases for a cylinder parallel to the x-axis the θ_y is proportional to the forward Abel transform of the field profile. This means that a reverse Abel transform can be used to extract the field profile [132].

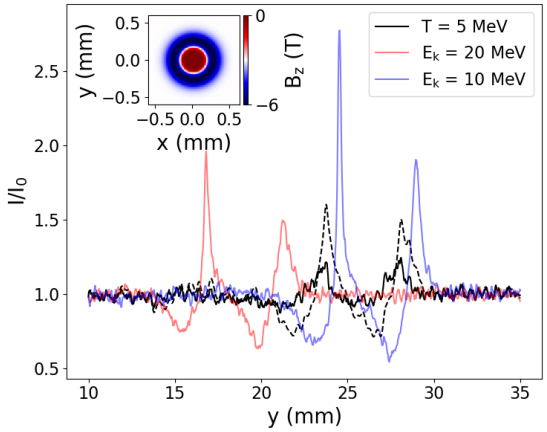

Figure 5.13: Synthetic lineouts showing the normalised intensity profile from a layer of RCF from a proton radiography experiment. The proton beam is deflected as it passes through an applied magnetic field, where the centre has been cavitated by the Nernst effect (inset). The effect of smearing is demonstrated by comparing the lineouts obtained from mono-energetic proton sources with $E_\mathrm{k} = 10$ and 20 MeV, to a poly-energetic proton source with a temperature of $T = 5$ MeV. The dashed line shows the $T = 5$ MeV result after deconvolution with the smearing kernel.

5.2.3 Effects of smearing

While the energy dependence of the proton deflections for both electric and magnetic fields can prove a useful tool in the analysis of proton radiography data, the finite energy resolution of the detector means that a range of proton energies are observed in a single image. Attributing this image to a single energy, when the typical energy spread exceeds 20% for protons with $E_\mathrm{k} < 5$ MeV (fig. 5.4), can lead to erroneous conclusions. Here, a more detailed analysis is required. Such an effect was demonstrated earlier when it was shown that incorrect values of N and T for the proton spectrum were found if the deposition of high energy protons in the front of the stack was not considered. In the case of deflection measurements the scaling of eq. 5.13 means that lower energy particles are deflected less than those with higher energy. Thus, the signal is blurred, reducing the spatial resolution, unless the source is monoenergetic. A quantitative assessment of this process was given by Arran *et al.* [102] which is reviewed here.

Each image obtained from a layer in the RCF stack can be considered a summation formed of radiographs at successive energies. As the proton energy increases the deflection angle decreases and the signal is offset further from the lowest energy detectable signal, which is shown in fig. 5.13 by comparing two mono-energetic sources with E_k 10 and 20 MeV. Typically, the energy associated with a layer of RCF is that which deposits the maximum energy, which is roughly the lowest energy observed in the layer spectrum (fig. 5.3b). The impact of a broad spectrum is then to reduce the

observed deflection. For this reason, the smearing kernel is asymmetric, as will be seen later in fig. 5.15. Observing the result for a poly-energetic source with $T = 5$ MeV, measured by a layer of RCF with a Bragg peak energy of 10.6 MeV, the signal has decreased amplitude and is broader with a reduced deflection.

To approximate whether blurring is of concern eq. 5.13 is used, where the deflection angle was assumed to be small. The relative offset between two beamlets of energy $E_{k,1}$ and $E_{k,2}$ is then $\Delta s = L(\theta_{\perp,2} - \theta_{\perp,1})$ so

$$\Delta s = \frac{Lq}{2E_{k,1}}\left(\nabla\Phi_1 - \frac{\nabla\Phi_2}{\Delta E_{\text{frac}}+1}\right) = L\theta_{\perp,1}\left(1 - \frac{\nabla\Phi_2}{\nabla\Phi_1}\frac{1}{\Delta E_{\text{frac}}+1}\right) \tag{5.26}$$

where $\Delta E_{\text{frac}} = E_{k,2}/E_{k,1} - 1$ is the fractional energy spread, which is obtained from fig. 5.4b) for $E_{k,2} > E_{k,1}$ and $E_{k,1} = E_{\text{Bragg}}$. For an electric field $\nabla\Phi_1 = \nabla\Phi_2 = \int \phi \mathrm{d}z_0$, while for a magnetic field $\mathbf{B} = (B_x, 0, 0)$

$$\Delta s = \frac{Ls_z q \int B_x \mathrm{d}z_0}{\sqrt{2m_p E_{k,1}}}\left(\sqrt{\frac{1}{\Delta E_{\text{frac}}+1}} - 1\right) = -L\theta_{y,1}\left(1 - \sqrt{\frac{1}{\Delta E_{\text{frac}}+1}}\right) \tag{5.27}$$

with $\theta_{y,1}$ the deflection angle for a mono-energetic beam with $E_k = E_{k,1}$. These expressions are found in the image plane, but in the limit of small deflections the mapping $y_0 \to y/M$ can be used to return to the object plane. The condition to resolve a feature is that the minimum spatial length scale in the plasma $a_{\min} \gg \Delta s/M$, which on substituting eq. 5.27

$$a_{\min} \gg \Delta s/M = |l_0\theta_{y,1}(1 - (\Delta E_{\text{frac}}+1)^{-1/2})|. \tag{5.28}$$

The relations shown in eq. 5.26 and eq. 5.28 convey several key points regarding smearing of a poly-energetic proton source due to both electric and magnetic field structures. Firstly, the term in brackets on the right-hand side that depends on ΔE_{frac} is the term responsible for smearing. In the limit $\Delta E_{\text{frac}} \to 0$ the source is mono-energetic, and the terms inside the bracket cancel with no smearing of the signal. As ΔE_{frac} increases the fraction which depends on it becomes smaller, becoming negligible once $\Delta E_{\text{frac}} \gg 1$. At this point the smearing reaches a maximum $\Delta s = -L\theta_{\perp,1}$, which conveys how the trajectory of the highest energy protons is effectively unperturbed by the deflection potential. Thus, the signal is smeared from the position of the lowest energy protons in the image plane to lower angles.

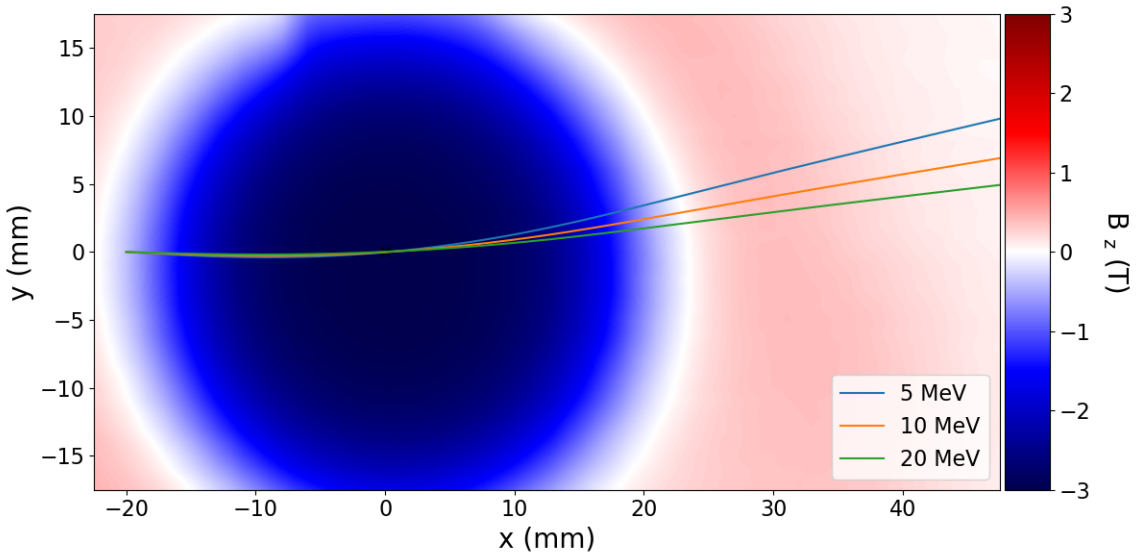

Figure 5.14: A magnetic field map of an electromagnet with maximum field strength $B_z = -3$ T. Shown are the trajectories of protons with kinetic energy 5, 10 and 20 MeV originating at $x = -20$, $y = 0$ mm as they pass through target-chamber centre (TCC) at $x = 0$, $y = 0$ mm, where they are deflected by the magnetic field.

However, for finite ΔE_{frac} as found experimentally, whether smearing requires consideration rests upon the deflection angle $\theta_{\perp,1}$. As the acquired deflection increases, the absolute difference between the path of the lowest and highest energy protons will increase reducing the spatial resolution. For most experiments small angle deflections occur, as typically the path-integrated field in the plasma is small due to its spatial scale, so this absolute difference is small. However, large path-integrated fields can arise, notably in experiments which use applied fields that occupy a large volume. This is of interest in this thesis, as an electromagnet was used to pre-magnetise a plasma so that the Nernst effect could be investigated. As shown in fig. 5.14 this field occupied a region spanning 10s of millimetres, reaching strengths of several T, with a resulting path integrated field approaching $B_x \mathrm{d}z \approx 100$ T mm. Re-arranging eq. 5.28, an expression can be found providing a lower-bound on the path-integrated magnetic field after which smearing is notable; for the setup used in the Vulcan-Nernst experiment to achieve a spatial resolution of 10 µm this is found to be $B_x \mathrm{d}z \ll 4$ T mm for a layer of RCF with a Bragg peak at 10.6 MeV.

Having identified the mechanism through which a proton radiograph is smeared the task is now to correct for this effect. This was first approached by Arran *et al.* [102] who considered the case of a strong background magnetic field, as shown here, using a linear deconvolution. The deconvolution requires obtaining the smearing kernel, a point spread function, which relies upon an understanding of how the trajectory of each energy band is modified by the field, and the relative contribution of each energy band to the final image. Thus, knowledge of three properties of the

radiography system are required; the displacement of the proton beam due to the known background field, the response of the RCF stack, and the proton spectrum.

In fig. 5.14 computational proton tracking was used to demonstrate the change in deflection angle as E_k is varied, resulting in an offset in the image plane for particles passing through target-chamber centre (TCC). Here, a function is used to find the angle of closest approach to TCC on leaving the same position at the source. The displacement of the proton beam from TCC in the image plane, y_d, can then be found as a function of E_k, as shown in fig. 5.15a) for $L = 167$ mm. Alternatively, if the background field has not been characterised it must be obtained during the experiment. The proton beam displacement is fitted to the function $y_d = a + b/\sqrt{E_\mathrm{k}}$ to allow values to be found across the energy range. As the gradient of the function becomes steeper, the change in deflection angle with energy increases, and the effect of smearing is more significant.

Acquisition of the RCF response curves (fig. 5.3b) and the proton spectrum (fig. 5.10) were outlined in section 5.1. Combining these results gives the energy deposition curves in each layer of the stack (fig. 5.4a), the second component that is required to obtain the smearing kernel. These energy deposition curves typically have three characteristic properties; a region where negligible energy is deposited at low energy that does not contribute to smearing, a sharp rise to a maximum which corresponds to the energy band with the strongest signal, and an exponential decay as the population of higher energy protons decreases while also losing less energy. It is the width of this final region that then effects the amount of smearing (fig. 5.4b).

Considering how the significance of smearing changes through the stack, the first point to note was mentioned previously - the relative energy spread decreases with each successive layer, so smearing is less significant at the back of the stack. However, as can be seen in fig. 5.15a) the gradient in the deflection of the proton beam is also reduced at higher energy, further reducing smearing. Thus, there is a two-fold benefit to making measurements at higher proton energies.

Now the smearing kernel will be derived in order to remove the effects of the background magnetic field for the case of a 1D radiograph. The mapping from the object plane to the image plane as given by eq. 5.16b) (where $M \gg 1$) with θ_y given by eq. 5.10b). If $dz = v_{z0}dt$ then deflections are small, which can be checked in the absence of electric fields by ensuring $r_g \ll L$. The magnetic field is decomposed such that $B_x = B_\mathrm{sig} + B_\mathrm{bg}$ where the subscripts 'sig' and 'bg' denote contributions from the signal and background fields respectively. The mapping is then

$$y = L\left(\frac{y_0}{l} + \theta_\mathrm{sig} + \theta_\mathrm{bg}\right) = y_d + L\left(\frac{y_0}{l} + \theta_\mathrm{sig}\right) \tag{5.29}$$

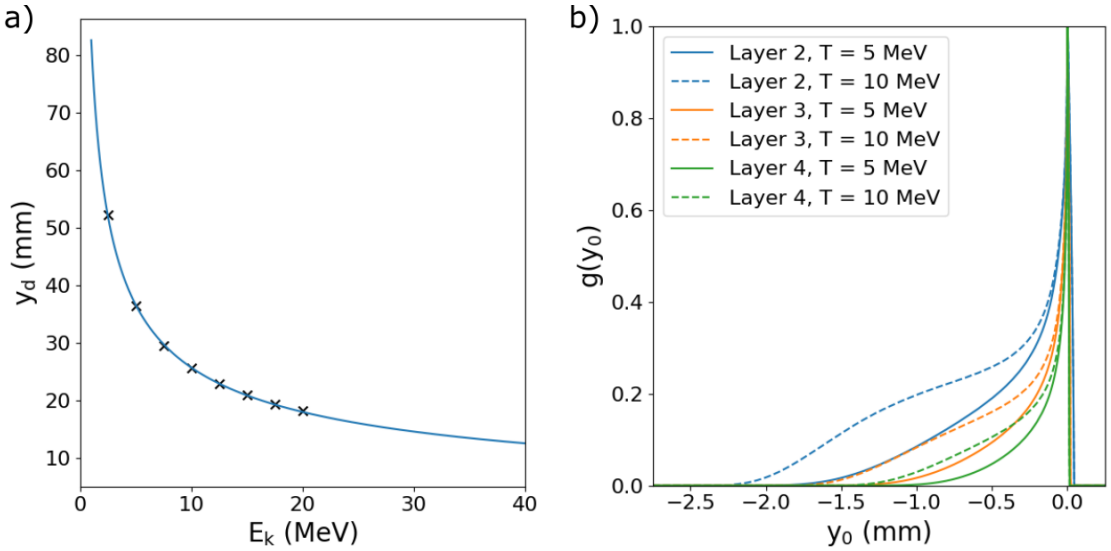

Figure 5.15: a) The mapping from TCC $x = 0$, $y = 0$ mm to the image plane for protons of varying kinetic energy passing through the magnetic field shown in fig. 5.14. This is shown fitted to the function $a + b/\sqrt{E_\mathrm{k}}$. b) The smearing kernel in the object plane for a proton beam imaged with an RCF stack at $L = 167$ mm, after passing through the electromagnet field. Here the results for layers 2, 3, and 4 in stack design 'C' from the Vulcan-Nernst experiment are shown, where the proton beam is characterised by either a 5 or 10 MeV Maxwellian spectrum.

where $y_d = L\theta_\mathrm{bg}$.

If the path-integrated magnetic field is much larger for the background region than the signal region, then $y_d \gg L\theta_\mathrm{sig}$ and the mapping is primarily influenced by the background field. As was demonstrated earlier in eq. 5.27, smearing is also proportional to the path-integrated field, and so if $\int B_\mathrm{bg} dz \gg \int B_\mathrm{sig} dz$ the smearing kernel can be found using only the background field. As the spatial scale of the background field is much larger than that of the signal, this is likely to be the case.

However, as found in eq. 5.23 it is the derivative of y which determines changes in the relative intensity of the proton beam in the image plane. Provided variations in the background field occur over much longer length scales than the signal field, such that $\partial\theta_\mathrm{sig}/\partial y_0 \gg \partial\theta_\mathrm{bg}/\partial y_0$, then the intensity profile can be attributed solely to the signal field. In the case of a mono-energetic radiograph, the final image will then depend only on the signal field.

The intensity profile due to the signal field is assumed to be the same over the energy range of protons that deposit energy in a layer of RCF. At lower energy proton energies the deflection increases, so this will lead to inaccuracies in cases where there are strong signal fields, low proton energies, or large energy spreads. Thus, the smearing kernel will typically perform better towards the back of the stack where protons are measured with higher energy and smaller energy spread.

A surface containing a distribution of protons is mapped to the image plane via

$$\frac{dI_j(y,E)}{dE} = \frac{dI_{0,j}(y_0,E)}{dE}\frac{dS_0}{dS} \tag{5.30}$$

where the spectral intensity $dI_{0,j}(y_0,E)/dE$ varies for a given shot j. Assuming that there is no spatial dependence on the energy distribution then $I_{0,j}(y_0,E) = I_0 I_{y,j}(y_0) I_{E,j}(E)$, where I_0 is a constant and $I_{y,j}$ and $I_{E,j}$ respectively are functions of space and energy only. Then

$$\frac{dI_j(y,E)}{dE} = I_0\frac{dI_{E,j}}{dE}I_{y,j}(y_0)\frac{dS_0}{dS} = I_0\frac{dI_{E,j}}{dE}f(y - y_d(E); E_0) \tag{5.31}$$

with $f(y)$ a function describing the spatial intensity profile in the image plane for an energy $E \approx E_0$ resulting from the signal, and y_d the deflection due to the background field. In other words, as described earlier the sharp gradients in the signal field control the shape of the image, while the mapping from object to image plane and smearing is dependent upon the background. The energy E_0 of the mono-energetic radiograph is chosen to be that which deposits the most energy in the layer of RCF.

Substituting this into eq. 5.2, the dose deposited in a layer of RCF is

$$D_{i,j}(y) = I_0\int R_i(E)\frac{dI_{E,j}}{dE}f(y - y_d(E); E_0)dE \tag{5.32}$$

which after changing the limits of integration using dy_d/dE gives

$$D_{i,j}(y) = D_{0,j}\int g_{i,j}(y_d)f(y - y_d; E_0)dy_d. \tag{5.33}$$

This equation takes the form of a linear convolution of the mono-energetic radiograph with a kernel

$$g_{i,j}(y_d) = R_i(E(y_d))\frac{dI_{E,j}(E(y_d))}{dE}\frac{dE}{dy_d} \tag{5.34}$$

from which $D_{0,j}f(y)$ can then be obtained via deconvolution with the dosed radiograph. In the linear regime this convolution kernel is general for any radiograph or source position.

Using the mapping provided by eq. 5.29 in the limit $\theta_{\text{bg}} \gg \theta_{\text{sig}}$, the convolution kernel can be provided as a function of y_0 in the object plane. The width of the kernel then describes the smearing-limited spatial resolution.

In fig. 5.15b) the kernel is shown for the example problem considered here. The kernel has a sharp peak at $y_0 = 0$, corresponding to the ideal mono-energetic radiograph with $E_0 = E_{\text{Bragg}}$, with a long tail towards lower deflection corresponding to the higher energy tail of the distribution function. For a 5 MeV source using the stack design shown in fig. 5.3b), smearing reduces the spatial resolution to ~ 1.5 mm, which is undesirable for observing features smaller than 100 µm. This compares favourably with the approximation provided by eq. 5.27, which estimates $\Delta s = 0.8$ mm. The underestimation is likely a result of the full energy spread being considered by the smearing kernel, instead of 50% in the approximated ΔE of eq. 5.27.

Progressing to layers 3 and 4 of the stack the width of the smearing kernel decreases, reaching ~ 1 mm at the 4th layer, as both the deflection angle and energy spread in each layer decreases. This makes measurements at greater proton energy desirable as the width of the smearing kernel decreases, resulting in an increase in the spatial resolution.

On increasing the temperature of the distribution to 10 MeV the smearing kernel can be seen to become broader in every layer, a result of the increased population of higher energy protons. As increasing the temperature of the spectrum is often desirable in order to achieve greater doses of high energy protons, this would suggest there is a trade off between increasing the temperature of the spectrum and maximising the spatial resolution. If the cut-off proton energy did not change with increasing temperature, such that the maximum measured proton energy was unchanged, then provided the signal was observable in all layers it would be undesirable to increase the temperature further. However, provided increasing the temperature also allows measurements of higher energy protons, then there is benefit to be found in generating hotter spectra.

Now that the smearing kernel has been obtained in fig. 5.15b), a mono-energetic radiograph can be found from the poly-energetic radiograph shown in fig. 5.13. Here the Richardson-Lucy deconvolution technique is used [133, 134]. Comparing the results before and after deconvolution in fig. 5.13, use of the kernel can be seen to increase the contrast in the recovered image such that it more closely resembles the mono-energetic radiograph.

Applying the full mapping procedure in combination with the smearing kernel, using the processes outlined in section 5.2, the magnetic field profiles can now be recovered. These are shown in fig. 5.16 for the synthetic data in fig. 5.13, where the input magnetic field profile was taken from a simulation of the Vulcan-Nernst experiment at $t = 1.1$ ns. As will be explored in chapter 6, this was obtained from a VFP simulation of a laser-heating problem in which a nitrogen plasma with

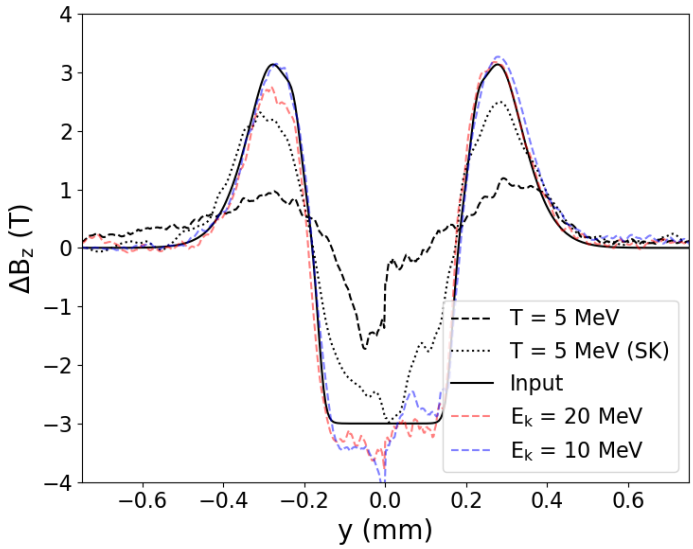

Figure 5.16: Comparison between the input and reconstructed change in the magnetic field spatial profile. Reconstructions were performed after imaging the input field with either a 10 or 20 MeV mono-energetic proton source, or a poly-energetic spectrum with $T = 5$ MeV, with the intensity profiles shown in fig. 5.13. For the poly-energetic source the result after utilising the smearing kernel in fig. 5.15b) is shown.

$n_e = 2.2 \times 10^{24}$ m^{-3} with an applied magnetic field of $B_z = 3$ T was heated.

The magnetic field reconstruction can be seen to perform well for both mono-energetic cases where $E_k = 10$ and 20 MeV. Using an Abel transform means that noise is amplified on axis in the region where $\Delta B_z = -3$ T and $B_z = 0$ T, and the reconstruction performs most poorly. However, the regions which experience field amplification due to advection show a good match to the input field profile. It is here where the ability to recover the field is most important, as this most strongly influences this calculated advection velocity and as a result the inferred transport coefficients.

In the poly-energetic case with a $T = 5$ MeV spectrum, the reconstruction shows significant deviations from the input profile. This is noticeable both on axis and in the amplified regions, with the amplitude of the peaks both shallower and broader, resulting in greater uncertainty in the calculated advection velocity. The average error is 38% compared to 6.2% and 6.5% for the 10 and 20 MeV mono-energetic cases respectively. Furthermore, the reconstruction can be seen to be asymmetric with a larger dip and broader peak on the left half of the image where $y < 0$ mm, a result of the asymmetric smearing effect. After performing the smearing deconvolution the result improves significantly, with the average error decreasing to 15%. While this is still greater than the mono-energetic result, the shape of the input and reconstructed fields match much more closely, and there is greater

certainty in the advection velocity.

Future use of a kernel offers the possibility of reducing the effects of smearing, thereby increasing the spatial resolution. If the smearing field is unknown, utilising an iterative technique where the integrated field is first approximated without a smearing kernel, and then used as an input for the smearing kernel, the unknown field may be found. This is most directly applicable to cases of spatially uniform fields of greater scale than the signal field. Such an approach is similar to performing a blind Richardson-Lucy deconvolution, in which the initial point spread function is unknown [135].

Of greater interest though would be the application of such a technique to cases in which it is the signal field that results in smearing of the radiograph, although this would require a kernel that also varies in space. Magnetic fields exceeding 100 T would likely be required for plasmas less than 1 mm in size, but such a scenario can be encountered in laser-driven capacitor-coils and solid-target Biermann battery experiments. Alternatively, this could also be applied to electron radiography [136] due to the much lower mass and resulting greater deflection experienced by electrons, as well as the typically larger energy spread in film detectors. However, it is likely that such experiments will lie in either the non-linear injective or caustic regimes.

5.3 Summary

Proton radiography's ability to image electric and magnetic structures makes it a core diagnostic in the assessment of transport phenomena. The TNSA sources characteristics, namely high spatial and temporal resolution, allow the measurement of fine electric and magnetic field structures in plasmas which evolve over sub-nanosecond timescales in long-pulse laser experiments. This chapter first focused on the characterisation of proton beams using radiochromic film, which is a crucial step for obtaining quantitative information. To achieve this, it is essential to understand the dose-response function, which can then be applied to characterise the proton radiography image. In the case of proton beams generated through target-normal sheath-acceleration, the properties of the distribution can be accurately determined.

Through inverse analysis, the electric and magnetic field structures can be analytically extracted from the radiography data, following post-processing to obtain the intensity profile, as outlined in the second part of this chapter. The complexity of this analysis depends on the characteristics of the electric and magnetic fields. For example, symmetry may simplify the process, enabling the mapping to be performed in one dimension instead of two. Additionally, the extent to which the

fields cause significant deflections of the protons is crucial, as strong gradients in the path-integrated field can lead to caustics in the image plane, complicating the analysis. If radiography is conducted in the presence of a background field, or if the path-integrated field is sufficiently large, the poly-energetic source may experience smearing due to variations in deflection with proton energy. This smearing leads to a reduction in the spatial resolution of images captured on radiochromic film, which have finite energy resolution. However, by applying a smearing kernel, it is possible to recover a mono-energetic image with improved spatial resolution.

Several avenues for future development of the proton radiography diagnostic remain. These include the application of advanced sources and detectors [137]. Next-generation laser systems have higher power, energy, and repetition rate, offer significant potential for enhancing diagnostic capabilities. For instance, higher energy proton beams, which experience smaller deflections, are less susceptible to caustic formation. Additionally, higher energy protons enable imaging of denser plasmas due to reduced scattering. However, the development of such laser systems, especially those with higher repetition rates, also necessitates the development of TNSA sources and detectors compatible with these systems. The radiochromic film detector discussed here is not suitable for integration with these sources.

There are further challenges in reconstructing the electric and magnetic field structures. A major source of uncertainty is the knowledge of the unperturbed proton beam structure, which is essential for performing deflection mapping and can vary between laser shots. Statistical methods are available to address this issue [131]. Modifying the experimental setup by placing radiochromic film both before and after the protons pass through the plasma may enable simultaneous imaging of the beam with and without deflections. Additionally, improvements are being made to reconstruction schemes that account for the poly-energetic nature of the proton source. While deflection scaling with energy is already used to differentiate between electric and magnetic fields, more refined approaches could help resolve current uncertainties arising from the temporal evolution of the fields [138]. Furthermore, images taken at different energies may help to constrain the electric and magnetic field structures when caustics are present [139].

Chapter 6

Simulations investigating transport in laser-plasmas

This chapter demonstrates the emergence of kinetic effects in high-power laser-plasma experiments by comparing VFP and extended MHD simulations. Unmagnetised simulations show that without a magnetic field, decreasing collision frequency increases relative anisotropy, enhancing non-local transport. With an applied magnetic field, anisotropic transport perpendicular to the field is suppressed, and decreasing collision frequency leads to more local transport. This trend is explained through the analysis of relative anisotropy from chapters 3 and 4. The Nernst effect, which forms a magnetic transport barrier by expelling the magnetic field with heat-flow, is also discussed in this context.

Kinetic simulations have previously investigated the effects of non-local transport and magnetic field dynamics on transport, and the interplay between these effects. The transport effects at the centre of these studies have been those associated with thermal conduction, namely the Biermann battery [92, 93] and Nernst effect [49, 39]. However, these studies have often considered either the role of the Knudsen number $\lambda_T/|l_T|$ or the magnetisation χ_T, without considering the effect magnetisation has on the effective mean-free-path and how this varies for different electron populations.

The problem is addressed by examining laser-plasma heating experiments with cylindrical symmetry, both in unmagnetised and pre-magnetised plasmas. This choice of geometry enables the isolation of the thermo-electric effect, which is central to the Biermann battery, and Nernst effect. This approach is required to develop an experimental platform where proton radiography can be used to clearly diagnose electric and magnetic field structures, providing a basis for benchmarking kinetic and extended MHD transport models.

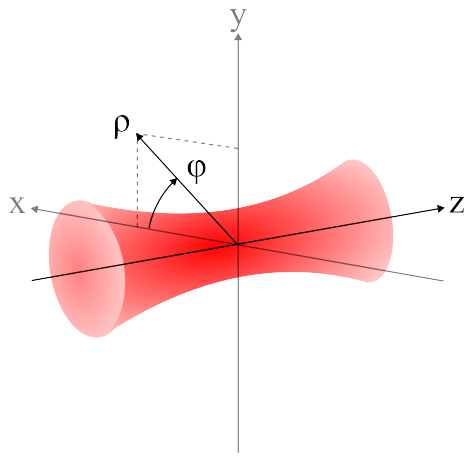

Figure 6.1: Schematic diagram of the laser geometry in cylindrical coordinates.

6.1 Plasmas with cylindrical symmetry

The experiment design concept here will be that of a single long-pulse laser incident on an under-dense gas ($n_e \ll n_c$). A Gaussian laser spot is used to achieve cylindrical symmetry, in combination with a long focal-length such that the Rayleigh range is greater than the length of the region being studied. Use of a long focal-length laser then ensures minimal gradients along the laser axis, provided the heating rate along the length of the plasma column is uniform. The geometry is shown in fig. 6.1. The resulting temperature gradient in cylindrical coordinates is given by $\nabla T_e = (\partial_\rho T_e, 0, 0)$. Transport will then occur perpendicular to the z-axis. For experiments involving an applied magnetic field this will be orientated parallel to the z-axis, so transport is also perpendicular to the magnetic field axis.

For the laser heating rate to be considered constant across the length of the plasma the coupling between the laser and the plasma must be low, such that the loss of laser energy is small and the intensity remains roughly constant. As the plasma becomes increasingly transparent to the laser at higher temperature, an analytic solution to the fractional energy loss of the laser is non-trivial. However, assuming both n_e and T_e do not change with time then for fixed laser intensity the energy deposited in the plasma as a fraction of the laser energy is

$$\frac{\Delta E}{E_l} \sim \frac{n_e}{n_c}\frac{\nu_B}{c} L_n \tag{6.1}$$

where L_n is the length of the plasma column. Provided $n_e \ll n_c$ then the plasma can typically be considered uniform across its length. A second requirement is that there must not be many collisions during the period the laser pulse passes through the plasma, such that $\tau_B \sim L_n/c$, as otherwise a significant fraction of the laser

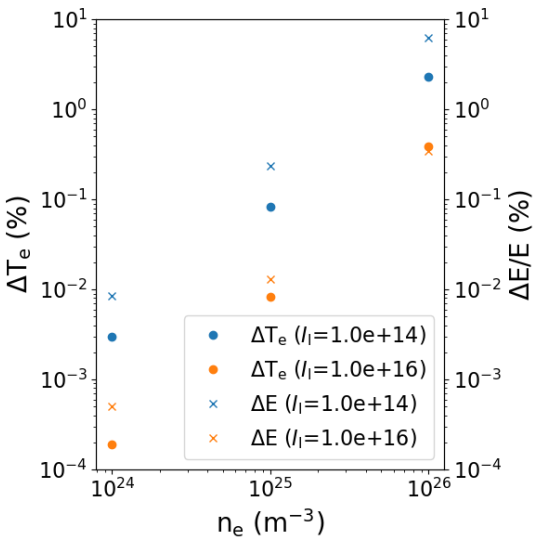

Figure 6.2: Normalised variation in the temperature across a $L_n = 1$ mm plasma column (initial $T_e = 20$ eV, $Z = 7$, $\ln \Lambda_{ei} = 6$) due to inverse bremsstrahlung heating (Langdon [70]) by a $\lambda_l = 1.054$ µm laser with a 1 ns square pulse and varying intensity of I_l. The energy loss normalised by the initial laser energy $\Delta E/E$ is also shown.

energy can be converted to thermal energy even when $n_e \ll n_c$. As L_n is set by the gas jet profile, this is typically of the order of 1 mm so the laser transit time is much less than the collision time.

Assuming the temperature of the plasma is given by the initial temperature T_0, then eq. 6.1 will overestimate the deposited energy as $\partial_t U \propto T_e^{-3/2}$. More detailed calculations of the energy deposition are displayed in fig. 6.2 for a laser pulse propagating through a uniform density plasma in 1D. In these calculations the energy of the laser pulse and intensity decrease as laser energy is converted to thermal energy of the plasma, using the super-Gaussian heating operator (eq. 2.127). It can be seen that as n_e increases more energy is coupled into the plasma, resulting in a greater temperature variation across the column. Decreasing the laser intensity also causes the variation to increase, as the energy in the laser pulse decreases and a larger fraction of the laser energy is converted to thermal energy.

6.2 Simulations considerations

The simulations conducted in this chapter utilise the VFP code IMPACT and extended-MHD code CTC as outlined in section 2.6. The IMPACT simulations will include both electron inertia ($\partial_t \mathbf{f}_1$) and hydrodynamic ion motion, unless stated otherwise to allow the effects of these terms to be separated or for reasons of stabil-

ity. Similarly, all terms will be enabled in the CTC equation matrix, allowing for the full range of extended-MHD transport effects as well as hydrodynamic ion motion, except when stated otherwise to allow the effects of specific terms to be separated. Flux-limited CTC simulations will not be conducted here.

These simulations are 1D Cartesian in x, with typical spatial resolutions of $\Delta x =$ 5 and 1 µm for IMPACT and CTC respectively, and the magnetic field axis z. Boundary conditions are reflective in IMPACT and periodic in CTC. In IMPACT the normalising density is 1×10^{25} m^{-3} and the normalising temperature $T_{e0} = 90.75$ eV. The normalised thermal velocity is then $v_{T0} = \sqrt{2eT_{e0}/m_e} = 5.65 \times 10^6$ ms^{-1}, with the v grid having a maximum of $v_{max} = 25v_{T0}$ and a spacing of $\Delta v = v_{T0}/40$. This encompasses the hottest heat-carrying electron population.

As the simulations are performed in a 1D Cartesian geometry the advection of energy, material, and magnetic field are constrained. Compared to cylindrical simulations, an increase in the advection velocity is typically expected in planar geometry as the expansion proceeds linearly with r, instead of r^2, with gradient only along a single axis. As a result, for conserved quantities such as the mass and magnetic flux (in the absence of sources or sinks) greater rarefaction or compression is observed for diverging or converging flows.

Both IMPACT and CTC use the Langdon operator, resulting in a super-Gaussian distribution if transport is prohibited. As it of relevance to the Nernst experiment discussed in section 7.1 all simulations here will use a laser wavelength of $\lambda_l = 1.054$ µm unless explicitly stated otherwise. This also motivates the choice of laser energy, temporal profile, and spatial profile. These will be $E_l = 205$ J, $t_{\mathrm{FWHM}} \approx 1.5$ ns, $w_{\mathrm{FWHM}} \approx 19$ µm leading to a peak intensity of $I_l \approx 1.5 \times 10^{16}$ Wcm^{-2}, again unless stated otherwise. The temporal and spatial properties of the laser will be examined in greater detail in section 7.1. At this intensity heating in the under-dense plasma heating is dominated by inverse bremsstrahlung.

The laser is used to heat a nitrogen gas with density $\rho = 7.5 \times 10^{-3}$ to 75×10^{-3} kgm^{-3}. In the IMPACT and CTC simulations conducted here, which do not include ionisation physics, the gas will be pre-ionised to $Z = 7$. The electron density is initially uniform, ranging from $n_e = 2.2 \times 10^{24}$ to 2.4×10^{25} m^{-3}, with an initial temperature of $T_e = 20$ eV. The fully ionised electron density relative to the critical density is then $n_e/n_c = 0.0239$, so the gas is under-dense with little variation in the temperature across the plasma column expected (fig. 6.2). A Coulomb logarithm of $\ln \Lambda_{ei} = 6$ is used throughout.

As discussed in section 2.4, laser heating rapidly ionises and heats the plasma in laser experiments. In fig. 6.3 the ionisation state of nitrogen was calculated

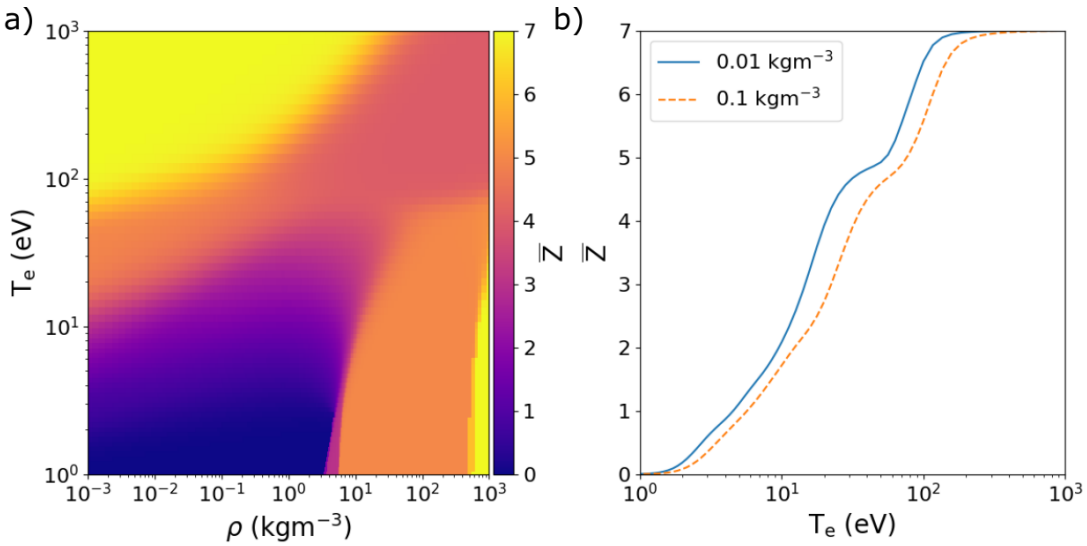

Figure 6.3: The average ionisation state, $\overline{Z}$, of nitrogen obtained using the FEOS model [140] a) as a function of mass density and electron temperature, with b) lineouts shown at $\rho = 0.01$ and 0.1 kgm^{-3}.

using the FEOS model [140]. For mass densities below $\rho = 1$ kgm^{-3} an increase in electron temperature results in greater ionisation. As the mass density increases, the ionisation state decreases slightly, but this change is minimal and does not have a significant impact within the mass density range considered in this context. Below temperatures of 100 eV the outer shell electrons ($Z \leq 5$) ionise rapidly, with a slight plateau occurring before the inner shell electrons are ionised around 100 eV. In fig. 2.7 it was demonstrated that temperatures on the order of 100 eV should be achieved in the first 10s of picoseconds in the laser-heated region, justifying the use of an ionisation state of $Z = 7$ here. Whether the use of $Z = 7$ is justified throughout the remainder of the simulation will be dependent upon the magnitude of the heat-flow at the heat-front.

It is worth noting that inner shell electrons are ionised at temperatures well below their ionisation energy. As an example, the ionisation energy required to transition from $Z = 6$ to 7 is $I_P = 667$ eV. This results from several contributing factors, including collisional ionisation by electrons in the hot tail of the electron distribution and Coulomb interactions within the Debye sphere, which lead to ionization potential depression. [2].

The collision fix is included in both IMPACT and CTC simulations to gain improved agreement with the transport coefficients appropriate for a fully ionised nitrogen ($Z = 7$) plasma. As discussed earlier in fig. 2.8 this will be most appropriate for simulations of weakly magnetised plasmas, where it will provide a better approximation than if the Lorentz limit was taken.

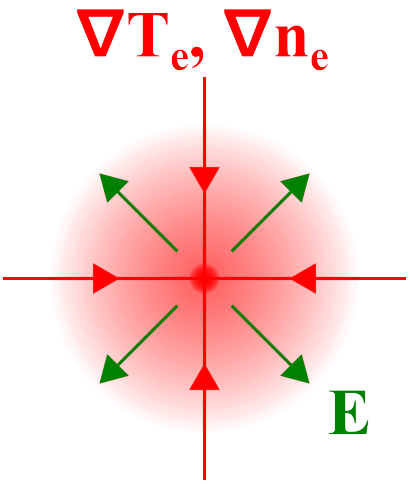

Figure 6.4: Diagram showing the initial temperature and density gradient vectors when a laser heats an under-dense gas with cylindrical symmetry in the radial plane. An electric field is formed via the thermo-electric effect that opposes these gradients.

6.3 Thermo-electric effect

In the absence of an applied field the geometry precludes the generation of magnetic fields; taking the Biermann battery as an example all density and temperature gradients are parallel. The remaining terms in Ohms' law (eq. 2.86) are then those associated with the pressure gradient and thermo-electric tensor. For the geometry under investigation here only the radial component of the electric field is then left

$$E_\rho = -\frac{T_e}{e}\left[(1+\beta_\parallel)\frac{\partial_\rho T_e}{T_e} + \frac{\partial_\rho n_e}{n_e}\right], \tag{6.2}$$

as shown in fig. 6.4.

The non-local form of this equation is found by taking the 6th velocity moment of the Ohm's law as written in eq. 4.19

$$E_\rho = -\frac{m_e}{6e}\frac{\partial_\rho(n_e\langle v^5\rangle) + 3\nu_c n_e J_\rho}{n_e\langle v^3\rangle} \tag{6.3}$$

where $\nu_c = 4\pi/[Zn_e(e^2/\epsilon_0 m_e)^2 \ln\Lambda_{ei}]$ are the terms in the collision frequency which are independent of velocity ($\ln\Lambda_{ei}$ is assumed constant). The current term then disappears if the assumption $\nabla\times\mathbf{B} = \mu_0\mathbf{J}$ is made. When f_0 is Maxwellian this reduces to the local form as the moments are then $\langle v^n\rangle = (2/\sqrt{\pi})\Gamma[(n+3)/2]v_T^n$.

Characterising the thermo-electric field is of great interest in part as it is the

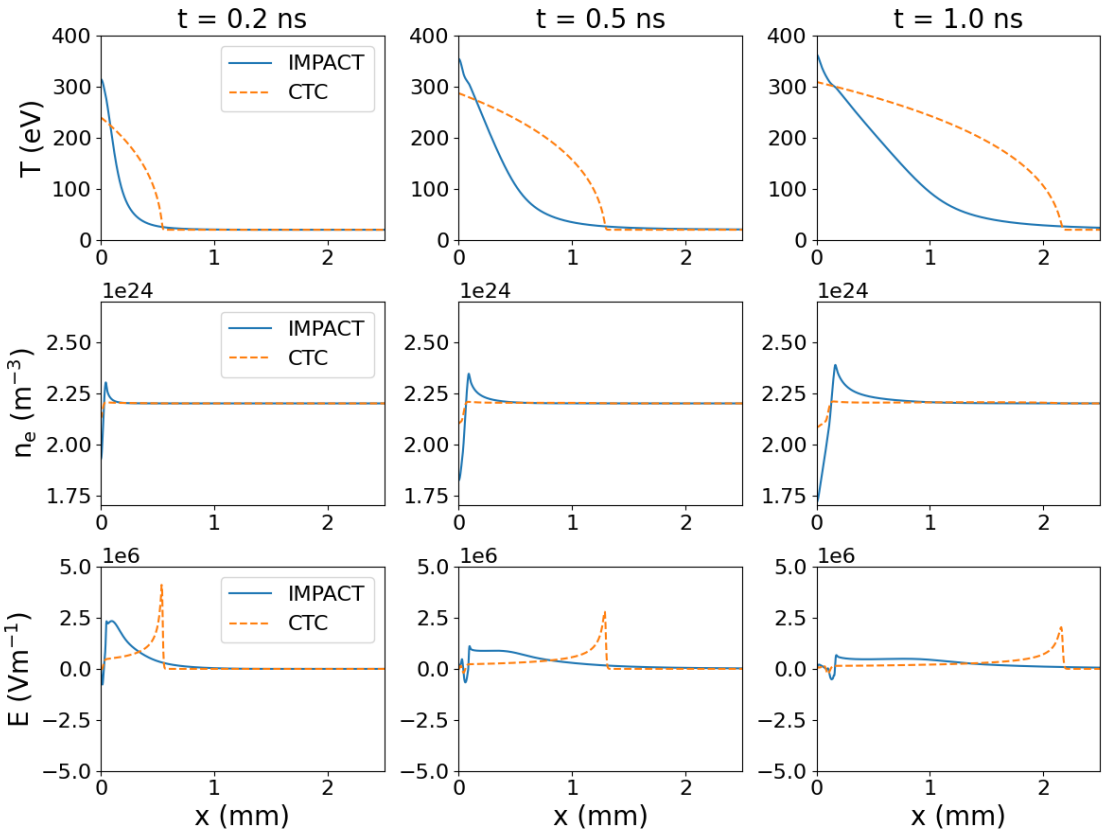

Figure 6.5: Temporal evolution of the temperature, density, and electric field profiles during laser-heating of an initially uniform nitrogen plasma ($Z = 7$) with $n_e = 2.2 \times 10^{24}$ m^{-3}, comparing the results of IMPACT (with electron inertia) and CTC.

seed field for the Biermann battery, and therefore affects the generation of magnetic fields in a wide range of plasma environments from astrophysical shocks to laser-driven inertial confinement fusion experiments. Non-local transport distorts the electron distribution function under such conditions, suppressing the Biermann battery producing electric field [92]. The use of flux limiters to account for the non-local heat-flux suppression in these scenarios leads to spuriously large temperature gradients, as they do not capture electron pre-heat which smooth these gradients, increasing the magnitude of the locally predicted electric field further [141].

6.3.1 Kinetic and fluid simulations

Example profiles obtained during the heating of a nitrogen plasma are shown in fig. 6.5, comparing the results from IMPACT and CTC. It is immediately clear that non-local transport is significant due to the discrepancies between the temperature profiles, so much so that one might mistakenly draw the conclusion that pre-heat is more significant in the MHD simulations due to the progression of the heat-front. However, this is due to the significantly larger heat-flow predicted by the

local model, leading to more rapid advection of the internal energy. In this case, heat streams freely through the plasma, with the heat-flow approaching the free-streaming limit. The non-local pre-heat is still significant and would be most notable if the local simulations were flux-limited such that both IMPACT and VFP had the same maximum heat-flow.

Additionally, as heat is more rapidly advected away from the region heated by the laser, the maximum temperature remains lower in the local simulation. As a result, more energy is coupled into the simulation as the collision rate remains higher, leading to greater inverse bremsstrahlung heating. This is compounded by the shallower depth of the electron density cavity in the local simulation also resulting in a higher collision rate.

The properties of the temperature profile are reflected in the electron density. In these unmagnetised simulations it is gradients in the thermal pressure which drive bulk flows in the ion population (eq. 2.91). As ionisation is not included, heating leads to an immediate cavitation in the density profile. The cavity grows steadily with time after an initial period during which the heavier ions are accelerated. As ∇P_e remains higher in the centre of the VFP simulation, due to the reduction in the heat-flow caused by non-local transport, a deeper cavity is formed. Meanwhile, in the local simulation the rapidly progressing heat-front causes an extended region where the pressure gradient may accelerate ions. As a result, hydrodynamic flow is driven throughout this region, although the maximum flow speed is much lower than the sound speed. While the heat-front expands at a velocity above the sound speed, the pressure associated with it is not sufficient to accelerate the ions above the sound speed.

The pressure gradient is reflected in the electric field. In local simulations $\mathbf{E} \propto \nabla T_e$ in the regime explored here, while in the non-local case there are greater differences between the electric field and the pressure gradient due to the dependence on different moments of the distribution function. The non-local pressure gradient is (neglecting anisotropy due to $\mathbf{f}_2$) $\partial_\rho P_e \propto \partial_\rho \int w^2 f_0 v^2 dv$ in comparison to eq. 6.3.

The manifestation of the electric field in the local and non-local cases are in contrast. The local simulations having a pronounced spike at the edge of the heated plasma where the heat-front is, while in the non-local case the electric field is greatest closer to the core. As the gradients relax over time the magnitude of the fields then decreases. In both instances gradients in the electron density are dominant in the centre of the cavity, causing the sign of the electric field to change from positive to negative, with the effect more pronounced for the non-local case.

In these simulations the assumption that $Z = 7$ is reasonable in the bulk of

the plasma, but less justified in the sheath region where the temperature is lower. Considering the diffusive heat-flow equation, where the conductivity is given by $(n_e T_e \tau_B / m_e)\xi\kappa_\parallel$ using the collision fix, the heat-front may be expected to expand more rapidly at lower ionisation as the conductivity scales as ξ/Z. However, this neglects the conversion of thermal energy into the internal energy of the plasma required to ionise electrons. This is expected to be the dominant effect, resulting in reduced expansion of the heat-front and an increase in the temperature gradient for both kinetic and fluid simulations.

6.3.2 Effect of non-local transport

These results implicitly demonstrate the suppression of the electric field by non-local heat-flow. Although the magnitude of the electric field is lower in the kinetic simulations, the differences in their evolution compared to the fluid simulation make direct comparison challenging. To quantitatively demonstrate this suppression the local Ohm's law (eq. 6.2) can be used, as demonstrated in fig. 6.6. The result is similar to that expected by non-local heat-flow, with a reduction in the maximum of $\sim 50\%$ while also extending further into the cold plasma. The reduction in the heat-flow is even more severe, approaching $\sim 90\%$.

That the reduction in the heat-flow is so large is almost certainly a result of both significant non-local transport and strong IB heating, resulting in the distribution function being distorted towards a Langdon distribution in the heated region. In all simulations it is found that $\alpha_M \gg 1$ within the laser FWHM, resulting in $m \approx 5$ using the formula of Matte (eq. 2.128). To distinguish the balance between non-local transport and IB heating simulations should be conducted with a Maxwellian heating operator, which would also provide an opportunity to investigate the effect of super-Gaussian transport on the electric field in greater detail.

A rough idea of the importance of super-Gaussian transport for the thermo-electric simulations shown here is provided by calculating the ratio of the classical transport coefficients to the super-Gaussian transport coefficients [47]. For simplicity gradients in the density, which become important due to the breaking of Onsager symmetry for non-Maxwellian distributions, are also neglected here. For the electric field and heat-flow equation the ratios of interest are then

$$\left(\frac{E_{SG}}{E}\right)_{\rho,\chi_T=0} = \frac{\gamma_{\parallel,SG} + \beta_{\parallel,SG}}{1+\beta_\parallel} \quad \text{and} \quad \left(\frac{q_{SG}}{q}\right)_{\rho,\chi_T=0} = \frac{\kappa_{\parallel,SG} + \phi_{\parallel,SG}}{\kappa_\parallel} \tag{6.4}$$

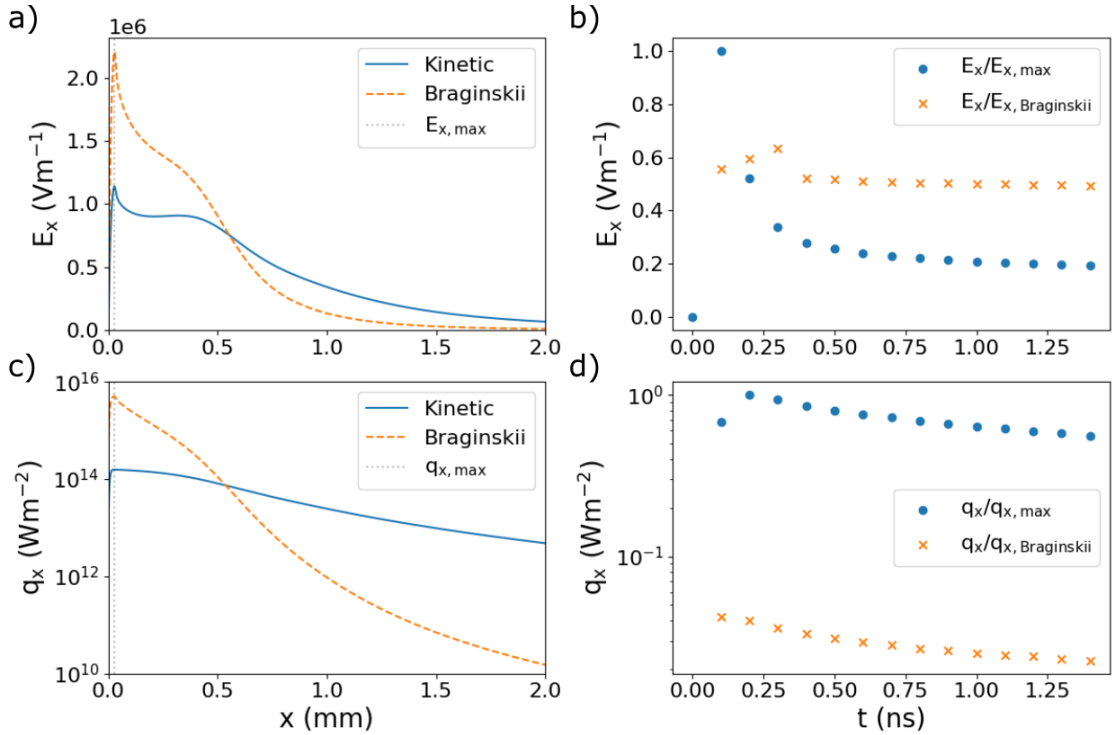

Figure 6.6: IMPACT simulations with the same initial conditions as fig. 6.5, although ion motion is disabled. The top panels show the electric field compared to that calculated using the local Ohm's law. Hydrodynamic motion of the ions is disabled so the maximum is not dominated by gradients in the electron density. In a) the spatial profiles are compared at $t = 0.5$ ns, while in b) the normalised electric field value and the ratio of the maximum to the local prediction are shown where E_x is at a maximum. The bottom panels show the heat-flow compared to the Braginskii heat-flow. In c) the spatial profiles at $t = 0.5$ ns are shown, while in d) the normalised heat-flow value and the ratio of the maximum to the local prediction are shown where $q_{\mathrm{x,Braginskii}}$ is at a maximum. A change in the ratio $E_{\mathrm{x,max}}/E_{\mathrm{x,Braginskii}}$ is seen between $t = 0.3$ and 0.4 ns due to $E_{\mathrm{x,max}}$ shifting away from the maximum in $E_{\mathrm{x,Braginskii}}$.

where the subscript 'SG' refers to the super-Gaussian transport coefficients. In the limit $m = 5$ then $E_{SG}/E = 0.73$ and $q_{SG}/q = 0.23$, showing that the modification to the heat-flow is greater than that to the electric field due to super-Gaussian transport - although a moderate reduction in E_ρ is still expected.

6.3.3 Knudsen number and inertia

To quantify the significance of non-local transport in these unmagnetised simulations the Knudsen number $|\lambda_T/l_T|$ is evaluated, as shown in fig. 6.7. It can be seen that $|\lambda_T/l_T|$ remains at a maximum near the heated region, with the laser power near its maximum at all times shown here. The maximum value is $|\lambda_T/l_T| = 0.60$ after 200 ps suggesting significant non-local transport, which was seen in the previous figures.

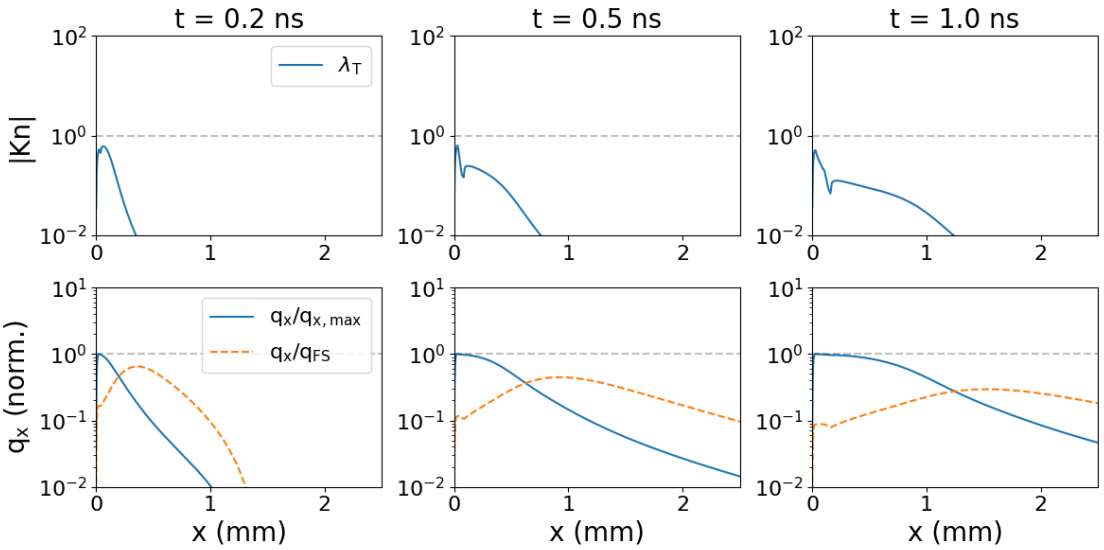

Figure 6.7: Temporal evolution of the non-local parameter and heat-flow profiles for the IMPACT simulations shown in fig. 6.5. The non-local parameter is evaluated using the ratio λ_T/l_T, while the heat-flow is shown normalised with both the maximum heat-flow and the free-streaming limit.

The heat-flow can also be seen to reach a maximum near this position.

A second metric of interest is the ratio of the heat-flow to the free-streaming limit. As described in section 4.3.1 this provides an alternative metric for judging the significance of non-local transport, by means of a weighted average of the relative anisotropy within the heat-carrying population. Here the classic definition of q_{FS} is used, although similar results are found using eq. 4.17. The ratio can be seen to exceed 10% for the bulk of the hot-plasma, extending to the edge of the heat-front, with a maximum of $|q_x/q_{FS}| = 0.65$ at 200 ps. The maximum is located at the base of the heat-front, where collisionless electrons pre-heat the cold plasma.

The variation in the non-local parameter $|q_x/q_{FS}|$ as the electron density is varied in these simulations is shown in fig. 6.8 at two different positions. The first position in the hot plasma experiences a reduction in heat-flow due to non-local transport, while at the second heat-flow is increased. The relative anisotropy increases rapidly with time, having reached a maximum at both points by $t = 0.2$ ns, before decaying over a longer timescale. At both positions decreasing n_e leads to an increase in non-local in the unmagnetised plasma. Fundamentally, this increase in non-local transport with decreasing density is tied to the variation in the IB heating rate with density, and the resulting effect on $\lambda_T/|l_T|$.

First, consider the variation in the mean-free-path with electron density. As $\lambda_T \propto T_e^2/n_e$, increasing the density will result in larger values of λ_T. However, this also results in a decrease in the IB heating rate, which causes the temperature to

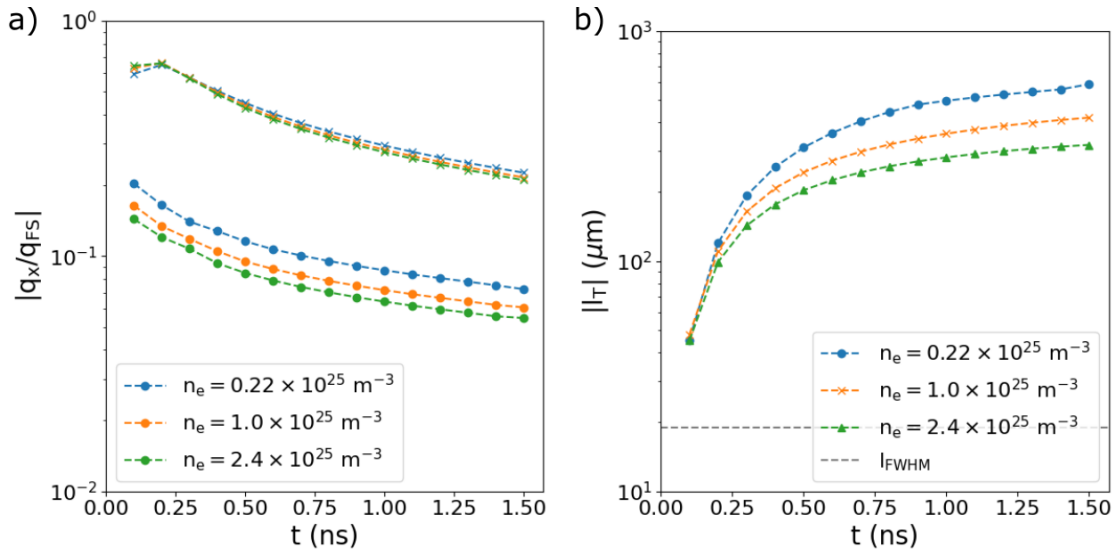

Figure 6.8: Temporal evolution of plasma parameters for laser-heating simulations of an initially uniform nitrogen plasma ($Z = 7$) with varying density. In a) the heat-flow as a fraction of the free-streaming limit is evaluated where q_x is at a maximum (circles) in the hot plasma, and where q_x/q_{FS} is at a maximum (crosses) near the base of the heat-front. In b) the absolute minimum of the temperature length scale is shown, as well as the length scale of the laser intensity profile at $x = w_{\mathrm{FWHM}}$.

decrease. For λ_T to increase as n_e decreases, the heating rate must be such that for a fixed laser profile the power law scaling of T_e with n_e is less than 1/2. This can be shown to be the case for the simple case of 0D heating tests, such as those shown in fig. 2.7. However, the inclusion of transport effects complicates this simple picture.

The global minimum l_T perpendicular to the laser axis is found to be coupled with the length scale of the laser intensity spatial profile; for a Gaussian spot this is given by $|l_I| = w_{\mathrm{FWHM}}/(8 \ln 2)$ at $x = w_{\mathrm{FWHM}}$, which is shorter than the minimum in l_T after 100 ps for all simulations shown here as seen in fig. 6.8. Initially the minimum l_T is found to be independent of n_e, before approaching a quasi-steady value in these 1D simulations which is dependent on n_e that relaxes with time.

A final consideration then regards the importance of electron inertia, which has so far been included in all IMPACT simulations. Fig. 6.9 shows that despite values of $|\lambda_T/l_T| = 0.6$, electron inertia has little effect on either the heat-flow or the electric field. It is postulated that the presence of strong IB heating may distort the distribution function in such a way as to reduce electron inertia, by providing a source of thermal electrons at increasing temperature. Studying the relaxation of the temperature perturbation after laser heating is finished may provide insight into this problem, and is subject for future investigation. Additionally, the validity of the diffusion approximation in this regime is also in question, which would require comparison with a code that retains terms of higher order than $\mathbf{f}_1$.

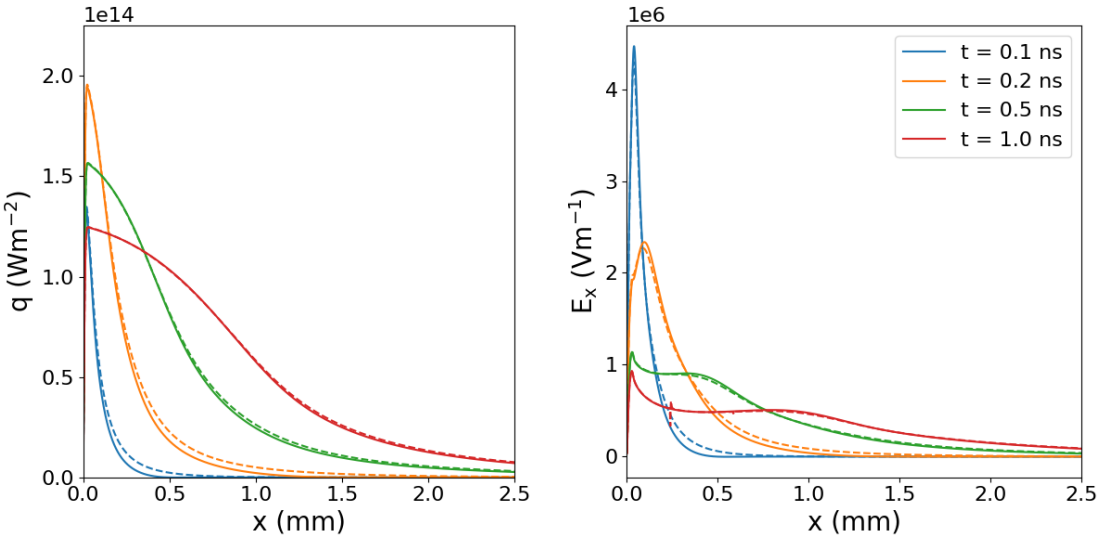

Figure 6.9: Heat-flow and electric field profiles at varying times for the simulation setup at $n_e = 0.22 \times 10^{25}$ m^{-3} shown in fig. 6.5, comparing the result with and without electron inertia. Hydrodynamic ion motion is disabled in these simulations as including hydrodynamic motion without electron inertia is found to be unstable. A small kink can be seen to from in the electric field at late time that is attributed to the numerical grid.

6.4 Nernst effect

The addition of an applied magnetic field to the experiment setup, aligned parallel to the laser axis, the z-axis, means that the magnetic terms in Ohm's law can now affect transport and the induction equation becomes non-zero. Considering the induction equation for problems with cylindrical symmetry, there are no gradients along the z-axis , which results in $E_z = 0$, with only $\partial_t B_z$ being non-zero. The induction equation then reads

$$\frac{\partial B_z}{\partial t} = \partial_\rho E_\phi. \tag{6.5}$$

with the expressions for the radial and azimuthal components of the electric field given by

$$E_\rho = -\frac{T_e}{e}\left[\frac{\partial_\rho n_e}{n_e} + (1+\beta_\perp)\frac{\partial_\rho T_e}{T_e} - \frac{2}{\beta}\left(1 - \frac{\alpha_\wedge}{\chi_B}\right)\frac{b_z \partial_\rho B_z}{|B_z|}\right] \tag{6.6}$$

and

$$E_\phi = u_\rho B_z - \frac{T_e}{e}\left[\beta_\wedge b_z \frac{\partial_\rho T_e}{T_e} + \frac{2}{\beta}\frac{\alpha_\perp}{\chi_B}\frac{\partial_\rho B_z}{|B_z|}\right] \tag{6.7}$$

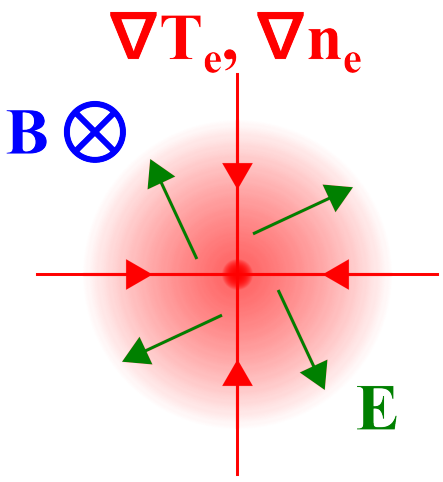

Figure 6.10: Diagram showing the temperature and density vectors resulting when a laser heats and under-dense gas with cylindrical symmetry in the radial plane. A circulating electric field is then formed via the thermo-electric effect in the presence of an applied field, where the radial component opposes the gradient in the pressure and the azimuthal component has the opposite sign to the product of $b_z \partial_\rho T_e$.

following the form shown in eq. 3.12 and eq. 3.13, with the axial component zero.

The azimuthal component can be substituted into eq. 6.5 to give an equation governing the evolution of the magnetic field. Provided the direction of the magnetic field remains constant, the direction of E_ϕ can be shown to depend on the magnetic field unit vector (i.e. reversing the direction of the magnetic field causes E_ϕ to change sign). A schematic diagram of the electric and magnetic field structure is shown in fig. 6.10. E_ϕ consists of contributions from the diffusive term and the radial component of the advective term in Ohm's law. Only components of the advection velocity $\mathbf{v_B}$ (eq. 2.106) perpendicular to the magnetic field axis give rise to an electric field. Note that for the Nernst effect it is the second derivative of T_e that is responsible; this changes sign where $\partial_\rho T_e$ is at a maximum and a turning point is found, resulting in suppression of the magnetic field towards the top of the heat-front and amplification at the base.

Comparing eq. 6.7 to the expression for the magnetic field advection velocity provided by eq. 2.106, it can be seen that there is actually some ambiguity in the manner with which the resistive terms advect magnetic field. While it may seem more natural to take the ratio of the $\gamma_\perp$ to $\delta_\perp$ term when seeking to quantify the importance of thermally versus current driven advection effects [63], actually the more appropriate ratio is that of the $\gamma_\perp$ to $\delta_\wedge$ term. This is a result of making the approximation $\nabla \times \mathbf{B} = \mu_0 \mathbf{J}$, as the field is then advected with respect to gradients in $\mathbf{B}$ which give rise to the current. If the magnetic field varies over the same length

scale as the temperature then the ratio between the thermal and current driven advection velocities is

$$\frac{|\mathbf{v}_{N\perp}|}{|\mathbf{v}_{R\wedge}|} \approx \frac{\chi_B \beta}{2} \frac{\gamma_\perp}{\delta_\wedge} \approx \beta \tag{6.8}$$

which is almost solely dependent upon the ratio of the thermal pressure to magnetic pressure as $(\chi_B \gamma_\perp)(2\delta_\wedge) \approx 1$. This result holds with thermal effects dominant over current effects provided $\beta \gg 1$ and $l_B \leq l_T$ [50], with the latter point found to be true due to the coupling between magnetic field advection and heat-flow as mentioned previously.

The plasmas considered here are expected to have $\beta > 1$ in both the bulk and at the heat-front. The regions of the plasma where β is smallest are those close to the bottom of the heat-front, where the magnetic field is amplified due to advection and the electron temperature is cooler. In these regions, the ratio of the thermal pressure to magnetic pressure, based on the applied field strength, provides a reliable estimate for whether current driven effects are likely to be important in the plasma; if $\beta \gg 1$ here, then current driven effects are unlikely to be significant. This ratio can be estimated using

$$\beta = \frac{n_e T_e}{|\mathbf{B}|^2/2\mu_0} \approx \frac{n_e}{10^{25}\mathrm{m}^{-3}} \frac{T_e}{\mathrm{eV}} \frac{|\mathbf{B}|}{\mathrm{T}}^{-2}. \tag{6.9}$$

Higher density laser plasmas tend to have $\beta \gg 1$, as both the electron density increases and the temperature increases due to greater IB heating.

Under these conditions, eq. 6.7 reduces to

$$E_\phi = u_\rho B_z - \frac{T_e}{e} \beta_\wedge b_z \frac{\partial_\rho T_e}{T_e} \tag{6.10}$$

so changes to the magnetic field structure are attributed to either hydrodynamic motion or the Nernst effect.

Having established that thermal transport effects will be most significant in the plasmas considered here, the remaining question is whether Nernst advection can be separated from hydrodynamic motion; for a definitive measurement of the Nernst effect $\mathbf{v}_{N\perp} \gg \mathbf{u}$. The hydrodynamic velocity can be estimated using eq. 2.91 as

$$\mathbf{u} \approx -\frac{\nabla P_e}{\rho_i} \Delta t \tag{6.11}$$

where the gradient in the magnetic pressure has been dropped relative to gradients in the thermal pressure, and the pressure gradients is assumed constant. While the Nernst velocity is near instantaneous, owing to the response of the electrons, the hydrodynamic velocity increases over a longer timescale Δt as the heavier ions are accelerated. The ratio of the velocities is then

$$\frac{|\mathbf{v}_{N\perp}|}{|\mathbf{u}|} = \frac{\tau_B}{\Delta t}\frac{\rho_i}{\rho_e}\gamma_\perp = \frac{\tau_B}{\Delta t}\frac{m_i}{Zm_e}\gamma_\perp = \frac{1}{\omega_g \Delta t}\frac{m_i}{Zm_e}\beta_\wedge \tag{6.12}$$

provided $l_T \gg l_n$ [63]. This expression initially overestimates the impact of hydrodynamics when the plasma column is forming, but then underestimates the hydrodynamic velocity later in the plasma evolution as it does not account for the ion inertia.

The fundamental parameter that quantifies that the advection mechanism is a competition between electron and ion effects is m_i/Zm_e; as this is much larger than one electron behaviour and the Nernst effect is dominant on short timescales as mentioned previously. While the ratio is only weakly dependent on the choice of gas as when fully ionised $m_i/Zm_e \approx m_p/m_e = 1836$, it can vary for different isotopes of an element. This is most notable for lighter elements such as hydrogen, with the Nernst effect being more significant for heavier isotopes due to the relative decrease in the hydrodynamic velocity.

$\tau_B/\Delta t$ is a measure of the collisionality of the electrons over the hydrodynamic timescale, with less collisional plasmas (greater τ_B) experiencing stronger Nernst advection. This would appear to suggest that plasmas for which the Nernst effect is significant are less likely to obey the fluid approximation. As time progresses the ion response increases, while collisions also become more significant within the electron population, providing the mechanism via which hydrodynamic advection can become dominant. When $\Delta t \gg 1836\tau_B$ this can be expected to occur for $\chi_B < 1$.

As seen in fig. 2.5, $\gamma_\perp$ describes the effect of magnetisation on the Nernst effect; $\gamma_\perp$ is constant at low magnetisation, increasing magnetisation past $\chi_B \simeq 1$ leads to a reduction in $\gamma_\perp$, and increasing Z leads to an order of magnitude increase when $\chi_B \ll 1$ but has almost no impact when $\chi_B \gg 1$. However, this exposes a fundamental conundrum - plasmas for which the magnetic field most significantly impact thermal transport are impacted less by the Nernst effect, a result which is implicit in eq. 4.25. Furthermore, as $\chi_B \propto \tau_B$ making the plasma collisionless also magnetises the plasma, in turn leading to a maximum degree of non-local transport when $\chi_B \approx 1$. With $\gamma_\perp(\chi_B \gg 1) \propto \chi_B^{-2}$, the Nernst advection velocity then

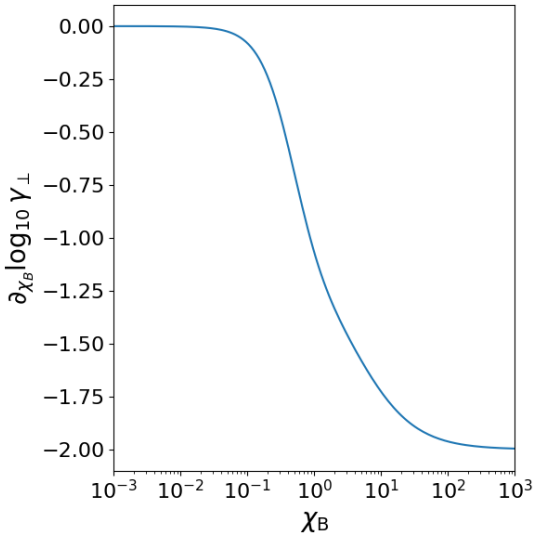

Figure 6.11: Power law scaling of the transport coefficient $\gamma_\perp$ with magnetisation.

decreases linearly with τ_B in this regime. In fact, taking the gradient of $\gamma_\perp$ in fig. 6.11 it can be shown that increasing τ_B for fixed χ_B only leads to an increase in the advection velocity provided $\chi_B < 1$ initially, regardless of Z.

Due to the coupling between magnetic field advection and heat-flow the requirement for non-local Nernst advection is simply that non-local heat-transport occurs with a magnetic field present, which can be arbitrarily small, so can be expected to readily occur in most laser-plasmas. However, for non-local Nernst advection to occur in a plasma where the magnetic field is of interest requires both $\chi_H \approx 1$ (so the heat-flow is impacted by the field) and $r_{g,H} \approx \lambda_H \gtrsim |l_T|$ (so the transport is non-local). This occurs because the heat-carrying electrons are more rapidly magnetised than the thermal population, leading to a much more restrictive condition. To increase r_g for fixed χ both the electron temperature and density must be increased. If the electron density is not increased then the plasma will become strongly magnetised, leading to a reduction in the relative anisotropy as the temperature is increased following the theory outlined in chapter 4.

6.4.1 Kinetic and fluid simulations

Simulations comparing the results of IMPACT and CTC for the heating of a nitrogen plasma with $n_e = 0.22 \times 10^{25}$ m^{-3} and an applied magnetic field of $B_z = 3$ T are shown in fig. 6.12. Electron inertia has not been included in the IMPACT simulations due to the growth of significant unexplained oscillations in the magnetic field profile, which has the additional consequence of meaning that the hydrodynamic motion of the ions must also be prevented to maintain stability. However, as was demonstrated

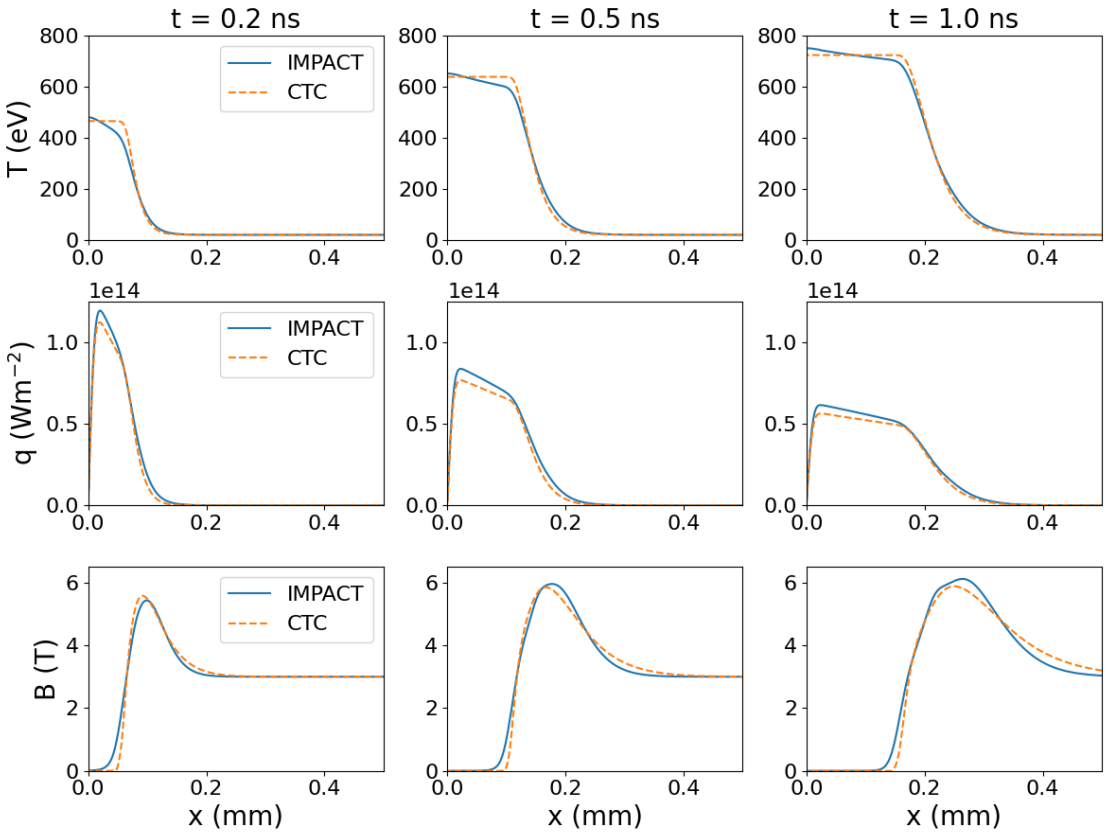

Figure 6.12: Temporal evolution of the temperature, heat-flow and magnetic field profiles during laser-heating of an initially uniform nitrogen plasma ($Z = 7$) with $n_e = 2.2 \times 10^{24}$ m^{-3} and an applied field of $B_z = 3$ T, comparing the results of IMPACT (without electron inertia) with CTC.

in fig. 6.9 electron inertia has little effect on the unmagnetised simulations, and as magnetisation reduces inertial effects this may be justified. The effect of ion motion will be considered again in section 6.4.4

The most noticeable difference between the simulations with and without (fig. 6.5) an applied magnetic field is the increase in electron temperature and the confinement of the heat-front. This is a result of the magnetisation of the electrons, which causes the perpendicular thermal conductivity to be reduced. Previously for the IMPACT simulations at $t = 0.5$ ns the maximum temperature was $T_e \approx 350$ eV with the heat-front extending to $x \approx 1$ mm, whereas with an applied field of $B_z = 3$ T the maximum temperature increases to $T_e \approx 650$ eV while the heat-front is confined to $x \approx 0.25$ mm.

As hydrodynamic ion motion is not included, the dominant mechanism via which the magnetic field is able to evolve here is the Nernst effect. Initially magnetic field is advected from the region heated by the laser to the edge of the heat-front, with demagnetisation further enhancing the rate of advection within the cavity.

The Nernst velocity remains large in the cavity, as while the temperature gradient decreases the temperature increases, causing complete expulsion of the magnetic field. As more of the magnetic field is swept up by the expanding heat-front the cavity grows, and amplification of the field at the heat-front increases. Where B_z is at a maximum $|\mathbf{v}_{N\perp}| \sim 10^5$ ms^{-1}. At the heat-front the advection velocity decreases with time; initially this is caused by an increase in the magnetisation, while after $t \sim 0.5$ ns it is a result of the relaxation of the temperature gradient.

Unlike simulations of the thermo-electric effect, which had the same laser and initial plasma conditions but no applied magnetic field, the discrepancies between the simulations are seen to be relatively minor. These are most noticeable inside the magnetic field cavity and at the edge of the heat-front. However, the maximums and advection speeds seen in all profiles are generally very similar. For this reason, the use of CTC simulations to examine the balance between hydrodynamic and Nernst advections will be considered representative of what might be expected had IMPACT simulations with hydrodynamic ion motion been possible.

In these magnetised simulations the increase in the plasma temperature is likely to increase the validity of the assumption that the plasma is fully ionised, although discrepancies are likely to arise in the behaviour found in the sheath. Similar to the unmagnetised simulations shown in section 6.3 the plasma's thermal energy will be reduced as it is converted into internal energy during ionisation. The inclusion of a magnetic field makes the effect of ionisation more complex than in an unmagnetised plasma, owing to the dependence of transport effects on the magnetisation. Specifically, in the sheath region, variations in the collision frequency will influence the degree of magnetisation. However, more substantial changes may arise from variations in the plasma's resistivity. Currently, in the fully ionised simulations with a background temperature of 20 eV, the plasma exhibits very low resistance, behaving almost like an ideal conductor. If the resistivity increases, resistive diffusion will become more pronounced, smoothing the magnetic field gradients and reducing the peak of the amplified field.

6.4.2 Validity of fluid approximation

The agreement between fluid and kinetic simulations appears surprising as the mean-free-path of thermal electrons is of the order of 100 µm, while the minimum length scale is almost an order of magnitude shorter than in the simulations with no applied magnetic field, resulting in $\lambda_H \gg |l_T|$ as seen in fig. 6.13. However, the effects of the magnetic field must be considered. The properties of the plasma will be considered in two separate regions; the heat-front where length scales are short and transport

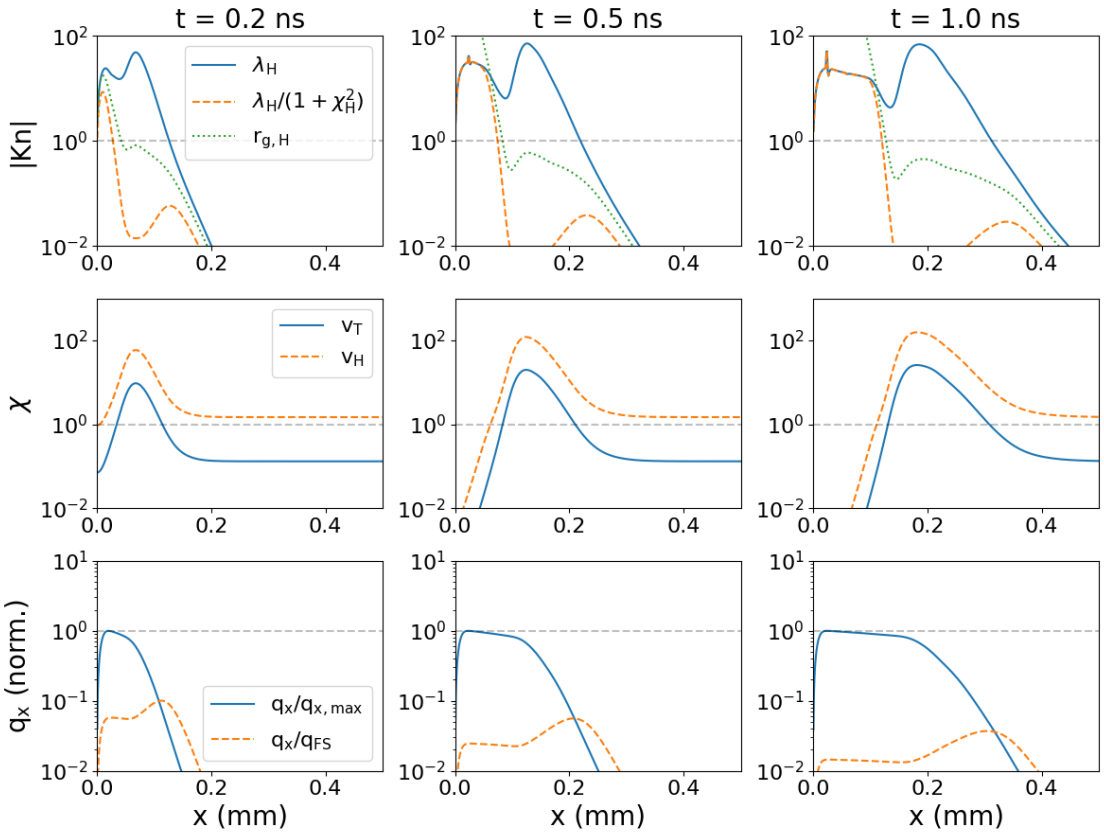

Figure 6.13: Temporal evolution of the non-local parameter, magnetisation and heat-flow profiles for the IMPACT simulations shown in fig. 6.12. The non-local parameters is evaluated using three values for the electron diffusion length of the heat-carrying electrons relative to the temperature length scale; these are λ_H, $r_{g,H}$, and $\lambda_H/(1+\chi_H^2)$. The magnetisation is provided for both thermal and heat-carrying electrons. Heat-flow is then shown normalised by both the maximum heat-flow and the free-streaming limit.

most noticeably influences the evolution of the plasma, and the hot core which is demagnetised by the Nernst effect.

The magnetisation at the heat-front is such that the heat-carrying population is initially strongly magnetised, with electron diffusion in this regime limited by the gyro-radius rather than the mean-free-path. Still, with $r_{g,H} \sim |l_T|$ non-local transport may be expected to be significant. However, as $\chi_H \gg 1$ the electron diffusion distance is further constrained with the effective mean-free-path $\lambda_{f1,H} = \lambda_H/(1+\chi_H^2) \approx r_{g,H}/\chi_H$ in this regime. It is important to remember here that only considering the thermal population (i.e. using $\chi_B \approx \chi_T$) may mistakenly lead to the conclusion the plasma is not strongly magnetised and the identification of incorrect trends - for transport effects it is the suprathermal electrons that are important. As time progresses amplification of the magnetic field by the Nernst effect causes the magnetic transport barrier to become more significant, further localising transport.

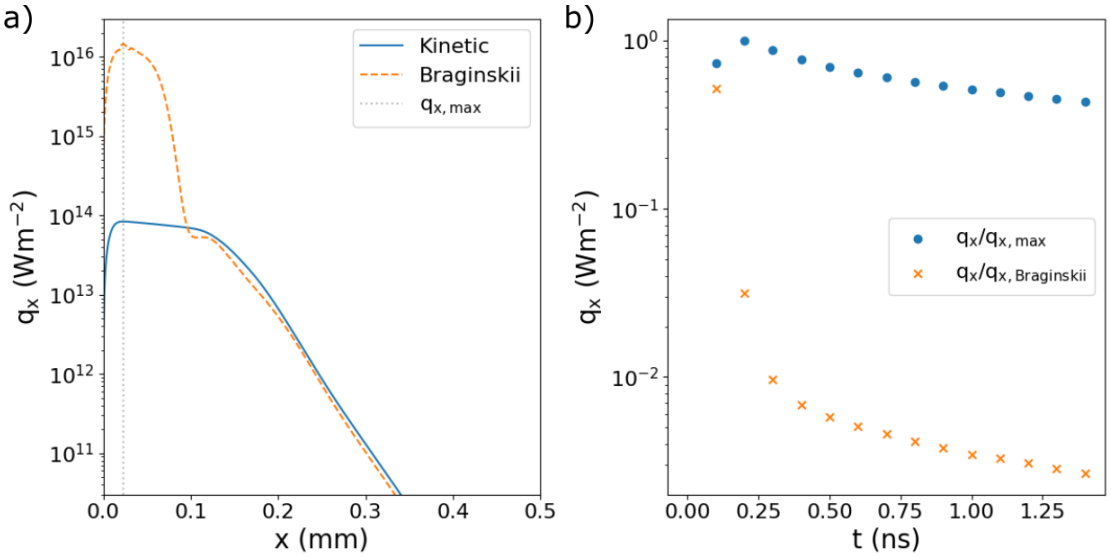

Figure 6.14: Comparison of the heat-flow from the IMPACT simulation shown in fig. 6.12 with the predicted local Braginskii heat-flow. Shown are a) the spatial profiles at $t = 0.5$ ns and b) the evolution at the point where q_x it at a maximum of both the normalised heat-flow and the ratio of the heat-flow to the local prediction.

However, the localising effect at the heat-front is in stark contrast to the demagnetising effect inside cavity, where expulsion of the magnetic field causes non-local transport to occur within an initially localised plasma [49]. In fig. 6.14 the local heat-flow obtained from the IMPACT simulation in fig. 6.12 is shown. While both fluid and kinetic simulations have similar heat-flow profiles, the subtle gradient in temperature of the kinetic simulation causes the predicted local heat-flow to be two-orders of magnitude larger. A combination of IB heating driving the distribution function towards a super-Gaussian, and non-local transport as $\lambda_H/|l_T| \gg 1$ with $\chi_H \ll 1$, cause the distribution function to become highly distorted with an absence of heat-carrying electrons. However, the heat-carrying electrons which travel down the temperature gradient are immediately localised by the magnetic transport barrier at the heat-front. For an electron with $\sim 2\ v_T$ originating in the hot cavity at $t = 0.5$ ns initially $\lambda_{ei} \approx 10$ mm and $\chi_{ei} \approx 0$, but on reaching the transport barrier it will be restricted to $r_g \approx 30$ µm with $\chi_{ei} \approx 350$.

Thus, while the system exhibits both local and non-local transport it is the localising effect of the transport barrier which dominates the behaviour. If the simulation was allowed to progress further, with heating maintained, it appears unlikely that differences arising due to variations in the transport within the cavity become significant due to the reduction in the IB heating rate at higher temperature.

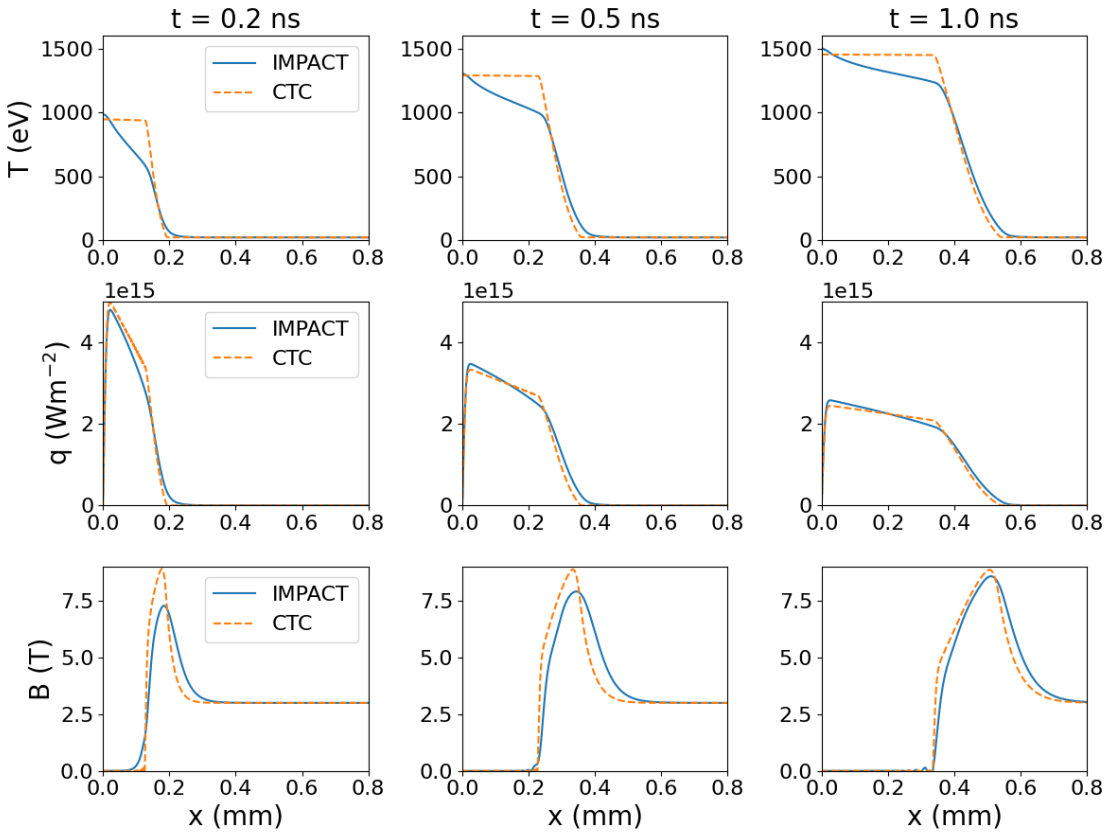

Figure 6.15: The same figure as fig. 6.12, but now with an increased electron density of $n_e = 2.4 \times 10^{25}$ m^{-3}.

6.4.3 Effect of varying electron density

By increasing the electron density the magnetisation of the plasma can be decreased, leading to an increase in anisotropy of the distribution which results in greater advection and more non-local transport. This result defies typical expectation in laser-plasmas, where one would expect a more collisional plasma to exhibit more local transport. That magnetisation increases with density is linked to the variation of IB heating with density in a similar manner to that of the increase in non-local transport with decreasing density. Now though as $\chi_T \propto \tau_T \propto T_e^{3/2}/n_e$ the plasma will magnetised for a fixed laser profile provided the power law scaling of T_e with n_e is less than 2/3.

To demonstrate this effect IMPACT and CTC simulations are conducted at an increased electron density of $n_e = 2.4 \times 10^{24}$ m^{-3} in fig. 6.15, compared to $n_e = 0.22 \times 10^{25}$ m^{-3} in fig. 6.12. For the temperature profile both the maximum electron temperature and extent of the heat-front increase by a factor of ~ 2. The Nernst velocity and cavity radius also increase, with the amplitude of the maximum magnetic field increasing by $\sim 50\%$. While the mean-free-path has decreased by a factor of ~ 2 the gyro-radius has increased by a similar amount, with the net effect a

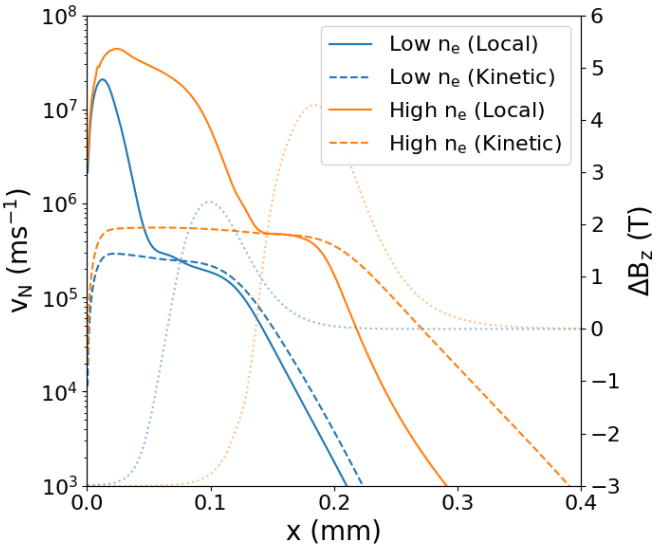

Figure 6.16: Spatial profile of the Nernst velocity from the simulations shown in fig. 6.12 and fig. 6.15 at $t = 0.2$ ns, where $n_e = 0.22 \times 10^{25}$ (low) and 2.4×10^{25} m^{-3} (high) respectively. Both the local and kinetic Nernst velocity are shown, as well as the change in amplitude of the magnetic field profile relative to the applied field of $B_z = 3$ T.

factor of ~ 4 change in the magnetisation in the heated plasma. In the cold plasma the collision time increases by a factor of ~ 10 as the temperature remains the same, with both the thermal and heat-carrying electrons now initially weakly magnetised.

The difference between the kinetic and fluid simulations is now more apparent, particularly at early times. Evidence of non-local transport can be seen in both the temperature and heat-flow profiles, with the loss of heat-carrying electrons causing pre-heating of the cold plasma in the kinetic simulation and a reduction in the peak heat-flow. Additionally, non-local 'pre-Nernst' is seen in the magnetic field profile [39]. Even though the absolute magnitude of the heat-flow is small in this region the heat-flow remains at $\sim 10\%$ of the free-streaming limit, so the relative anisotropy is significant and the Nernst velocity (eq. 4.25) an order of magnitude larger than the local prediction (eq. 2.119) at $|\mathbf{v}_N| \approx 10^5$ ms^{-1} as seen in fig. 6.16. In comparison, significant pre-Nernst is not observed in the lower density simulations.

Later in the simulation the transport barrier formed by the Nernst effect acts to keep the heat-flow in an increasingly local regime, despite the magnetic field inside the cavity falling to zero. As was seen earlier transport within the cavity remains highly kinetic, as is evident from the significant increase in the Nernst velocity relative to the local result in fig. 6.16. However, localisation by the transport barrier and a reduction in the IB heating mean that non-local transport is most significant early in the plasma evolution.

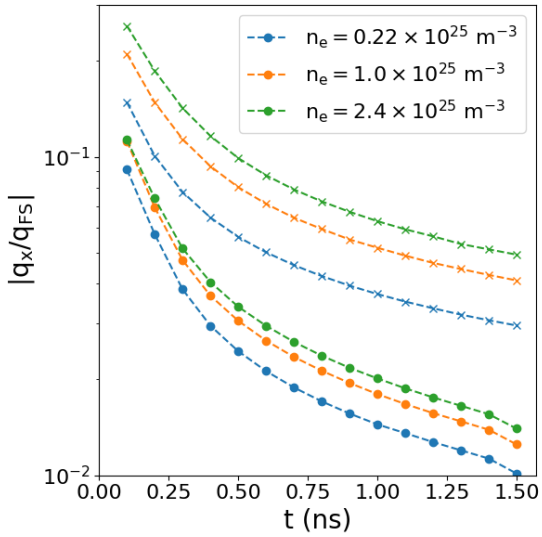

Figure 6.17: Temporal evolution of the heat-flow as a fraction of the free-streaming limit for simulations of the laser-heating of a nitrogen plasma at varying density. The heat-flow is evaluated where q_x is at a maximum (circles) in the hot plasma, and where q_x/q_{FS} is at a maximum (crosses) near the base of the heat-front.

In fig. 6.17 the variation in $|q_x/q_{FS}|$ with time, reflecting the relative anisotropy and significance of non-local transport in the plasma, is shown for simulations at varying density as was done in the unmagnetised case in fig. 6.8. The change in the ratio $|q_x/q_{FS}|$ between unmagnetised and magnetised simulations is deceptively small, only varying by a factor of ~ 2, as the increase in non-local transport is clearly significant in the unmagnetised case. As was examined in fig. 4.12 this is due to the reduction of the mobility of the heat-carrying population with magnetisation, causing the point at which maximum relative anisotropy occurs within the heat-carrying population to shift to larger values of $|q_x/q_{FS}|$. As the density increases here the increase in $|q_x/q_{FS}|$ always corresponds to greater non-local transport. This is because in all cases where $|q_x/q_{FS}|$ increases with decreasing magnetisation, the relative anisotropy decreases, although the increase is not linear. Maximum relative anisotropy in the simulations is achieved before $t = 0.1$ ns and then decreases as the simulation progresses, with the rate of decrease greatest initially.

To understand how greater magnetic non-locality can be observed, where heat-carrying electrons are able to escape the magnetic transport barrier [92], fig. 4.9 which describes the variation of the effective mean-free-path with key plasma parameters can be revisited. The simplest approach to increasing anisotropy here would be to decrease the strength of the magnetic field as the heat-carrying electrons remain strongly magnetised, even in the highest density simulation. This would lower the magnetisation and increase the gyro-radius for all electron populations, resulting in increased anisotropy.

Increasing the density further may also initially result in an increase in relative anisotropy compared to the highest density simulation shown here, but there are diminishing returns as while the hottest electrons become less magnetised their mean-free-path also decreases resulting in a smaller increase in relative anisotropy as seen in fig. 6.17. Eventually a point will be reached when the heat-carrying electrons are weakly magnetised, and increasing the density will again localise transport.

Similarly, decreasing the temperature may result in a slight increase in the relative anisotropy. The existence of this trend was identified during this simulation campaign, with results showing a decrease in the initial plasma temperature from $T_e = 50$ to 20 eV led to an increase in non-local transport. It may seem that increasing the temperature may provide access to a more non-local regime due to the greater gyro-radius, with electron inertia then becoming more important. However, due to the linear scaling of the gyro-radius with velocity ($\propto T_e^{1/2}$), higher magnetisation at increased temperature, and decreased effectiveness of IB heating it is unlikely to be a worthwhile avenue of pursuit. The bizarre result that arises from this is that decreasing the laser intensity can lead to more non-local transport, despite coupling less energy into the plasma, provided the magnetisation of the heat-carrying electrons does not drop below $\chi_H = 1$ at which point the electrons will enter the weakly magnetised regime. However, at lower intensity the oscillation velocity decreases, leading to less distortion towards a Langdon distribution which will act to somewhat counter the increased non-local transport.

6.4.4 Simulations with ion hydrodynamics

The simulations discussed in the previous section (fig. 6.12 and 6.15) did not include ion hydrodynamics. To assess the competition between advection driven by the Nernst effect and ion hydrodynamics CTC simulations will be performed here. In these simulations comparisons will be made between runs that include both the Nernst effect and ion hydrodynamics in the equation matrix (Full), those where ion hydrodynamics are disabled so that the Nernst effect will be responsible for advection (Nernst), or where the Nernst effect is disabled so that ion hydrodynamics drive advection (Hydro).

As it has now been established that the applied magnetic field causes transport to remain in a regime where the fluid approximation performs remarkably well, despite $\lambda_T \sim r_{g,T} \sim |l_T|$, the initial assumption is that these fluid simulations should be representative of what would be found in kinetic IMPACT simulations.

Comparing simulations with ion hydrodynamics only to those which include the

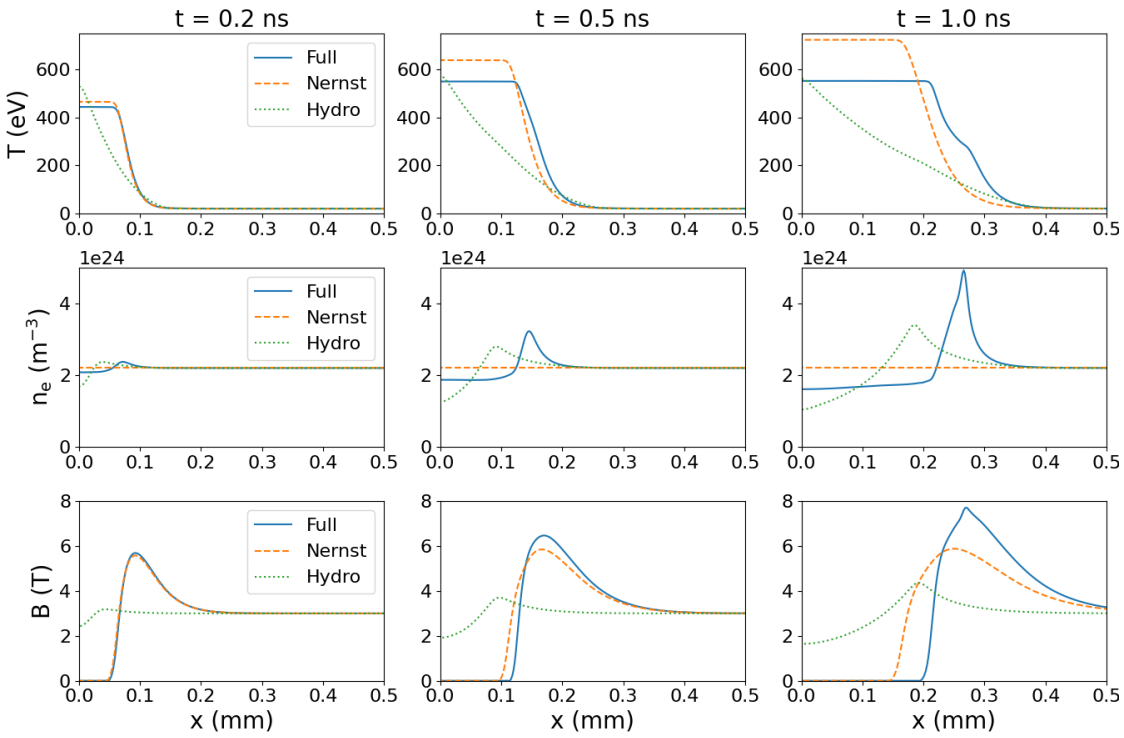

Figure 6.18: Temporal evolution of the temperature, density and magnetic field profiles during laser-heating of an initially uniform nitrogen plasma ($Z = 7$) with $n_e = 0.22 \times 10^{25}$ m^{-3} and an applied field of $B_z = 3$ T performed using CTC. Simulations are shown including both hydrodynamic ion motion and the Nernst effect (Full), only the Nernst effect (Nernst), or only ion motion (Hydro).

Nernst effect, it is clear that only including ion hydrodynamics significantly alters the temperature and magnetic field profiles in the plasma. This is largely a result of reduced magnetic field advection at early times in ion hydrodynamic only simulations. As the magnetic field is largely frozen to the ions (with current effects negligible) it reflects the density profile. Simulations with only ion hydrodynamics then have reduced heat-flow due to higher magnetisation in the region where the plasma temperature is highest, causing a slight increase in the maximum temperature, but reducing the overall thermal energy density of the plasma. A deeper cavity forms in the electron density profile than in the earlier simulations with no applied magnetic field, as the gradient in the thermal pressure remains large in the central region, which continues to develop over the course of the simulation. The peak magnetic field is lower than when the Nernst effect is included due to the lower advection velocity, although it continues to grow with time, forming a less significant transport barrier that allows the heat-front to expand at a faster rate.

When both ion hydrodynamics and the Nernst effect are included there is initially little difference with the Nernst only simulations at $t = 0.2$ ns, as it takes time for the ions to be accelerated by thermal pressure and perturb the density profile. By

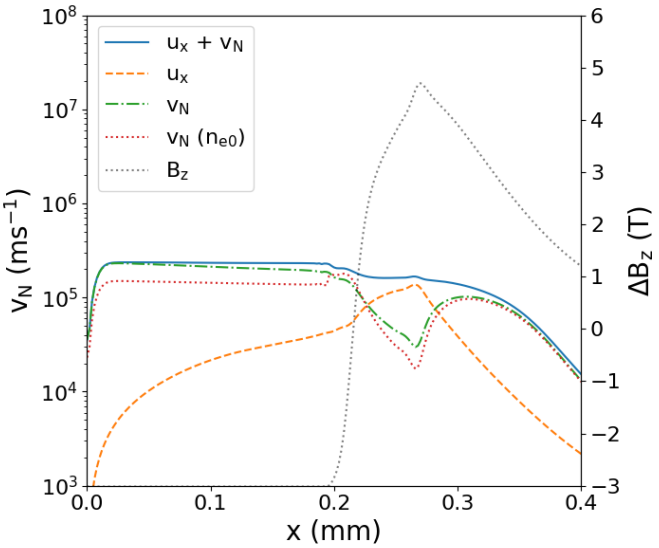

Figure 6.19: Spatial profile of the hydrodynamic velocity u_x and the Nernst advection velocity v_N for the simulation shown in fig. 6.18 at $t = 1.0$ ns. The combined advection velocity $(u_x + v_N)$ is shown, as well as the Nernst velocity under the assumption the electron density is uniform $v_N(n_{e0})$. The magnetic field profile B_z is overlayed.

$t = 0.5$ ns the ion bulk flow has begun to more greatly perturb the density profile and increase the advection of magnetic field, with the heat front seen to progress a similar amount to the cavity. That the peak temperature is lower is attributed to the conversion of thermal energy to ion kinetic energy; the IB heating rate is higher in the simulations with hydrodynamic motion despite the decrease in electron density. At $t = 1.0$ ns there is then a significant difference with the Nernst only case, demonstrating the importance of hydrodynamics.

There is a coupling between heat-flow and ion hydrodynamics; variations in density effect the heat-flow and the rate at which the internal energy changes, which in turn effects the temperature gradient and the ion hydrodynamics. At higher magnetisation variation in the density becomes increasingly significant in dictating heat-flow. Comparing the local conductivity $\kappa_\perp(\chi_B \to 0) = \kappa_\parallel$ is independent of density, while $\kappa_\perp(\chi_B \to \infty) \propto \chi_B^{-2} \propto n_e^2$. For the plasmas considered here, ion motion leads to an increase in the thermal conductivity, most noticeably by reducing the magnetisation of the plasma at the magnetic transport barrier. The variation in magnetisation has farther reaching consequences, which will be examined now.

Considering the electron density profile again when both hydrodynamic and Nernst advection occur the depth of the cavity decreases. This is due to demagnetisation and increased heat-flow reducing the pressure gradient compared to simulations with only hydrodynamic motion. Hydrodynamic motion alone is then unable to cause complete cavitation of the magnetic field. However, Nernst advection is

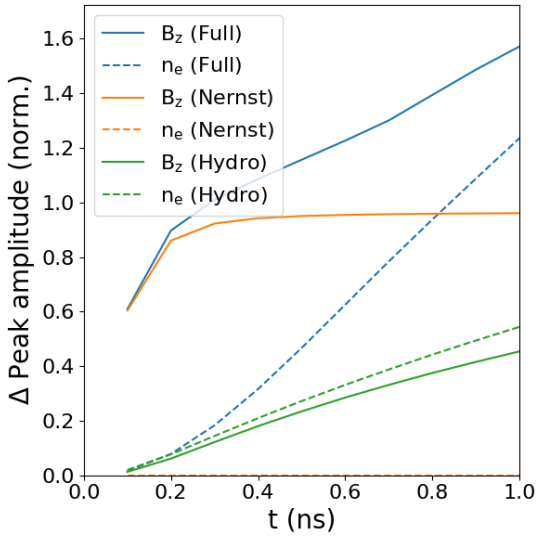

Figure 6.20: Temporal evolution of the maximum in the magnetic field and density profiles for the simulations shown in fig. 6.18.

then increased by the variation in the electron as shown in fig. 6.19, resulting in complete expulsion of field from the cavity.

A positive reinforcement between hydrodynamic and Nernst advection is then found to occur at the heat-front, increasing the amplitude and sharpening both the peak magnetic field and electron density (fig. 6.20). At late time hydrodynamic motion has a demagnetising effect where the density is at a maximum, but behind this point increased magnetisation is found in the region which is less dense and hotter, fed by Nernst advection in the density cavity. This leads to a reduction in the heat-flow and steeping of the temperature gradient that increases hydrodynamic advection, with a kink seen in the temperature profile appearing, which then increases the amplitude of the peak in both the density and magnetic field.

The relative anisotropy is quantified using $|q_x/q_{FS}|$ in fig. 6.21. As is to be expected from an increase in heat-flow and the Nernst velocity, hydrodynamic motion in combination with Nerst advection causes the simulations to become more anisotropic compared to those with only the Nernst effect. For this reason, non-local transport is expected to increase, challenging the initial assumption of these simulations being near-local and representative of the kinetic result. Initially there is little discrepancy, to be expected as hydrodynamic motion is less significant at early time. While the largest relative increase in $|q_x/q_{FS}|$ is seen in the hot core, this is unlikely to be of much significance in these simulations due to the magnetic transport barrier. Where $|q_x/q_{FS}|$ is at a maximum near the barrier, a small increase is seen due to a reduction in magnetisation.

The other observation of note relates to simulations with only hydrodynamic

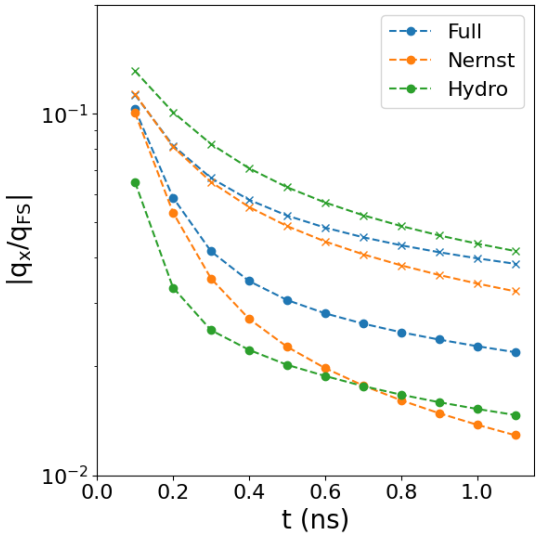

Figure 6.21: Temporal evolution of the heat-flow as a fraction of the free-streaming limit for the simulations shown in fig. 6.18. The heat-flow is evaluated where q_x is at a maximum (circles) in the hot plasma, and where q_x/q_{FS} is at a maximum (crosses) near the base of the heat-front.

motion. These demonstrate the least anisotropy in the hot-plasma, although at late time they appear to be slightly more anisotropic than the Nernst only simulations. However, the point at which $|q_x/q_{FS}|$ results in non-locality increases with magnetisation. For this reason, these are expected to be more local, as they hot core remains highly magnetised compared to the unmagnetised core in simulations including the Nernst effect. At the base of the heat-front hydrodynamic only simulations demonstrate the greatest anisotropy, as these do not form a significant transport barrier.

On varying the density of the simulations the position of the peak in the magnetic field and electron density increase as the density increases as seen in fig. 6.22a); this is due to increased cross-field transport at higher density as examined in the previous section. Initially the peak in magnetic field lies ahead of the peak in the electron density, but as time progresses hydrodynamic advection exceeds Nernst advection and the positions coincide.

The advection velocities are also found to increase as the density increases, but this does not mean that hydrodynamics motion is more important at higher density. Rather, hydrodynamic advection is found to be more important in the lower density simulations; evidence for this is found in fig. 6.22b), with u_x exceeding v_N at earlier time. As the hydrodynamic advection velocity is not large enough to completely cavitate the density profile the peak in the density is also found to increase as the density decreases, attributed to the advection velocity at a given point remaining larger for a longer period of time.

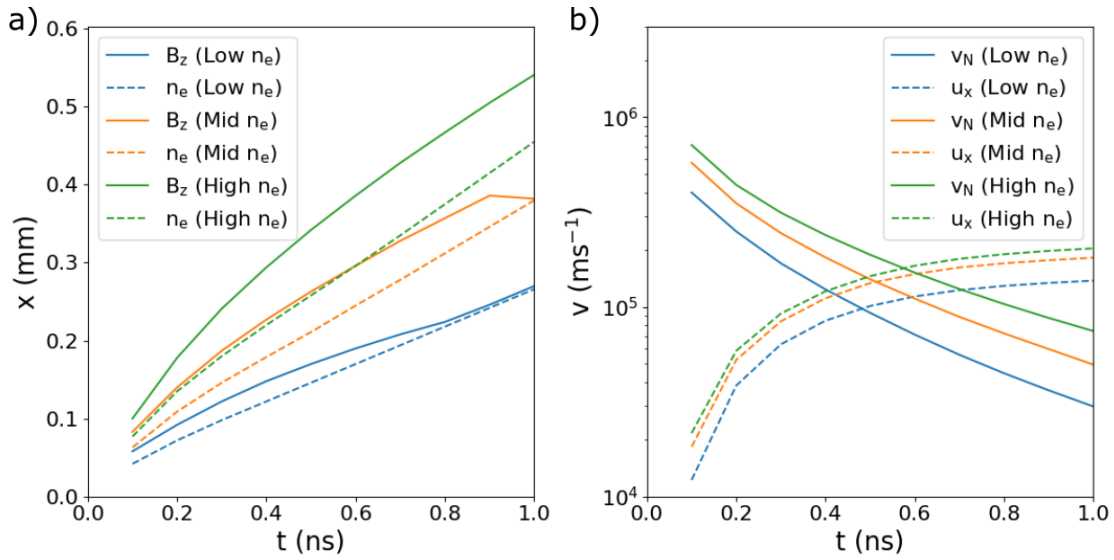

Figure 6.22: Effect of varying density on the temporal evolution of a) the position of the peak in the magnetic field and density profiles and b) the Nernst and hydrodynamic advection velocities at peak density. The densities studies are $n_e = 0.22 \times 10^{25}$ (Low n_e), 1.0×10^{25} (Mid n_e), and 1.0×10^{25} m^{-3} (High n_e).

In all these simulations the ion sound speed is $v_s \sim 10^6$ ms^{-1}, increasing slightly with density as $v_s \propto T_e^{1/2}$, so the ion hydrodynamic velocity is sub-sonic. Ahead of the heat-front the gradient in magnetic pressure is more significant, but in the hot plasma where the ion velocity peaks the gradient in thermal pressure is greater. The gradient in thermal pressure increases with density.

6.5 Summary

The main purpose of this chapter has been to demonstrate how non-local transport effects arise during laser-plasma experiments using the VFP code IMPACT and extended MHD code CTC. To guide this task two terms in the extended MHD equation have been explored, the thermo-electric effect and the Nernst effect, which can be isolated by exploiting either planar or cylindrical symmetry in unmagnetised and pre-magnetised laser-heating experiments respectively. The thermo-electric field is found to be significantly modified by non-local transport under the conditions simulated here, affecting both the heat-flow and electric field. Despite being in a highly non-local regime electron inertia is not found to significantly affect transport, a topic worthy of further study. Meanwhile magnetisation and the formation of a transport barrier mean that the Nernst simulations remain in a near-local regime. The transport barrier is key in ensuring transport progresses in a local manner, as the region demagnetised by the Nernst effect can experience significance non-locality.

The increased collision rate that occurs at higher density is found to result in greater non-local transport when in the strongly magnetised regime, a result predicted when considering the Knudsen number of heat-carrying electrons with velocity v_H described using an effective mean-free-path given by $\lambda_{ei}/(1+\chi_{ei}^2)$. The use of $|q_x/q_{FS}|$, which provides a distribution averaged Knudsen number that implicitly includes this scaling, provides the simplest route to assessing non-local transport in both kinetic and fluid simulations. This result is applicable to non-local transport in plasmas for which $\lambda_H \gg |l_T|$ provided $r_{g,H} \sim |l_T|$; if the gyro-radius is much larger than the length scale inertial effects are expected to become significant.

The conditions that were studied here are designed to aid in the understanding of an experiment that is described in the following chapter, where the electric and magnetic field structure during laser-heating of an unmagnetised and pre-magnetised nitrogen gas were probed using proton radiography. This experiment provides a benchmark that can be used to validate kinetic and extended MHD transport models. On the nanosecond timescale Nernst advection should be the dominant mechanism via which magnetic field is transported, with hydrodynamic ion motion becoming significant later in the simulation. The coupling between the Nernst effect and hydrodynamic ion motion offers an interesting avenue for future exploration. While the conditions studied here are limited to the scope of this experiment, the non-local transport trends that have been identified aid in the understanding of a much broader parameter space. It is the inverse bremsstrahlung heating rate that influences many of the observed trends; specifically the increase in mean-free-path and magnetisation when varying density.

In these simulations, the equation of state was that of an ideal gas, with no ionisation effects. This simplification is expected to introduce the largest discrepancies when comparing the results to an equivalent experimental system, such as one with a planar geometry. For the unmagnetised simulations investigating the thermo-electric field, this simplification is expected to reduce the rate at which the heat front expands, as thermal energy is converted into internal energy. A similar effect is expected in the simulations with an applied field, though additional, more complex effects are likely to arise. Specifically, in the sheath region, the resistivity is expected to be significantly higher due to decreases in both temperature and ionisation state. This will enhance resistive diffusion, causing the magnetic field to diffuse into the sheath and reducing its peak amplitude. As a result, perpendicular heat conduction may be less suppressed due to the weaker field, and magnetic field advection may become more pronounced. Another missing aspect in the simulations is radiation transport. While the emissivity of the nitrogen may be high, its opacity is likely low due to the plasma's density. Thus, radiation is likely to act primarily

as a loss mechanism, lowering the plasma temperature and smoothing temperature gradients.

Chapter 7

Experiments investigating transport in laser-plasmas

In this chapter an experiment is described which provides the first direct measurement of the Nernst effect–the transport of magnetic field driven by heat-flow. The work presented was published by Arran, Bradford, Dearling *et al.* [1], with simulations conducted by the author. The analysis presented here represents the culmination of the work described in this thesis, which has advanced our understanding of how magnetisation suppresses anisotropic electron transport and non-local effects. The results also provide valuable insights for assessing kinetic and extended MHD models in the context of laser-plasma experiments.

Experiment design is an iterative process that requires several key components for success; identifying a novel platform to explore, determining the necessary diagnostics for measurement, and understanding the expected outcomes. The experiment described here represents the next step in a series aimed at understanding non-local transport using laser-heated gas jets on the nanosecond timescale. As discussed in the previous chapter, this approach simplifies the transport problem to one-dimension. The first experiment in this series could be considered that of Gregori *et al.* [142]. who investigated the nanosecond heating of an unmagnetised nitrogen gas target using Thomson scattering. While not the first to use a gas jet target, earlier experiments focused on the picosecond heating of atomic gas clusters [143]. Following this, Froula *et al.* [89] conducted a similar experiment but added an applied magnetic field of varying strength aligned with the laser axis. Thomson scattering measurements demonstrated the localisation of transport by magnetisation. This sequence of experiments is part of a broader campaign to understand transport effects in laser plasmas.

Diagnostic developments, notably in Thomson scattering, have been foundational

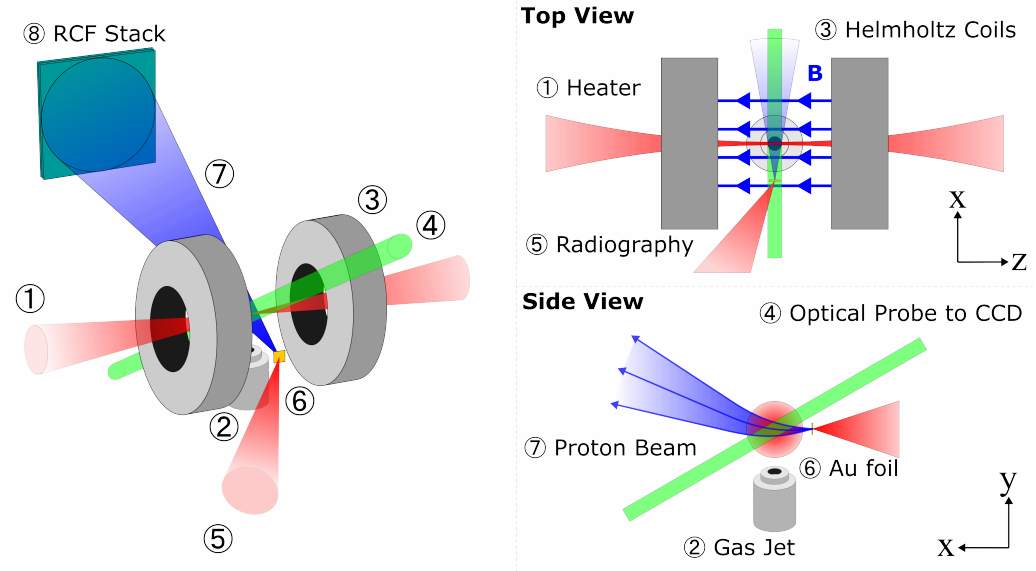

Figure 7.1: Schematic diagrams showing the experiment setup used at the Vulcan TAW facility. On the left a full 3D schematic is shown, with 2D views of the top and side shown on the right.

in these measurements. Recently, it has been shown that direct measurements of the electron distribution function can be made using Thomson scattering [144, 72, 145], which will no doubt prove key in next-generation transport experiments. Here, proton radiography will be used to provide the measurements of the electric and magnetic field structure, with conditions relevant to ICF and laboratory astrophysics. The goal is to observe non-local modifications to the electric and magnetic field structure, which have so far only been studied via kinetic simulation.

7.1 Nernst experiment in an under-dense plasma

For the experiment configuration discussed in the previous chapter it was shown the only two mechanisms in the extended MHD model that can cause advection of the magnetic field are hydrodynamic motion and the Nernst effect. In order to isolate Nernst advection measurements of both the magnetic and density profile in the plasma are required. A conclusive measurement is then provided by demonstrating the decoupling of the magnetic field from the bulk motion of the plasma.

The platform used in this experiment is shown in fig. 7.1. Central to the experiment is the gas-jet, which supplied nitrogen at a backing pressure between 1 and 10 bar via a 1 mm diameter nozzle. The gas-jet was surrounded by a pulse-powered electromagnet in a Helmholtz coil configuration, capable of achieving magnetic field strengths of $|B_z| = 3$ T which was measured pre-experiment as shown earlier in fig. 5.14. The magnet current was measured using a Rogowski coil with the trigger-

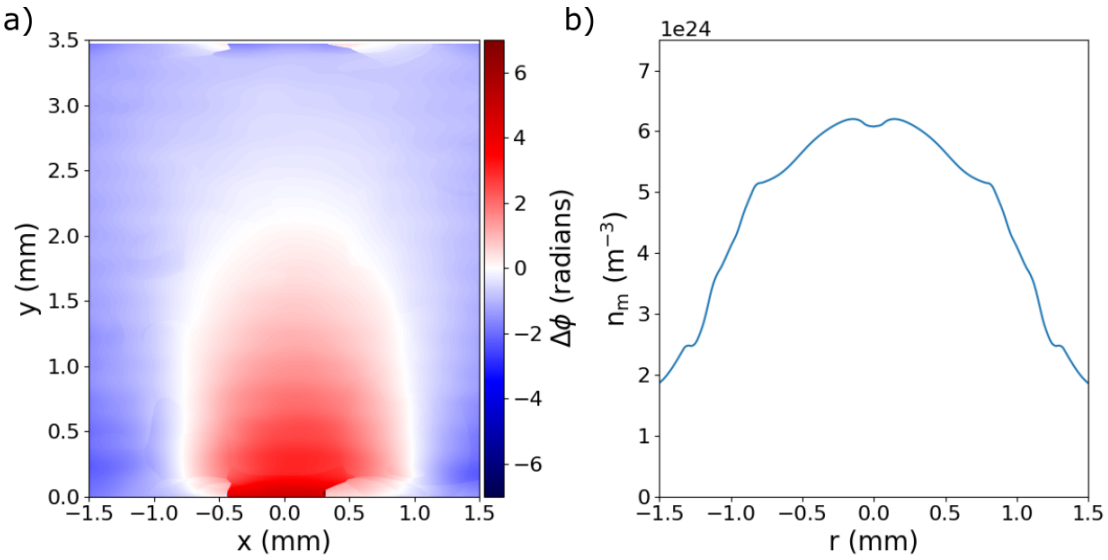

Figure 7.2: Gas jet a) phase map and b) recovered molecular density at $y = 2$ mm after Abel inverting at a backing pressure of 38 bar from Arran *et al.* [1].

ing such that the laser used to heat the nitrogen plasma arrived at TCC when the Rogowski current is zero, at which point the magnetic field was at a maximum.

Neutral gas interferometry was performed pre-experiment to calibrate the gas jet and understand what backing pressure to operate at during the experiment. The calibration was done using Argon as the neutral gas. The phase shift was recovered using a Fourier transform algorithm [146]. Using an inverse Abel transform then allows extraction of the density as the gas jet has cylindrical symmetry. The relationship for a neutral gas is

$$n_m(\rho, z) = -\frac{\lambda_l}{4\pi^2 K}\int_r^\infty \frac{d\Delta\phi(y,z)}{dy}\frac{dy}{\sqrt{y^2 - r^2}} = \frac{\lambda_l}{4\pi K}\Delta\phi'(\rho, z) \tag{7.1}$$

where K is a constant that varies between gases. In fig. 7.2a) the recovered molecular density profile is shown. At $y = 2$ mm the calibrated molecular density was $n = (1.6 \pm 0.1) \times 10^{23}$ m^{-3}/bar, averaged over the central region where the density is fairly uniform. As molecular nitrogen is diatomic, this then gives an electron density of $n_e = (0.22 \pm 0.01) \times 10^{25}$ m^{-3}/bar assuming full ionisation at $Z = 7$.

7.1.1 Laser characterisation

The nitrogen gas was ionised and heated by a nanosecond laser with a wavelength of $\lambda_l = 1.054$ µm (1ω) that delivered $E_l = 205 \pm 8$ J on target. The laser passed through the centre of the gas jet and magnetic field assembly, aligned in a direction anti-parallel to the magnetic field axis which defines the z-axis. The beam was focussed

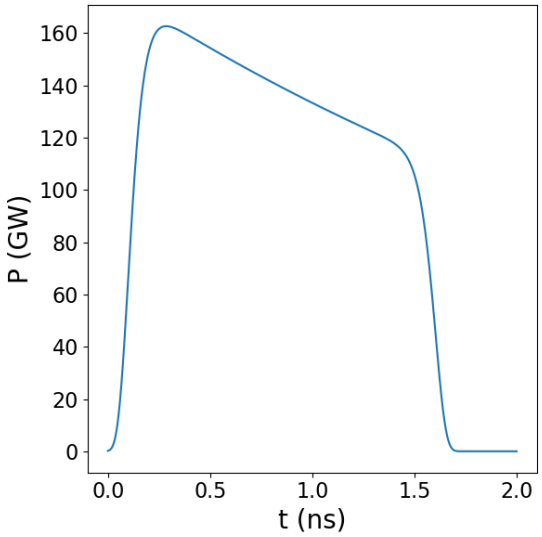

Figure 7.3: Laser power as a function of time for 205 J.

using an $f/10$ lens with a focal length of 1.2 m to a point 2 mm above the centre of the gas jet. For a collimated beam diameter of 15 cm, the diffraction limited width is $w_{\mathrm{FWHM}} = 12.6$ µm with a Rayleigh range of $(\pi w_{\mathrm{FWHM}}^2)/(\lambda_l\sqrt{2\ln 2}) = 0.341$ mm.

The laser temporal profile is shown in fig. 7.3. While ideally a top-hat function, the front of the beam was found to be amplified more than the rear as it passes through the amplifier chain due to saturation of the gain medium. This results in a super-Gaussian profile modified by an exponential decay, with the decay weakly correlated with increase laser energy, described by the function

$$P(t) = a \exp\left[-\left(\frac{t-t_0}{c}\right)^{16}\right] \exp\left(-\frac{t}{d}\right). \tag{7.2}$$

The FWHM of the laser pulse was $t_{\mathrm{FWHM}} = 1.47$ ns giving $c = 0.755$. The exponent d was fitted by $d = 1.3 - 8.16 \times 10^{-3}E$, which with a pulse energy of 205 J gave $d = 3.425$. After normalising the profile the amplitude can then be related to the maximum power P_0 by $a = P_0/0.9104$, and $t_0 = 0.8526$ ns is then set so the pulse at $t = 0$ starts at 0.1% of maximum power. The maximum power is found following an iterative process to be $P_0 = 163 \pm 6$ GW.

An example focal spot is shown in fig. 7.4. This is characterised by finding the intensity contour at 50% relative to the background and then fitting with an ellipse. The focal spot obtained pre-shot is elliptical, with a semi-major axis of 32.3 ± 0.2 µm and a semi-minor axis of 23.4 ± 0.2 µm at FWHM giving an updated Rayleigh range of 1.96 ± 0.02 mm. The peak intensity of the laser-pulse can then be found as

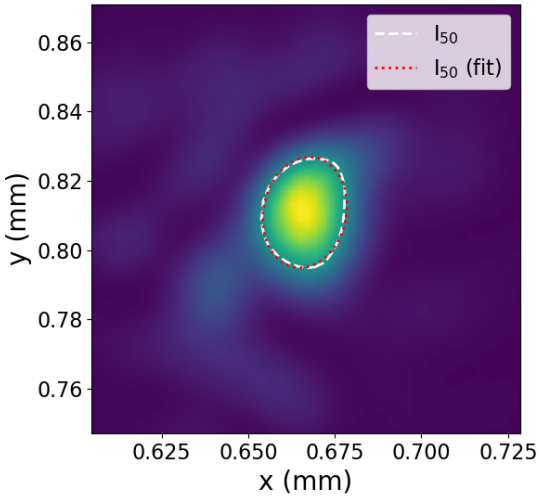

Figure 7.4: Focal spot image showing the contour at 50% of the maximum intensity, fitted with an ellipse.

$$I_0 = \frac{4\ln 2}{\pi 10^4} \frac{P_0}{w_{\mathrm{FWHM,x}} \times w_{\mathrm{FWHM,y}}} \tag{7.3}$$

with intensity units of Wcm^{-2}. As can be seen in this focal spot image there is excess energy in the wings, with $36 \pm 5\%$ contained within the FWHM intensity contour compared to 76% for a perfect Gaussian. Reducing intensity accordingly, the peak intensity is found to be $I_0 = 9 \pm 1 \times 10^{15}$ Wcm^{-2}.

7.1.2 Proton radiography

A short-pulse laser at 1ω with an energy of $E = 74 \pm 11$ J in a 1 ps pulse was used to generate a proton beam for radiography. The beam was focussed onto a 50 µm thick gold foil using an $f/3$ off-axis paraboloid mirror with a focal length of 0.6 m at 15° to the normal surface, leading to the generation of a proton beam via TNSA. This source was located $l_0 = 20$ mm away from TCC along the x-axis in the negative x-direction. The proton beam was imaged using an RCF stack with the front face of the stack placed $L = 167$ mm in the positive x-direction from TCC, giving a magnification of $M = 9.35$. Due to the deflection of the proton beam in the applied magnetic field (fig. 5.14) the RCF stack was raised 33 mm above TCC in the positive y-direction. The design of the stack is tabulated in tbl. 7.1, with the response curves shown earlier in fig. 5.3. Both the radiography and heater laser were timed at TCC, with the radiography beam arriving at the foil $-l_0/c = -67$ earlier in time. The radiography beam was then offset by either 0 or 700 ps allowing different points in the evolution of the plasma to be probed.

Layer	Filter	Material	Energy (MeV)	Probe time (ps)
1	Al 16 µm + Mylar 100 µm	HDV2	3.2	743
2	Mylar 200 µm	EBT3	7.6	460
3	Mylar 200 µm	EBT3	10.6	377
4	Mylar 300 µm	EBT3	13.6	329
5	Mylar 300 µm	EBT3	16.1	298
6	Mylar 300 µm	EBT3	18.3	276
7	Mylar 300 µm	EBT3	20.3	259

Table 7.1: Stack design detailing the filtering and RCF material used in each layer. The kinetic energy and probe time at TCC are associated with the Bragg peak for each RCF layer.

Experimental measurements of the electric and magnetic field structure were made using the proton radiography setup described previously. To reconstruct these fields, the first step is the recovery of the proton intensity in the image plane (section 5.1.2). This was done using the green and blue channels from the RCF image, which was scanned using a Nikon CoolScan 9000, with pixel value converted to net optical density.

In an applied magnetic field deflections occur due to the background, which blurs and changes the symmetry of the response, and must be accounted for in the intensity profile. The smearing kernel is found for shots in an applied magnetic field with a Richardson-Lucy deconvolution used to recover the dose from a monoenergetic proton beam (section 5.2.3); the response of the RCF stack, deflection by the background magnetic field, and proton spectrum are accounted for. The proton beam distribution was found to be approximately Maxwellian with a temperature that varied shot-to-shot between $E_k = 2$ and 6 MeV (section 5.1.3). Accounting for smearing the spatial resolution post-deconvolution is approximately 50 µm at 10.6 MeV, which decreases at higher energy [102].

The normalised intensity $I(x, y)/I_0(x, y)$ is estimated to perform the mapping from the image plane to the object plane (5.2.2). Due to shot-to-shot variation the spatial distribution of the proton source $I_0(x, y)$ is estimated by assuming that the source is slowly varying compared to the electric and magnetic field. Convolution is then performed with a circular Hann window with a diameter that is half that of the signal region to give the spatial distribution of the source. A second smaller Hann window with diameter spanning several pixels is also used to reduce higher frequency speckle that appears in the image. It is this smoothing which provides an upper limit on the spatial resolution of around 50 µm.

Reconstructions are performed using a 2D Voronoi cell algorithm found in Kasim

et al. [129], using 80^2 cells corresponding to a spatial resolution of 50 µm. This returns the deflection potential $\Phi(x, y)$ which can then be differentiated to give the deflections θ_x and θ_y. The symmetry axis was found by autoconvolution.

Deflections by the magnetic field are given by

$$\theta_y(y, z) = -\frac{s_z q}{2 m_p E_k} \int B_z(\rho, z) dx \tag{7.4}$$

which is an Abel transform of the radial magnetic field profile as B_z has cylindrical symmetry. The Abel transform of an axially symmetric function $f(r)$ is given by

$$F(y) = 2 \int_0^\infty f(r) \frac{r}{\sqrt{r^2 - y^2}} dr. \tag{7.5}$$

This allows the magnetic field to be extracted using an inverse Abel transform

$$f(r) = -\frac{1}{\pi} \int_r^\infty \frac{dF(y)}{dy} \frac{1}{\sqrt{y^2 - r^2}} dy. \tag{7.6}$$

However, for deflections by the electric field

$$\theta_y(y, z) = \frac{q}{2 E_k} \int E_y(\rho, \phi, z) dx \tag{7.7}$$

which cannot be Abel inverted directly as E_y does not have cylindrical symmetry. Instead, this can be integrated to give a result in terms of the electric field potential

$$\Phi(y, z) = \int \theta_y(y, z) \partial y = -\frac{q}{2 E_k} \int \phi(\rho, z) dx. \tag{7.8}$$

As ϕ has cylindrical symmetry it can be obtained using an Abel inversion, and then differentiated to find the electric field profile. Abel inversions are performed in both cases using pyAbel with the Hansen-Law algorithm [132].

To determine whether the data does indeed have cylindrical symmetry during processing Abel inversions are performed separately for each half of the image, and then compared to see whether the two Abel inversion match. Provided these closely resemble one another the use of an Abel inversion is justified.

Due to the singularity in the integral of eq. 7.6 the Abel inversion can generate very large errors on axis when $r = 0$. Furthermore, the derivative of $F(y)$ can greatly enhance noise which accumulates on axis. As a result, in much of the data processing found later in this chapter the most significant errors will be observed

on-axis.

7.1.3 Interferometry

An optical probe at 1ω with a pulse duration of 1 ps was used to obtain the electron density profile. The probe was obtained using a 1-inch pick-off from the radiography beam, which passed through a delay line before reaching TCC collimated at an angle 30° to the x-axis. This was imaged using two successive lenses in an imaging line giving a magnification of $M = 4.74$, before passing through a Mach-Zehnder interferometer onto an Andor Neo CCD camera. The fringe spacing was 97 ± 8 µm. The optical probe was timed to allow simultaneous measurements using interferometry and proton radiography, with an offset of either 434 or 1134 ps from the time the heater beam arrived at TCC dependent on the delay of the radiography beam.

The phase shift accumulated by an optical probe propagating through an under-dense plasma ($\omega_p \ll \omega_l$) in the x-direction is

$$\Delta\phi(y,z) = \frac{\lambda_l e^2}{4\pi m_e \epsilon_0 c^2} \int n_e(x,y,z)dx. \tag{7.9}$$

The phase change is encoded in the intensity profile recorded on the CCD camera after interference with a second identical reference beam that has experienced no change in phase. The processing of an interferogram consists of three phases; obtaining the phase profile, unwrapping the phase profile, and retrieval of the electron density [147].

Ideally phase information would be recovered from the interferograms using the Fourier transform based Takeda algorithm, as was done for the neutral gas interferometry, but steep gradients in the phase at high backing pressure mean that this technique was insufficient for recovery. Steep gradients cause high frequency components in Fourier space which are clipped when applying a window function to remove the background, and the formation of discontinuous fringes which makes the phase unwrapping ambiguous. Instead, the minima in the intensity was manually traced along each fringe, repairing the broken fringes, and assigned a known phase. The background phase was then estimated using a linear fit in regions of the interferogram far from the plasma, and subtracted to find the phase change due to the plasma. The phase map was then smoothed with a circular Hann window with a diameter of four fringe periods. An estimate of the phase map is then retrieved, with a spatial resolution better than $\pi/2 \approx 50$ µm that is limited by the tracing. Use of a higher frequency probe would have resulted in a smaller change in phase,

allowing automated recovery of the phase change and higher spatial resolution.

Assuming cylindrical symmetry, eq. 7.9 has the form of an Abel transform of the electron density profile, which can then be recovered using an inverse Abel transform. Again, this was done using pyAbel with the Hansen-Law algorithm, with the axis of symmetry found via autoconvolution. The symmetry can again be tested by Abel inverting the upper and lower halves of the image separately, justifying the use of an Abel inversion if the two halves of the image match. This was found to be the case for all the data processed during the experiment, although discontinuities appear on axis to the sensitive of the Abel inversion to noise. The data was symmetrised to create the plots that are shown later in this chapter, removing these discontinuities.

7.2 Synthetic radiography

Synthetic proton radiography is a powerful tool that can be used to check the proton radiography setup, investigate alternative geometries, and compare with experimental results. To simulate the passage of the proton beam through the electric and magnetic field structure ray-tracing techniques are employed, with particle-in-cell (PIC) codes such as EPOCH [148] commonly used for this function; typically interactions between particles are disabled to approximate the quasi-neutral nature of the proton beam. However, for a 3D grid with high-resolution this can quickly become computationally expensive.

Here the code used to produce the results in section 5.2.3 is again used as it is designed for deflections in 1D, with arbitrary source characteristics easily specified. In order to increase the computational efficiency of the code the paraxial approximation can be made. This in essence works by finding the deflection potential for the initial field configuration, and reducing the number of cells along the direction of proton beam propagation accordingly; in the limit of small deflections this can decrease the number of calculations from $O(N^2)$ to $O(N)$for a square domain. A more advanced approach has been shown to allow for the creation of extremely high-resolution proton radiographs provided deflections are not in the diffusive regime [127]; by sending a selection of test-particles through the field configuration the perpendicular deflection field can be obtained using a scattered interpolation algorithm, which then assigns perpendicular velocities to the full distribution of test particles.

In the following section synthetic radiography will be conducted of simulations shown in the previous chapter which are relevant to this experiment, using the proton radiography setup described previously with $l = 20$ mm and $L = 167$ mm. To simplify the results a mono-energetic proton beam with $E_k = 10.6$ MeV will be used

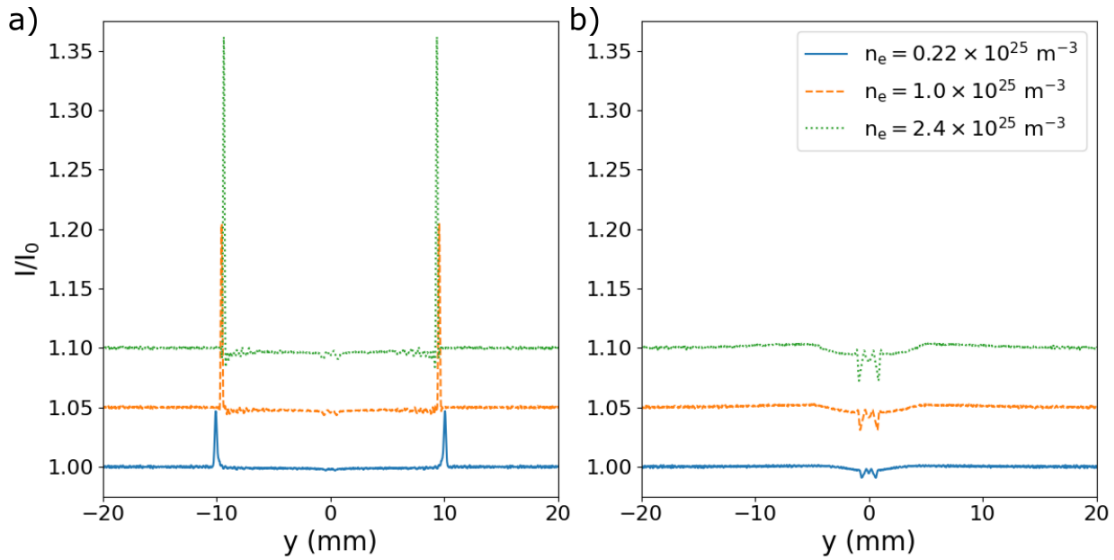

Figure 7.5: Synthetic radiographs of the thermo-electric field configuration after $t = 0.4$ ns at varying electron density. Simulations are conducted using a) CTC and b) IMPACT (including electron inertia) with both sets of simulations including hydrodynamic motion. In each plot successive densities are offset by 0.05 from $I/I_0 = 1$.

along with a point source, allowing the accuracy of the reconstructions to be tested in this ideal case; these assumptions will increase the spatial resolution compared to what is expected experimentally, and more significantly prevent smearing.

7.2.1 Thermo-electric effect

In fig. 7.5 synthetic radiographs are shown of the thermo-electric field configuration. Deflections due to the electric field are weak, with the maximum deflection of the order of 0.05-0.2 mrad which increases with density (fig. 7.10). The synthetic radiographs of the fluid and kinetic simulations are clearly distinguishable, a reflection of the differences found in the electric field profiles. At the edge of the fluid simulations the gradient in the electric field is at maximum, causing the greatest change in the intensity as the gradient in the deflection angle is at a maximum. While the magnitude of the deflection angle is similar in the kinetic simulations, the gradient is much shallower so the variation in the intensity profile is much smaller. Reconstructions of this field are the most challenging for a real proton beam as the variation in the expected intensity is of the order of 1%, which can be difficult to separate from structure in the beam.

The radial component of the electric field is reconstructed in fig. 7.6. To generate these images the mapping procedure in section 5.2.2 is followed. As deflections due to the electric field are anti-symmetric these are converted to deflection potential

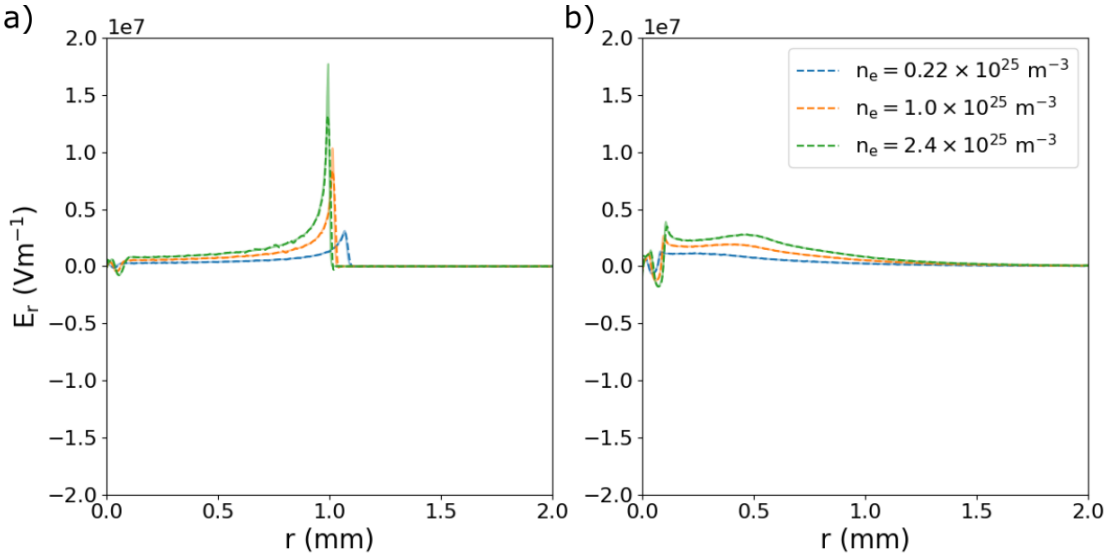

Figure 7.6: Reconstructed electric fields from the synthetic radiographs shown in fig. 7.5 compared to the input electric field (solid lines) simulated using a) CTC and b) IMPACT.

(eq. 5.13) which is symmetric before Abel inverting. It is then straightforward to convert from deflection potential to electric field. These are almost exact in both cases demonstrating the effectiveness of the reconstruction algorithm.

7.2.2 Temperature measurement

A novel use of the proton radiography technique is found in inferring temperature measurements from the reconstructed electric field [1]. This is possible for the radial thermo-electric field configuration described here by eq. 6.2, which can be rearranged in terms of the temperature profile

$$\frac{\partial T_e}{\partial \rho} + \frac{1}{1+\beta_\parallel}\frac{\partial \ln n_e}{\partial \rho} T_e = -\frac{eE_\rho}{1+\beta_\parallel}. \tag{7.10}$$

Here the integrating factor I can be found to give a solution for T_e of the form

$$T_e(\rho) = -\frac{e}{I}\int_\infty^\rho \frac{IE_\rho}{1+\beta_\parallel} d\rho \tag{7.11}$$

where

$$I = \exp\left(\int_\infty^\rho \frac{1}{1+\beta_\parallel}\frac{\partial \ln n_e}{\partial \rho} d\rho\right) \tag{7.12}$$

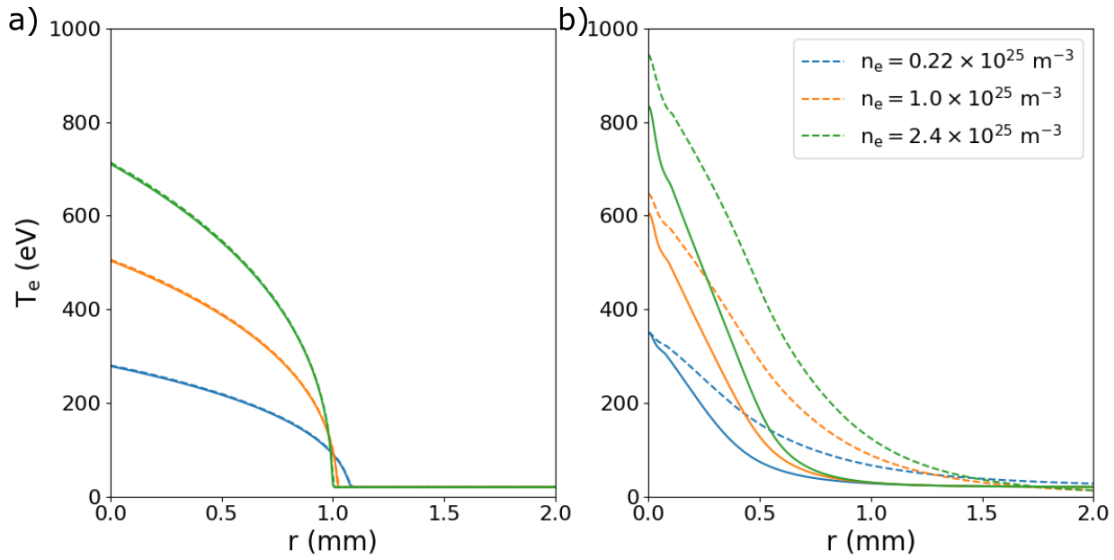

Figure 7.7: Temperature profiles obtained from the thermo-electric field reconstructions shown in fig. 7.6 for a) CTC and b) IMPACT.

To solve this equation then requires additional knowledge of both the electron density and the ionisation level which $\beta_\parallel$ depends upon. While the electron density can be obtained using interferometry, the ionisation level typically varies spatially and tends to depend on the temperature. Unless a supporting diagnostic is available, progress can be made via an iterative approach; an initial guess is made for $\beta_\parallel$ which is used to calculate the temperature profile, that can then be used to update the estimate for $\beta_\parallel$ until a self-consistent solution is found. As $\beta_\parallel$ lies in the range 0.70-1.21 for a nitrogen plasma, this should be fairly robust.

This method is demonstrated in fig. 7.7 where the temperature profile is obtained from reconstructed electric fields for simulations where $Z = 7$. For simulations of the electric field obtained using a fluid code the reconstruction is exact, showing that the approach is valid in the local limit. In the kinetic simulations non-local transport is significant and the electric field is no longer given by the local Ohm's law, which was the starting assumption for this approach, and is instead given by eq. 6.3. The reconstruction fails in regions where pre-heat is significant but obtains increasingly reliable estimates up the point of maximum temperature, where the error is $\sim 10\%$ for the synthetic radiographs shown here.

The problem can also be approached in the more general case of a magnetised plasma with radial symmetry where $\beta \gg 1$, such as that studied in the Nernst effect configuration. In this case the transport coefficient $\beta_\parallel$ is replaced with $\beta_\perp$, which is also dependent upon the magnetisation. As with the ionisation level the magnetisation is also temperature dependent so an iterative process is required find a self-consistent solution for T_e, but in the weakly magnetised limit $\beta_\perp \approx \beta_\parallel$ which

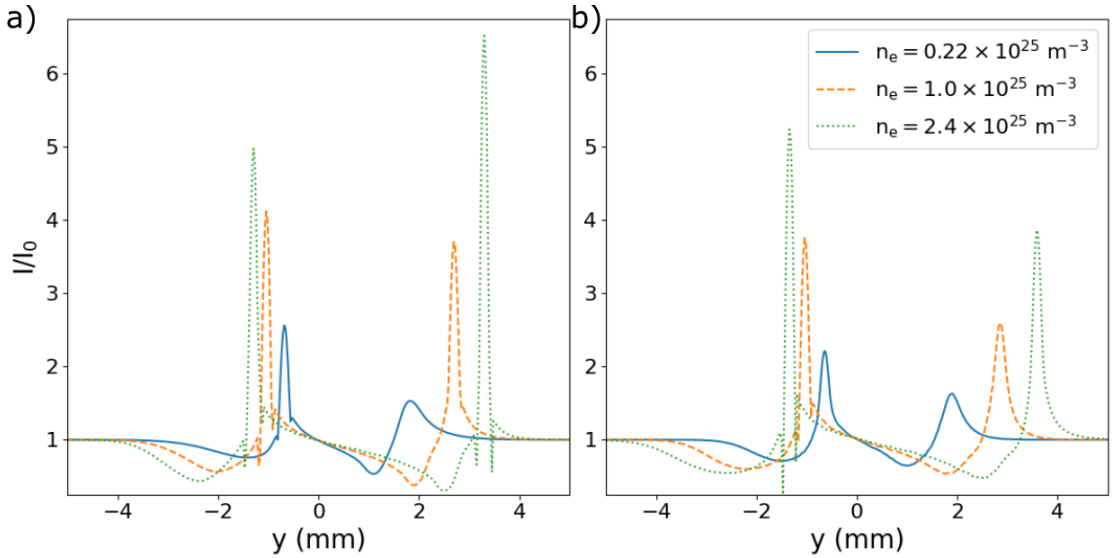

Figure 7.8: Synthetic radiographs of the thermo-electric field configuration at $n_e = 0.22 \times 10^{25}$, 1.0×10^{25}, and 2.4×10^{25} m^{-3} at $t = 0.4$ ns. Simulations are conducted using a) CTC and b) IMPACT (excluding electron inertia) with hydrodynamic motion disabled in both sets of simulations. The electric field is included in all radiography but has little effect as the deflections attributed to it are small.

somewhat constrains the problem. This process does pose a greater challenge as the electric field is weak, and separating the deflections from those of the magnetic field which are strong can result in large errors in the recovered electric field.

7.2.3 Nernst effect

In fig. 7.8 synthetic radiographs are shown of the Nernst effect field configuration. The maximum deflection is almost an order of magnitude larger than those of the thermo-electric configuration between 2-5 mrad (fig. 7.10), which again increases with density as gradients in the deflection become larger. The similarity between radiographs of fluid and kinetic simulations are now much greater as the discrepancy between fluid and kinetic simulations is smaller. However, as the density increases and the simulation becomes more non-local there is a change in the asymmetry between the peaks in the intensity profile, with the peak on the right of each lineout now having greater magnitude than that on the peak on the left. While the simulations include both electric and magnetic fields the signal is dominated by the magnetic field, which can be expected to cause the mapping to enter the non-linear injective regime ($\mu < \mu_c \sim 1$). Deflections associated with the radial component of the electric field cause deflections of the order of ~ 0.1 mrad, while the path-integral of the azimuthal electric field is approximately zero.

The magnetic field reconstruction is shown in fig. 7.9. Again, the same procedure

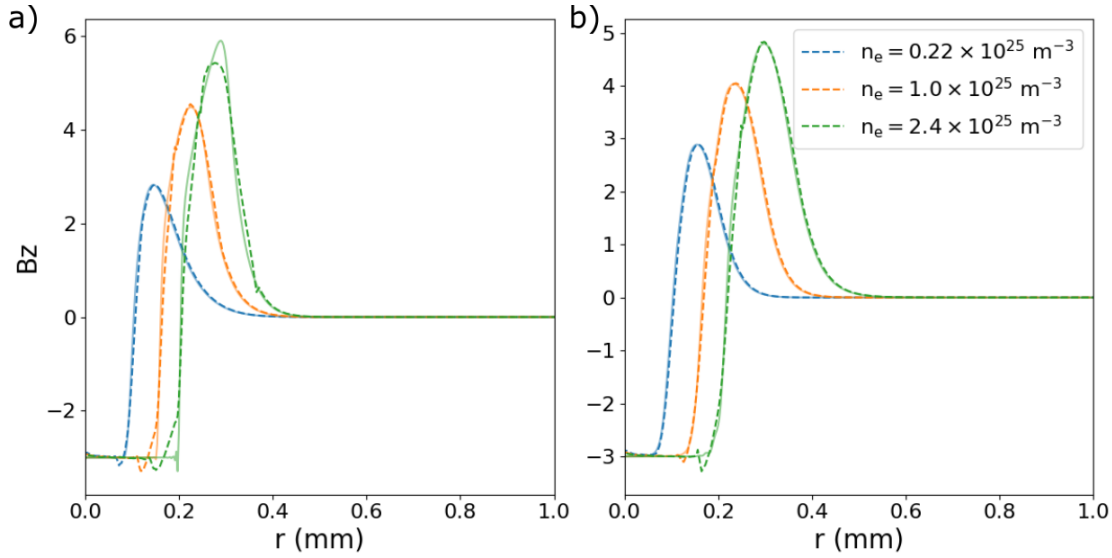

Figure 7.9: Reconstructed magnetic fields from the synthetic radiographs shown in fig. 7.8 compared to the input magnetic field simulated using a) CTC and b) IMPACT. The deflection maps were symmetrised to account for deflections by the electric field.

is used as outlined in section 5.2.2. Deflections due to the magnetic field are symmetric unlike the electric field, so can be converted to the path-integrated magnetic field and then Abel inverted directly. The recovered magnetic field again closely approximates the input field; slight discrepancies may be caused by deflections in the non-linear regime, which could be improved using a Voronoi cell based method [129].

7.2.4 Deflection symmetry

The symmetry properties of the deflections have several advantageous properties that can be exploited during analysis. For a plasma with cylindrical symmetry deflections due to an electric field will be anti-symmetric about the axis, while for a magnetic field they are symmetric. This is shown in fig. 7.10. By measuring deflections that are either largely anti-symmetric or symmetric, the field can be primarily attributed to either an electric or magnetic field respectively. When both an electric and magnetic field are present the absolute symmetry of the deflection profile is broken. As shown in synthetic radiographs of the Nernst experiment the electric field introduces an asymmetry in the deflection profile, with the amplitude of deflections above the axis of symmetry increased compared to those below the axis. This comparison should be made after deconvolving any effects caused by the smearing of a poly-energetic proton beam, as this is also a source of asymmetry.

After identifying the axis of symmetry this result can be used to separate electric

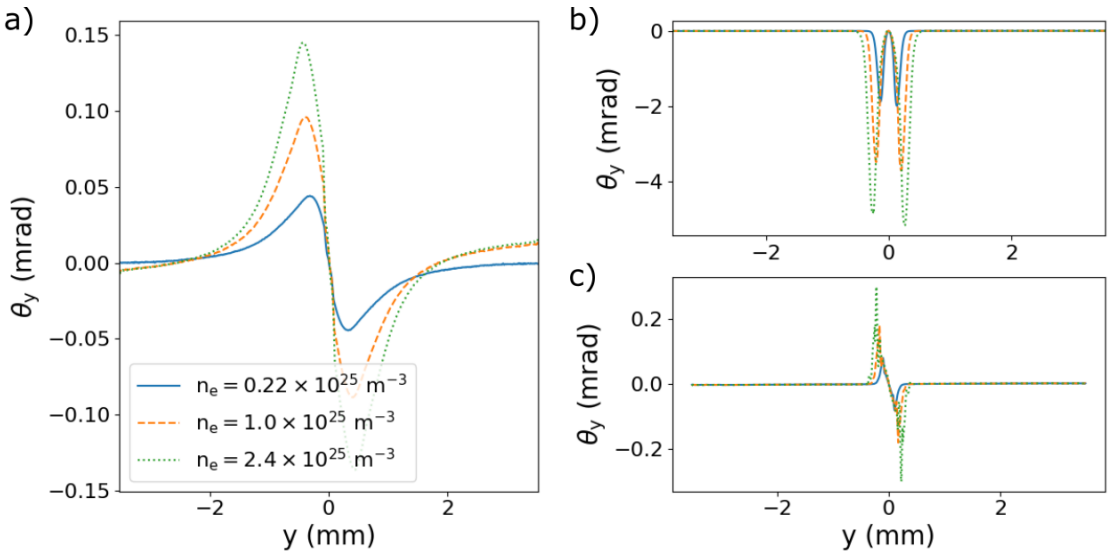

Figure 7.10: Deflection mapping from the synthetic radiographs of IMPACT simulations of a) the thermo-electric configuration and b) Nernst configuration, shown in fig. 7.5 and fig. 7.8 respectively. For the thermo-electric the total deflection is shown, while for the Nernst configuration both the total and anti-symmetric contribution caused by the electric field are shown.

and magnetic field structures. Symmetrising the deflection by finding the average of the lower and upper half of the cylinder the magnetic field is obtained, as anti-symmetric contributions cancel. Meanwhile, the difference in deflection gives the electric field deflection which is recovered in 7.10; this means that estimates of the temperature profile can also be found from radiographs of the Nernst configuration. This provides stronger motivation for making all the recovered magnetic field maps symmetric, which was previously done to remove discontinuities on axis due to the Abel inversion.

7.3 Measurement of the thermo-electric effect

In shots without an applied magnetic field interferometry shown in fig. 7.11a) a plasma channel forms along the laser axis. The plasma is just over 1 mm in length with a radius of about 0.1 mm after 400 ps. The peak electron density is found in fig. 7.11b) to be in excess of 5×10^{25} m^{-3}, slightly higher than the peak electron density expected from the calibration of 2.3×10^{25} m^{-3}. Periodic modulations along the length of the plasma column suggest that there is likely an issue with the phase recovery on this shot. There is no evidence that the plasma has begun to cavitate at this time, with the plasma not yet expected to have fully ionised.

The proton radiography also shows a narrow horizontal column along the laser

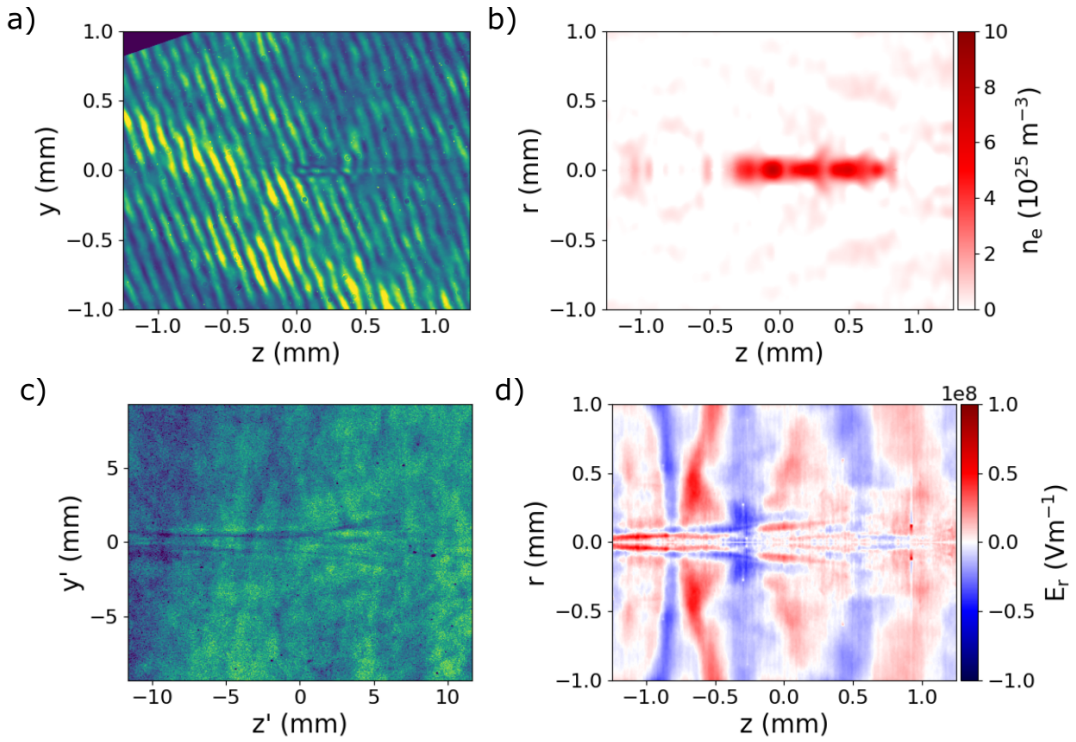

Figure 7.11: Experimental data obtained when imaging the thermo-electric field configuration at a backing pressure of 10.7 bar after $t = 0.4$ ns. Interferometry data shows a) the raw image with the contrast again adjusted to make the signal clear, and b) the map of the reconstructed electron density. Proton radiography data is shown of c) the raw proton image with the contrast adjusted to make the signal clear, and d) the map of the reconstructed radial electric field is shown.

axis as shown in fig. 7.11c), similar in dimension to the structure seen in the interferometry. Along the y-axis the proton flux in the middle of the column is lower forming a void, with higher flux at the edges of the void. Accounting for the magnification the length of the column along the z-axis is around 2 mm, and is approximately uniform over a 1 mm region in the centre which is roughly equal to the laser Rayleigh range. Approaching the end of the column the structure expands radially and dissipates, with structure within the channel possibly attributed to the filamentation instability [149]; this suggests the laser intensity should be decreased and focal spot size increased.

The deflection profile is found to be anti-symmetric, confirming the structure is due to an electric field which is reconstructed in fig. 7.11b). The signal is weak with proton deflections below 0.1 mrad, making the separation of the signal from structure in the proton beam challenging. In the reconstruction a central column can be seen which spans the z-axis, where the amplitude of the peak electric field is of the order of $E_r = 10^7$ Vm^{-1} and the radius ~ 0.1 mm. The column is surrounded by spurious signals that are attributed to noise, masking any real signal in the region $|r| \gtrsim 0.1$ mm. An electric field arising due to thermal pressure should predominantly be

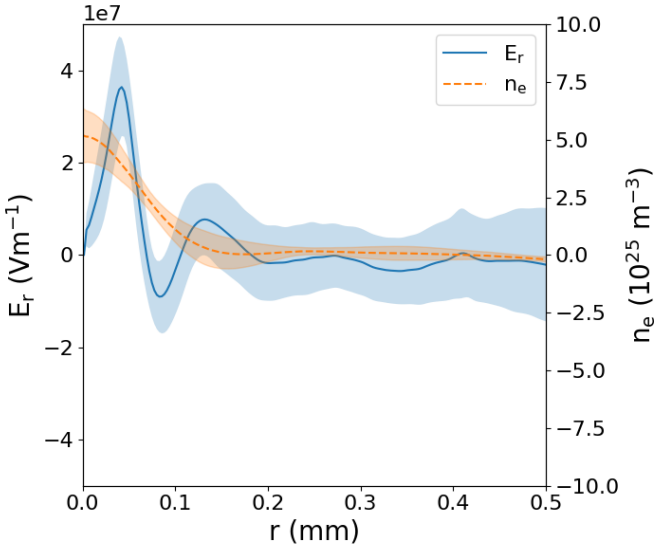

Figure 7.12: Lineouts of the reconstructed electric field and electron density as a function of radius obtained from the interferometry and proton radiography measurements in fig. 7.11 at $t = 0.4$ ns. These are longitudinally averaged over the central 0.5 mm of the plasma column, with the shaded regions showing the standard deviation.

directed radially outwards from the heated region, particularly in the sheath where significant gradients in the electron density are not expected. This is not always the case here, with significant regions found where the electric field is in the opposite direction to what is expected.

In fig. 7.12 lineouts averaged over the length of the plasma column are shown. At 40 µm the electric field reaches a maximum with an amplitude of $(4 \pm 1) \times 10^7$ Vm^1, with the standard deviation large across the entire radius of the column. The peak electron density is $(5 \pm 1) \times 10^{25}$ m^{-3} with a full-width at half-maximum of 70 ± 10 µm. As the plasma channel has not cavitated these results appear most comparable to simulations without hydrodynamic motion. The presence of the maximum on axis rather than in the sheath region also suggests that the kinetic description better describes the behaviour of the plasma. In these the electric field remains close to the edge of the laser spot compared to those with hydrodynamic motion (fig. 7.6), where the maximum moves away and reduces in magnitude more rapidly. When hydrodynamic motion is not present the radially electric field remains positive at all points in space, suggesting that there is an issue with the reconstruction.

The temperature profile in the column can be estimated using these properties, giving a temperature change of 500 ± 300 eV between $r = 0$ and 100 µm. As the temperature cannot be reconstructed from the edge of the plasma (i.e. as $r \to \infty$) this value is relative rather than absolute. The challenge in the temperature reconstruction can be attributed to the minimum observable signal, and therefore

the noise level, for both the proton radiography and interferometry diagnostics; both are required for an accurate reconstruction at a given point in the plasma.

The minimum proton deflection measurable in the proton radiography is limited by the random noise in the proton distribution. This can be estimated by looking at the recovered deflection in a region away from the signal. In this region the root-mean-square deflection is around 0.3 mrad, which for a proton energy of 10.6 MeV corresponds to root-mean-square noise in the integrated electric field of 6 MVmm. The noise is expected to overwhelm most of the electric field measurements, particularly in the sheath plasma. Either a proton beam with significantly improved quality, or a much stronger electric field would be required for a definitive measurement of the electric field.

Similarly, while interferometry performs well in the denser bulk of the plasma, it is unable to recover the electron density in the sheath region due to its limited dynamic range. Despite the plasma being tenuous in this region it is expected to be hot ($\sim$ 100 eV), with the heat-flow and electric field properties here important for the overall understanding of transport within the plasma. Based on the probe wavelength, fringe spacing, and CCD resolution the minimum detectable fringe shift is $\Delta\phi = 67 \pm 6$ mrad, corresponding to an integrated density of $2.3 \pm 2 \times 10^{22}$ m^{-3}mm. In practice tracing of the experimental data limited the spatial resolution rather than the CCD, increasing the minimum detectable signal by a factor of ~ 10. Increasing the wavelength to improve the phase shift would be detrimental to the bulk, where estimates of the density profile have already been affected by steep gradients in the phase, although multiple wavelengths could be used to improve the dynamic range.

7.4 Measurement of the Nernst effect

In shots with an applied magnetic field the interferograms measure a plasma column much longer than it is wide along the laser axis, with the recovered density shown in fig. 7.13. Here a plasma column forms 0.4 ns after the start of the heater beam at the highest density of 10.7 bar. The radius is around 150 µm over a length of slightly under 2 mm longitudinally, with a peak density around 10^{25} m^{-3}. At these relatively early times, the plasma is not yet fully ionised and the plasma column shows no sign of cavitation. As the heater beam continues to ionise more gas and the plasma expands, a density cavity forms inside the plasma column by 1.1 ns after the start of the heater beam.

Measurements were made at backing pressures of 1, 4.5, and 10.7 bar, corresponding to peak electron densities of $n_e = 0.22 \times 10^{25}$, 1.0×10^{25}, and 2.4×10^{25}

m^{-3}. The interferometry results are broadly in agreement with these expectations. At all densities a cavity was found to have formed in the electron density profile after 1.1 ns. As the density decreased both the length and radius of the cavity decreased.

Proton radiography of these shots show a large horizontal column forming along the laser axis as shown in fig. 7.14. The structure is distinct from that found in shots with only an applied magnetic. Notable differences include a cavity that is wider, asymmetry above and below the centre of the cavity, and greater longitudinal uniformity, all of which may be attributed to magnetisation of the plasma. Confirmation that this structure is primarily due to a magnetic field is provided after the deflection mapping, with the deflection profile found to be largely symmetric.

The differences in the intensity profile along the y-axis are as expected when compared with the synthetic radiography performed earlier. That a larger cavity is seen, when the plasma is now confined by a magnetic field, does not reflect a greater extent of the plasma compared to the unmagnetised case. Rather, as the deflections caused by changes in the magnetic field profile are larger it is easier to see where the edge of the plasma might be located, compared to the thermo-electric field image where only the very intense electric field on-axis causes significant deflection. The smearing of the proton beam by the background field is also noticeable, particularly for the peak below the centre of the cavity which is blurred towards $y = 0$ by higher energy protons which are deflected less by the field. In some images the edge of this blurred signal can even be seen to reduce for layers further into the RCF stack which observe higher energy protons.

That the column is approximately uniform across the longitudinal axis, with the field of view ~ 3 mm, is surprising given it is much longer than Rayleigh range of the laser. However, when the plasma is magnetised significant asymmetry is to be expected along this axis, with heat-flow perpendicular to the axis restricted while parallel it is unaffected. This leads to significant directional anisotropy of the heat-flow, a result that has been seen to cause asymmetry in magnetised ICF implosions [17]. Axial expansion of the column would then be enhanced compared to the unmagnetised case due to larger temperature gradients, caused by the suppression of perpendicular heat-flow.

In fig. 7.15 reconstructions are performed of the experimental data set. At the highest density of 10.7 bar the cavity is seen to expand radially between $t = 0.4$ and 1.1 ns. Complete cavitation of the magnetic field is observed with $\Delta B_z = -3$ T, while the magnetic field is increasingly amplified outside of this region. Although not seen in the reconstruction, a periodic structure with a wavelength of $\lambda = 240 \pm 40$ µm is found to occur at late time in the raw radiograph. This forms along the lower

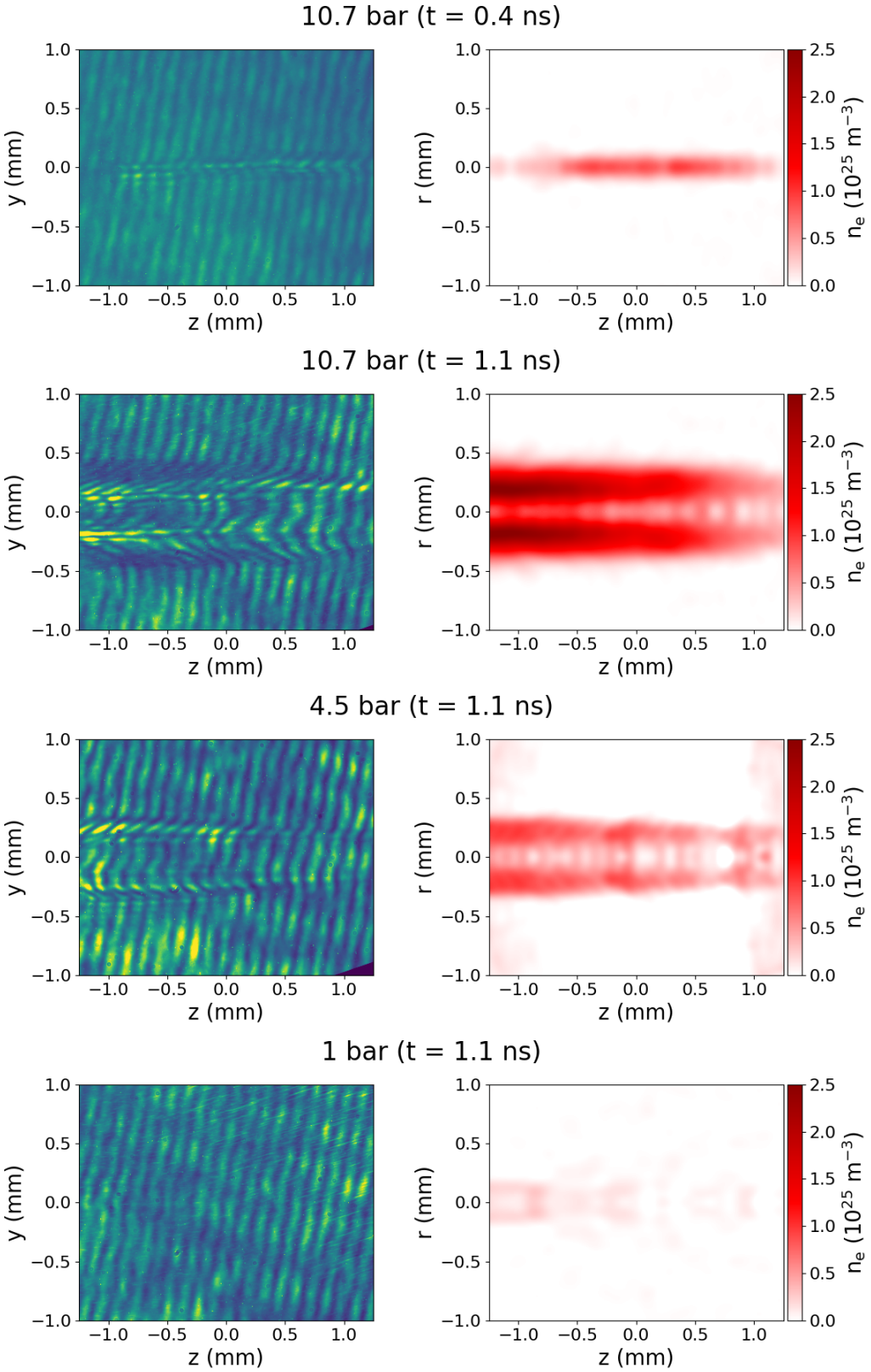

Figure 7.13: Interferometry data when imaging the Nernst effect configuration at varying backing pressure and time. On the left are the raw interferograms, where the image contrast has been adjusted to make the signal clear, while on the right the map of the reconstructed electron density is shown.

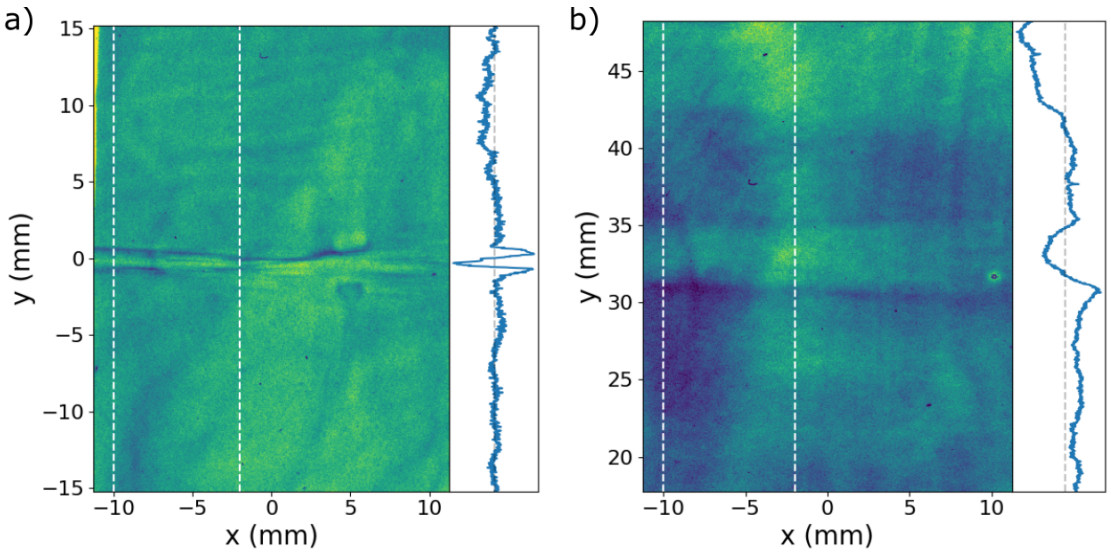

Figure 7.14: Proton radiography of shots a) with and b) without an applied magnetic field at a backing pressure of 10.7 bar after $t = 0.4$ ns. Normalised lineouts are shown over the x-axis taken between the dashed-white vertical lines.

edge of the cavity, extending radially inwards towards the centre of the plasma.

As the backing pressure and electron density decrease, the radius and depth of the cavity also decrease. This leads to a reduction in the path-integrated magnetic field, which can make the recovery of the deflection profile challenging at the lowest density. The random noise in the proton distribution corresponds to noise in the integrated magnetic field of 0.1 Tmm, which is significant at 1 bar where the field amplification is on the order of $\Delta B_z = 0.1$ T.

There is a clear decoupling between the magnetic field profile and the plasma flow in these measurements. This is most evident at 0.4 ns for a backing pressure of 10.7 bar, with significant cavitation of the magnetic field observed despite no cavitation of the electron density. This separation of effects allows the first experimental measurement of the Nernst effect to be made [1].

7.4.1 Separation of hydrodynamic and Nernst advection

The magnetic field and electron density profiles are compared for a backing pressure of 10.7 bar at 0.4 and 1.1 ns in fig. 7.16. Initially it is seen that the magnetic field is rapidly advected into the sheath region of the plasma beyond 200 µm, increasing the maximum field strength by $\Delta B_z \approx 0.3$ T. In the hot plasma the magnetic field is reduced by $\Delta B_z \approx -1$ T compared to the initial field strength of $B_{z0} = 3$ T, forming before any cavitation in the electron density profile. In this regime Nernst advection is significantly faster than hydrodynamic motion over this timescale; this

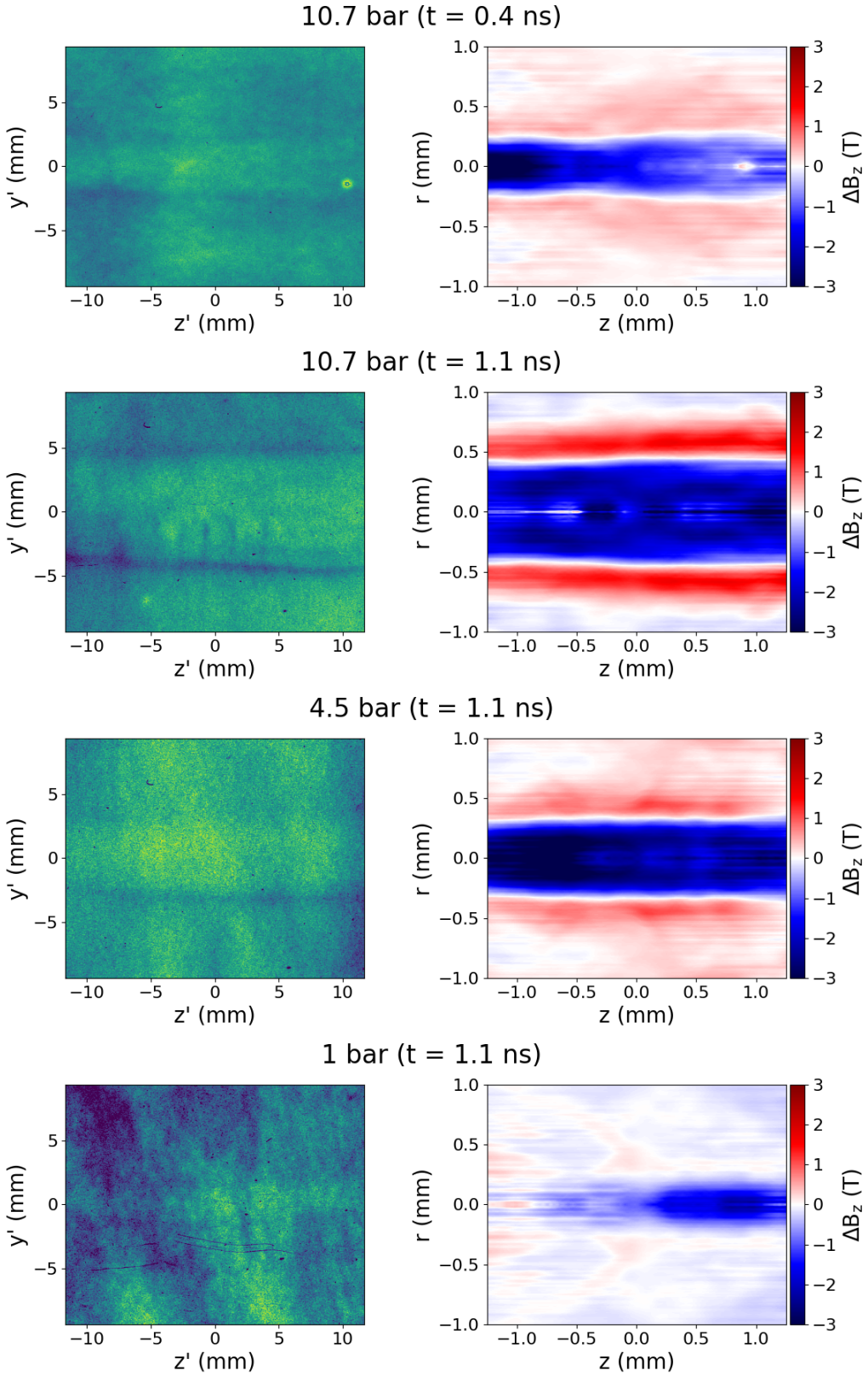

Figure 7.15: Proton radiography data when imaging the Nernst effect configuration at varying backing pressure and time. On the left are the raw radiographs, where the image contrast has been adjusted to make the signal clear, while on the right the map of the reconstructed magnetic field relative to the applied field is shown.

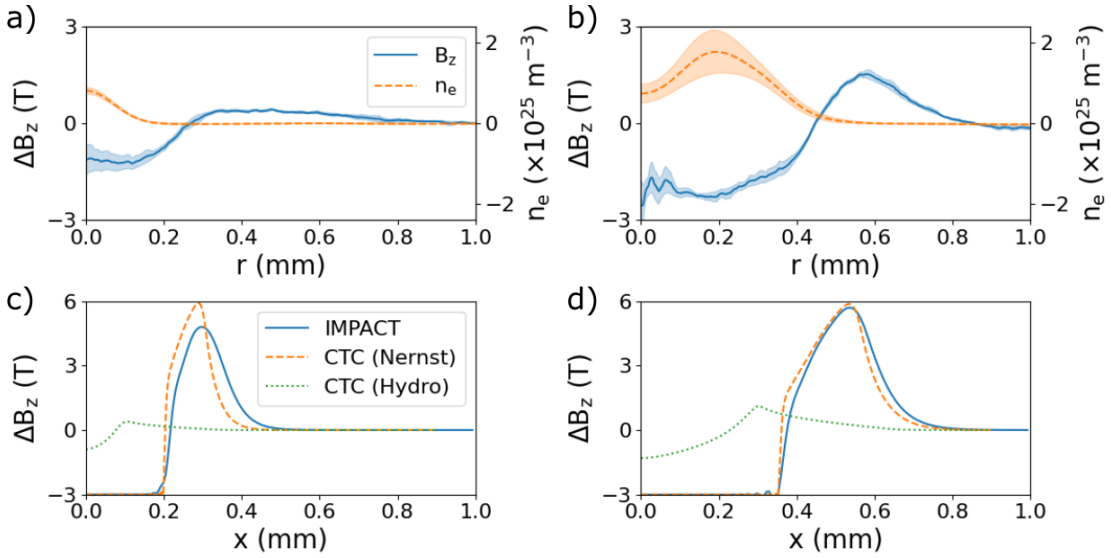

Figure 7.16: Lineouts of the reconstructed magnetic field and electron density as a function of radius measured at a) 0.4 and b) 1.1 ns at a backing pressure of 10.7 bar. These profiles are longitudinally averaged over the central 1 mm of the plasma column, with the shaded regions showing the standard deviation. The magnetic field predicted by 1D Cartesian IMPACT and CTC simulations at c) 0.4 and d) 1.1 ns of the experiment in a Cartesian geometry. IMPACT simulations do not include hydrodynamic motion, while CTC simulations either include the Nernst effect or hydrodynamic motion.

is expected from eq. 6.12 as the collision time is long relative to the hydrodynamic timescale. Due to the coupling of Nernst advection with heat-flow, this implies that the electron pre-heat extends out to $r > 0.5$ mm.

Later on at 1.1 ns, the magnetic field cavity has continued to expand with the reduction in the magnetic field strength in the hot plasma now $\Delta B_z \approx -2$ T, while in the sheath region the magnetic field has been amplified further to $\Delta B_z \approx 1.2$ T. However, the average advection velocity of the peak has decreased as the Nernst velocity and heat-flow reduce with time. The plasma column has now expanded significantly though, with cavitation of the density profile observed. At this point measuring the maximum in the electron density profile gives an average hydrodynamic advection velocity of approximately $(1.8 \pm 0.5) \times 10^5$ ms^{-1}.

To confirm that the measured advection is indeed caused by the Nernst effect, key parameters describing the plasma regime can be obtained using measurements of the thermo-electric field to obtain the temperature; this is estimated to be 700 ± 300 eV with a length scale of approximately 100 µm at 10.7 bar after 0.4 ns. At this temperature full ionisation of nitrogen ions to $Z = 7$ can be expected. Under these conditions the magnetisation is then between $\chi_T \approx 1 - 10$, with the magnetic field and heat-flow strongly coupled. The ratio of the thermal pressure to magnetic

pressure is $\beta \gg 1$ suggesting that the thermal terms will be dominant in Ohm's law.

Evaluating the terms in the induction equation in more detail, the magnetic Reynolds number is $\mathrm{Re}_M \gg 1$ making advection the dominant term in the induction equation and allowing diffusion and resistivity gradient flow to be neglected. Meanwhile, the thermal Peclet number, which measures the importance of the heat-flux relative to bulk flow in energy transport, is $\mathrm{Pe} < 1$ with the heat-flux then the more important effect. No spontaneous generation of magnetic field was observed in the absence of an applied field, confirming that the Biermann term is negligible. Nernst advection is then the only remaining candidate which can be invoked to explain the scale of the measured magnetic field cavitation.

The results of IMPACT and CTC simulations conducted in a 1D Cartesian geometry, described previously in section 6.4, are provided for comparison in fig. 7.16. Models which do not include the Nernst effect are unable to correctly predict the scale of the cavitation in the magnetic field; instead being frozen to the density profile. On inclusion of the Nernst effect, both kinetic and fluid simulations capture the shape of the magnetic field profile after 1.1 ns.

There remain qualitative differences between the experimental and simulation profiles, although these differences are largely explained by the use of 1D Cartesian simulations instead of either 1D radial or 2D simulations. In 2D, the advection velocity is initially reduced by the increased energy spread resulting in shallower temperature gradients. This is expected to result in both incomplete cavitation of the plasma, as seen in the experiment, and a reduction in the magnetic transport barrier at later time. The second effect, a reduction in the transport barrier, should then drive faster advection in two-dimensions than one leading to the broader peak.

However, at the earlier time of 0.4 ns, it is believed that additional heating mechanisms attributed to the higher laser intensity, such as those due to collective laser-plasma interactions rather than inverse bremsstrahlung heating, are responsible for the significantly faster magnetic field advection and heat-flow. Even if the laser intensity was increased significantly, as was done for simulations in fig. 7.17, it would appear that inverse bremsstrahlung is incapable of driving such rapid advection. Evidence for such processes have already been seen in the raw radiographs for shots without an applied field. That both the plasma temperature and advection velocity are fairly insensitive to changes in the laser intensity, with $T_e \propto I_l^{0.34\pm0.1}$ and $v_B \propto T_e^{0.42\pm0.8}$, provides further confidence in our results.

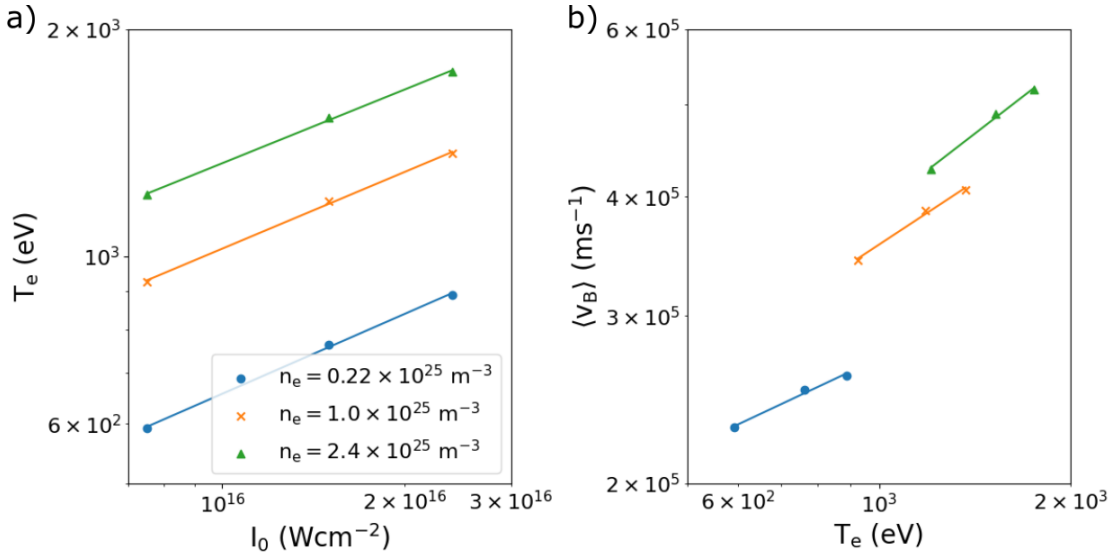

Figure 7.17: IMPACT simulations showing the variation in a) the on-axis ($x = 0$) electron temperature and b) the average magnetic field advection velocity with laser intensity at $t = 1.1$ ns.

7.4.2 Nernst advection velocity and heat-flow

The magnetic field advection velocity is inferred by measuring the radius of the peak magnetic field as a function of time as shown in fig. 7.18; for each shot a times series can be obtained from the RCF stack, with layers 2-5 having Bragg peak energies between 7.6 and 16.1 MeV corresponding to a time window of 162 ps. At early time when the Nernst velocity greatly exceeds the hydrodynamic velocity an estimation of the Nernst velocity can then be made, which is found to be $v_N = (7 \pm 2) \times 10^5$ ms^{-1}. These agree to within error of the simulated results. Comparing the velocity of the magnetic field peak in the simulation with the calculated Nernst velocity, it is seen that this approach is likely to slightly overestimated the true Nernst velocity.

Using eq. 4.25 the following expression is obtained

$$\frac{\mathbf{q}}{q_{FS}} = \frac{5}{2}\frac{\mathbf{v}_N}{v_T} \tag{7.13}$$

which relates the Nernst velocity as a fraction of the thermal velocity to the heat-flow as a fraction of the free-streaming limit. Following the work in section 4.3.1 the ratio $\mathbf{v}_N/v_T$ can be seen to also act as non-local parameter, corresponding to the relative anisotropy of the heat-carrying population. For an electron thermal velocity at 700 eV of $v_T = 1.6 \times 10^7$ ms^{-1}, the heat-flow is estimated to be approximately $|\mathbf{q}|/q_{FS} = 0.02 \pm 0.01$.

Later in time the advection velocity of the magnetic field decreases to ($2 \pm$

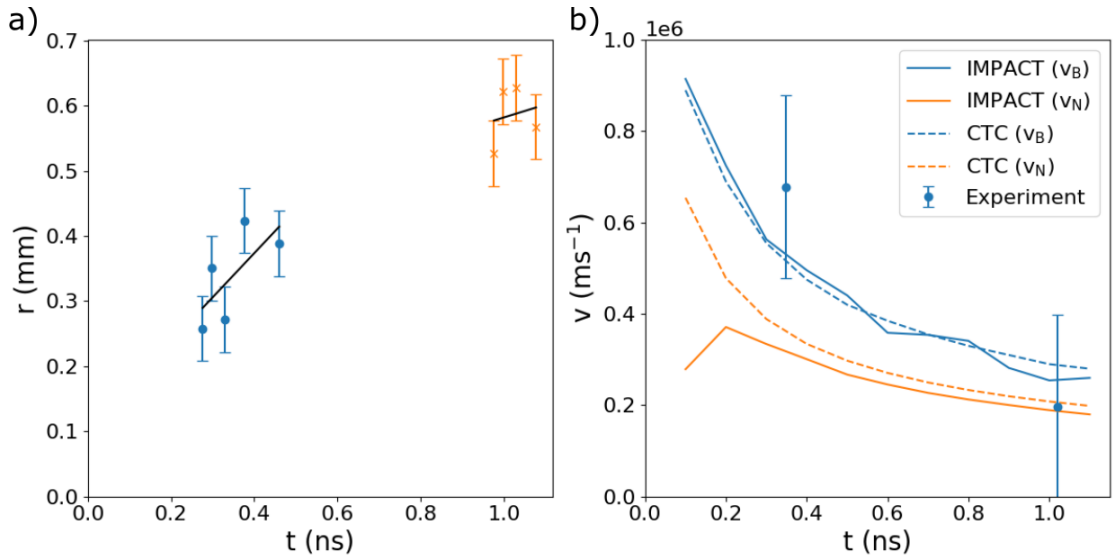

Figure 7.18: In a) the position of the maximum field as a function of time is plotted for an early and late-time shot at 10.7 bar. Fitting a linear trend to each dataset allows the magnetic field advection velocity to be estimated in b), which is compared with the velocity of the peak in the magnetic field and Nernst velocity at this point from IMPACT and CTC simulations.

2) $\times 10^5$ ms^{-1}, while the hydrodynamic advection velocity has increased. At this point in time both the Nernst effect and hydrodynamic motion are responsible for the advection of magnetic field, and directly inferring the Nernst velocity from the magnetic field profile is not possible. For the case shown here, where advection continues in the sheath region, the significant decoupling between the magnetic field and density profiles demonstrate that the Nernst effect is the dominant mechanism.

In general, when the hydrodynamic velocity begins to approach and exceed the Nernst velocity it does not mean that the latter effect can be neglected though. Depending on the plasma regime, different regions of the plasma can continue to experience magnetic field advection dominated by the Nernst effect and vice-versa as was seen in fig. 6.19.

The emergence of non-local transport under these conditions has been the subject of much of this thesis, with this specific problem examined previously in section 6.4. Despite mean-free-paths on the order of 100 µm, where the fluid model should break down, the increase in the magnetic field at the edge of the hot plasma means the Hall parameter at the heat front reaches $\chi_B \approx 10$ by 1.1 ns. In this regime the heat transport becomes limited by the electron gyro-radius rather than by the mean-free-path. The suppression of the Nernst velocity by non-local transport described by Sherlock and Bissell [92] which scales with λ_T/l_T is invalid in this regime, with the gyro-radius a more appropriate quantity. At early times the kinetic and fluid simulations predict different heat-flows, but at later times the Nernst effect increasingly

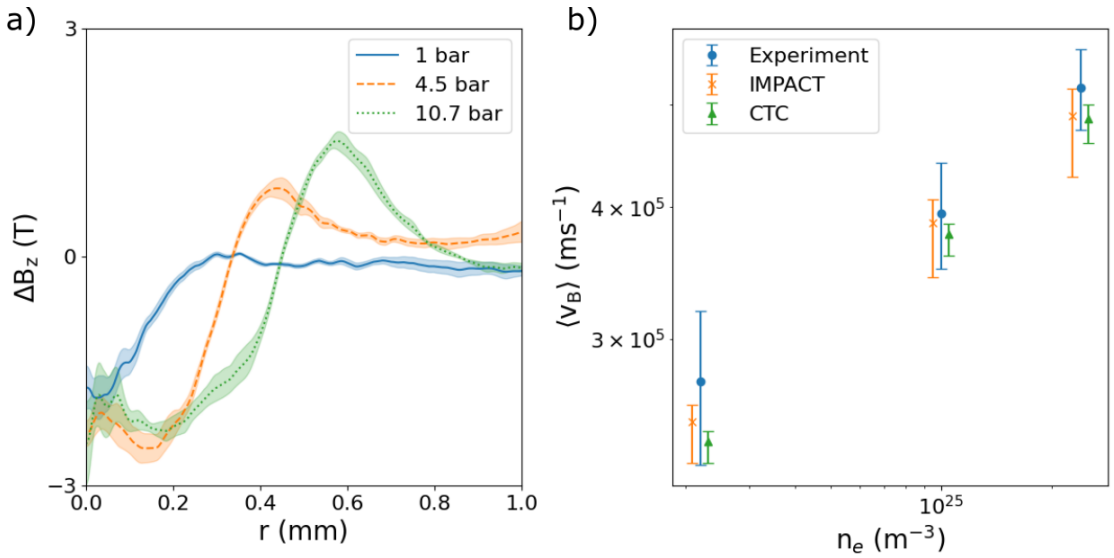

Figure 7.19: a) Lineouts of the reconstructed magnetic field profiles as a function of radius for varying backing pressure at $t = 1.1$ ns, averaged over the central 1 mm of the plasma column. b) The average advection velocity of the peak magnetic field as a function of electron density compared to IMPACT and CTC simulations, with simulation uncertainty calculated by increasing the laser intensity by ±50%.

leads to a magnetic transport barrier which keeps the heat-flow in a relatively local regime, even as the magnetic field inside the cavity falls to zero.

7.4.3 Magnetisation and non-local transport

To further explore the role of non-locality in both thermal and magnetic field transport shots at three different backing pressure were performed. At lower densities the plasma is less collisional, causing the inverse bremsstrahlung heating rate to decrease. As explored in section 6.4, this results in an increase in the mean-free-path to a maximum of $\lambda_T \approx 1$ mm at 1 bar after 1.1 ns, but also makes the plasma more strongly magnetised with a maximum of $\chi_B \approx 36$. The net result is a reduction in relative anisotropy that reduces both the heat-flow and the advection of the magnetic field. The expected scaling of the Nernst velocity with density and temperature is $v_N \propto \tau_B \gamma_\perp$. In the intermediate magnetisation regime this scales as $\tau_B^{1+m} \propto (T_e^{1.5}/n_e)^{1+m}$, where $-2 \geq m \geq 0$ and can be found in fig. 6.11 to be around $m \approx -1$ at $\chi_B = 1$.

The magnetic field profiles from these shots at 1.1 ns are shown in fig. 7.19. The Nernst advection rate is approximated by finding the average velocity of the peak in the magnetic field for both the experimental data, as well as IMPACT and CTC simulations. As expected, the advection velocity falls with decreasing density, with the simulations closely reproducing the behaviour measured in the

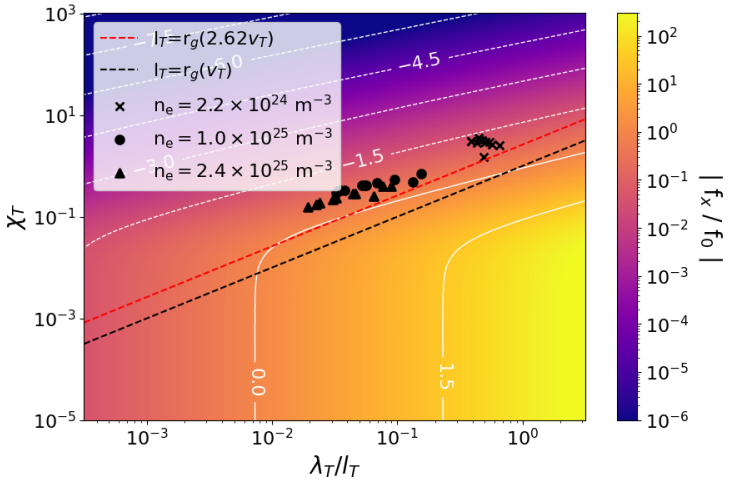

Figure 7.20: A map of the non-local parameter space as a function of λ_T/l_T and χ_T obtained using the relative anisotropy parameter in eq. 4.3 with $v = v_H(\chi_T)$. Overlaid are points obtained from 1D Cartesian IMPACT simulations of the Nernst experiment, obtained at the point where l_T is at a minimum between $t = 0.1$ and 1.1 ns. Dashed lines show where the gyro-radius is equal to the temperature length scale for thermal and heat-carrying electrons with velocity $v = 2.62\ v_T$.

experiment. Fitting the measured average advection velocities to a power law gives a trend $\langle v_B \rangle \propto n_{e0}^{0.30 \pm 0.03}$. Ideally, the fitting should be done against collision time or magnetisation, as otherwise this approach assumes there is little variation in the temperature. However, the nature of the trend implies that the experiment has been conducted in the strongly magnetised regime, with anisotropic transport processes reducing as the density and collision rate decrease.

In fig. 7.20 the position the simulations occupy in the non-local parameter space is explored. While the Knudsen number λ_T/l_T increases at lower density, the magnetisation increases and the ratio of the gyro-radius to the length scale remains largely unchanged. That the ratio r_g/l_T remains almost constant at the heat-front is a result of both r_g and l_T being insensitive to changes in the electron density. Heat-carrying electrons are strongly magnetised at the heat-front causing their effective mean-free-path to then decrease relative to the temperature length-scale. The result is a localisation of transport as the plasma becomes increasingly collisionless, with the mobility of hotter electrons most affected. This result has been demonstrated in the experiment, where the Nernst advection velocity, which is coupled with the heat-flow, is reduced at lower density.

Future experiments in this regime should pursue several avenues of investigation. The first, which can be seen to complete the data set obtained during this experiment, would be to demonstrate the transition from weakly to strongly magnetised transport. Under the same laser conditions this would be done by increasing the

electron density further, at which point a maximum in the Nernst advection velocity should be found on entering the weakly magnetised regime. The next result that is sought is the suppression of the Nernst by an increasing magnetic field, with the suppression by magnetisation already demonstrated here through reduction of the collision rate. At the same time, these results equally demonstrate enhancement of Nernst advection as the magnetisation decreases. To access the non-local Nernst regime the simplest path forward is a reduction in the magnetic field strength, as this is the parameter which can be most easily tuned during laser-plasma experiments. Field strengths around $B_z = 1$ T should result in a noticeable increase in non-local transport, with the effective mean-free-path scaling as $\lambda_{ei}/(1 + \chi_{ei}^2) \propto B_z^{-2}$ in the strongly magnetised regime, while also providing changes in the path-integrated magnetic field that are observable using proton radiography.

7.5 Summary

In summary, the results presented here mark the first direct measurement of magnetic cavitation driven by the Nernst effect, demonstrating the coupling of the magnetic field with heat-flow rather than hydrodynamic ion motion. Models simulating the plasma evolution in this regime which do not include the Nernst effect predict a spuriously high magnetic field within the hot plasma. Suppression of the Nernst effect by magnetisation is observed, driven by an increase in the collision time at lower density. Under these conditions at moderate magnetisation ($\chi_B > 1$) extended MHD models agree surprisingly well with kinetic VFP simulations despite both long mean free paths and demagnetisation of the hot plasma; the heat-flow at the edge of the hot plasma remaining relatively local due to the formation of a transport barrier, with the gyro-radius limiting cross-field transport. Furthermore, the relative anisotropy is reduced at lower density by increasing confinement to the magnetic field, causing a decrease in heat-flow and non-local transport.

The implications of magnetic cavitation driven by the Nernst effect are significant for plasmas with either self-generated or applied fields. Thermal transport effects are typically most significant in laser heating experiments, where large temperature gradients form in the rapidly heated plasma. As a result, the Nernst effect is often the dominant mechanism in the transport of magnetic fields. The formation of self-generated Biermann fields can be modified substantially which has relevance to experiments investigating astrophysics, particularly magnetic reconnection [59, 150], and hydrodynamic instabilities [151, 152]. Self-generated and applied fields are also of interest in inertial confinement fusion experiments, leading to higher hot spot temperature and reducing instability growth [89, 90, 51, 17]. The expulsion of

magnetic field from the hot plasma will increase the field strengths required in these experiments [153, 154].

Exploring the thermo-electric field, both in unmagnetised and magnetised shots, our understanding of transport phenomena is further improved. This is possible because the geometry probed here allows for the separation of electric and magnetic field effects, owing to the cylindrical symmetry of the plasma resulting in a change in the symmetry of the deflection potential. Novel measurements of the temperature profile can then be obtained in this manner. Furthermore, this allows us to consider routes by which the thermo-electric field can be explored in the future, an effect which underpins the Biermann battery.

While discrepancies were observed between the simulations and the experiments, these are attributed to limitations of the simulations rather than to significant novel physics. As discussed in this chapter, these discrepancies are primarily due to the use of 1D Cartesian simulations instead of more physically accurate 2D Cartesian or 1D cylindrical geometries. These will result in a reduced peak magnetic field and higher advection velocities as the transport barrier is relaxed. Additionally, as outlined in chapter 6, the use of an ideal gas equation of state and inclusion of ionisation effects are expected to modify the magnetic field profile by allowing it to diffuse into the sheath. Future simulations should address these limitations to enable more rigorous benchmarking.

Chapter 8

Conclusion

The work presented in this thesis has investigated the effect of magnetic fields on plasmas in which thermal transport effects are dominant. It has been shown how magnetisation suppresses anisotropic transport effects. These results are used to understand an experiment in which the first direct measurement of the Nernst effect was made.

8.1 Test problems for magnetised transport

In chapter 3 it was seen how after expanding the distribution function in Cartesian tensors the anisotropic components naturally appear as the ratio of an effective mean-free-path to a length scale. This effective mean-free-path was $\lambda_{ei}/(1+\chi_{ei}^2)$, which differs from the values of either λ_{ei} (when $\chi_B \ll 1$) or r_g (when $\chi_B > 1$) used previously when assessing the non-locality parameter. In particular, it suggests that in the strongly magnetised regime the effective mean-free-path can be reduced below the gyro-radius.

The local limit was first considered to gain a greater understanding of how the anisotropy perturbs the distribution function. Magnetisation was found to reduce the heat-carrying velocity, suggesting that magnetised plasmas are naturally more resilient to non-local transport as the relative increase in the electron diffusion distance with velocity is reduced. The rate at which the distribution function was perturbed was then found to increase with the ratio $|\mathbf{f}_1|/f_0$, which is the ratio of the effective mean-free-path to length scale.

Kinetic VFP simulations were then performed in chapter 4, demonstrating a correlation between an increase in the relative anisotropy and the degree to which the isotropic distribution is perturbed away from a Maxwellian. This confirms that

the ratio $\mathbf{f}_1/f_0$ is an appropriate metric for considering non-local transport trends. The magnetised parameter space was explored by varying the gyro-frequency and the collision frequency, using the magnetic field and density, respectively. As expected an increasing magnetic field always led to the localisation of transport, with the reduction scaling as expected when using the effective mean-free-path. In the case of varying collision frequency the behaviour was again as expected for the effective mean-free-path, with both λ_{ei} and r_g failing to capture the trend observed in the strongly magnetised regime. These results suggest the effective mean-free-path should be used when calculating the non-locality parameter.

The relationship between the relative anisotropy, heat-flow, and magnetic advection velocity was highlighted. Of particular note was that the ratio of the heat-flow to the free-streaming limit $\mathbf{q}/q_{FS}$ was seen to provide a distribution averaged value of the relative anisotropy, weighted towards heat-carrying particles. This is a much easier number to interpret than the effective mean-free-path, as it is not velocity-dependent. However, q_{FS} is found to be magnetisation dependent-although only weakly-so if $\mathbf{q}/q_{FS}$ is the same at two points in the plasma it does not necessarily suggest the relative anisotropy is actually the same.

In future, it may be worth starting with a less extreme temperature perturbation, as the trends nearer to LTE will likely be clearer when the distribution function is not highly distorted. Additionally, it would be beneficial to perform simulations with a code that includes higher order terms in the distribution function, as it is unclear whether this may change any of the results.

8.2 Laser heating experiments

In chapter 6, the modelling of an experiment investigating transport in a plasma with cylindrical geometry was presented. As expected, simulations without a magnetic field were highly non-local. The purpose of these simulations was primarily to highlight the differences that can arise due to significant non-local transport. A more complete investigation into the effect of non-local transport on the electric field would be of interest.

For simulations with an applied magnetic field, both VFP and extended MHD simulations were in broad agreement. The MHD and kinetic simulations close agreement is attributed to the formation of a magnetic transport barrier. Non-local transport, while significant in the cavity, did not affect the overall progress of the heat front in this regime. Transport trends followed the effective mean-free-path trends explored earlier. Including ion hydrodynamics in the MHD simulations it

was seen that some positive feedback appeared to be occurring between Nernst and hydrodynamic advection. A more thorough investigation is worthwhile.

It is noted that the most significant improvement that could be made is to conduct these simulations in either a one-dimensional cylindrical geometry or in two dimensions. This would suppress the magnetic transport barrier, and likely result in a stronger non-local signal. In these experiments it is unlikely the ions would be magnetised, so it would also be interesting to investigate their behaviour.

Finally, in chapter 7 the Nernst effect was demonstrated experimentally with an advection velocity of $v_N = (7 \pm 2) \times 10^5$ ms^{-1}, with the magnetic field and density profiles decoupled. Suppression of the Nernst effect was then observed as the density decreased. Based on the simulations it is expected that this is caused by the collision frequency decreasing while the magnetisation increases. However, the difficulty in obtaining the temperature profile in the sheath region makes confirmation of this result challenging.

As discussed at the end of that chapter, several avenues can be pursued to develop the Nernst experiment data set. These include running at different magnetic field strengths, performing a broader density scan, and changing the gas. Regarding the thermo-electric field measurements, greater consideration should be given to maximising the integrated electric field to provide a strong signal in the radiography.

Bibliography

[1] C. Arran et al. "Measurement of Magnetic Cavitation Driven by Heat Flow in a Plasma". In: *Physical Review Letters* 131.1 (July 2023), p. 015101. ISSN: 10797114. DOI: 10.1103/PHYSREVLETT.131.015101/FIGURES/5/MEDIUM. URL: https://journals.aps.org/prl/abstract/10.1103/PhysRevLett.131.015101.

[2] R Paul Drake. *High-Energy-Density Physics*. Cham: Springer International Publishing, 2018. ISBN: 978-3-319-67710-1. DOI: 10.1007/978-3-319-67711-8.

[3] S. I. Braginskii. "Transport Processes in a Plasma". In: *Reviews of Plasma Physics* 1 (1965), pp. 205–311.

[4] Stefano Atzeni and Jürgen Meyer-ter-Vehn. *The Physics of Inertial Fusion: Beam Plasma Interaction, Hydrodynamics, Hot Dense Matter*. Oxford University Press, June 2004. ISBN: 9780198562641. DOI: 10.1093/acprof:oso/9780198562641.001.0001.

[5] Francis F. Chen. *Introduction to Plasma Physics and Controlled Fusion*. Third Edition. Springer International Publishing, 2016.

[6] Kim Molvig et al. "Low Fuel Convergence Path to Direct-Drive Fusion Ignition". In: *Physical Review Letters* 116.25 (June 2016), p. 255003. ISSN: 10797114. DOI: 10.1103/PHYSREVLETT.116.255003/FIGURES/3/MEDIUM. URL: https://journals.aps.org/prl/abstract/10.1103/PhysRevLett.116.255003.

[7] E. M. Campbell et al. "Laser-direct-drive program: Promise, challenge, and path forward". In: *Matter and Radiation at Extremes* 2.2 (Mar. 2017), pp. 37–54. ISSN: 2468-080X. DOI: 10.1016/J.MRE.2017.03.001.

[8] H. S. Park et al. "High-adiabat high-foot inertial confinement fusion implosion experiments on the national ignition facility". In: *Physical Review Letters* 112.5 (Feb. 2014), p. 055001. ISSN: 00319007. DOI: 10.1103/PHYSREVLETT.

112.055001/FIGURES/4/MEDIUM. URL: https://journals.aps.org/prl/abstract/10.1103/PhysRevLett.112.055001.

[9] P. Michel et al. "Symmetry tuning via controlled crossed-beam energy transfer on the National Ignition Facility". In: *Physics of Plasmas* 17.5 (May 2010). ISSN: 1070664X. DOI: 10.1063/1.3325733/921925. URL: /aip/pop/article/17/5/056305/921925/Symmetry-tuning-via-controlled-crossed-beam-energy.

[10] H. Abu-Shawareb et al. "Lawson Criterion for Ignition Exceeded in an Inertial Fusion Experiment". In: *Physical Review Letters* 129.7 (Aug. 2022), p. 075001. ISSN: 10797114. DOI: 10.1103/PHYSREVLETT.129.075001/FIGURES/7/MEDIUM. URL: https://journals.aps.org/prl/abstract/10.1103/PhysRevLett.129.075001.

[11] H. Abu-Shawareb et al. "Achievement of Target Gain Larger than Unity in an Inertial Fusion Experiment". In: *Physical Review Letters* 132.6 (Feb. 2024), p. 065102. ISSN: 10797114. DOI: 10.1103/PHYSREVLETT.132.065102/FIGURES/4/MEDIUM. URL: https://journals.aps.org/prl/abstract/10.1103/PhysRevLett.132.065102.

[12] *Achieving Fusion Ignition — National Ignition Facility & Photon Science*. URL: https://lasers.llnl.gov/science/achieving-fusion-ignition.

[13] L. Divol et al. "Thermonuclear performance variability near ignition at the National Ignition Facility". In: *Physics of Plasmas* 31.10 (Oct. 2024). ISSN: 10897674. DOI: 10.1063/5.0222265/3316174. URL: /aip/pop/article/31/10/102703/3316174/Thermonuclear-performance-variability-near.

[14] L. J. Perkins et al. "The potential of imposed magnetic fields for enhancing ignition probability and fusion energy yield in indirect-drive inertial confinement fusion". In: *Physics of Plasmas* 24.6 (June 2017). ISSN: 10897674. DOI: 10.1063/1.4985150.

[15] M. Hohenberger et al. "Inertial confinement fusion implosions with imposed magnetic field compression using the OMEGA Laser". In: *Physics of Plasmas* 19.5 (May 2012). ISSN: 1070664X. DOI: 10.1063/1.3696032/596932. URL: /aip/pop/article/19/5/056306/596932/Inertial-confinement-fusion-implosions-with.

[16] O. V. Gotchev et al. "Laser-Driven magnetic-flux compression in high-energy-density plasmas". In: *Physical Review Letters* 103.21 (Nov. 2009), p. 215004. ISSN: 00319007. DOI: 10.1103/PHYSREVLETT.103.215004/FIGURES/6/MEDIUM. URL: https://journals.aps.org/prl/abstract/10.1103/PhysRevLett.103.215004.

[17] A. Bose et al. “Effect of Strongly Magnetized Electrons and Ions on Heat Flow and Symmetry of Inertial Fusion Implosions”. In: *Physical Review Letters* 128.19 (May 2022), p. 195002. ISSN: 10797114. DOI: 10.1103/PHYSREVLETT.128.195002/FIGURES/4/MEDIUM. URL: https://journals.aps.org/prl/abstract/10.1103/PhysRevLett.128.195002.

[18] W. A. Farmer et al. “Simulation of self-generated magnetic fields in an inertial fusion hohlraum environment”. In: *Physics of Plasmas* 24.052703 (May 2017). DOI: 10.1063/1.4983140.

[19] C. A. Walsh et al. “Self-Generated Magnetic Fields in the Stagnation Phase of Indirect-Drive Implosions on the National Ignition Facility”. In: *Physical Review Letters* 118.15 (Apr. 2017), p. 155001. ISSN: 10797114. DOI: 10.1103/PHYSREVLETT.118.155001/FIGURES/3/MEDIUM. URL: https://journals.aps.org/prl/abstract/10.1103/PhysRevLett.118.155001.

[20] A. R. Bell, R. G. Evans, and D. J. Nicholas. “Electron energy transport in steep temperature gradients in laser-produced plasmas”. In: *Physical Review Letters* 46.4 (1981), pp. 243–246.

[21] Bruce A. Remington et al. “A review of astrophysics experiments on intense lasers”. In: *Physics of Plasmas* 7.5 (May 2000), pp. 1641–1652. ISSN: 1070-664X. DOI: 10.1063/1.874046. URL: /aip/pop/article/7/5/1641/267249/A-review-of-astrophysics-experiments-on-intense.

[22] Bruce A. Remington, R. Paul Drake, and Dmitri D. Ryutov. “Experimental astrophysics with high power lasers and Z pinches”. In: *Reviews of Modern Physics* 78.3 (Aug. 2006), pp. 755–807. ISSN: 00346861. DOI: 10.1103/REVMODPHYS.78.755/FIGURES/38/THUMBNAIL. URL: https://journals.aps.org/rmp/abstract/10.1103/RevModPhys.78.755.

[23] B. Albertazzi et al. “Laboratory formation of a scaled protostellar jet by coaligned poloidal magnetic field”. In: *Science* 346.6207 (Oct. 2014), pp. 325–328. ISSN: 10959203. DOI: 10.1126/SCIENCE.1259694/SUPPL{_}FILE/ALBERTAZZI.SM.PDF. URL: https://www.science.org/doi/10.1126/science.1259694.

[24] G. Gregori et al. “Generation of scaled protogalactic seed magnetic fields in laser-produced shock waves”. In: *Nature 2012 481:7382* 481.7382 (Jan. 2012), pp. 480–483. ISSN: 1476-4687. DOI: 10.1038/nature10747. URL: https://www.nature.com/articles/nature10747.

[25] Jena Meinecke et al. “Strong suppression of heat conduction in a laboratory replica of galaxy-cluster turbulent plasmas”. In: *Science Advances* 8.10 (Mar. 2022), p. 6799. ISSN: 23752548. DOI: 10.1126/SCIADV.ABJ6799/SUPPL{_}FILE/SCIADV.ABJ6799{_}SM.PDF. URL: https://www.science.org/doi/10.1126/sciadv.abj6799.

[26] Y. Kuramitsu et al. “Time evolution of collisionless shock in counterstreaming laser-produced plasmas”. In: *Physical Review Letters* 106.17 (Apr. 2011), p. 175002. ISSN: 00319007. DOI: 10.1103/PHYSREVLETT.106.175002/FIGURES/4/MEDIUM. URL: https://journals.aps.org/prl/abstract/10.1103/PhysRevLett.106.175002.

[27] Abraham Chien et al. “Direct measurement of non-thermal electron acceleration from magnetically driven reconnection in a laboratory plasma”. In: (Jan. 2022). URL: http://arxiv.org/abs/2201.10052.

[28] B. Albertazzi et al. “Triggering star formation: Experimental compression of a foam ball induced by Taylor-Sedov blast waves”. In: *Matter and Radiation at Extremes* 7.3 (May 2022). ISSN: 2468080X. DOI: 10.1063/5.0068689/2844510. URL: /aip/mre/article/7/3/036902/2844510/Triggering-star-formation-Experimental-compression.

[29] D. Ryutov et al. “Similarity Criteria for the Laboratory Simulation of Supernova Hydrodynamics”. In: *The Astrophysical Journal* 518.2 (June 1999), pp. 821–832. ISSN: 0004-637X. DOI: 10.1086/307293/FULLTEXT/. URL: https://iopscience.iop.org/article/10.1086/307293%20https://iopscience.iop.org/article/10.1086/307293/meta.

[30] D. D. Ryutov, R. P. Drake, and B. A. Remington. “Criteria for Scaled Laboratory Simulations of Astrophysical MHD Phenomena”. In: *The Astrophysical Journal Supplement Series* 127.2 (Apr. 2000), pp. 465–468. ISSN: 0067-0049. DOI: 10.1086/313320/FULLTEXT/. URL: https://iopscience.iop.org/article/10.1086/313320%20https://iopscience.iop.org/article/10.1086/313320/meta.

[31] É Falize, C. Michaut, and S. Bouquet. “SIMILARITY PROPERTIES AND SCALING LAWS OF RADIATION HYDRODYNAMIC FLOWS IN LABORATORY ASTROPHYSICS”. In: *The Astrophysical Journal* 730.2 (Mar. 2011), p. 96. ISSN: 0004-637X. DOI: 10.1088/0004-637X/730/2/96. URL: https://iopscience.iop.org/article/10.1088/0004-637X/730/2/96%20https://iopscience.iop.org/article/10.1088/0004-637X/730/2/96/meta.

[32] T. J. M. Boyd and J. J. Sanderson. *The Physics of Plasmas*. Cambridge University Press, Jan. 2003. ISBN: 9780521459129. DOI: 10.1017/CBO9780511755750. URL: https://www.cambridge.org/core/product/identifier/9780511755750/type/book.

[33] F. Pérez et al. "Improved modeling of relativistic collisions and collisional ionization in particle-in-cell codes". In: *Physics of Plasmas* 19.8 (Aug. 2012). ISSN: 1070664X. DOI: 10.1063/1.4742167.

[34] Y. Sentoku and A. J. Kemp. "Numerical methods for particle simulations at extreme densities and temperatures: Weighted particles, relativistic collisions and reduced currents". In: *Journal of Computational Physics* 227.14 (July 2008), pp. 6846–6861. ISSN: 10902716. DOI: 10.1016/J.JCP.2008.03.043.

[35] Marshall N. Rosenbluth, William M. MacDonald, and David L. Judd. "Fokker-Planck Equation for an Inverse-Square Force". In: *Physical Review* 107.1 (July 1957), p. 1. ISSN: 0031899X. DOI: 10.1103/PhysRev.107.1. URL: https://journals.aps.org/pr/abstract/10.1103/PhysRev.107.1.

[36] I. P. Shkarofsky, T. W. Johnston, and M. P. Bachynski. *The Particle Kinetics of Plasmas*. Addison-Wesley, 1966.

[37] T. W. Johnston. "Cartesian Tensor Scalar Product and Spherical Harmonic Expansions in Boltzmann's Equation". In: *Physical Review* 120.4 (1960), pp. 1103–1111.

[38] E. M. Epperlein and R. W. Short. "A practical nonlocal model for electron heat transport in laser plasmas". In: *Physics of Fluids B: Plasma Physics* 3.11 (Nov. 1991), pp. 3092–3098. ISSN: 0899-8221. DOI: 10.1063/1.859789. URL: /aip/pfb/article/3/11/3092/449682/A-practical-nonlocal-model-for-electron-heat.

[39] J. P. Brodrick et al. "Incorporating kinetic effects on Nernst advection in inertial fusion simulations". In: *Plasma Physics and Controlled Fusion* 60.084009 (June 2018). DOI: 10.1088/1361-6587/aaca0b.

[40] A R Bell and M Sherlock. "The fastVFP code for solution of the Vlasov–Fokker–Planck equation". In: *Plasma Physics and Controlled Fusion* 66.3 (Feb. 2024), p. 035014. ISSN: 0741-3335. DOI: 10.1088/1361-6587/AD2278. URL: https://iopscience.iop.org/article/10.1088/1361-6587/ad2278%20https://iopscience.iop.org/article/10.1088/1361-6587/ad2278/meta.

[41] A. G.R. Thomas et al. "A review of Vlasov-Fokker-Planck numerical modeling of inertial confinement fusion plasma". In: *Journal of Computational Physics* 231.3 (2012), pp. 1051–1079. ISSN: 10902716. DOI: 10.1016/J.JCP.2011.09.028.

[42] R. J. Kingham and A. R. Bell. "An implicit Vlasov-Fokker-Planck code to model non-local electron transport in 2-D with magnetic fields". In: *Journal of Computational Physics* 194.1 (Feb. 2004), pp. 1–34. ISSN: 00219991. DOI: 10.1016/j.jcp.2003.08.017.

[43] Sydney Chapman and T.G. Cowling. *The Mathematical Theory of Non-Uniform Gases*. Cambridge University Press, 1953.

[44] Per Helander and Dieter J. Sigmar. *Collisional Transport in Magnetized Plasmas*. 2005. ISBN: 9780521020985.

[45] E. M. Epperlein. "The accuracy of Braginskii's transport coefficients for a Lorentz plasma". In: *Journal of Physics D: Applied Physics* 17.9 (Sept. 1984), p. 1823. ISSN: 0022-3727. DOI: 10.1088/0022-3727/17/9/007. URL: https://iopscience.iop.org/article/10.1088/0022-3727/17/9/007%20https://iopscience.iop.org/article/10.1088/0022-3727/17/9/007/meta.

[46] E. M. Epperlein and M. G. Haines. "Plasma transport coefficients in a magnetic field by direct numerical solution of the Fokker–Planck equation". In: *Physics of Fluids* 29.4 (1986), p. 1029. DOI: 10.1063/1.865901.

[47] C. P. Ridgers et al. "Transport in the presence of inverse bremsstrahlung heating and magnetic fields". In: *Physics of Plasmas* 15.9 (Sept. 2008), p. 44. ISSN: 1070664X. DOI: 10.1063/1.2978092/281988. URL: /aip/pop/article/15/9/092311/281988/Transport-in-the-presence-of-inverse.

[48] James D. Sadler, Christopher A. Walsh, and Hui Li. "Symmetric Set of Transport Coefficients for Collisional Magnetized Plasma". In: *Physical Review Letters* 126.7 (Feb. 2021). ISSN: 10797114. DOI: 10.1103/PhysRevLett.126.075001.

[49] C. P. Ridgers, R. J. Kingham, and A. G.R. Thomas. "Magnetic cavitation and the reemergence of nonlocal transport in laser plasmas". In: *Physical Review Letters* 100.7 (Feb. 2008). ISSN: 00319007. DOI: 10.1103/PhysRevLett.100.075003.

[50] James D. Sadler, Hui Li, and Kirk A. Flippo. "Parameter space for magnetization effects in high-energy-density plasmas". In: *Matter and Radiation at Extremes* 6.6 (Nov. 2021), p. 65902. ISSN: 2468080X. DOI: 10.1063/5.0057087/253213. URL: /aip/mre/article/6/6/065902/253213/Parameter-space-for-magnetization-effects-in-high.

[51] C. A. Walsh et al. “Perturbation modifications by pre-magnetisation of inertial confinement fusion implosions”. In: *Physics of Plasmas* 26.2 (Feb. 2019). ISSN: 10897674. DOI: 10.1063/1.5085498/253631. URL: /aip/pop/article/26/2/022701/253631/Perturbation-modifications-by-pre-magnetisation-of.

[52] J. J. Bissell, C. P. Ridgers, and R. J. Kingham. “Field compressing magnetothermal instability in laser plasmas”. In: *Physical Review Letters* 105.17 (Oct. 2010), p. 175001. ISSN: 00319007. DOI: 10.1103/PHYSREVLETT.105.175001/FIGURES/3/MEDIUM. URL: https://journals.aps.org/prl/abstract/10.1103/PhysRevLett.105.175001.

[53] Russell M. Kulsrud et al. “The Protogalactic Origin for Cosmic Magnetic Fields”. In: *The Astrophysical Journal* 480.2 (May 1997), pp. 481–491. ISSN: 0004-637X. DOI: 10.1086/303987/FULLTEXT/. URL: https://iopscience.iop.org/article/10.1086/303987%20https://iopscience.iop.org/article/10.1086/303987/meta.

[54] C. K. Li et al. “Observations of electromagnetic fields and plasma flow in hohlraums with proton radiography”. In: *Physical Review Letters* 102.20 (May 2009), p. 205001. ISSN: 00319007. DOI: 10.1103/PHYSREVLETT.102.205001/FIGURES/5/MEDIUM. URL: https://journals.aps.org/prl/abstract/10.1103/PhysRevLett.102.205001.

[55] I. V. Igumenshchev et al. “Self-generated magnetic fields in direct-drive implosion experiments”. In: *Physics of Plasmas* 21.6 (June 2014). ISSN: 10897674. DOI: 10.1063/1.4883226/212583. URL: /aip/pop/article/21/6/062707/212583/Self-generated-magnetic-fields-in-direct-drive.

[56] J. A. Stamper et al. “Spontaneous Magnetic Fields in Laser-Produced Plasmas”. In: *Physical Review Letters* 26.17 (Apr. 1971), p. 1012. ISSN: 00319007. DOI: 10.1103/PhysRevLett.26.1012. URL: https://journals.aps.org/prl/abstract/10.1103/PhysRevLett.26.1012.

[57] L. Gao et al. “Precision mapping of laser-driven magnetic fields and their evolution in high-energy-density plasmas”. In: *Physical Review Letters* 114.21 (May 2015), p. 215003. ISSN: 10797114. DOI: 10.1103/PHYSREVLETT.114.215003/FIGURES/4/MEDIUM. URL: https://journals.aps.org/prl/abstract/10.1103/PhysRevLett.114.215003.

[58] P. T. Campbell et al. “Measuring magnetic flux suppression in high-power laser–plasma interactions”. In: *Physics of Plasmas* 29.1 (Jan. 2022). ISSN: 1070-664X. DOI: 10.1063/5.0062717. URL: https://pubs.aip.org/pop/

article/29/1/012701/2847716/Measuring-magnetic-flux-suppression-in-high-power.

[59] P. M. Nilson et al. "Magnetic reconnection and plasma dynamics in two-beam laser-solid interactions". In: *Physical Review Letters* 97.25 (2006). ISSN: 00319007. DOI: 10.1103/PhysRevLett.97.255001.

[60] R. J. Kingham and A. R. Bell. "Nonlocal Magnetic-Field Generation in Plasmas without Density Gradients". In: *Physical Review Letters* 88.4 (2002), p. 4. ISSN: 10797114. DOI: 10.1103/PhysRevLett.88.045004.

[61] Erich S. Weibel. "Spontaneously Growing Transverse Waves in a Plasma Due to an Anisotropic Velocity Distribution". In: *Physical Review Letters* 2.3 (Feb. 1959), p. 83. ISSN: 00319007. DOI: 10.1103/PhysRevLett.2.83. URL: https://journals.aps.org/prl/abstract/10.1103/PhysRevLett.2.83.

[62] E. M. Epperlein. "A comparison of the kinetic and 2 electron fluid models of the collisional Weibel instability in laser-plasmas". In: *Plasma Physics and Controlled Fusion* 27.9 (Sept. 1985), p. 1027. ISSN: 0741-3335. DOI: 10.1088/0741-3335/27/9/008. URL: https://iopscience.iop.org/article/10.1088/0741-3335/27/9/008%20https://iopscience.iop.org/article/10.1088/0741-3335/27/9/008/meta.

[63] C. A. Walsh et al. "Extended-magnetohydrodynamics in under-dense plasmas". In: *Physics of Plasmas* 27.2 (Feb. 2020). ISSN: 10897674. DOI: 10.1063/1.5124144.

[64] A Nishiguchi et al. "Convective Amplification of Magnetic Fields in Laser-Produced Plasmas by the Nernst Effect". In: *Physical Review Letters* 53.3 (1984).

[65] T. H. Kho and M. G. Haines. "Nonlinear electron transport in magnetized laser plasmas". In: *Physics of Fluids* 29.8 (1986), p. 2665. ISSN: 00319171. DOI: 10.1063/1.865508.

[66] A. Nishiguchi, T. Yabe, and M. G. Haines. "Nernst effect in laser-produced plasmas". In: *The Physics of Fluids* 28.12 (Dec. 1985), pp. 3683–3690. ISSN: 0031-9171. DOI: 10.1063/1.865100. URL: /aip/pfl/article/28/12/3683/812233/Nernst-effect-in-laser-produced-plasmas.

[67] M. G. Haines. "Heat flux effects in Ohm's law". In: *Plasma Physics and Controlled Fusion* 28.11 (Nov. 1986), p. 1705. ISSN: 0741-3335. DOI: 10.1088/0741-3335/28/11/007. URL: https://iopscience.iop.org/article/10.1088/0741-3335/28/11/007%20https://iopscience.iop.org/article/10.1088/0741-3335/28/11/007/meta.

[68] Kasra Amini et al. “Symphony on strong field approximation”. In: *Reports on Progress in Physics* 82.11 (Oct. 2019), p. 116001. ISSN: 0034-4885. DOI: 10.1088/1361-6633/AB2BB1. URL: https://iopscience.iop.org/article/10.1088/1361-6633/ab2bb1%20https://iopscience.iop.org/article/10.1088/1361-6633/ab2bb1/meta.

[69] Paul Gibbon. *Short Pulse Laser Interactions with Matter*. PUBLISHED BY IMPERIAL COLLEGE PRESS and DISTRIBUTED BY WORLD SCIENTIFIC PUBLISHING CO., Sept. 2005. ISBN: 978-1-86094-135-1. DOI: 10.1142/p116.

[70] A. Bruce Langdon. “Nonlinear Inverse Bremsstrahlung and Heated-Electron Distributions”. In: *Physical Review Letters* 44.9 (Mar. 1980), p. 575. ISSN: 00319007. DOI: 10.1103/PhysRevLett.44.575. URL: https://journals.aps.org/prl/abstract/10.1103/PhysRevLett.44.575.

[71] J P Matte and J Virmont. “Electron Heat Transport down Steep Temperature Gradients”. In: *Physical Review Letters* 49.26 (1982), pp. 1936–1939.

[72] A. L. Milder et al. “Measurements of Non-Maxwellian Electron Distribution Functions and Their Effect on Laser Heating”. In: *Physical Review Letters* 127.1 (July 2021), p. 015001. ISSN: 10797114. DOI: 10.1103/PHYSREVLETT.127.015001/FIGURES/3/MEDIUM. URL: https://journals.aps.org/prl/abstract/10.1103/PhysRevLett.127.015001.

[73] D. R. Gray and J. D. Kilkenny. “The measurement of ion acoustic turbulence and reduced thermal conductivity caused by a large temperature gradient in a laser heated plasma”. In: *Plasma Physics* 22.2 (Feb. 1980), p. 81. ISSN: 0032-1028. DOI: 10.1088/0032-1028/22/2/001. URL: https://iopscience.iop.org/article/10.1088/0032-1028/22/2/001%20https://iopscience.iop.org/article/10.1088/0032-1028/22/2/001/meta.

[74] R C Malone, R L McCrory, and R L Morse. “Indications of Strongly Flux-Limited Electron Thermal Conduction in Laser-Target Experiments*”. In: *Physical Review Letters* 34.12 (1974), pp. 721–724.

[75] O. S. Jones et al. “Towards a more universal understanding of radiation drive in gas-filled hohlraums”. In: *Journal of Physics: Conference Series* 717.1 (May 2016), p. 012026. ISSN: 1742-6596. DOI: 10.1088/1742-6596/717/1/012026. URL: https://iopscience.iop.org/article/10.1088/1742-6596/717/1/012026%20https://iopscience.iop.org/article/10.1088/1742-6596/717/1/012026/meta.

[76] M. D. Rosen et al. "The role of a detailed configuration accounting (DCA) atomic physics package in explaining the energy balance in ignition-scale hohlraums". In: *High Energy Density Physics* 7.3 (Sept. 2011), pp. 180–190. ISSN: 1574-1818. DOI: 10.1016/J.HEDP.2011.03.008.

[77] D. A. Chapman et al. "A preliminary assessment of the sensitivity of uniaxially driven fusion targets to flux-limited thermal conduction modeling". In: *Physics of Plasmas* 28.7 (July 2021), p. 72702. ISSN: 10897674. DOI: 10.1063/5.0047627/1059466. URL: /aip/pop/article/28/7/072702/1059466/A-preliminary-assessment-of-the-sensitivity-of.

[78] John Bissell. *Flux-Limited Heat-flow and Magnetic-Field Transport in Laser-Plasmas*. Tech. rep. Central Laser Facility, 2012, pp. 1–4.

[79] J. P. Brodrick et al. "Testing nonlocal models of electron thermal conduction for magnetic and inertial confinement fusion applications". In: *Physics of Plasmas* 24.092309 (Sept. 2017). DOI: 10.1063/1.5001079.

[80] G. P. Schurtz, P. D. Nicolaï, and M. Busquet. "A nonlocal electron conduction model for multidimensional radiation hydrodynamics codes". In: *Physics of Plasmas* 7.10 (2000), pp. 4238–4249. ISSN: 1070664X. DOI: 10.1063/1.1289512.

[81] Ph D. Nicolaï, J. L.A. Feugeas, and G. P. Schurtz. "A practical nonlocal model for heat transport in magnetized laser plasmas". In: *Physics of Plasmas* 13.3 (2006). ISSN: 1070664X. DOI: 10.1063/1.2179392.

[82] M. Strauss et al. "Magnetic field effects on electron heat transport in laser-produced plasmas". In: *Physical Review A* 30.5 (Nov. 1984), p. 2627. ISSN: 10502947. DOI: 10.1103/PhysRevA.30.2627. URL: https://journals.aps.org/pra/abstract/10.1103/PhysRevA.30.2627.

[83] J. F. Luciani, P. Mora, and A. Bendib. "Magnetic Field and Nonlocal Transport in Laser-Created Plasmas". In: *Physical Review Letters* 55.22 (Nov. 1985), p. 2421. ISSN: 00319007. DOI: 10.1103/PhysRevLett.55.2421. URL: https://journals.aps.org/prl/abstract/10.1103/PhysRevLett.55.2421.

[84] G. Schurtz et al. "Revisiting nonlocal electron-energy transport in inertial-fusion conditions". In: *Physical Review Letters* 98.9 (Feb. 2007). ISSN: 00319007. DOI: 10.1103/PhysRevLett.98.095002.

[85] John Joseph Bissell. "Magnetised Transport and Instability in Laser Produced Plasmas". PhD thesis. London: Imperial College London, 2011.

[86] C. A. Walsh and M. Sherlock. "Kinetic corrections to heat-flow and Nernst advection for laser heated plasmas". In: *Physics of Plasmas* 31.10 (Oct. 2024). ISSN: 10897674. DOI: 10.1063/5.0225592/3316383. URL: /aip/pop/article/31/10/102704/3316383/Kinetic-corrections-to-heat-flow-and-Nernst.

[87] D. W. Hill and R. J. Kingham. "Enhancement of pressure perturbations in ablation due to kinetic magnetized transport effects under direct-drive inertial confinement fusion relevant conditions". In: *Physical Review E* 98.2 (Aug. 2018), p. 021201. ISSN: 24700053. DOI: 10.1103/PHYSREVE.98.021201/FIGURES/6/MEDIUM. URL: https://journals.aps.org/pre/abstract/10.1103/PhysRevE.98.021201.

[88] E. R. Tubman et al. "Observations of pressure anisotropy effects within semi-collisional magnetized plasma bubbles". In: *Nature Communications* 12.1 (Dec. 2021). ISSN: 20411723. DOI: 10.1038/s41467-020-20387-7.

[89] D. H. Froula et al. "Quenching of the nonlocal electron heat transport by large external magnetic fields in a laser-produced plasma measured with imaging Thomson scattering". In: *Physical Review Letters* 98.13 (Mar. 2007). ISSN: 00319007. DOI: 10.1103/PhysRevLett.98.135001.

[90] P. Y. Chang et al. "Fusion yield enhancement in magnetized laser-driven implosions". In: *Physical Review Letters* 107.3 (July 2011). ISSN: 00319007. DOI: 10.1103/PhysRevLett.107.035006.

[91] A. S. Joglekar et al. "Kinetic modeling of Nernst effect in magnetized hohlraums". In: *Physical Review E* 93.4 (Apr. 2016). ISSN: 24700053. DOI: 10.1103/PhysRevE.93.043206.

[92] M. Sherlock and J. J. Bissell. "Suppression of the Biermann Battery and Stabilization of the Thermomagnetic Instability in Laser Fusion Conditions". In: *Physical Review Letters* 124.5 (Feb. 2020), p. 055001. ISSN: 10797114. DOI: 10.1103/PHYSREVLETT.124.055001/FIGURES/3/MEDIUM. URL: https://journals.aps.org/prl/abstract/10.1103/PhysRevLett.124.055001.

[93] J. R. Davies. "Nonlocal suppression of Biermann battery magnetic-field generation for arbitrary atomic numbers and magnetization". In: *Physics of Plasmas* 30.7 (July 2023), p. 72701. ISSN: 10897674. DOI: 10.1063/5.0152530/2901079. URL: /aip/pop/article/30/7/072701/2901079/Nonlocal-suppression-of-Biermann-battery-magnetic.

[94] A V Brantov et al. “Linear theory of nonlocal transport in a magnetized plasma”. In: *Physics of Plasmas* 10.12 (Dec. 2003), pp. 4633–4644. ISSN: 1070-664X. DOI: 10.1063/1.1624249. URL: /aip/pop/article/10/12/4633/1014254/Linear-theory-of-nonlocal-transport-in-a.

[95] D. Del Sorbo et al. “Extension of a reduced entropic model of electron transport to magnetized nonlocal regimes of high-energy-density plasmas”. In: *Laser and Particle Beams* 34.3 (2016), pp. 412–425. ISSN: 0263-0346. DOI: 10.1017/S0263034616000252.

[96] M. Sherlock, J. P. Brodrick, and C. P. Ridgers. “A comparison of non-local electron transport models for laser-plasmas relevant to inertial confinement fusion”. In: *Physics of Plasmas* 24.082706 (Aug. 2017). DOI: 10.1063/1.4986095.

[97] N. R. Shaffer et al. “An extended Vlasov-Fokker-Planck approach for kinetic simulations of laser plasmas”. In: *Physics of Plasmas* 30.4 (Apr. 2023), p. 43906. ISSN: 10897674. DOI: 10.1063/5.0143248/2884882. URL: /aip/pop/article/30/4/043906/2884882/An-extended-Vlasov-Fokker-Planck-approach-for.

[98] J. R. Davies et al. “The importance of electrothermal terms in Ohm’s law for magnetized spherical implosions”. In: *Physics of Plasmas* 22.112703 (Nov. 2015). DOI: 10.1063/1.4935286.

[99] A. V. Brantov, V. Yu Bychenkov, and W. Rozmus. “Relaxation of a thermal perturbation in a collisional plasma”. In: *Plasma Physics Reports* 32.4 (Apr. 2006), pp. 337–343. ISSN: 1063780X. DOI: 10.1134/S1063780X0604009X/METRICS.

[100] J. P. Brodrick, D. Del Sorbo, and C. P. Ridgers. “An alternative justification for the stationary assumption made by many reduced models for nonlocal electron heat flow in plasmas”. In: *Physics of Plasmas* 30.5 (May 2023). ISSN: 10897674. DOI: 10.1063/5.0134966/2891424. URL: /aip/pop/article/30/5/054501/2891424/An-alternative-justification-for-the-stationary.

[101] Jay P. Boris. “Relativistic plasma simulation—Optimization of a hybrid code”. In: *Proceedings of the Conference on the Numerical Simulation of Plasmas (4th)*. Ed. by Jay P. Boris and Ramy A. Shanny. Washington: National Technical Information Service, July 1971, pp. 3–67. URL: https://apps.dtic.mil/sti/citations/ADA023511.

[102] C. Arran, C. P. Ridgers, and N. C. Woolsey. "Proton radiography in background magnetic fields". In: *Matter and Radiation at Extremes* 6.4 (July 2021), p. 46904. ISSN: 2468080X. DOI: 10.1063/5.0054172/253070. URL: /aip/mre/article/6/4/046904/253070/Proton-radiography-in-background-magnetic-fields.

[103] M. Borghesi et al. "Proton imaging: a diagnostic for inertial confinement fusion/fast ignitor studies". In: *Plasma Physics and Controlled Fusion* 43.12A (Nov. 2001), A267. ISSN: 0741-3335. DOI: 10.1088/0741-3335/43/12A/320. URL: https://iopscience.iop.org/article/10.1088/0741-3335/43/12A/320%20https://iopscience.iop.org/article/10.1088/0741-3335/43/12A/320/meta.

[104] S. Kar et al. "Modeling of laser-driven proton radiography of dense matter". In: *High Energy Density Physics* 4.1-2 (Apr. 2008), pp. 26–40. ISSN: 1574-1818. DOI: 10.1016/J.HEDP.2007.11.002.

[105] Hiroyuki Daido, Mamiko Nishiuchi, and Alexander S. Pirozhkov. *Review of laser-driven ion sources and their applications*. Tech. rep. 056401. Apr. 2012. DOI: 10.1088/0034-4885/75/5/056401.

[106] C. K. Li et al. *Monoenergetic proton backlighter for measuring e and B fields and for radiographing implosions and high-energy density plasmas (invited)*. Tech. rep. 10E725. 2006. DOI: 10.1063/1.2228252.

[107] Donna Strickland and Gerard Mourou. "Compression of amplified chirped optical pulses". In: *Optics Communications* 56.3 (Dec. 1985), pp. 219–221. ISSN: 0030-4018. DOI: 10.1016/0030-4018(85)90120-8.

[108] S C Wilks et al. "Energetic proton generation in ultra-intense laser–solid interactions". In: *Physics of Plasmas* 8.2 (Feb. 2001), pp. 542–549. ISSN: 1070-664X. DOI: 10.1063/1.1333697. URL: /aip/pop/article/8/2/542/264618/Energetic-proton-generation-in-ultra-intense-laser.

[109] A. Higginson et al. "Near-100 MeV protons via a laser-driven transparency-enhanced hybrid acceleration scheme". In: *Nature Communications* 9.1 (Dec. 2018). ISSN: 20411723. DOI: 10.1038/s41467-018-03063-9.

[110] F. Nürnberg et al. "Radiochromic film imaging spectroscopy of laser-accelerated proton beams". In: *Review of Scientific Instruments* 80.033301 (2009). DOI: 10.1063/1.3086424.

[111] T. E. Cowan et al. "Ultralow emittance, multi-MeV proton beams from a laser virtual-cathode plasma accelerator". In: *Physical Review Letters* 92.20 (May 2004), p. 204801. ISSN: 00319007. DOI: 10.1103/PHYSREVLETT.92.

204801/FIGURES/5/MEDIUM. URL: https://journals.aps.org/prl/abstract/10.1103/PhysRevLett.92.204801.

[112] N. L. Kugland et al. "Invited Article: Relation between electric and magnetic field structures and their proton-beam images". In: *Review of Scientific Instruments*. Vol. 83. 10. Oct. 2012. DOI: 10.1063/1.4750234.

[113] A. B. Zylstra et al. *Using high-intensity laser-generated energetic protons to radiograph directly driven implosions*. Jan. 2012. DOI: 10.1063/1.3680110.

[114] P. Bradford et al. "EMP control and characterization on high-power laser systems". In: *High Power Laser Science and Engineering* 6 (2018). ISSN: 2095-4719. DOI: 10.1017/hpl.2018.21.

[115] P. R. Bolton et al. "Instrumentation for diagnostics and control of laser-accelerated proton (ion) beams". In: *Physica Medica* 30.3 (May 2014), pp. 255–270. ISSN: 1120-1797. DOI: 10.1016/J.EJMP.2013.09.002.

[116] Azam Niroomand-Rad et al. "Report of AAPM Task Group 235 Radiochromic Film Dosimetry: An Update to TG-55". In: *Medical Physics* 47.12 (Dec. 2020), pp. 5986–6025. ISSN: 2473-4209. DOI: 10.1002/MP.14497. URL: https://onlinelibrary.wiley.com/doi/full/10.1002/mp.14497%20https://onlinelibrary.wiley.com/doi/abs/10.1002/mp.14497%20https://aapm.onlinelibrary.wiley.com/doi/10.1002/mp.14497.

[117] Wayne D. Newhauser and Rui Zhang. "The physics of proton therapy". In: *Physics in medicine and biology* 60.8 (Apr. 2015), R155. ISSN: 13616560. DOI: 10.1088/0031-9155/60/8/R155. URL: /pmc/articles/PMC4407514/%20/pmc/articles/PMC4407514/?report=abstract%20https://www.ncbi.nlm.nih.gov/pmc/articles/PMC4407514/.

[118] James F. Ziegler, M. D. Ziegler, and J. P. Biersack. "SRIM - The stopping and range of ions in matter (2010)". In: *Nuclear Instruments and Methods in Physics Research, Section B: Beam Interactions with Materials and Atoms* 268.11-12 (June 2010), pp. 1818–1823. ISSN: 0168583X. DOI: 10.1016/j.nimb.2010.02.091.

[119] S. N. Chen et al. *Absolute dosimetric characterization of Gafchromic EBT3 and HDv2 films using commercial flat-bed scanners and evaluation of the scanner response function variability*. Tech. rep. 073301. Mar. 2016. DOI: 10.1063/1.4954921.

[120] D. S. Hey et al. "Use of GafChromic film to diagnose laser generated proton beams". In: *Review of Scientific Instruments* 79.5 (May 2008), p. 33. ISSN: 00346748. DOI: 10.1063/1.2901603/353408. URL: /aip/rsi/article/

79/5/053501/353408/Use-of-GafChromic-film-to-diagnose-laser-generated.

[121] George Hicks. "Ion beams accelerated by laser irradiation of thin foils and their applications". PhD thesis. London: Imperial College London, 2016.

[122] P. Bradford et al. "Measuring magnetic fields in laser-driven coils with dual-axis proton deflectometry". In: *Plasma Physics and Controlled Fusion* 63.8 (Aug. 2021). ISSN: 13616587. DOI: 10.1088/1361-6587/ac0bca.

[123] Lan Gao et al. "Ultrafast proton radiography of the magnetic fields generated by a laser-driven coil current". In: *Physics of Plasmas* 23.4 (Apr. 2016). ISSN: 10897674. DOI: 10.1063/1.4945643.

[124] A J Mackinnon et al. "Proton radiography as an electromagnetic field and density perturbation diagnostic (invited)". In: *Review of Scientific Instruments* 75.10 (Oct. 2004), pp. 3531–3536. ISSN: 0034-6748. DOI: 10.1063/1.1788893. URL: /aip/rsi/article/75/10/3531/350240/Proton-radiography-as-an-electromagnetic-field-and.

[125] J. L. Peebles et al. *An assessment of generating quasi-static magnetic fields using laser-driven "capacitor" coils*. Aug. 2022. DOI: 10.1063/5.0096784.

[126] M. Borghesi et al. "Multi-MeV Proton Source Investigations in Ultraintense Laser-Foil Interactions". In: *Physical Review Letters* 92.5 (Feb. 2004), p. 4. ISSN: 10797114. DOI: 10.1103/PHYSREVLETT.92.055003/FIGURES/3/MEDIUM. URL: https://journals.aps.org/prl/abstract/10.1103/PhysRevLett.92.055003.

[127] A. F. A. Bott et al. "Proton imaging of stochastic magnetic fields". In: *Journal of Plasma Physics* 83.6 (Dec. 2017), p. 905830614. ISSN: 0022-3778. DOI: 10.1017/S0022377817000939. URL: https://www.cambridge.org/core/journals/journal-of-plasma-physics/article/proton-imaging-of-stochastic-magnetic-fields/059EAA71A09C60E2B52CFCCE56C49479.

[128] C. A.J. Palmer et al. "Field reconstruction from proton radiography of intense laser driven magnetic reconnection". In: *Physics of Plasmas* 26.8 (Aug. 2019), p. 83109. ISSN: 10897674. DOI: 10.1063/1.5092733/15856788/083109{_}1{_}ACCEPTED{_}MANUSCRIPT.PDF. URL: /aip/pop/article/26/8/083109/1059453/Field-reconstruction-from-proton-radiography-of.

[129] Muhammad Firmansyah Kasim et al. "Quantitative shadowgraphy and proton radiography for large intensity modulations". In: *Physical Review E* 95.2 (Feb. 2017), p. 023306. ISSN: 24700053. DOI: 10.1103/PHYSREVE.95.023306/FIGURES/7/MEDIUM. URL: https://journals.aps.org/pre/abstract/10.1103/PhysRevE.95.023306.

[130] Carlo Graziani et al. “Inferring morphology and strength of magnetic fields from proton radiographs”. In: *Review of Scientific Instruments* 88.12 (Dec. 2017), p. 123507. ISSN: 10897623. DOI: 10.1063/1.5013029/13477084/123507{_}1{_}ACCEPTED{_}MANUSCRIPT.PDF. URL: /aip/rsi/article/88/12/123507/362103/Inferring-morphology-and-strength-of-magnetic.

[131] M. F. Kasim et al. “Retrieving fields from proton radiography without source profiles”. In: *Physical Review E* 100.3 (Sept. 2019). ISSN: 24700053. DOI: 10.1103/PhysRevE.100.033208.

[132] Daniel D. Hickstein et al. “A direct comparison of high-speed methods for the numerical Abel transform”. In: *Review of Scientific Instruments* 90.6 (June 2019). ISSN: 10897623. DOI: 10.1063/1.5092635/360138. URL: /aip/rsi/article/90/6/065115/360138/A-direct-comparison-of-high-speed-methods-for-the.

[133] William Hadley Richardson. “Bayesian-Based Iterative Method of Image Restoration*”. In: *JOSA, Vol. 62, Issue 1, pp. 55-59* 62.1 (Jan. 1972), pp. 55–59. ISSN: 0030-3941. DOI: 10.1364/JOSA.62.000055. URL: https://opg.optica.org/viewmedia.cfm?uri=josa-62-1-55&seq=0&html=true%20https://opg.optica.org/abstract.cfm?uri=josa-62-1-55%20https://opg.optica.org/josa/abstract.cfm?uri=josa-62-1-55.

[134] L. B. Lucy. “An iterative technique for the rectification of observed distributions”. In: *Astronomical Journal* 79.6 (June 1974), p. 745. ISSN: 0004-6256. DOI: 10.1086/111605. URL: https://ui.adsabs.harvard.edu/abs/1974AJ.....79..745L/abstract.

[135] J. G. Walker et al. “Blind deconvolution by means of the Richardson–Lucy algorithm”. In: *JOSA A, Vol. 12, Issue 1, pp. 58-65* 12.1 (Jan. 1995), pp. 58–65. ISSN: 1520-8532. DOI: 10.1364/JOSAA.12.000058. URL: https://opg.optica.org/viewmedia.cfm?uri=josaa-12-1-58&seq=0&html=true%20https://opg.optica.org/abstract.cfm?uri=josaa-12-1-58%20https://opg.optica.org/josaa/abstract.cfm?uri=josaa-12-1-58.

[136] Brandon K. Russell et al. “Ultrafast relativistic electron probing of extreme magnetic fields”. In: *Physics of Plasmas* 30.9 (Sept. 2023), p. 93105. ISSN: 10897674. DOI: 10.1063/5.0163392/2911971. URL: /aip/pop/article/30/9/093105/2911971/Ultrafast-relativistic-electron-probing-of-extreme.

[137] Derek B. Schaeffer et al. “Proton imaging of high-energy-density laboratory plasmas”. In: *Reviews of Modern Physics* 95.4 (Oct. 2023), p. 045007. ISSN: 15390756. DOI: 10.1103/REVMODPHYS.95.045007/FIGURES/29/MEDIUM. URL: https://journals.aps.org/rmp/abstract/10.1103/RevModPhys.95.045007.

[138] Bao Du et al. “Separating the contributions of electric and magnetic fields in deflecting the probes in proton radiography with multiple proton energies”. In: *Matter and Radiation at Extremes* 6.3 (May 2021). ISSN: 2468080X. DOI: 10.1063/5.0033834/913878. URL: /aip/mre/article/6/3/035903/913878/Separating-the-contributions-of-electric-and.

[139] Joseph M. Levesque and Lauren J. Beesley. “Reconstructing magnetic deflections from sets of proton images using differential evolution”. In: *Review of Scientific Instruments* 92.9 (Sept. 2021). ISSN: 10897623. DOI: 10.1063/5.0054862/15815118/093505{_}1{_}ACCEPTED{_}MANUSCRIPT.PDF. URL: /aip/rsi/article/92/9/093505/1030723/Reconstructing-magnetic-deflections-from-sets-of.

[140] Steffen Faik, Anna Tauschwitz, and Igor Iosilevskiy. “The equation of state package FEOS for high energy density matter”. In: *Computer Physics Communications* 227 (June 2018), pp. 117–125. ISSN: 0010-4655. DOI: 10.1016/J.CPC.2018.01.008.

[141] C. P. Ridgers et al. “The inadequacy of a magnetohydrodynamic approach to the Biermann battery: Kinetic effects on the Biermann battery”. In: *Philosophical Transactions of the Royal Society A: Mathematical, Physical and Engineering Sciences* 379.2189 (Jan. 2021). ISSN: 1364503X. DOI: 10.1098/rsta.2020.0017.

[142] G. Gregori et al. “Effect of nonlocal transport on heat-wave propagation”. In: *Physical Review Letters* 92.20 (May 2004). ISSN: 00319007. DOI: 10.1103/PhysRevLett.92.205006.

[143] T Ditmire et al. “Time-Resolved Study of Nonlocal Electron Heat Transport in High Temperature Plasmas”. In: *Physical Review Letters* 80.4 (1998), pp. 720–723.

[144] R. J. Henchen et al. “Observation of Nonlocal Heat Flux Using Thomson Scattering”. In: *Physical Review Letters* 121.12 (Sept. 2018), p. 125001. ISSN: 10797114. DOI: 10.1103/PHYSREVLETT.121.125001/FIGURES/5/MEDIUM. URL: https://journals.aps.org/prl/abstract/10.1103/PhysRevLett.121.125001.

[145] E. P. Hartouni et al. "Evidence for suprathermal ion distribution in burning plasmas". In: *Nature Physics 2022 19:1* 19.1 (Nov. 2022), pp. 72–77. ISSN: 1745-2481. DOI: 10.1038/s41567-022-01809-3. URL: https://www.nature.com/articles/s41567-022-01809-3.

[146] Mitsuo Takeda, Hideki Ina, and Seiji Kobayashi. "Fourier-transform method of fringe-pattern analysis for computer-based topography and interferometry". In: *JOSA, Vol. 72, Issue 1, pp. 156-160* 72.1 (Jan. 1982), pp. 156–160. ISSN: 00303941. DOI: 10.1364/JOSA.72.000156. URL: https://opg.optica.org/viewmedia.cfm?uri=josa-72-1-156&seq=0&html=true%20https://opg.optica.org/abstract.cfm?uri=josa-72-1-156%20https://opg.optica.org/josa/abstract.cfm?uri=josa-72-1-156.

[147] Jason Cole. "Diagnosis and Application of Laser Wake field Accelerators". PhD thesis. London: Imperial College, 2016, pp. 73–93.

[148] T. D. Arber et al. *Contemporary particle-in-cell approach to laser-plasma modelling*. Sept. 2015. DOI: 10.1088/0741-3335/57/11/113001.

[149] V Yu Bychenkov et al. "Theory of filamentation instability and stimulated Brillouin scattering with nonlocal hydrodynamics". In: *Physics of Plasmas* 7.5 (May 2000), pp. 1511–1519. ISSN: 1070-664X. DOI: 10.1063/1.873970. URL: /aip/pop/article/7/5/1511/267224/Theory-of-filamentation-instability-and-stimulated.

[150] L. Willingale et al. "Proton deflectometry of a magnetic reconnection geometry". In: *Physics of Plasmas* 17.4 (Apr. 2010), p. 43104. ISSN: 1070664X. DOI: 10.1063/1.3377787/970209. URL: /aip/pop/article/17/4/043104/970209/Proton-deflectometry-of-a-magnetic-reconnection.

[151] M. J.E. Manuel et al. "First measurements of Rayleigh-Taylor-induced magnetic fields in laser-produced plasmas". In: *Physical Review Letters* 108.25 (June 2012), p. 255006. ISSN: 00319007. DOI: 10.1103/PHYSREVLETT.108.255006/FIGURES/5/MEDIUM. URL: https://journals.aps.org/prl/abstract/10.1103/PhysRevLett.108.255006.

[152] L. Gao et al. "Magnetic field generation by the Rayleigh-Taylor instability in laser-driven planar plastic targets". In: *Physical Review Letters* 109.11 (Sept. 2012), p. 115001. ISSN: 00319007. DOI: 10.1103/PHYSREVLETT.109.115001/FIGURES/5/MEDIUM. URL: https://journals.aps.org/prl/abstract/10.1103/PhysRevLett.109.115001.

[153] S. A. Slutz et al. “Pulsed-power-driven cylindrical liner implosions of laser preheated fuel magnetized with an axial field”. In: *Physics of Plasmas* 17.5 (May 2010), p. 56303. ISSN: 1070664X. DOI: 10.1063/1.3333505/922150. URL: /aip/pop/article/17/5/056303/922150/Pulsed-power-driven-cylindrical-liner-implosions.

[154] Ryan D. McBride and Stephen A. Slutz. “A semi-analytic model of magnetized liner inertial fusion”. In: *Physics of Plasmas* 22.5 (May 2015), p. 52708. ISSN: 10897674. DOI: 10.1063/1.4918953/13780440/052708{_}1{_}ACCEPTED{_}MANUSCRIPT.PDF. URL: /aip/pop/article/22/5/052708/110890/A-semi-analytic-model-of-magnetized-liner-inertial.